MICROWAVE RADIOMETRIC THERMOMETRY IN LAYERED TISSUE STRUCTURES

by

Mark S Hawley
BSc

A thesis submitted for the
degree of Doctor of Philosophy
Department of Medical Physics
and Clinical Engineering,
University of Sheffield

July 1986

Summary

Microwave radiometric thermometry in layered tissue structures

Mark S Hawley

Non-invasive thermal imaging and temperature measurement by microwave radiometry is investigated for medical diagnostic applications and monitoring hyperthermia treatment of cancer, in the context of the heterogeneous body structure.

The temperature measured by a radiometer is a function of the emission and propagation of microwaves in tissue and the receiving characteristics of the radiometric probe. Propagation of microwaves in lossy media is analysed by a spectral diffraction approach. Extension of this technique via a cascade transmission line model provides an efficient algorithm for predicting the field patterns of aperture antennas contacting multi-layered tissue. Comparisons of computer simulations with field measurements in homogeneous and bi-layered tissue-equivalent media confirm the validity of the algorithm.

A coherent radiative transfer analysis is used to relate the field pattern of a radiating antenna to its receiving characteristics when used as a radiometer probe, leading to a method for simulating radiometric data. The design and construction of a 4.6 GHz radiometer is described and good agreement is found between computer simulations and radiometer measurements in tissue equivalent phantoms. Measurements and simulations are used to assess the effect of overlying fat layers upon radiometer response to temperature hot-spots in muscle-type media. It is shown that dielectric layering in tissue greatly influences measured temperatures and should be accounted for in the interpretation of radiometric data.

The feasibility of employing microwave radiometry for tomographic mapping of differential temperature distributions induced by hyperthermia is examined. A suitable reconstruction algorithm is proposed; however the limited 'depth of view' in lossy tissue is shown to restrict the volume which can be imaged and thus its use for monitoring deep hyperthermia is doubtful. Alternative applications of this technique in medical diagnostics are proposed.

Acknowledgements

I would like to express my gratitude to Professor A P Anderson and Dr J Conway for their supervision and assistance throughout the course of this work.

Acknowlegements are due to Professor M M Black for the facilities made available in the Department of Medical Physics and Clinical Engineering at Weston Park Hospital and to Professor F A Benson for those of the Department of Electronic and Electrical Engineering.

I wish to acknowledge the financial support of the James Morrison Research Fellowship from Weston Park Hospital.

Many thanks to my colleagues, especially to Dr P A Cudd for his help and for providing Appendix 1 of this thesis, and to Professor B H Brown and Mr F C Smith for many useful discussions.

I am also grateful to Dr A J T Whitaker for his assistance with the VAX computer and to Mr D J Williams for writing the software for the BBC computer. Thanks are due to the workshop staff of both departments.

I am indebted to Mrs J Hedge for her efficient typing of this thesis.

Finally, I would like to thank my friends and family for their much needed support.

TABLE OF CONTENTS

Page Number

Introduction 1

Chapter 1 Microwave Radiometry 4

1.1 Principles of temperature measurement by microwave radiometry 4

- 1.1.1 Thermal radiation 4
- 1.1.2 Propagation of radiation in lossy tissue 5
- 1.1.3 Microwave antennas 7
- 1.1.4 Microwave receivers 8

1.2 Applications of microwave radiometry 9

- 1.2.1 Applications of microwave radiometry in the control of hyperthermia treatment of malignant diseases 9
  - 1.2.1.1 Hyperthermia treatment of malignant disease 9
  - 1.2.1.2 The importance of temperature control in hyperthermia 11
  - 1.2.1.3 Invasive temperature monitoring 14
  - 1.2.1.4 The suitability of microwave radiometry for hyperthermia monitoring 14
- 1.2.2 Applications of microwave radiometry in medical diagnosis 16
  - 1.2.2.1 Detection of thermal irregularities in the human body 16
  - 1.2.2.2 Infra-red thermography 17
  - 1.2.2.3 The suitability of microwave radiometry as a diagnostic tool 19

1.3 Principal investigators in microwave thermography 21

- 1.3.1 Radiometry systems 21
- 1.3.2 Principal Centres of Research 23

1.4 The interpretation of radiometric measurements 30

Chapter 2 An incremental spectral diffraction method for predicting field patterns of contacting aperture antennas radiating into lossy layered media 33

2.1 Prediction of the field patterns of radiating aperture antennas in tissue 33

Page Number

2.2 Spectral diffraction in homogeneous media 34

2.2.1 Theory for homogeneous media 34
2.2.2 Analysis of a wavefront as an angular spectrum of plane waves 37
2.2.3 The spectral filter 40

2.3 Incremental spectral diffraction in layered structures 41

2.4 Application of the incremental spectral diffraction method to the prediction of field patterns of tissue-contacting aperture antennas 45

2.5 Computer implementation of the field prediction method 47

Chapter 3 Measurement of radiometer probe field patterns in homogeneous and layered tissue-equivalent phantoms and comparison with computer simulations 49

3.1 Measurement of aperture field patterns in phantoms 49

3.1.1 Microwave measurement apparatus 49
3.1.2 Tissue-simulating phantom materials 50
3.1.3 Computer controlled scanning and data logging system 52
3.1.4 Details of the measurement procedure 53

3.2 Comparison of simulations with measurements in homogeneous and bi-layered media 54

3.2.1 Comparison in a homogeneous medium 54
3.2.2 Comparison in bi-layered media 55
3.2.3 Correspondence of simulation to experimental models 57
3.2.4 Discussion of results 59

3.3 Simulated field patterns of rectangular apertures radiating into lossy media 60

Chapter 4 Prediction of radiometer response to temperature distributions in layered tissue 63

4.1 Prediction of radiometric temperature by radiative transfer 63

4.1.1 Incoherent Radiative Transfer theory 63
4.1.2 Coherent Radiative Transfer theory 65

4.2 A method for predicting radiometric temperature 67

4.3 Practical implementation of the temperature prediction method 72

Page Number

Chapter 5 Design, construction and operation of a 4.6 GHz radiometer 75

5.1 Description of the radiometer 75

5.2 The design and construction of a contacting waveguide probe 78

5.2.1 Design considerations 78
5.2.2 Construction of the filled waveguide probe 79

5.3 Radiometer performance 80

5.3.1 Calibration of the radiometer 80
5.3.2 Temperature resolution and stability 81

5.4 The radiometer in a null-balancing mode 85

Chapter 6 Radiometric measurement of raised temperature regions in homogeneous and bi-layered tissue-equivalent phantoms and comparison with simulations 88

6.1 Radiometric measurements in a homogeneous water phantom 88

6.1.1 Radiometric linear scanning of a raised temperature region within a constant temperature water bath 88
6.1.2 Sources of measurement uncertainty 90
6.1.3 Comparison of simulated with measured results 91

6.2 The influence of tissue layers on radiometric measurements 95

6.2.1 Comparison of radiometric scans in homogeneous and bi-layered structures 95
6.2.2 Discussion 98

Chapter 7 A feasibilty study of tomographic reconstruction of microwave radiometric data for thermal mapping during hyperthermia treatment 101

7.1 Proposal for a radiometric measurement system to monitor hyperthermia treatment 101

7.2 Back-projection algorithm for tomographic reconstruction of temperature difference data 103

7.2.1 Tomographic reconstruction by back-projection 103
7.2.2 An algorithm for reconstruction of radiometric data 104
7.2.3 Tomographic computer model 106

Page Number

7.3 Measurement and reconstruction of experimental tomographic data 110

7.3.1 Measurement and reconstruction of elliptical scan data 110
7.3.2 Measurement and reconstruction of linear scan data 111

7.4 The feasibility of tomographic reconstruction of temperature distributions in the body 114

Chapter 8 Conclusions 116

References

Appendix 1

Appendix 2

Publications

Introduction

Temperature has always been an important diagnostic indicator for the medical clinician. Under normal conditions, the distribution of temperature within the human body is inherently stable and follows recognisable patterns. Abnormal variations, particularly local hot areas or left to right asymmetry, may signify general or local breakdown of body function. In the earliest manifestations of diagnosis by thermometry, fevers and inflammations were detected by touch. Subsequent development of the mercury-in-glass thermometer permitted quantification of general body temperature but gave no indication of local anomalies.

With the advent of infra-red thermography in the 1950s, the first thermal imaging of the body was realised by exploiting the radiative nature of matter. With infra-red cameras, variations in skin temperature are converted to optical images, thus allowing a doctor experienced in the interpretation of thermograms to pinpoint any irregularities. However, such measurements are restricted to surface temperatures only by the penetration depth of infra-red radiation in tissue. The majority of irregularities of interest occur in subcutaneous regions.

At microwave frequencies, the decreased opacity of tissue allows radiation emitted at greater depth within the body to reach the surface. Subcutaneous thermal distributions may therefore be detected. Microwave radiometry was developed as a technique for sensing thermal emissions in the 1940s, with applications in radio astronomy and remote sensing of the earth and its atmosphere. The application of this technique in medicine was first proposed by

Barrett et al in the early 1970s [1], who employed a contacting waveguide antenna to couple microwave radiation emitted by tissue into a comparison type or 'Dicke' radiometer working at a centre frequency of 3.3 GHz. In the same period Edrich et al [2] developed a millimetre wavelength scanning system employing a remote dish antenna to give images of thermal distributions. Since 1974, developments of these basic radiometer designs have improved the capability of the technique and widened its applications.

Originally, the primary application envisaged was screening for breast cancer. The technique has since been applied experimentally to the detection of various types of cancers and to a wide range of pathologies with associated raised temperatures, such as inflammation of the joints and spinal nerve irritation. Another application, which has emerged more recently, is the monitoring of hyperthermia, a treatment for malignant disease which aims to destroy cancer cells by inducing elevated temperatures, either as a treatment by itself or through its synergistic effect with radiation or chemotherapy. Although the therapeutic value is now generally recognised, progress in clinical hyperthermia is limited by inadequate temperature monitoring. Microwave radiometry shows potential as a means of non-invasively monitoring the induced thermal distribution.

In both areas of diagnosis and treatment monitoring, quantitative temperature measurement or qualitative imaging procedures using microwave radiometry require careful interpretation of radiometric data. This can only be achieved with an understanding of the emission and propagation of microwave radiation in tissue structures and the interaction with the radiometer antenna or probe. The object of this research is to study these factors in both homogeneous and layered tissue structures to facilitate improved interpretation of radiometric data from both single probe scanning and tomographic imaging in the context of the heterogeneous body.

Chapter 1

Microwave Radiometry

1.1 Principles of temperature measurement by microwave radiometry

  1.1.1 Thermal radiation

  1.1.2 Propagation of radiation in lossy tissue

  1.1.3 Microwave antennas

  1.1.4 Microwave receivers

1.2 Applications of microwave radiometry

  1.2.1 Applications of microwave radiometry in the control of hyperthermia treatment of malignant diseases

    1.2.1.1 Hyperthermia treatment of malignant disease

    1.2.1.2 The importance of temperature control in hyperthermia

    1.2.1.3 Invasive temperature monitoring

    1.2.1.4 The suitability of microwave radiometry for hyperthermia monitoring

  1.2.2 Applications of microwave radiometry in medical diagnosis

    1.2.2.1 Detection of thermal irregularities in the human body

    1.2.2.2 Infra-red thermography

    1.2.2.3 The suitability of microwave radiometry as a diagnostic tool

1.3 Principal investigators in microwave thermography

  1.3.1 Radiometry systems

  1.3.2 Principal Centres of Research

1.4 The interpretation of radiometric measurements

1.1 Principles of temperature measurement by microwave radiometry

1.1.1 Thermal Radiation

Radiated electromagnetic energy results from changes in the energy states of atoms and molecules, caused by interactions of charges with each other and with electromagnetic waves. Matter contains enormous numbers of particles which, if at a temperature above absolute zero, continuously interact absorbing and emitting electromagnetic energy at all frequencies. The intensity spectrum of this emitted radiation depends on its physical temperature. Figure 1.1 shows the power radiated versus frequency by a black-body at the temperature of the human body (37 °C).

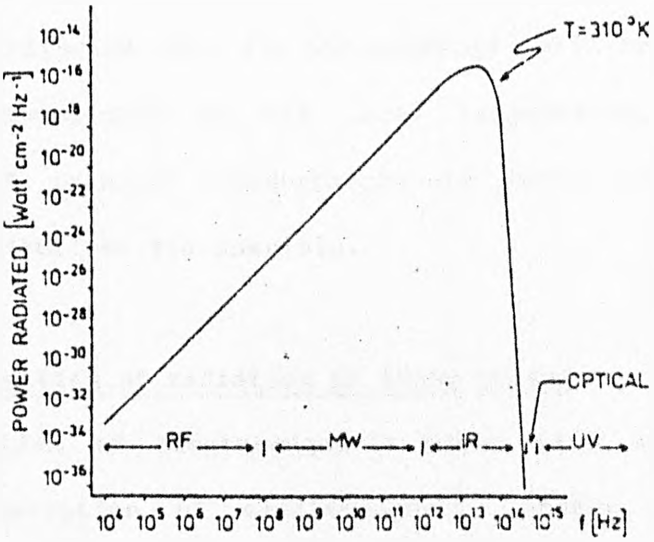

Fig. 1.1 Power radiated by a black body versus frequency at 310 °K (37 °C) (reproduced from [33])

The highest emitted power occurs at infra red frequencies ($\lambda \sim 10\ \mu m$); at microwave frequencies the power is lower by a factor of around 10^8. The emission of radiation by a black body is described by Planck's law which gives the power emitted by the body

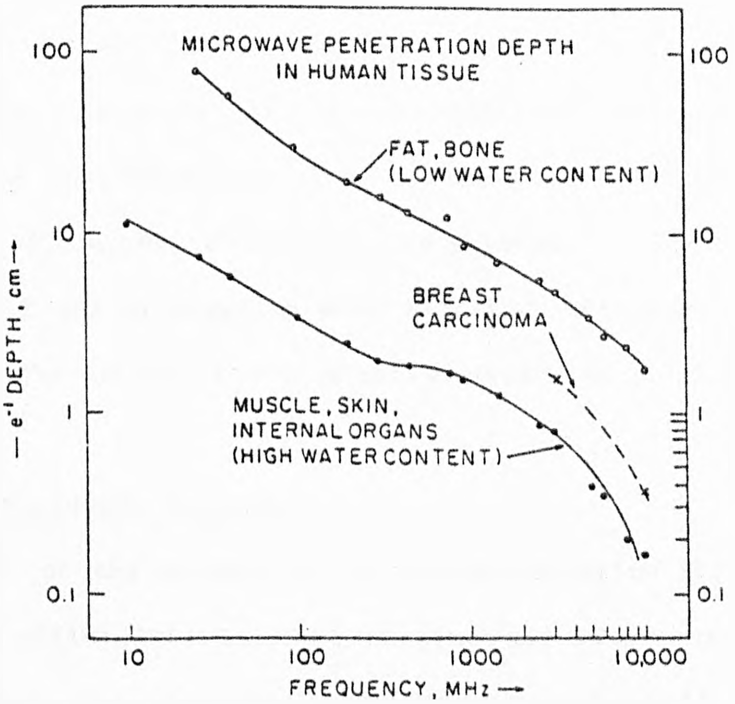

Fig. 1.2 1/e depth versus frequency for high water content and low water content tissues (reproduced from [35])

the various tissue types is the total water content of the tissue. Those with high water content, eg muscle and skin, attenuate microwaves more strongly than those with low water content, eg bone and fat. The absorption rate also increases with increasing frequency. This relationship determines the major advantages of microwave thermography over infra-red thermography. The penetration depth of infra-red radiation in tissue is of the order of 0.1 mm and only thermal radiation from the skin surface only is externally detectable. Microwave radiation has penetration depths varying from 1 mm at high frequencies to 10 cm from which information can be obtained concerning subcutaneous temperature distribution. The exponential attenuation results in temperatures measured by microwave radiometry which are an average of the temperature distribution with depth weighted by an exponential be matched to a mean value of tissue impedance, say 75 Ω, which diminishes the range of tissue emissivity values from 0.7 to 1.0 [3], allowing more accurate temperature measurement. Other types of contacting antenna, for example coaxial and microstrip-microslot, have also been employed successfully for microwave radiometry.

1.1.4 Microwave receivers

The power coupled into a microwave receiver by a perfect antenna from a uniform temperature medium is;

$$P = kTB \qquad 1.1$$

where k is Boltzmann's constant,

B is the measurement bandwidth,

and T is the tissue temperature

for a typical receiver with a bandwidth of 500 MHz and for normal body temperature, this power is 2.6×10^{-12} W. The temperature resolution necessary in medical microwave radiometry applications is generally considered to be 0.1°C [4]. The microwave receiver must, therefore, have the ability to distinguish power level changes of the order of 10^{-15} W.

The basic components necessary for a microwave receiver which can measure these low levels of power are a high amplification stage followed by a detector, converting the power level to a voltage which can be processed by low frequency electronic components. The microwave components, due to their physical temperature, add a significant amount of noise which is indistinguishable from the noise input from the antenna. Therefore, all components must be of high quality to minimize the system noise levels. The effect of system instabilities can also be reduced by selection of circuit design. The comparison radiometer [5] reduces the effect of gain fluctuations in the amplification stage by comparing the input temperature signal regularly with a known temperature signal.

1.2 Applications of microwave radiometry

1.2.1 Applications of microwave radiometry in the control of hyperthermia treatment of malignant disease

1.2.1.1 Hyperthermia treatment of malignant disease

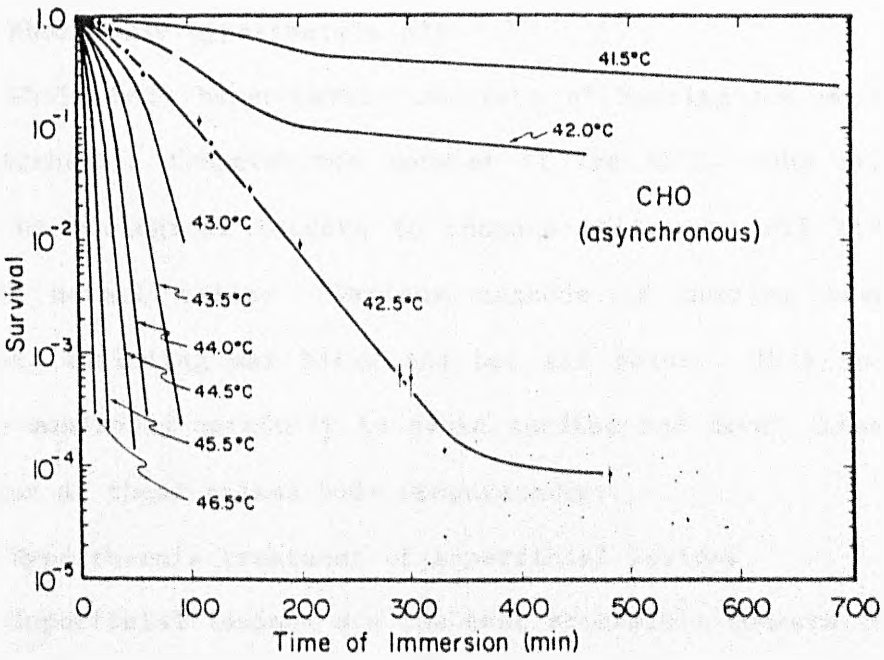

Fig. 1.3 Cell survival versus time at indicated temperatures.

Hyperthermia means 'raised temperature' and in this context describes a treatment for malignant disease which aims to destroy cancer cells through elevated temperatures. Figure 1.3 shows the malignant cell survival versus time of heating for a range of temperatures above body temperature. There is a critical temperature around 42.5°C above which the cell survival decreases dramatically. The aim of hyperthermia treatment is to heat the cancerous tissue to above this threshold for a given length of time but to minimise the heat damage caused to normal healthy tissue.

There is now general recognition that hyperthermia will become an important weapon in the fight against cancer. Clinical trials [6,7] indicate that radiation therapy when used in conjuction with hyperthermia, is more effective than using radiation therapy alone. The application of hyperthermia alone generally gives poorer results. However, the synergistic effect with radiation therapy is sufficiently important to warrant the large research effort.

Treatments can be divided into three groups:

- Whole body hyperthermia [8]:

Whole body hyperthermia consists of heating the whole body to hyperthermic temperatures between 41 and 42°C. The treatment relies on biological factors to enhance malignant cell kill over that of normal cells. Various methods of heating have been employed, including wax baths and hot air boxes. This technique must be monitored carefully to avoid cardiac and liver damage that may occur at these raised body temperatures.

- Hyperthermia treatment of superficial lesions

Superficial lesions are the most accessible tumours to treat with hyperthermia. The primary methods of microwave heating are by single or multi-applicator systems [9]. The low penetration of microwave power limits the therapeutic depth to less than 4 cm below the skin. Overheating of the surface layers can be reduced by use of skin cooling.

- Hyperthermia treatment of deep-seated lesions

The most difficult problem still remaining in hyperthermia is the treatment of deep-seated lesions. Two approaches to this problem have been termed 'regional' and 'localised' hyperthermia.

Regional hyperthermia is the heating of a region of the body that encompasses the tumour to hyperthermic temperatures while minimizing systemic heating. This method again relies on the biological enhancement factors but also employs techniques that attempt to preferentially deposit power at the site of the tumour. The most common techniques employ radio frequency (RF) or low frequency current sources. Heating can be achieved by means of inductive coils [10] or capacitive plates [11]. An alternative to these is to use aperture applicators, for example waveguides. Van Rhoon et al [12] used a water-filled ridged waveguide with a 60 x 30 cm aperture for regional hyperthermia at 27 MHz. Some control of the heated volume can be achieved using an annular array of applicators. Theoretical and experimental studies [13,14] have shown that uniform power deposition can be achieved within a homogeneous body by selection of phase and amplitude for each of eight aperture applicators arranged in a hexagonal array.

Localised hyperthermia of deep lesions within the body attempts the deposition of power only in the tumour volume with minimum heating of surrounding tissue. Non-invasive systems have yet to be assessed in a clinical situation. Research is progressing in two main areas; microwave phased arrays and ultrasound. The short wavelength of microwave radiation allows concentration of power in small volumes. It is expected [15] that by using a sufficient number of suitably phased radiators the enhancement of power deposition at the focus could overcome the problem of low penetration into tissue.

Ultrasound heating allows good localisation and good penetration in soft tissue. Significant disadvantages have been experienced due to large reflections at bone/soft tissue and gas/tissue interfaces, and high absorption in bone [10].

1.2.1.2 The importance of temperature control in hyperthermia

Extensive research has been carried out into different hyperthermia treatment methods [10]. However, the extent to which the temperature inside the body can be monitored sets a limit on the progress that is possible in this area. The efficacy of hyperthermia treatment relies on reaching and maintaining a sufficient temperature (Fig 1.3) throughout the treatment. Inhomogeneous power deposition in the tumour from the heating system will invariably cause cold or hot regions in the target volume. A cold region is an area which does not reach hyperthermic temperature, leading to deficient cell destruction in these areas and inevitably tumour recurrence. A hot region is an overheated area which may result in tissue necrosis. Cold and hot areas in a tumour may also occur due to the influence of blood flow. The centre of large tumours may have poor blood supplies and so heat is removed slowly compared with the peripheral areas which are usually highly vascularised and consequently difficult to heat.

Normal tissue cells are also damaged by heating to hyperthermic temperatures. Any heating which occurs outside the tumour volume is disadvantageous and may result in blistering, burns or irreparable tissue damage. All methods of producing hyperthermia inevitably deposit power outside the tumour volume. Although some success has been achieved in preferentially heating regions of the torso and abdomen, in general areas of normal tissues will often reach temperatures as high as those in the tumour. Using regional heating methods, standing waves may be induced due to inhomogeneities in the tissue, and high power deposition at muscle-bone interfaces have been measured. Higher frequency microwave radiation, as used for localised hyperthermia, may induce excessive heating in tissues with high water content and suffer from resonant conditions existing in subdermal fat layers. The small focal region found in ultrasonic induced hyperthermia may also result in poor thermal distribution unless the transducer is scanned over the surface to disperse the power deposition.

Computer and phantom modelling of many hyperthermia systems has been used to predict the heating patterns both prospectively and retrospective to treatment. These modelling procedures are often highly sophisticated; however, the situation inside the human body is extremely complex. Inhomogeneities in tissue and blood flow make successful prediction of temperature distributions difficult. It has been noted [16], from thermocouple measurements, that the temperature attained in different patients for similar treatment geometries are widely different. A modelling technique would in these cases have predicted similar temperature distributions.

The above arguments illustrate that application of hyperthermia techniques to the treatment of tumours requires detailed knowlege of the temperature distribution throughout the heated region. Although modelling techniques give some estimate of the likely heating pattern, in most cases the complexity of the local blood flow means that relating this to a temperature distribution is a major task. Therefore a system for measuring the actual temperature during heating is required.

1.2.1.3 Invasive temperature monitoring

The method used to monitor nearly all clinical hyperthermia treatments is by implantation of invasive temperature probes [17]. The use of invasive methods for this form of therapy is undesirable due to the excessive patient trauma involved. As outlined in the previous section, temperature monitoring throughout the heated region is necessary. Invasive probes, such as thermocouples, are only capable of measuring point temperatures. Large temperature gradients can be shown to exist within the tumour and within normal tissue during heating. Therefore, for successful treatment monitoring a large number of point measurements may be necessary. Invasive probes may also interfere with the treatment field. Implanted thermocouples interact with applied electromagnetic field, causing excess heating at the thermocouple site. Non-perturbing invasive probes are available, but are very expensive.

1.2.1.4 The suitability of microwave radiometry for hyperthermia monitoring

From the above discussion and by examining the collective experience of workers in hyperthermia, some desirable features of a practical temperature monitoring system can be listed:

- The system should be non-invasive.
- The measurements should be insensitive to secondary changes which may occur due to the heating process; for example, changes in the dielectric properties of tissue due to changes in blood flow.
- The system should be passive to the heating field.
- The resolution of the system should be better than:-

0.1°C temperature sensitivity

1 sec response time

1 cm spatial resolution.

- The system should be capable of measuring temperatures at depth.
- The ideal system for monitoring hyperthermia treatment would be tomographic, providing a temperature map throughout the heated volume.

Microwave radiometry is a non-invasive technique which directly measures noise temperature. Other proposed monitoring techniques [18, 19, 20] measure quantities (eg dielectric properties, proton spin relaxation time) which are a function of temperature, but microwave radiometry is less susceptible to changes in tissue properties and blood perfusion which occur during heating. However, since changes in blood flow and tissue dielectric properties alter the local emissivity, attentuation and scattering characteristics of the medium, the technique cannot be totally immune to these factors. Microwave radiometry should be compatible with most heating systems, however, some RF hyperthermia systems will cause interaction with the metallic radiometer components. This difficulty should not arise where microwave heating with contacting applicators leads to minimal stray radiation effects. A temperature resolution of 0.1°C for a one second response time can be achieved for state-of-the-art radiometers. The spatial resolution depends on the receiving frequency, on the size of the antenna probe and on the tissue structure. The depth in tissue from which useful information can be received is also highly dependent on these factors.

The idea of using microwave radiometry to control hyperthermia treatment has been under discussion for some time [21]. Systems have been designed to perform heating and temperature measurement at different frequencies to avoid intermodulation. An alternative method is to perform the heating at the centre frequency of the radiometer [22, 23], with the advantage that the same antenna may be used for both heating and monitoring. A system that employs microwave radiometers at two frequencies is available commercially [24]. Clinical results [24, 25] using this system have shown good correlation between radiometrically measured temperatures and those measured with implanted thermocouples. The conclusion is that microwave radiometry shows promise as a method of non-invasively controlling hyperthermia treatments.

1.2.2 Applications of microwave radiometry in medical diagnosis

1.2.2.1 Detection of thermal irregularities in the human body

The body's thermoregulatory system attempts to maintain the whole body at a constant temperature. Any local regions of high or low temperature, particularly asymmetry between left and right regions of the body, may be indicative of some pathological disorder; a region of abnormally high metabolic activity or a breakdown in the thermoregulatory system. Cancer is one of the causes of high metabolic activity in a localised area of the body. An active tumour growth is invariably hotter than the surrounding tissue [26] (Fig 1.4). Another cause may be inflammation of tissue, such as arthritis or appendicitis. Stenosis or blockage of the vascular system may result in a localised raised temperature around the source of the obstruction, such as in deep vein thromboses [27] (a serious cause of pulmonary embolism), or large regions of lower temperature in the case of an arterial occlusion. Spinal disorders are often associated with abnormal temperature in peripheral areas of the body [28] resulting from entrapment of the nerve roots. A means of imaging temperature distributions and measuring local temperatures within the body could give valuable information to improve diagnosis of these conditions.

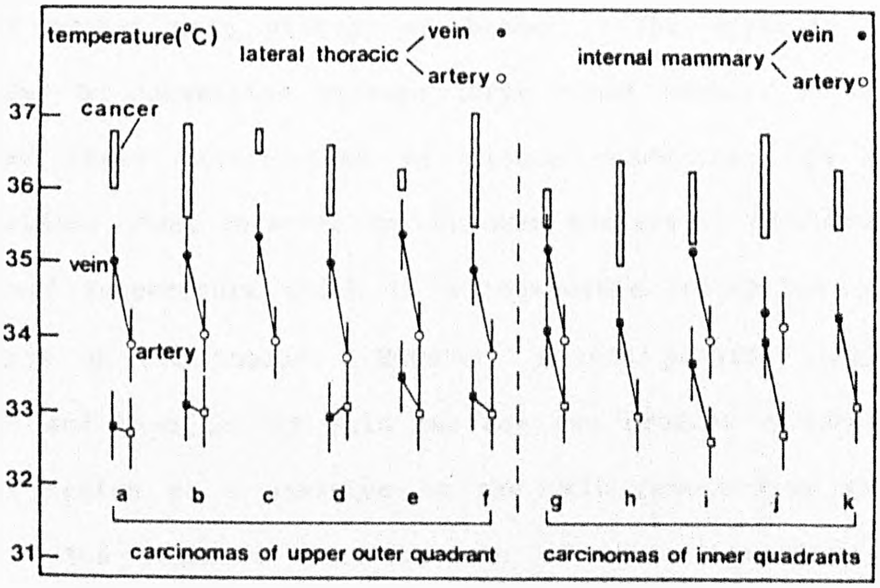

Fig. 1.4 Tumour and blood temperatures in breast carcinomas (reproduced from [26]).

1.2.2.2 Infra-red thermography

For nearly thirty years the technique of infra-red thermography has been applied extensively to the imaging of thermal distribution. The infra-red region of the electromagnetic spectrum was popular for two reasons. Over most of the infra-red spectrum, as in the microwave region, emitted power is proportional to the body temperature. Also, at body temperature most power is emitted in the infra-red region, a factor of 10^8 times the power emitted at microwave frequencies. Infra-red thermography, however, has many disadvantages. The small depth (~ μm) from which detectable infra-red radiation is emitted from tissue means that only skin temperature may be measured. The source of these raised temperatures in the body is often located at depth. A consequence of this is that infra-red techniques only measure temperatures that are referred to the skin surface by non-radiative mechanisms. Two mechanisms chiefly responsible are thermal conduction in over-lying tissues and convection via blood flow. Consider the case of a tumour buried deep within the breast. The capacity for heat transfer by convection through large blood vessels is up to one hundred times higher than by tissue conduction and capillary convection. Heat referred to the skin surface by conduction gives a raised temperature which is a reasonable indication as to the location of the tumour. However, a vein passing close to the tumour and then to the skin surface can produce a substantially hotter region at a position on the skin remote from the tumour site. The relative contributions of these transfer processes depends on tissue vascularity which may be significantly different for varying breast tissues, particularly under malignant conditions. In addition, changes in ambient temperature severely affect skin temperatures and may result in erroneous infra-red measurements. In view of these problems, the interpretation of infra-red thermograms is difficult and contains many uncertainties. Although some criteria for their interpretation can be established [29] the limitations of the technique have been recognised [30, 31] leading to reduced clinical use in the detection of tumours. The problems with detection of tumours are equally applicable to diagnosis of other conditions.

1.2.2.3 The suitability of microwave radiometry as a diagnostic instrument

Considering the limitations of infra-red measurement, the major requirements for a new technique for detecting thermal abnormalities are that temperatures at depth should be measurable directly by non-invasive means. Microwave radiometry should provide these desired features. The function of the radiometer, and therefore the performance requirements, are similar to those for hyperthermia monitoring. However, some differences should be noted. A major consideration is the transient nature of hyperthermia induced hot-spots in comparison to a thermal irregularity which results in a constant temperature distribution. The fast data collection times which are required for treatment monitoring are therefore not fundamental to diagnostic applications. The only constraint imposed is the time during which a patient can remain relatively still and comfortable. Tumour temperatures typically range from 1°C to 3°C above body temperature [32, 33] compared to hot-spots of between 5°C and 10°C during hyperthermia. In addition, the extent of the hot area is usually smaller. As a consequence, the differential signal which the radiometer is required to measure is substantially lower. However, accuracy in absolute terms is not essential; in order to detect a thermal abnormality, a temperature change only need be recognised.

The main application for microwave radiometry has been found in the detection of breast cancer. The technique could be particularly suitable for the screening of patients because of its non-invasive and non-hazardous nature. Results, using a non-contacting scanning radiometer system [34] at 30 GHz and 68 GHz, showed that the deeper detection potential at these frequencies allowed diagnosis of breast disease which was not evident from infra-red measurements. A clinical study of over 5000 women was carried out [35] by measuring with a 3.3 GHz contacting system, symmetrical points in the left and right breasts. Analysis of the results, by applying numerical criteria, determined whether the subject had cancer. The detection rate was compared to those of infra-red thermography and xeromammography and the conclusions drawn were that the detection rate by microwave radiometry was not significantly better than that by infra-red thermography, although the types of tumours which could be detected by the two methods were often different. Xeromammography gave the best results, but it was found that the combination of infra-red and microwave radiometry, followed up in the case of positive results by xeromammography, gave equally good diagnostic results, and led to less women being exposed to X-rays. Other studies [36, 37] concluded that microwave radiometry showed promise in the detection of primary and recurrent breast cancer and lymphoma. They also noted that several tumours were detected which could not be detected by xeromammography. Similar general conclusions have been reached [38, 39, 40] for the detection of brain, thyroid and bone tumours. Clinical assessment of microwave radiometry for medical diagnosis is continuing but fewer results have been published since 1982.

In conclusion, microwave radiometry has a role to play in the detection of cancer and other disease with associated thermal changes in tissue. Further work is still required to assess and interpret results.

1.3 Principal investigators in microwave thermography

In this section the work of the principal investigators in microwave radiometry is detailed. The discussion concentrates on the design of the radiometers that have been built at the different research centres and on variations on the basic design of microwave radiometry systems.

1.3.1 Radiometry Systems

The five types of radiometry system which are in use (or have been proposed) at present are:-

(i) Comparison type with contacting antenna

(ii) Conparison type with non-contacting antenna

(iii) Multi-frequency radiometer

(iv) Two-probe correlation radiometer

(v) Aperture synthesis thermography system (proposed)

A brief description of each of these systems will now be presented, with an outline of their respective advantages. A more detailed description can be found under the appropriate Research Centre sub-section.

(i) Comparison type with contacting antenna

The comparison type radiometer is based on a design by Dicke [5]. This design is most common for medical applications and most other radiometer types are refinements of this basic system. Many recent radiometer designs therefore employ a feedback/noise injection method, known as a self-balancing or null-balancing circuit, to compensate for variations in tissue emissivity. A comparison type radiometer and a feedback/noise injection system have been designed and built during the course of this work and a full description of both can be found in Chapter 5.

(ii) The comparison type with non-contacting antenna

The comparison method of receiving is again incorporated but a non-contacting elliptical dish antenna is employed to collect the microwave signal. This design allows non-contacting scanning of the patient to produce a two dimensional map of the temperature distribution close to the surface.

(iii) The multi-frequency radiometer

Measurements by a multi-frequency radiometer are used to provide more data regarding the distribution of temperature with depth into tissue. With reference to figure 1.2, the depth of penetration of radiation into tissue and therefore the depth from which temperature information can be gathered decreases as the radiation frequency increases. By taking radiometric temperature measurements at several frequencies a proportional amount of depth information may be collated.

(iv) The two probe correlation radiometer

The technique of correlation radiometry allows greater lateral resolution in the location of the temperature gradients. The correlation radiometer measures the correlation function between signals received by two probes placed close to each other on the tissue surface. This correlation signal is a function not only of the signal amplitude but also of the phase. As such, the system is sensitive to signals which originate in the volume coupled to both probes and is insensitive to signals from volumes coupled to only one probe. Another interesting feature is that the technique is unable to detect changes in a uniform temperature but is highly sensitive to temperature gradients. This technique therefore collects different, but complementary, information to that obtained by standard microwave radiometry.

(v) The aperture synthesis thermography system

Aperture synthesis is a technique which has been used in radio astronomy for some years. A system has been recently proposed whereby this technique can be applied to measurement of temperature distribution in tissue. In theory this system should allow much greater resolution and smaller measurement times for data acquisition over large areas of the body.

1.3.2 Principal centres of research

USA

Massachusetts Institute of Technology (MIT), Cambridge, MA

Workers at MIT were the first to apply the technique of microwave radiometry, which had been used for many years in radio astronomy, to the measurement of subcutaneous tissue temperature distributions [1]. The first radiometer to be built at MIT was a 3.3 GHz comparison type. The antennas were contacting open ended waveguide, filled with a low loss dielectric to reduce aperture dimensions. The radiometer had no means of compensating for changes in matching between the probe and tissue. Radiometers working at 1.3 GHz and 6 GHz were also constructed. The effects of penetration depth in different tissues, probe spatial resolution and tissue layers were analysed by simplified calculations (see #4.1). Much of their published work concerns the clinical application of the radiometer systems to the detection of breast cancer [41, 35].

University of Colorado

Radiometers developed in Denver, Colorado use remote elliptical dish antennas and operate at 30 GHz, 68 GHz [34], and 10 GHz [42]. A comparison type radiometer is again used as a receiver. The radiometer systems were designed for non-contacting measurements from patients by scanning the dish in a series of horizontal lines over the body. This type of system, termed a 'millimeter wavelength scanner', would seem to be a compromise in terms of spatial resolution and penetration depth between the infra red systems and the more common centimetre wavelength microwave radiometers.

Microwave Associates, Burlington, MA

The Microwave Associates radiometer [36] uses the comparison design, with no compensation for emissivity variation, working at a centre frequency of 4.7 GHz. Instead of the common superhetrodyne system, involving a local oscillator and intermediate frequency (IF) amplification, the radiometer uses square law detection at radio frequencies (RF). The antenna is a dielectrically filled contacting waveguide.

Limited clinical studies were carried out on cancer patients and these detection rates compared with those for xeromammography. The radiometer can also be operated in conjunction with low power microwave heating at 1.6 GHz, which enhances the temperature difference of the tumour over that of the surrounding tissue, giving increased detection potential.

RCA Laboratories, Princeton, NJ

A radiometer developed at the RCA Laboratories has been designed with a feedback/noise injection control system, allowing conversion to a self-balancing type, working at a centre frequency of 2.45 GHz [23]. The radiometer usually employs a dielectrically filled contacting waveguide for the antenna but has also been used with both microstrip and coaxial line antennas, which were developed for use with a 2.45 GHz hyperthermia system. The radiometer is used for the control of hyperthermia treatment by two methods. If hyperthermia at 2.45 GHz is induced a switching system allows the same antenna to be used for temperature sensing. When lower frequency hyperthermia is used, the applicator must be removed and the radiometer probe placed in contact with the heated volume.

A dual frequency radiometer system is also being developed at RCA. A suggested application for this equipment is the diagnosis of appendicitis. The system may also be used to control a scanning hyperthermia system [43].

Tufts University, Medford, MA

A correlation radiometer has been developed [44] which employs amplitude modulation and IF correlation. Experiments have been performed in free space using two open ended waveguides as antennas to measure the signal from a small heat source.

Great Britain

University of Glasgow

Work at the University of Glasgow has concentrated upon designing a microwave radiometer suitable for clinical use.

Different radiometer designs and individual components have been examined [45] in terms of performance, cost and portability to provide a system which is easy to use by staff in a hospital ward. A comparison radiometer, working at a centre frequency of 3.2 GHz, has been developed which uses a dielectrically filled circular contacting waveguide antenna. Analysis of the pre-amplification circuit specifications has been performed [46] to estimate and reduce resulting measurement errors and limited clinical tests have been carried out [4].

University of Leeds

A comparison radiometer utilising a non-contacting dish antenna and operating at a centre frequency of 10 GHz has been built in Leeds [47]. The spatial resolution of this device was examined in detail and signal processing techniques implemented to improve the final image. Thermographic scans of patients showed some success in diagnosing arterial obstructions in peripheral limbs.

University of Sheffield

Research reported in this thesis.

France

Université des Sciences et Techniques de Lille

One of the most prolific teams working in the field of microwave radiometry has been that based at the University of Lille. They have built self-balancing radiometers working at centre frequencies of 9 GHz and 3 GHz. The antennas are mainly rectangular dielectrically filled contacting waveguides but circular waveguide and microstrip microslot antennas [48] have also been used. Clinical studies carried out with these radiometers have included measurements of muscle heating during exercise [40] and detection of breast, thyroid, cerebral and bone tumours [39].

Any losses or reflections in the front end components of a radiometer seriously degrade the temperature resolution. Methods of optimising the transition between waveguide antenna and the coaxial cable feeding the radiometer [49], and minimising the reflection at the antenna/tissue interface [50] have been studied. Important work has also been reported [51] for modelling the radiation patterns of rectangular waveguide probes. This has led to a method for interpretation of radiometric scans and recognition of thermal patterns in homogeneous media (see # 1.4).

More recent developments have concentrated upon improvements in technology to widen the capabilities of microwave radiometry. A new radiometric system has been developed [52] which consists of a set of six probes arranged in a block, sequentially switched to a radiometer receiver. An image processing technique, based on knowledge of the probe radiation pattern, allows some improvement of spatial resolution.

The technique of correlation radiometry was originally applied to medical thermography in 1981 [53]. The correlation system built at Lille has two filled waveguide probes and employs phase modulation to measure the correlation function [54] of signals from thermal structures in a lossy medium. It has been reported that correlation radiometry gives improved spatial resolution and may also provide some depth information. However, the signal amplitudes are significantly lower than those measured with standard microwave radiometry.

Microwave radiometry systems have also been developed, by the group at Lille, for the non-invasive control of hyperthermia treatment. Early studies [22] proposed a heating system operating at the centre frequency of the radiometer, using the same antenna as applicator and radiometer probe. This idea has been further developed [24] by the use of two radiometers at 3 GHz and 1.2 GHz to form a commercial system named "Hylcar" produced by ODAM. Work is now in progress [48] to use temperature measurements at two frequencies, plus a surface thermocouple measurement, to reconstruct the temperature depth profile and provide improved control over hyperthermia treatment.

Germany

Philips GmbH, Hamburg

Work at Philips has concentrated upon improving the measurement accuracy of the single probe radiometer. The design for a null-balancing radiometer [55] has been reported and its performance compared with other null-balancing circuits. The initial system has been improved [3] to allow independent measurement of 'true' temperature (accounting for reflection coefficient) and emissivity. Further improvements [56] of the design have improved the receiver's accuracy by allowing for gain fluctuations.

Radiometers have been built to these specifications at centre frequencies of 2 GHz and 11.7 GHz using dielectrically filled contacting rectangular and circular waveguides as the receiving probe.

University of Erlangen-Nürnberg

The University of Erlangen Nürnberg have also developed [57] a modified null-balancing radiometer working around 4 GHz which simultaneously measures the 'true' temperatures and emissivity of the body. Some theoretical work [58] has also been carried out to invert multi-frequency data for reconstruction of temperature profiles in homogeneous media.

Max Planck Institut für Radioastronomie

A new system has been proposed [59, 60] that applies the technique of aperture synthesis, a technique widely used in radioastronomy, to measure thermal signals from the body. By this technique, a large single antenna is synthesised by many small antennas. The phase and amplitude received by each of these antennas is measured relative to a reference antenna by measuring the appropriate correlation function. Increased spatial resolution and reduced measurement time, compared with other radiometric techniques, are claimed. However, many technical and mathematical problems must be solved before this system becomes practical.

University of Bochum

Theoretical work has been carried out to study the propagation of microwaves through layered tissue structures and to invert simulated data to reconstruct temperature profiles [61]. Near field characteristics of contacing and non-contacting radiometer antennas have also been calculated. Experimental scanning using a dish antenna and radiometric measurements at 32 GHz and 90 GHz have provided some two dimensional maps of skin temperature [62].

Italy

University of Rome

Work began recently in Rome [63] to study theoretically the problem of radiation from a layered biological structure and inversion of simulated multifrequency data by analytical means. They propose [64] to build a radiometer with five frequency bands to validate their results.

1.4 The interpretation of radiometric measurements

The problem of interpretation of results is one which arises in most areas of science and medicine. For microwave radiometry, the final data in pictorial, graphical or numerical form must be explained in terms of the temperature distribution existing within the measurement volume. One approach is to interpret results by applying the measurement technique to a clinical situation. This method was followed by Barrett, Edrich and others (see # 1.2.2). The radiometer measurements were compared to biopsy results and to other diagnostic methods. Experience in interpretation of radiometric results, in terms of whether a temperature irregularity was present, was accumulated from experience with many patients.

Although this research is valuable, it requires a complementary analytical approach. Detailed interpretation requires the physical processes involved and the characteristics of the measuring apparatus to be thoroughly understood. The clinical approach has limited value, for instance, in the control of hyperthermia treatment by radiometry. To meet the design criteria for a monitoring system, inversion of radiometric data to give absolute temperature values is required. If this cannot be achieved, measurement by thermocouple will always be necessary as a supplementary check. Even where absolute values are not required, as in the use of microwave radiometers as feedback devices to maintain a constant temperature during treatment, the volume from which temperature information is being collected must be known. In diagnosis, less severe requirements upon accuracy of interpretation are imposed. However, there are dangers in interpretation of clinical results with only limited knowledge of the capabilities of the measurement method.

The ultimate aim of the analytical approach to the interpretation of radiometer measurements is the inverse process of reconstructing the temperature distribution in the underlying tissue from data taken on or above the skin surface. As a first stage in this inverse process, it is important that the forward propagation process is understood; that is, given a known thermal structure we should be able to predict a radiometric data set. This is a very complex electromagnetic problem and in turn involves an understanding of:

(a) the process of emission of microwave radiation,

(b) diffraction in a complicated dielectric structure,

(c) absorption in lossy tissue,

(d) the interaction of the emergent radiation with the measuring system (in this case the radiometer probe).

These processes have been studied extensively in the remote sensing of the earth [65, 66]. The applicable theory is that of radiative transfer.

Various workers have considered radiative transfer theory as applied to the calculation of the radiation reaching a radiometer from a biological medium. A full account of these studies can be found in Chapter 4. In order to find solutions to this electromagnetic problem, simplifications as to the dielectric structure, the temperature distribution, and the radiometer probe receiving characteristics are made. A common assumption is that of a homogeneous medium, which tends to be an over simplification of the real situation. A more realistic model is one which contains planar layering. Some models employ incoherent radiative transfer theory with which the partial coherence of emergent radiation, due to multiple reflections within layers, cannot be taken into account. Other workers assume a dielectric structure and temperature distribution which varies only with depth, and a radiometer probe which essentially receives plane waves, reducing the problem to a one dimensional model.

In this thesis, a solution is sought for the noise temperature received from a contacting aperture antenna, through a medium containing any number of layers and which has a given three dimensional temperature distribution. The solution is formulated by using a coherent radiative transfer approach. In this formulation, a number of approximations have been employed which will be discussed as they are introduced into the theory. The first stage is to calculate the receiving characteristics of a contacting radiometer probe. The receiving pattern of an antenna can be related directly to its characteristic radiation pattern when excited by a monochromatic signal. A means of calculating the radiation pattern of an aperture antenna in contact with a lossy layered medium is given in Chapter 2. The method by which the radiation pattern can be employed in calculating the measured temperature from a radiometer is described in Chapter 4.

Chapter 2

An incremental spectral diffraction method for predicting field patterns of contacting aperture antennas radiating into lossy layered media

2.1 Prediction of the field patterns of radiating aperture antennas in tissue

2.2 Spectral diffraction in homogeneous media

- 2.2.1 Theory for homogeneous media
- 2.2.2 Analysis of a wavefront as an angular spectrum of plane waves
- 2.2.3 The spectral filter

2.3 Incremental spectral diffraction in layered structures

2.4 Application of the incremental spectral diffraction method to the prediction of field patterns of tissue-contacting aperture antennas

2.5 Computer implementation of the field prediction method

2.1 Prediction of the field patterns of radiating aperture antennas in contact with tissue

Techniques for predicting field patterns of aperture antennas radiating into tissue have previously been developed both for the analysis of microwave radiometric measurements and to determine heating patterns for radio-frequency and microwave hyperthermia. Pioneering work was carried out by Guy [67], in the field of hyperthermia, who applied a Fourier transform solution [68, 69] to the problem of waveguide apertures radiating into bi-layered biological media. The solution was validated by comparing predicted heating patterns with measurements on phantoms [70]. Turner and Kumar [71] considered an aperture as a set of dipole sources to calculate the power deposition rate in homogeneous tissue delivered by elements of an annular array applicator. Theoretical and experimental studies were carried out by Cheung et al [72] to determine the effect of varying waveguide aperture size on the heat deposition in a homogeneous tissue-simulating liquid.

For studies of microwave radiometric signals, Robillard [50] employed two different techniques to calculate approximately the field pattern of a rectangular waveguide radiating into a homogeneous medium. The first model approximated the rectangular waveguide as a parallel plate waveguide, the fields being calculated by a Green's function method. In the second solution, the homogeneous half-space medium was modelled by a second waveguide of much larger dimensions, allowing the problem to be reduced to that of a waveguide discontinuity.

Propagation into multi-layer structures presents a considerable challenge for theoretical modelling. An analysis employing the dyadic Green's function has been suggested recently by Teodoridis et al [73]. In this chapter, a computationally efficient method employing a Fourier transform solution is proposed which enables the prediction of field patterns in multi-layer biological media produced by contacting waveguide apertures.

2.2 Spectral diffraction in homogeneous media

2.2.1 Theory for homogeneous media

The problem to be addressed in this section is that of describing the propagation of a scalar wavefront in an isotropic homogeneous medium with finite conductivity. The solution will eventually be applied to a planar aperture radiating into a layered lossy medium. Therefore the requirement is, given the field distribution on a plane, to determine the field on any parallel plane in the medium. The solution is formulated by employing scalar spectral diffraction theory [74, 75], and analysing the wavefront as an angular spectrum of plane waves [76].

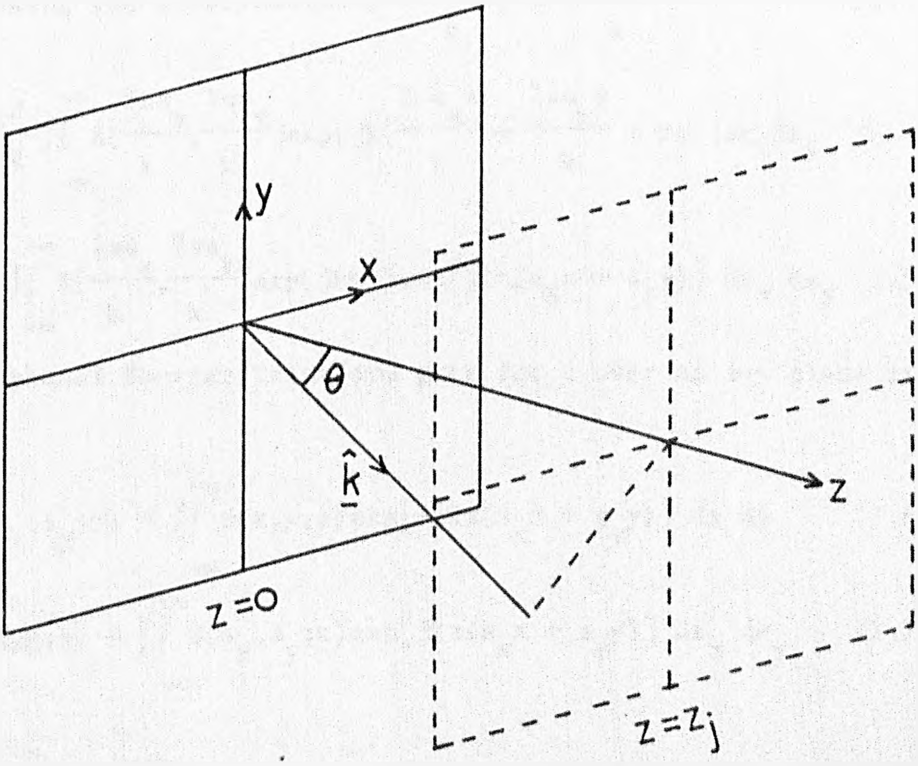

Fig. 2.1 Co-ordinate system for plane to plane propagation of a wavefront

With reference to Fig 2.1, a scalar field distribution $u(x,y;z_0)$ exists on the plane $z = 0$ and is to be propagated to a parallel plane $z = z_j$ (where $z_j > 0$). It is assumed that all sources of the field are in the region $z < 0$ so that, in the region $z > 0$, u satisfies the homogeneous scalar wave equation

$$\nabla^2 u + k^2 u = 0 \tag{2.1}$$

where k is the wave number $k = \frac{2\pi}{\lambda}(\varepsilon_c)^{1/2}$, λ is the free space wavelength and ε_c is the complex permittivity of the medium $\varepsilon_c = \varepsilon' + j\varepsilon''$.

A general solution to equation 2.1 in the region $z > 0$ has the form of a linear combination of plane wave functions [69, 74]

$$u(x,y;z) = \iint_{-\infty}^{+\infty} A(p,q)\, \exp[jk(px + qy + mz)]\, dp\, dq \tag{2.2}$$

where $m = (1 - p^2 - q^2)^{1/2}$, and p, q, m are the direction cosines of the propagation constant or wave number k for each plane wave function. Making the substitution $p = \frac{2\pi s_x}{k}$, $q = \frac{2\pi s_y}{k}$ (2.3)

$$u(x,y;z) = \frac{4\pi^2}{k^2} \iint_{-\infty}^{+\infty} A\left(\frac{2\pi s_x}{k}, \frac{2\pi s_y}{k}\right) \exp\left[jk\left(\frac{2\pi s_x x}{k} + \frac{2\pi s_y y}{k} + mz\right)\right] ds_x ds_y \tag{2.4}$$

$$= \frac{4\pi^2}{k^2} \iint_{-\infty}^{+\infty} A\left(\frac{2\pi s_x}{k}, \frac{2\pi s_y}{k}\right) \exp(jkmz) \exp[j2\pi(s_x x + s_y y)]\, ds_x\, ds_y \tag{2.5}$$

The two-dimensional Fourier transform pair for u over an x-y plane at z is

$$U(s_x,s_y;z) = \iint_{-\infty}^{+\infty} u(x,y;z) \exp[-j2\pi(s_x x + s_y y)]\, dx\, dy \tag{2.6}$$

$$u(x,y;z) = \iint_{-\infty}^{+\infty} U(s_x,s_y;z) \exp[j2\pi(s_x x + s_y y)]\, ds_x\, ds_y \tag{2.7}$$

Comparing (2.7) with (2.5)

$$U(s_x,s_y;z) = \frac{4\pi^2}{k^2} A\left(\frac{2\pi s_x}{k},\frac{2\pi s_y}{k}\right) \exp(jkmz) \tag{2.8}$$

Using (2.8) and (2.6) for the plane $z = 0$

$$A(p,q) = \frac{k^2}{4\pi^2} \iint_{-\infty}^{+\infty} u_0(x_0,y_0;\ z_0) \exp[-jk(px_0 + qy_0)]\, dx_0\, dy_0 \tag{2.9}$$

The field in the plane $z = z_j$ is obtained by substituting for $A(p,q)$ into (2.2)

$$u_j(x_j,y_j;\ z_j) = \frac{k^2}{4\pi^2} \iint_{-\infty}^{+\infty} dp\, dq\, \exp[jk(px_j + qy_j + mz_j)]$$

$$\iint_{-\infty}^{+\infty} dx_0\, dy_0\, u_0(x_0,y_0) \exp[-jk(px_0 + qy_0)] \tag{2.10}$$

Interchanging the order of integration and letting

$$h_{j0}(x_j-x_0,y_j-y_0;z_j) = \frac{k^2}{4\pi^2} \iint_{-\infty}^{+\infty} \exp\{jk[p(x_j-x_0)+q(y_j-y_0)+mz_j]\}dpdq \tag{2.11}$$

gives

$$u_j(x_j,y_j;z_j) = \iint u_0(x_0,y_0;z_0)\cdot h_{j0}(x_j-x_0,y_j-y_0,z_j)\, dx_0\, dy_0 \tag{2.12}$$

Thus the field u_j in the plane z_j is described in terms of the field u_0 on the plane $z = 0$ by a convolution with the kernel h_{j0}.

Taking the two-dimensional Fourier transform of (2.12) and using the convolution theorem [77],

$$U_j(s_x,s_y;z_j) = U_0(s_x,s_y;z_0)\, H_{j0}(s_x,s_y,z_j) \tag{2.13}$$

where

$$H_{j0}(s_x,s_y,z_j) = \exp[jkmz_j] \tag{2.14}$$

and $m = [1 - (\frac{2\pi s_x}{k})^2 - (\frac{2\pi s_y}{k})^2]^{1/2}$.

The field on z_j,$u_j(x_j,y_j;z_j)$ is obtained by taking the inverse Fourier transform of $U_j(s_x,s_y;z_j)$.

2.2.2 Analysis of a wavefront as an angular spectrum of plane waves

a) Lossless media

Initially, the analysis of the wavefront as an angular spectrum of plane waves is carried out for a lossless medium where $k = \frac{2\pi}{\lambda_m}$, λ_m is the wavelength in the medium. With reference to equation 2.8, on the plane z = 0, each Fourier coefficient $U(s_x,s_y)$ can be associated with a plane wave component A(p,q) propagating with direction cosines [74].

$$p = \lambda_m s_x,\ q = \lambda_m s_y,\ m = \left[1 - (\lambda_m s_x)^2 - (\lambda_m s_y)^2\right]^{1/2} \qquad (2.15)$$

The plane wave spectrum contains two types of waves.

For the case $(\lambda_m s_x)^2 + (\lambda_m s_y)^2 < 1$ the waves are homogeneous, propagating without attenuation at angles to the z axis in the range $(-\pi/2 < \theta < \pi/2)$ (see Fig 2.2a)

$$\cos\theta = m = \left[1 - (\lambda_m s_x)^2 - (\lambda_m s_y)^2\right]^{1/2}$$

A homogeneous wave is defined as one in which the planes of constant amplitude (amplitude fronts) and the planes of constant phase (phase fronts) coincide. In addition, the electric and magnetic field vectors are perpendicular to the direction of propagation and so homogeneous plane waves are transverse electromagnetic (TEM). Each plane wave propagates from the plane z = 0 to the plane $z = z_j$, its phase and amplitude being modified by the filter H_{j0} (equation 2.14).

$$\exp j \frac{2\pi}{\lambda_m} z_j \cos\theta$$

which describes a plane wave propagating in a lossless medium with $k = \frac{2\pi}{\lambda_m}$ for a distance $z_j \cos\theta$.

For the case $(\lambda_m s_x)^2 + (\lambda_m s_y)^2 > 1$, the square root must be chosen such that $\left[1 - (\lambda_m s_x)^2 - (\lambda_m s_y)^2\right]^{1/2} = j\left[(\lambda_m s_x)^2 + (\lambda_m s_y)^2 - 1\right]^{1/2}$. The

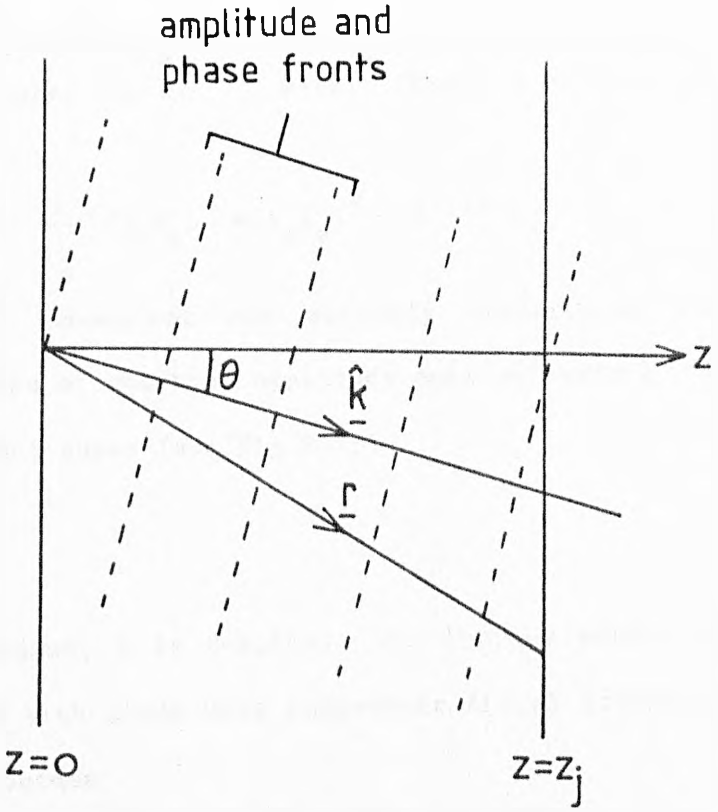

Fig. 2.2a Co-ordinate system for plane to plane propagation of a homogeneous plane wave

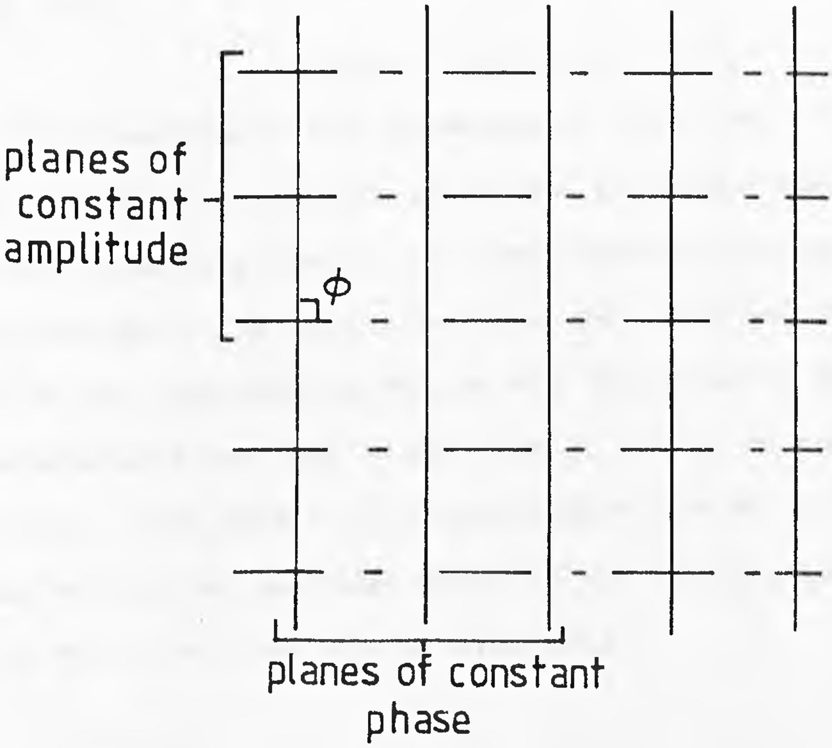

Fig. 2.2b Planes of constant phase and constant amplitude for an inhomogeneous plane wave in a lossless medium

waves are inhomogeneous, with propagation vectors lying in all directions perpendicular to the z axis. Their behaviour in the z direction is given by

$$\exp\left[-\frac{2\pi}{\lambda_m}\left[(\lambda_m s_x)^2+(\lambda_m s_y)^2-1\right]^{1/2} z_j\right]$$

The waves are evanescent and strongly attentuated in the z direction. The planes of constant amplitude make an angle $\phi = \pi/2$ with the planes of constant phase (see Fig 2.2b).

b) Lossy media

For a lossy medium, k is complex. The Fourier coefficients can again be associated with plane wave components A(p,q) propagating with complex direction cosines

$$p = \frac{2\pi s_x}{k},\quad q = \frac{2\pi s_y}{k},\quad m = \left[1-\left(\frac{2\pi s_x}{k}\right)^2-\left(\frac{2\pi s_y}{k}\right)^2\right]^{1/2} \qquad (2.16)$$

Examining the propagation of plane waves in a lossy medium, writing the plane wave function as $\exp(j\underline{k}\cdot\underline{r})$, $\underline{r} = (x,y,z)$ and $\underline{k} = \underline{k}_1 + j\underline{k}_2$,

$$\exp(j\underline{k}\cdot\underline{r}) = \exp(j\underline{k}_1\cdot\underline{r} - \underline{k}_2\cdot\underline{r})$$

Both homogeneous and inhomogeneous plane waves can exist in a lossy medium. A homogeneous plane wave is defined when $\underline{k}_1$ and $\underline{k}_2$ have the same direction; that is the wave propagates and attenuates in the same direction. In this situation, the phase and amplitude fronts coincide and the wave is TEM to the direction of propagation. An inhomogeneous plane wave exists when $\underline{k}_1$ and $\underline{k}_2$ do not have the same direction. The planes of constant phase are at an angle ϕ to the planes of constant amplitude where $0 < \phi < \pi/2$ (Fig 2.2c) and the wave is not TEM to the direction of propagation.

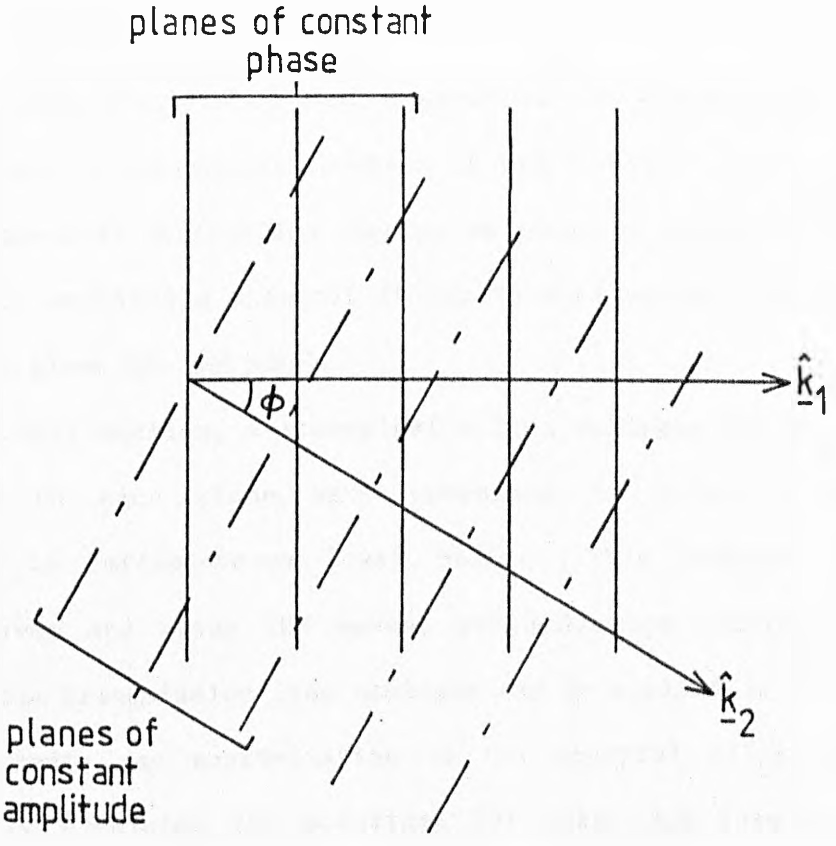

Fig. 2.2c Planes of constant phase and constant amplitude for an inhomogeneous plane wave in a lossy medium

For spectral diffraction, the plane wave components are, in general, inhomogeneous waves. The real part of the direction cosines (equation 2.16) is associated with the direction that the phase propagator $\underline{k}_1$ makes with the z axis, and the imaginary part is associated with the angle ϕ between $\underline{k}_1$ and $\underline{k}_2$.

The propagation process is described by

$$\exp \quad jk\left[1 - \left(\frac{2\pi s_x}{k}\right)^2 - \left(\frac{2\pi s_y}{k}\right)^2\right]^{1/2} z_j \quad .$$

2.2.3 The spectral filter

It has been established that a wavefront in a homogeneous medium can be analysed as an angular spectrum of plane waves. The propagation process in spectral diffraction theory, as given by equation (2.13), is equivalent to applying a spectral filter to this angular spectrum, the filter being given by exp[jkmz].

In the next section, a transmission line analogue for plane waves is applied to each plane wave component in order to describe propagation in heterogeneous lossy media. This analogue requires that the waves are plane TEM waves, and therefore homogeneous. In order that the transmission line analogue can be applied in conjunction with lossy media, an approximation to the spectral filter has been formulated by combining the solutions for lossy and lossless media. The spectral filter becomes

$$H = \exp\left[jk \left[1 - (\lambda_m s_x)^2 - (\lambda_m s_y)^2\right]^{1/2} z\right] \qquad (2.17)$$

where $k = \dfrac{2\pi}{\lambda_m} \left(1 + j \dfrac{\varepsilon''}{\varepsilon'}\right)^{1/2}$ is complex. Assuming this form of the filter, the wavefront is decomposed into its plane wave components as if the medium were lossless, but each component is propagated taking into account the attenuating term.

For the case $(\lambda_m s_x)^2 + (\lambda_m s_y)^2 < 1$, the direction cosines of the propagation vector are real and therefore the plane waves can be considered to be homogeneous and thus TEM. Attenuation is included for each component by using the complex propagation constant. Where $(\lambda_m s_x)^2 + (\lambda_m s_y)^2 > 1$, in a lossless medium this part of the spectrum contains evanescent waves, the planes of constant phase forming an angle $\phi = \pi/2$ with the planes of constant amplitude. These waves cannot be represented in the transmission line analogue for plane waves and are therefore excluded from the spectrum when layers are present.

2.3 Incremental spectral diffraction in layered structures

The spectral diffraction technique presented in the previous section describes the propagation of a scalar field in homogeneous lossy media. A realistic model for the human body must include multi-layered structuring. The problem of an aperture radiating into a bi-layered structure of fat overlying a muscle half-space has been investigated previously [67], but the complexity of the problem increases when more than one boundary is considered. In a structure consisting of three or more media, multiple reflections from boundaries leads to a situation where the field value at any point in the structure depends on the fields existing at every other point. This problem is now addressed by extending the incremental spectral diffraction approach for conducting scatterers [78, 79] to multilayer dielectrics. The assumption of the existence of a spectrum of homogeneous plane waves (# 2.1.3) forms the basis for this analysis.

Before generalisation to a medium containing many dielectric layers, the incremental diffraction method is applied to a single boundary. Assuming, for the moment, that total transmission occurs at the boundary, propagation of the wavefront across the boundary can be implemented in the spectral diffraction process simply by altering the propagation filter to describe propagation in the new medium. The propagation filter in the media is

$$\exp[\, jk_{1,2}[1 - (\lambda_{m_{1,2}} s_x)^2 - (\lambda_{m_{1,2}} s_y)^2]^{1/2}\ z_j]$$

where λ_m is the wavelength in the medium $\lambda_m = \frac{\lambda_0}{(\varepsilon')^{1/2}}$. Each Fourier component can be associated with a plane wave propagating at an angle θ to the normal to the boundary (Fig 2.3) where

$$\cos\theta_{1,2} = [1 - (\frac{\lambda s_x}{(\varepsilon'_{1,2})^{1/2}})^2 - (\frac{\lambda s_y}{(\varepsilon'_{1,2})^{1/2}})^2]^{1/2}$$

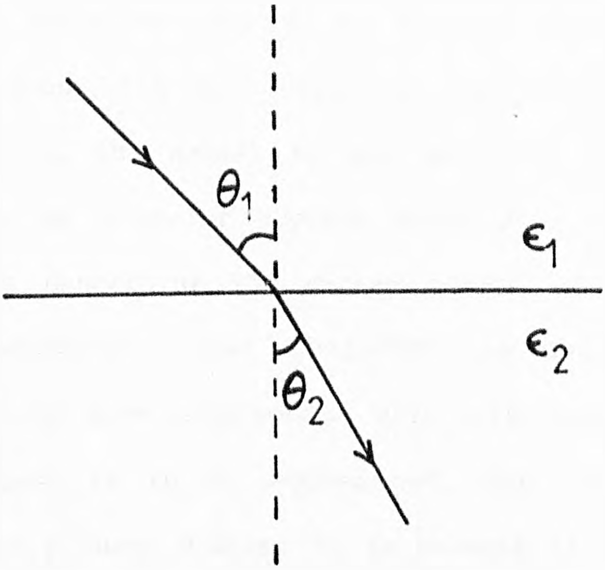

Fig. 2.3 Refraction of a plane wave at a dielectric boundary

For each of these plane wave components, the ratio

$$\frac{\sin\theta_1}{\sin\theta_2} = \frac{(\varepsilon'_2)^{1/2}}{(\varepsilon'_1)^{1/2}}$$

which is Snell's law for lossless media and is applicable to any number of boundaries between dielectrics. The assumption of a set of plane wave components and the method of obtaining these components for a homogeneous medium as described in section 2.1.3 can therefore be applied to a structure containing dielectric layers. This allows propagation of a wavefront through a layered structure to be carried out by the simpler propagation of plane waves.

In reality, part of the wavefront is reflected and part is transmitted at each boundary. This problem can be considered in terms of reflection and transmission of the individual plane wave components. Associated with any boundary there are two sets of reflection and transmission coefficients, one set for parallel and the other for perpendicular polarization of the plane wave. The terms perpendicular and parallel refer to the orientation of the electric field vector with respect to the plane containing the propagation vectors of the incident and reflected waves and the normal to the boundary. The spectral diffraction technique is a scalar process which does not yield the necessary information concerning the vector nature of the spectral components. An assumption must therefore be made about the polarisation of the plane wave components. With reference to the model with which this process is to be implemented, that of an aperture antenna radiating into a lossy medium, it is assumed in the remainder of this analysis that all of the plane wave components in the Fourier domain have perpendicular polarisation. Parallel polarisation and depolarisation effects are not considered. The reason for this particular choice is discussed in section 2.4.

Consider a plane $z = z_0$ in the first medium parallel to the boundary, upon which a wavefront exists, propagating towards the boundary. The field distribution upon the plane due to this wavefront is $u_{f_1}(x,y;z_0)$. In a steady state, the total field on the plane is the sum of this forward propagating field distribution plus a field distribution $u_b(x,y;z_0)$, due to a backward propagating wavefront reflected from the boundary. Beginning with the forward propagating wavefront u_{f_1} the incremental spectral diffraction technique is applied in the following manner. u_{f_1} is decomposed into it's Fourier components. Each component is propagated to the boundary, multiplied by the apropriate Fresnel expression for the reflection coefficient [80] and propagated back to z_0, where an inverse Fourier transform is applied to the spectrum to give u_b. The field u_{f_2} at a plane in the second medium is obtained from the Fourier spectrum existing at the boundary just inside the first medium. Each Fourier component is multiplied by the appropriate transmission coefficient and the propagation filter altered for the new medium.

In a dielectric medium containing three or more dielectric media, the solution becomes more complex due to multiple reflections and transmissions. Prediction of the field distribution on a plane using Fresnel expressions would involved propagating the wavefronts back and forth between boundaries, multiplying the plane wave spectrum by the appropriate reflection and transmission coefficients each time until the field contributions were attenuated enough to be negligible. However, as the field is decomposed into homogeneous plane wave components, it is possible to apply the cascade transmission line analogue. Appendix 1 explains the cascade technique for transmission lines and its application to the problem of plane wave propagation through layers. The cascade technique provides a rapid calculation of the steady state reflection and transmission coefficients at each boundary taking into account multiple reflections and transmissions due to all other boundaries in the system. As an example, consider a dielectric medium containing three layers, with the upper and lower dielectric media semi-infinite (Fig 2.4). The figure shows multiple reflections and transmission at the upper and lower boundaries for a single plane wave. For the first boundary the cascade technique calculates a reflection coefficient which takes into account the multiple reflections from the lower boundary including the effects and attenuation in the second medium. It should be noted that all of the reflected components from a single incident plane wave which finally travels upwards in the first medium all travel in the same direction, so a single reflection coefficient is appropriate. The transmission coefficient for the first boundary takes into account all the contributions which reflect from the second boundary and are

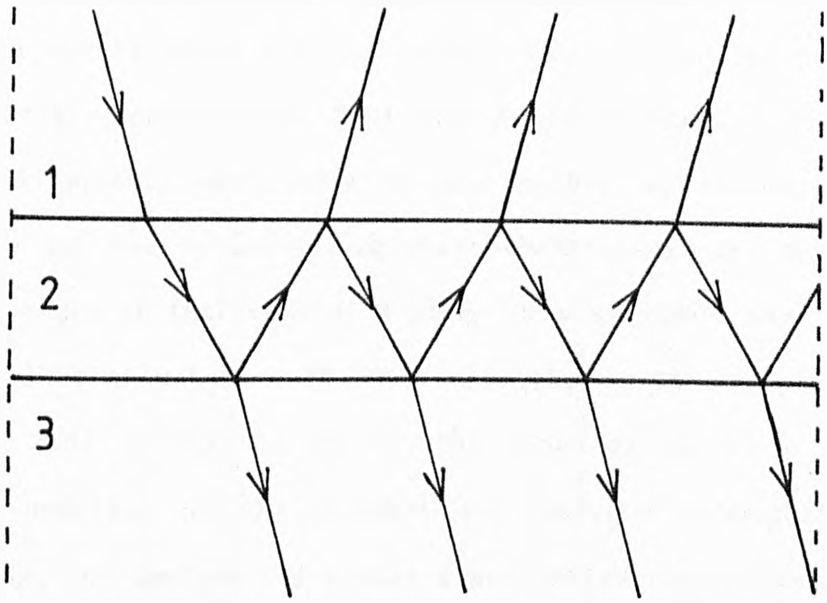

Fig. 2.4 Ray paths for a single plane wave in a three layer dielectric medium

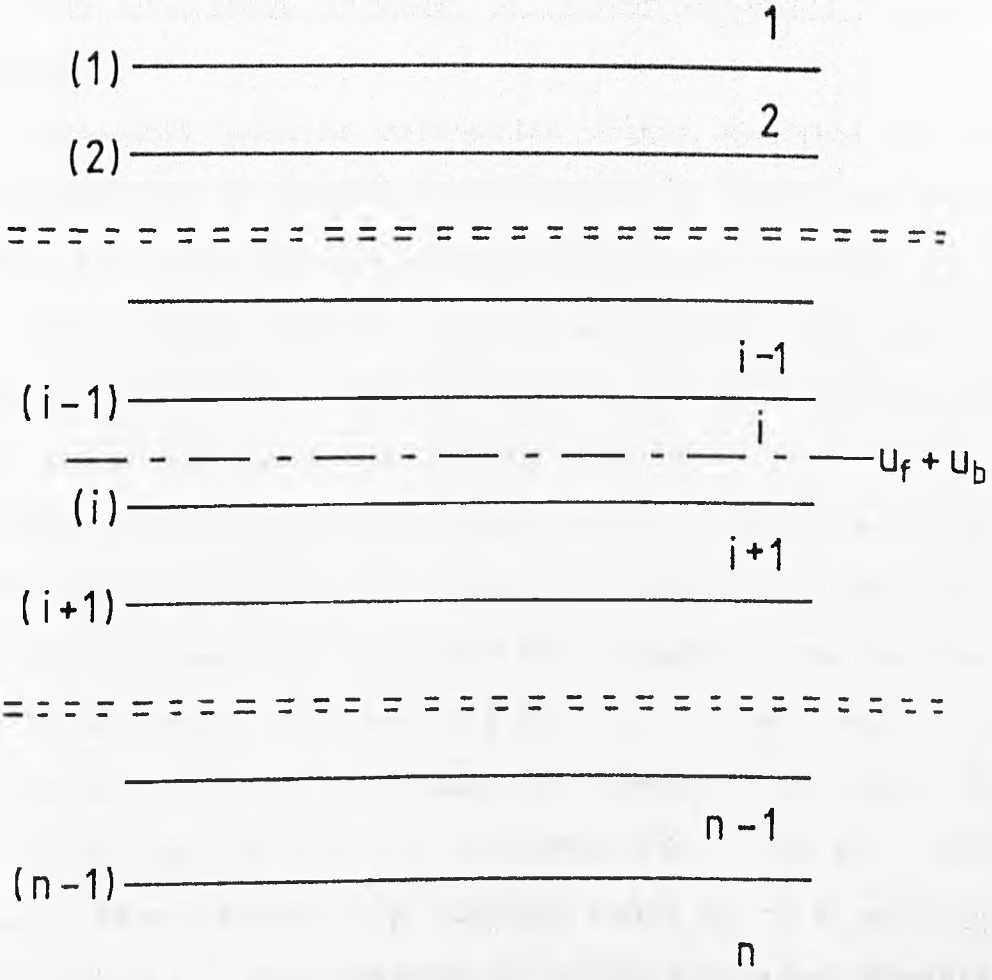

Fig. 2.5 Illustrating calculation of field within the ith layer of an n layer medium

re-reflected from the underside of the first boundary. Reflection and transmission coefficients for the second boundary similarly take into account multiple reflections from the first boundary. The cascade technique is equally applicable to any number of boundaries. The steady state reflection and transmission coefficients for any boundary and for any angle of incidence of a plane wave component can be readily calculated. The calculation of field distribution on any plane in the medium (fig 2.5) is carried out in the same way as for a two layer medium, by addition of the forward and backward propagating field distributions, but employs the steady state reflection and transmission coefficients.

2.4 Application of the incremental spectral diffraction method to the prediction of field patterns of tissue-contacting aperture antennas

The incremental spectral diffraction method described in the previous sections may be applied to the problem of finding the field distribution due to an aperture antenna contacting a layered, lossy medium. Although this method is equally applicable to any type of contacting aperture antenna, for the purposes of these studies the particular case of open-ended waveguide was examined.

Consider the medium to be a half-space consisting of any number of layers with varying dielectric properties. In contact with the upper layer of this half-space is an open-ended waveguide, the aperture surrounded by an infinite flange (Fig 2.6). The initial field to be propagated is that existing just inside the medium. This field is considered to be that of the TE_{10} waveguide mode. The TE_{10} mode contains only one polarisation of electric field, E_y, so in equation 2.12, u_0 becomes E_{y0}. The distribution of the y-polarised electric

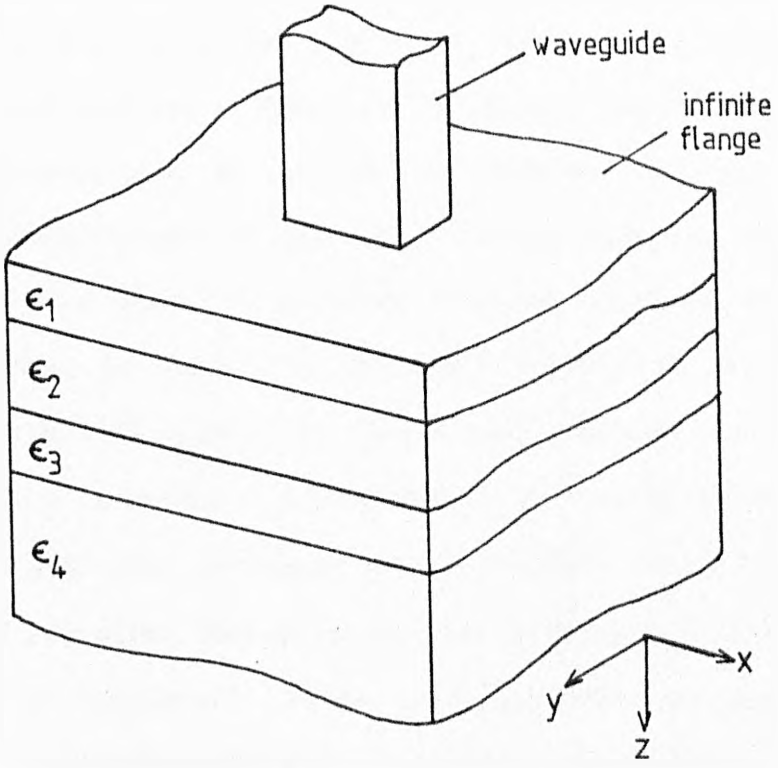

Fig. 2.6 Model for predicting field pattern of a contacting waveguide

field on any plane in the half space parallel to the aperture plane can then be calculated by performing the propagation process. A Fourier transform of E_{y0} is performed and the Fourier coefficients analysed as a spectrum of homogeneous plane waves. The spectrum is propagated through the medium, the effects of attenuation, refraction and reflection being taken into account as described in the previous sections for each plane wave component. Finally, an inverse Fourier transform is performed to give the distribution of E_y on the desired plane (u_j becomes E_{yj}).

If the aperture distribution is assumed to contain E_y components only, this scalar propagation process is directly applicable for homogeneous media. Propagation in the presence of a boundary, however, forces the vector nature of the plane wave spectrum to be considered because different reflection and transmission coefficients apply to different polarisations. Since no information is available from the spectral decomposition as to the polarisation of each plane wave component, a choice must be made as to the polarisation which is to be considered. The plane of greatest interest is the y = 0 plane or H-plane because, in Chapter 3, the field predictions are compared to measurements on this plane. The plane wave components propagating in the y = 0 plane possesses a y polarisation at the aperture. It can be assumed that when they propagate to the boundary this polarisation is retained and the waves have perpendicular polarisation with respect to their plane of incidence. Plane wave components propagating at an angle to the y = 0 plane may have, in general, field components in both polarisations. Therefore, when layers are present, the field predictions will be most accurate in the y = 0 plane.

2.5 Computer implementation of the field prediction method

The algorithm for prediction of fields in layered structures is designed for efficient computer implementation on a VAX 11/730 machine, utilising the one-dimensional fast Fourier transform (FFT) NAG routine. Recently, the processing time has been reduced by use of a two dimensional FFT routine implemented on an array processor. Use of the FFTs requires the sampling criterion to be observed; in this case sampling at intervals in the space domain of less than $\lambda_m/2$, where λ_m is the wavelength in the medium. In fact, the space domain was oversampled by this criterion due to the need to represent the aperture sufficiently. In most of the results presented here, the sample spacing was 1 mm ($\lambda_m/7$ in water and $\lambda_m/24$ in resin) giving, for a 16 mm x 8 mm aperture, 128 samples to represent the aperture.

The maximum capability for the VAX 11/730 machine allowed 256 x 256 point complex arrays. Under the constraints of the limit on the array size, finer sampling in the space domain led to coarser sampling in the Fourier domain. A convolution process occurs in the Fourier domain, and therefore only the central 128 x 128 points are uncontaminated by cyclic convolution.

A flow diagram of the multilayer propagation programme is given in Fig 2.7. The forward Fourier transform is performed only once. Operation on the angular spectrum of plane waves allows the propagation process to be carried out totally in the Fourier domain. Inverse Fourier transforms operate on the forward and backward propagating plane wave spectrum to give the required field distribution at each plane parallel to the aperture plane.

Use of Fast Fourier transforms and of the incremental approach to propagation through layers leads to a computationally efficient algorithm. The cascade technique allows field predictions in structures with any number of layers with only small increase in computing time over the homogeneous case. For experimental validation, in the following chapters the prediction algorithm will be compared with measured results in structures containing only two layers.

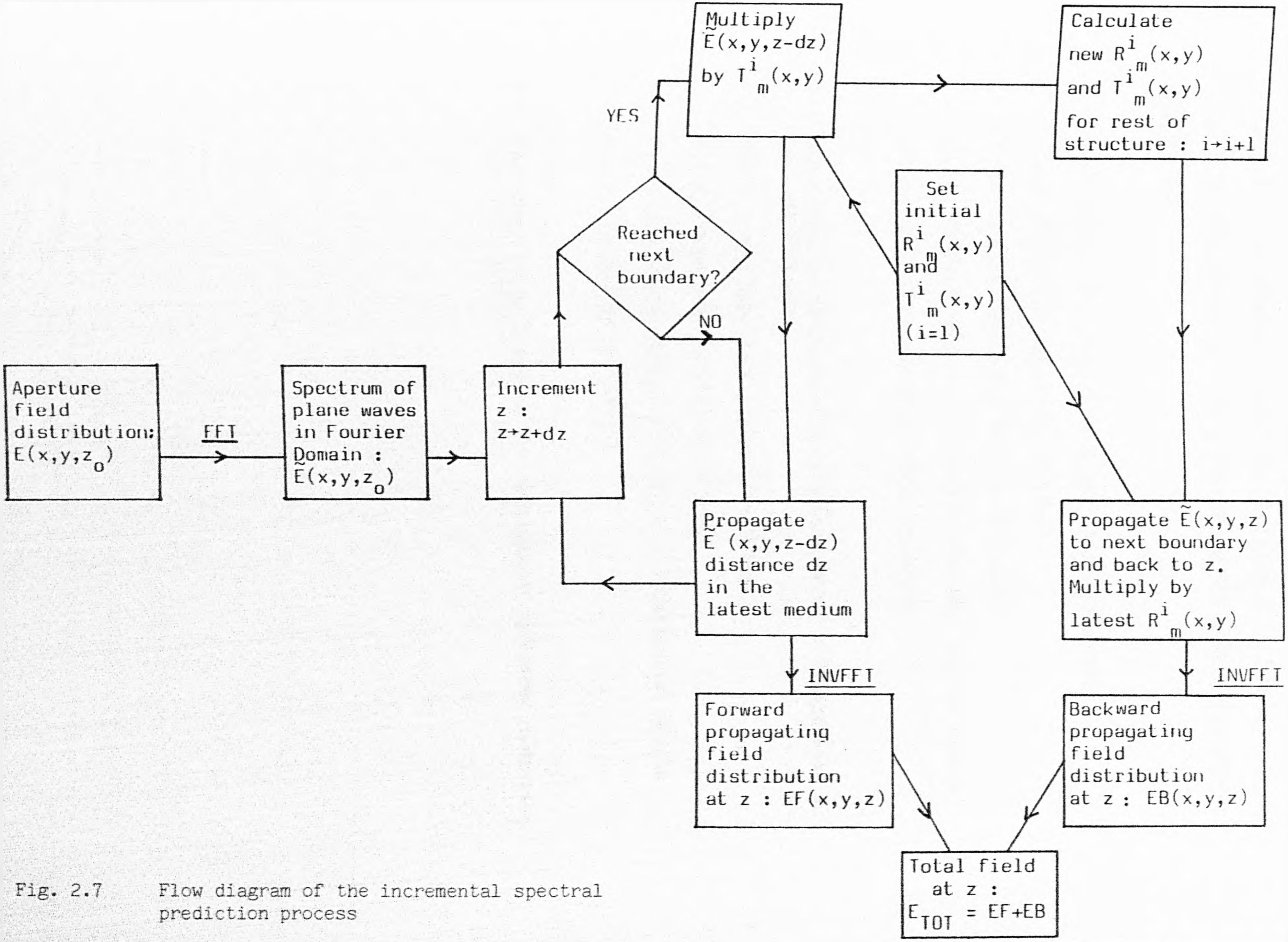

Fig. 2.7 Flow diagram of the incremental spectral prediction process

Chapter 3

Measurement of radiometer probe field patterns in homogeneous and layered tissue-equivalent phantoms and comparison with computer simulations

3.1 Measurement of aperture field patterns in phantoms

- 3.1.1 Microwave measurement apparatus
- 3.1.2 Tissue-simulating phantom materials
- 3.1.3 Computer controlled scanning and data logging system
- 3.1.4 Details of the measurement procedure

3.2 Comparison of simulations with measurements in homogeneous and bi-layered media

- 3.2.1 Comparison in a homogeneous medium
- 3.2.2 Comparison in bi-layered media
- 3.2.3 Correspondence of simulation to experimental models
- 3.2.4 Discussion of results

3.3 Simulated field patterns of rectangular apertures radiating into lossy media

3.1 Measurement of aperture field patterns in phantoms

Measurement of the field patterns of aperture antennas radiating into lossy media has previously been carried out for evaluation of hyperthermia applicator performance [81] and radiometer probe reception characteristics [50]. A description of apparatus for mapping the near-field pattern of a waveguide applicator in simulated biological tissue was given by Gajda et al [82]. A computer-controlled measurement system constructed for this study incorporates some aspects of these previously reported methods and takes advantage of automated scanning for mapping of aperture radiation patterns in liquid or layered liquid/solid phantoms. With reference to Fig 3.1 a single frequency signal from a microwave source was fed into the antenna which was submerged in the lossy liquid. A short monopole received the radiated field in the liquid and the signal was measured by a network analyser. The analogue output from the network analyser was sampled by a BBC micro computer which logged the data at every measurement point. Scanning the monopole in a raster using the computer-controlled scanning frame gave a two dimensional map of the field pattern. The apparatus can be divided by function into three parts:

- Microwave measurement apparatus
- Phantom materials
- Computer-controlled scanning and data logging system.

3.1.1 Microwave measurement apparatus

The microwave measurement apparatus is shown in Fig 3.1. The signal source fed the radiating waveguide antenna and also provided the reference for the network analyser. The antenna was the radiometer probe, a rectangular (16 mm x 8 mm) waveguide filled

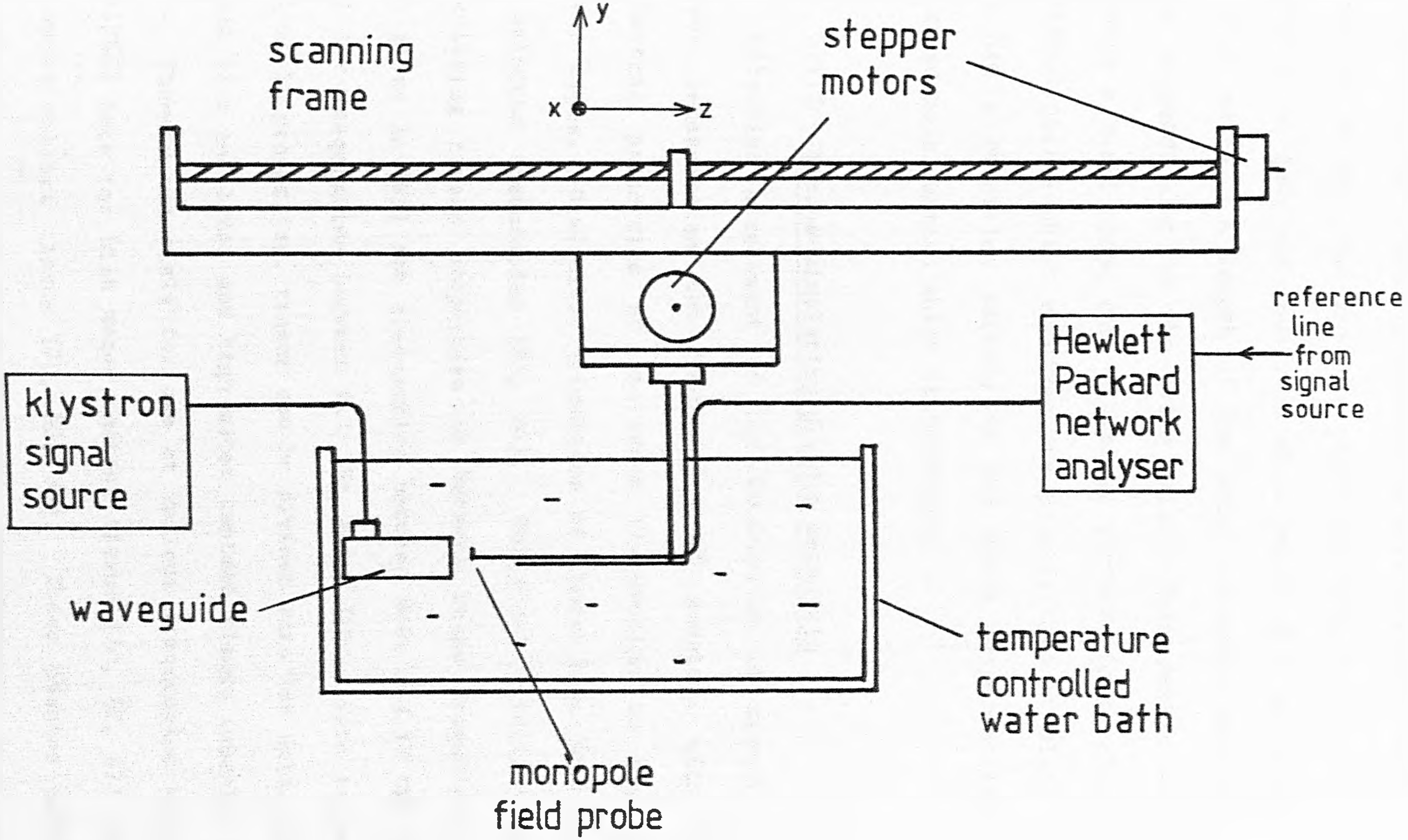

Fig. 3.1 Apparatus for measurement of waveguide field pattern

with a low loss ceramic of dielectric constant ε' = 9 (see # 5.2). A monopole probe received the radiated field, and the signal level was measured by a Hewlett Packard network analyser, with a dynamic range of 60 dB. The monopole probe was made to a design used by Gajda et al [82] and consisted of a length of 2 mm outer diameter coaxial cable. A length of the inner conductor was exposed and bent perpendicular to the cable axis. This design was used to produce a small probe with a minimal perturbational effect on the radiated fields which receives one polarization of electric field and has a receiving pattern in the plane perpendicular to the received polarization which is isotropic.

3.1.2 Tissue-simulating phantom materials

Effective assessment of the interaction of microwaves with tissue necessitates the fabrication of phantoms with similar dielectric properties at microwave frequencies to the various tissue types. Dielectric properties of tissue have been reported at selected frequencies [83, 84]. Empirical relationships for calculating tissue properties in between these frequencies have been given in [85] for frequencies between 0.01 and 17 GHz and in [86] for frequencies between 0.1 GHz and 3 GHz. With respect to dielectric properties, tissue can be divided into low water content tissue (fat and bone) and high water content tissue (muscle, brain etc). Phantom materials for use at various frequencies have been described both for high water content tissue [70, 82, 87] and for low water content tissue [70, 82, 88]. These phantom materials were designed for use in hyperthermia experiments. As a result, the dielectric properties of these materials are reported at ISM

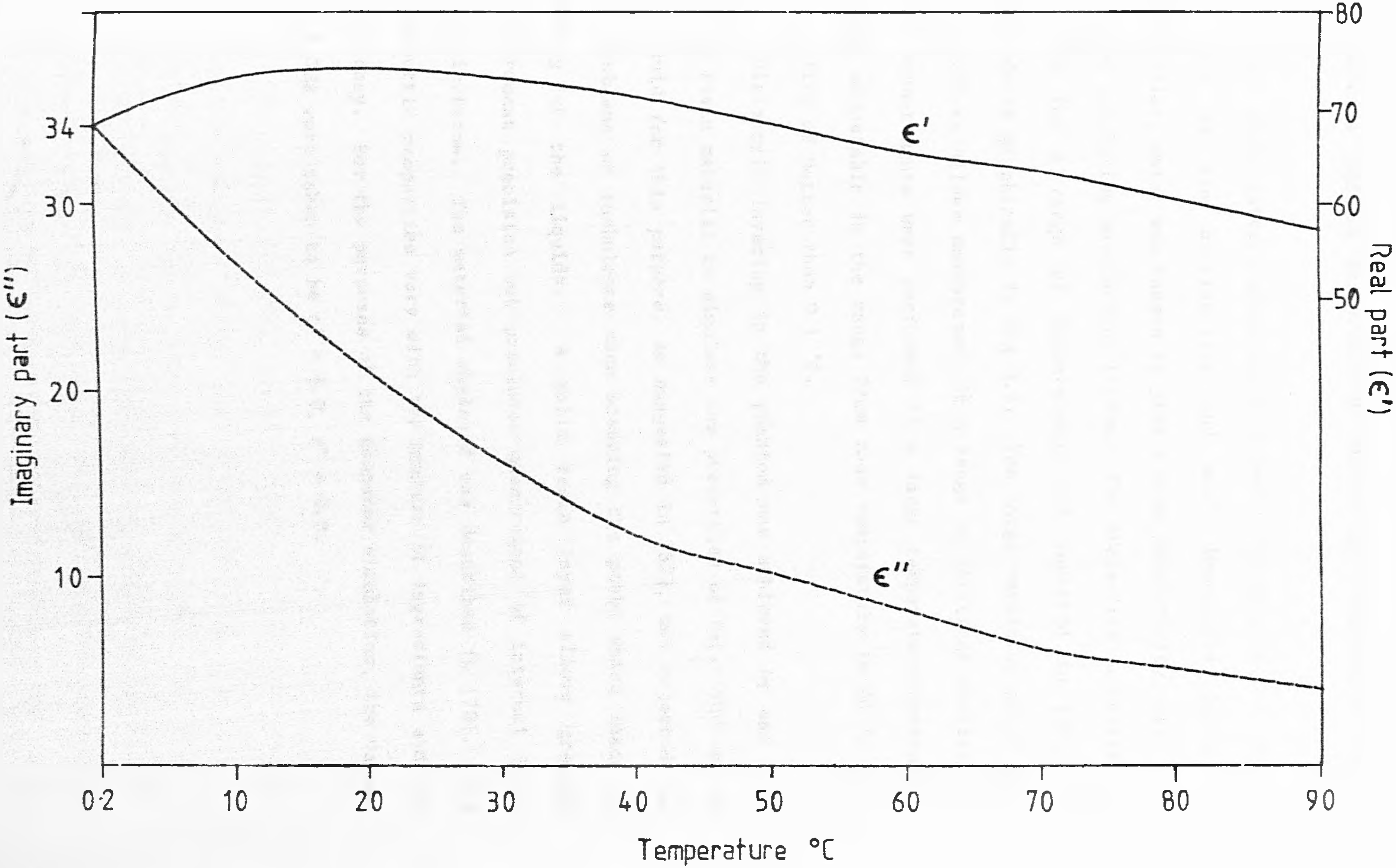

Fig. 3.2 Complex permittivity of water versus temperature at 5 GHz

frequencies and no documentation exists for frequencies around 5 GHz.

The field pattern measurement method requires a liquid medium. Because of its availability and well documented dielectric properties, water was chosen to give a high permittivity, high loss medium simulating muscle-type tissue. The dielectric properties at 5 GHz for a range of temperatures are reported in [89] and reproduced graphically in Fig 3.2. The large variation of ε" with temperature allows measurement in a range of different conditions. The measurements were performed in a large temperature-controlled bath, adjustable in the range from room temperature to 60 °C to a stability of better than 0.1 °C.

Dielectric layering in the phantom was achieved by use of a solid resin material to simulate the properties of fat. The use of a liquid for this purpose, as suggested in [82], was rejected due to problems of turbulence when scanning the probe which leads to mixing of the liquids. A solid resin layer allows greater measurement precision but precludes measurement of internal field distributions. The material employed was described in [70]. Its dielectric properties vary with the mixture of ingredients and the frequency. For the purposes of the computer simulation, the values at 5 GHz were taken to be $\varepsilon' = 6.0$, $\varepsilon'' = 0.8$.

3.1.3 Computer controlled scanning and data logging system

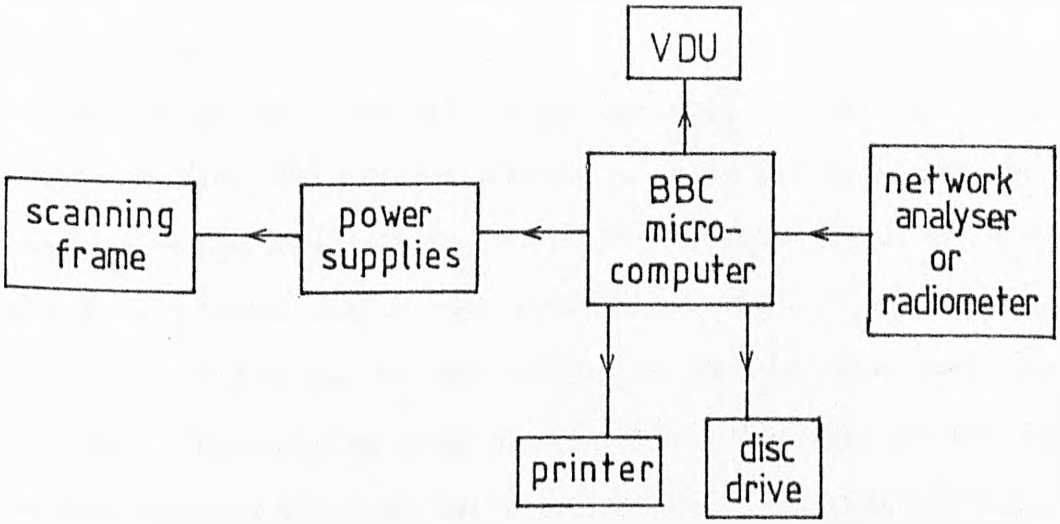

Fig. 3.3 Computer controlled scanning and data logging system.

Fig 3.3 shows the computer controlled scanning frame and data logging system. The scanning frame consists of two orthogonally mounted scanners with a 70 cm screw thread, allowing movement to any position in a 50 cm x 50 cm horizontal plane to a positional accuracy of 0.1 mm. The frame is supported on a gantry which allows vertical positioning. The scanners are moved by two 5 amp stepper motors which are driven by controllable power supplies incorporated into the top rack of the radiometer box. Control of the power supplies is achieved by the BBC micro-computer via its user port. The BBC computer also logs data which is collected at each sample point via its analogue input, and can process and display this data in graphical or pictorial form.

The scanning system has been designed for use in the measurement of field patterns and also for radiometric linear and tomographic scanning of temperature irregularities (chapters 6 and 7). General purpose software has been assembled for these functions, which is described in Appendix 2.

3.1.4 Details of the measurement procedure

The procedure for the measurement of field patterns in water was as follows:

The waveguide probe was clamped securely to the side of the water tank with the aperture facing out into the tank, the short dimension of the waveguide vertical. The monopole probe, which was held in a perspex jig to the moveable platform of the scanning frame, was positioned in the centre of the aperture face (see Fig 3.4a). The scanning frame was carefully positioned so that the monopole moved parallel to the aperture face. The tank was filled with water and allowed to reach the desired temperature. The microwave measurement equipment was then set up, the monopole was moved to its starting position and the scanning routine on the BBC computer initiated. Scanning and data logging were then fully automatic.

For measurement of fields in layered media the procedure was similar to that described above. When the waveguide and monopole probe were set up, a sheet of the resin fat-simulating material was attached to the tank and placed with the centre of one of its faces flush with the aperture face. With this method, there was always a thin layer of water between the waveguide filler and the resin. A second method of attaching the resin layer was also used. The waveguide aperture was dipped into the liquid resin mixture which was then allowed to set, ensuring a perfect contact between waveguide filler and resin. Field scans with both methods were compared and no discrepancy was noted. The tank was filled with water and a long period allowed for temperature stabilisation of the resin. The monopole was then scanned in the water on the far

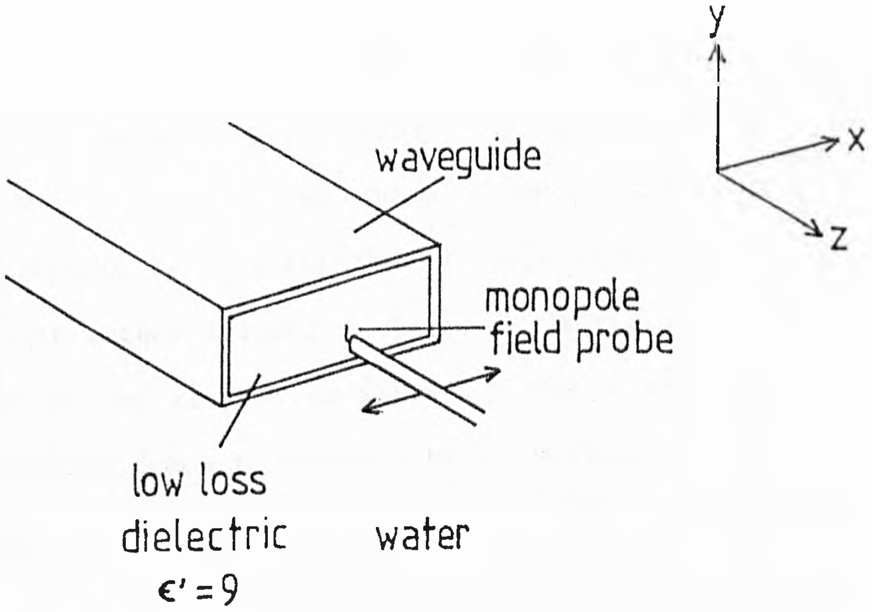

Fig. 3.4a Configuration of waveguide and field probe for scanning in homogeneous water, showing initial setting-up position.

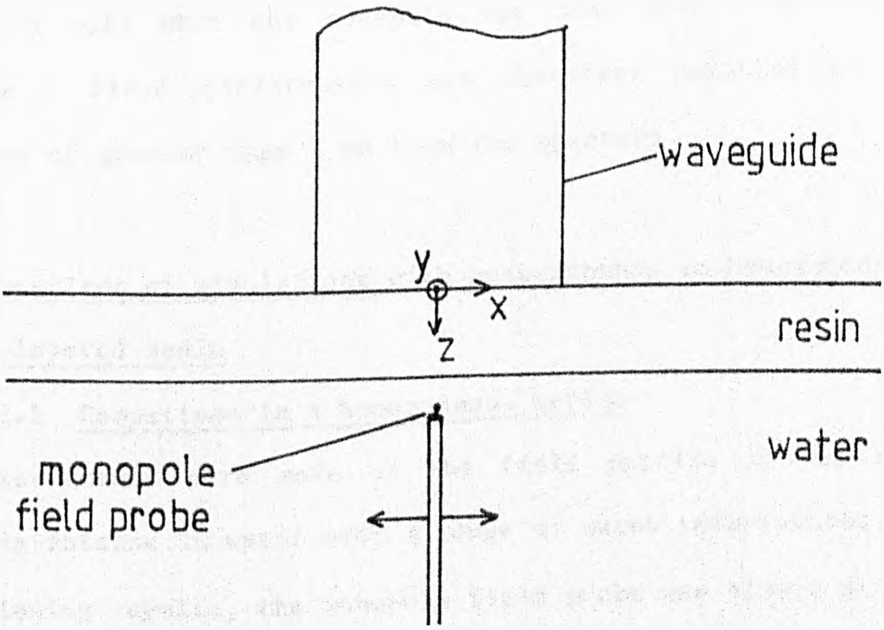

Fig. 3.4b Field measurement set-up for bi-layered media.

side of the resin, thus measuring the field in the second layer of this two layer structure (Fig 3.4b).

Errors arose in this experimental procedure due to the positioning of the monopole field probe. The initial position of the monopole, just in front of the centre of the waveguide, was set manually, and checked by ensuring that a field maximum occurs at this point. This method allowed an error in initial position of ±0.5 mm. Some of the results consequently show a small lateral offset. The scanning frame is accurate in its movement to ±0.1 mm, ensuring greater precision in the relative position of scan points.

Another source of error arose due to the interaction of the monopole with the source. In order to assess the importance of this interaction, the reflection coefficient of the waveguide antenna was measured as a function of monopole position. Variation was noted only when the monopole was less than 1 mm from the aperture. Field measurements are therefore reported only for distances of greater than 1 mm from the aperture.

3.2 Comparison of simulations with measurements in homogeneous and bi-layered media

3.2.1 Comparison in a homogeneous medium

Measurements were made of the field pattern of the filled waveguide antenna in water over a range of water temperatures. For the following results, the monopole field probe was always directed in the y direction and the measurements are compared with simulations in which the y component of the electric field only is considered. All measurements give field amplitude relative to a reference point. For direct comparison, the simulations in each

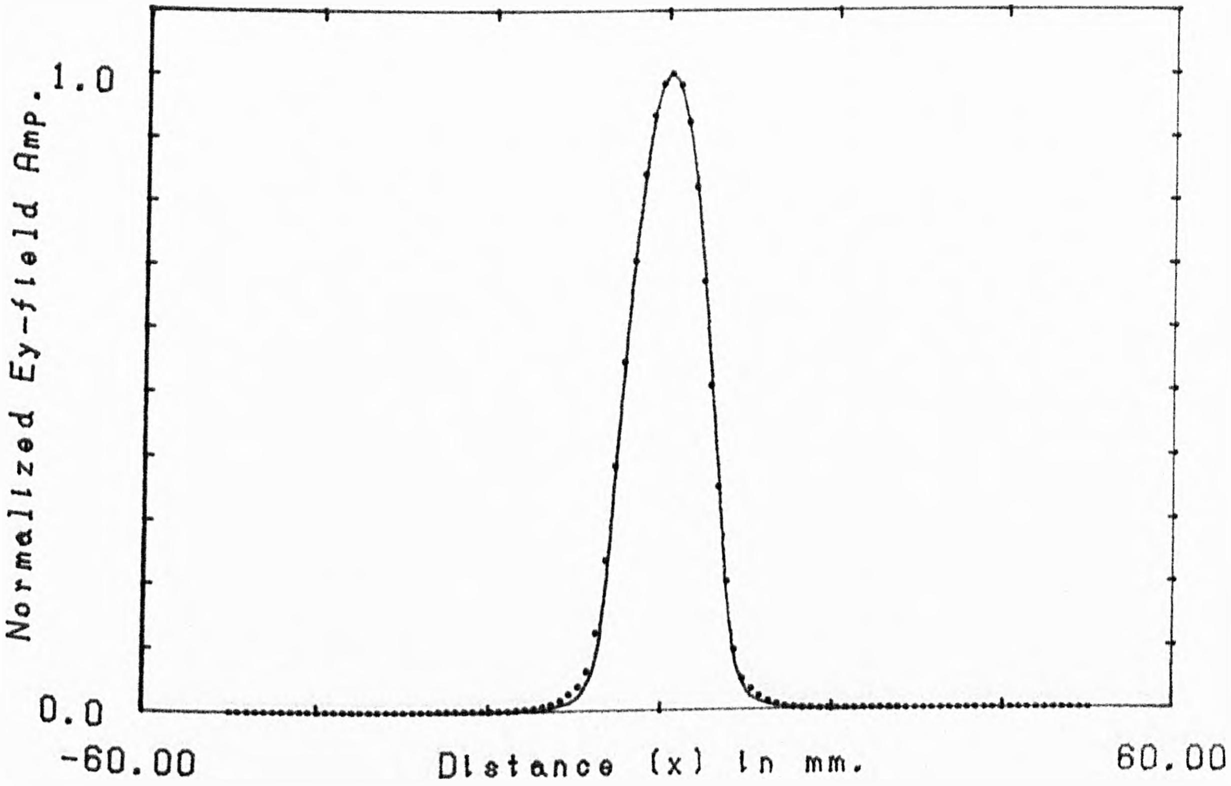

Fig.3.5a: Comparison of measured (.) with
simulated (–) X scan.
Water T=17°C. 5.0 GHz. Z=1mm.

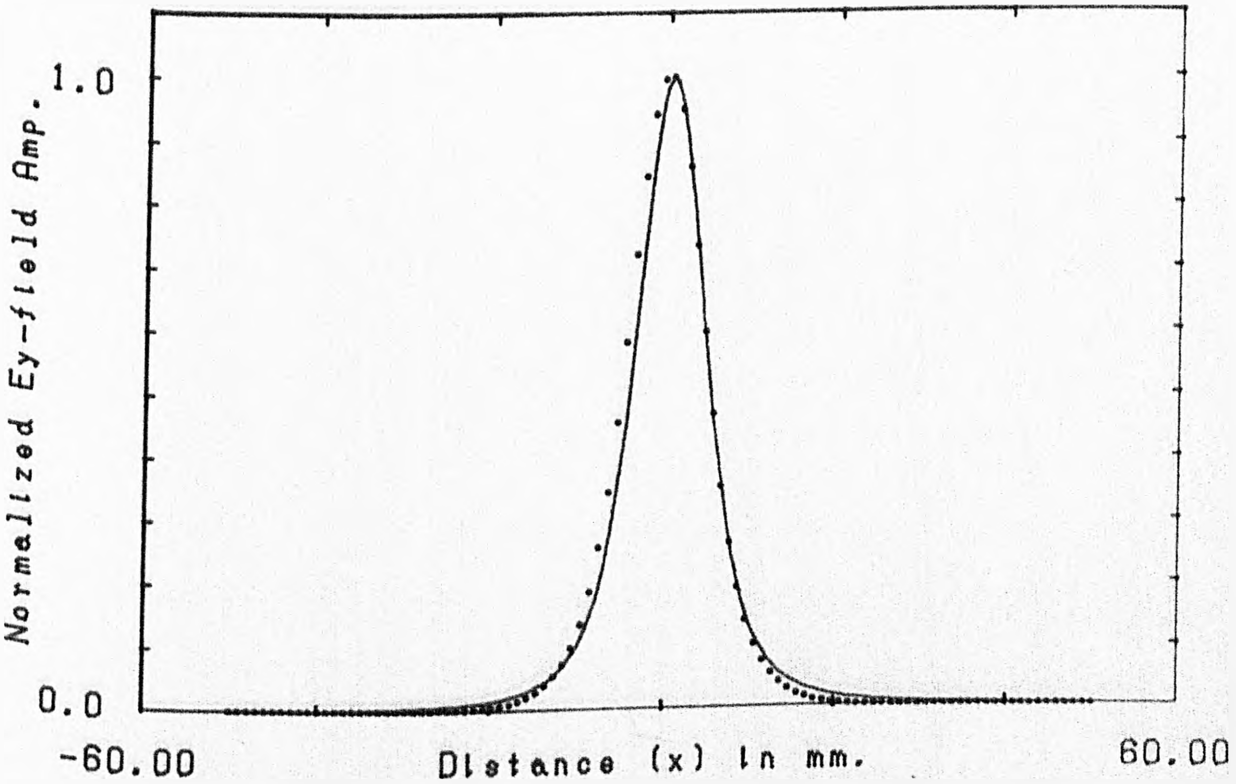

Fig.3.5b: Comparison of measured (.) with
simulated (–) X scan.
Water T=17°C. 5.0 GHz. Z=6mm.

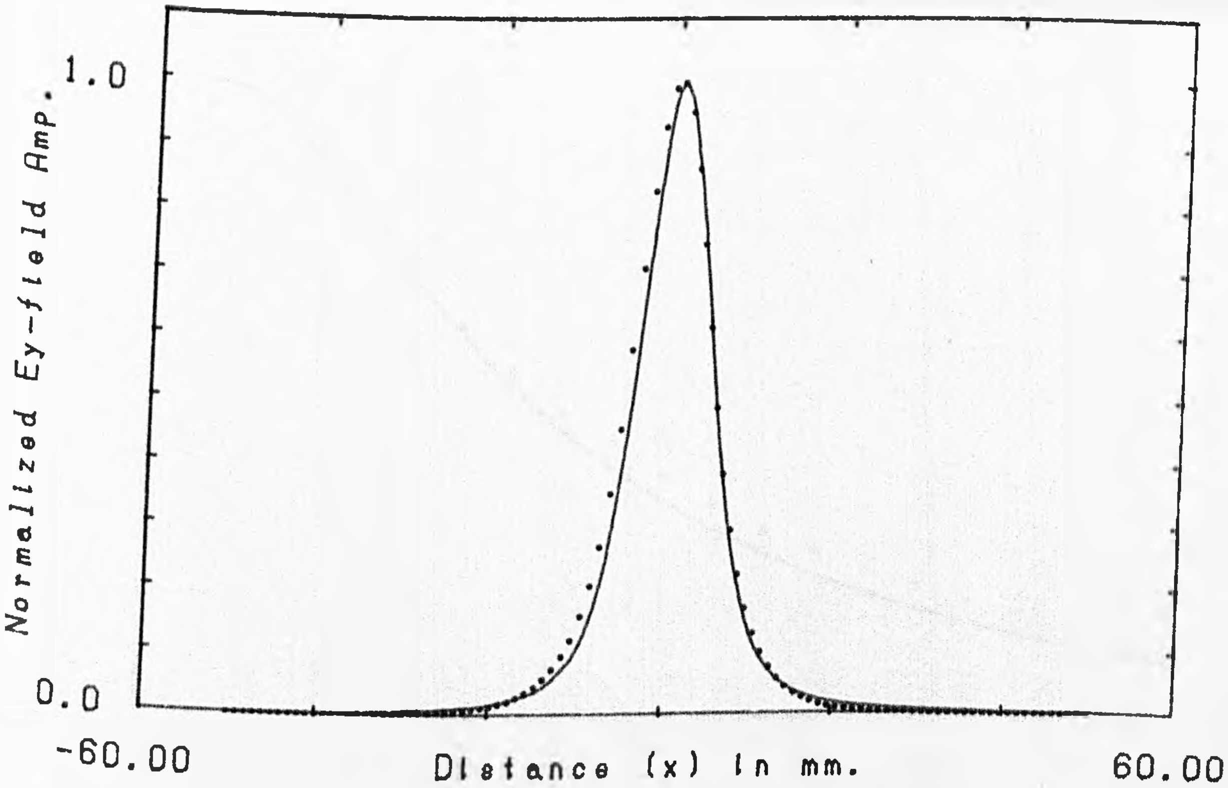

Fig.3.5d: Comparison of measured (.) with simulated (-) X scan. Water T=35°C. 4.6 GHz. Z=6mm.

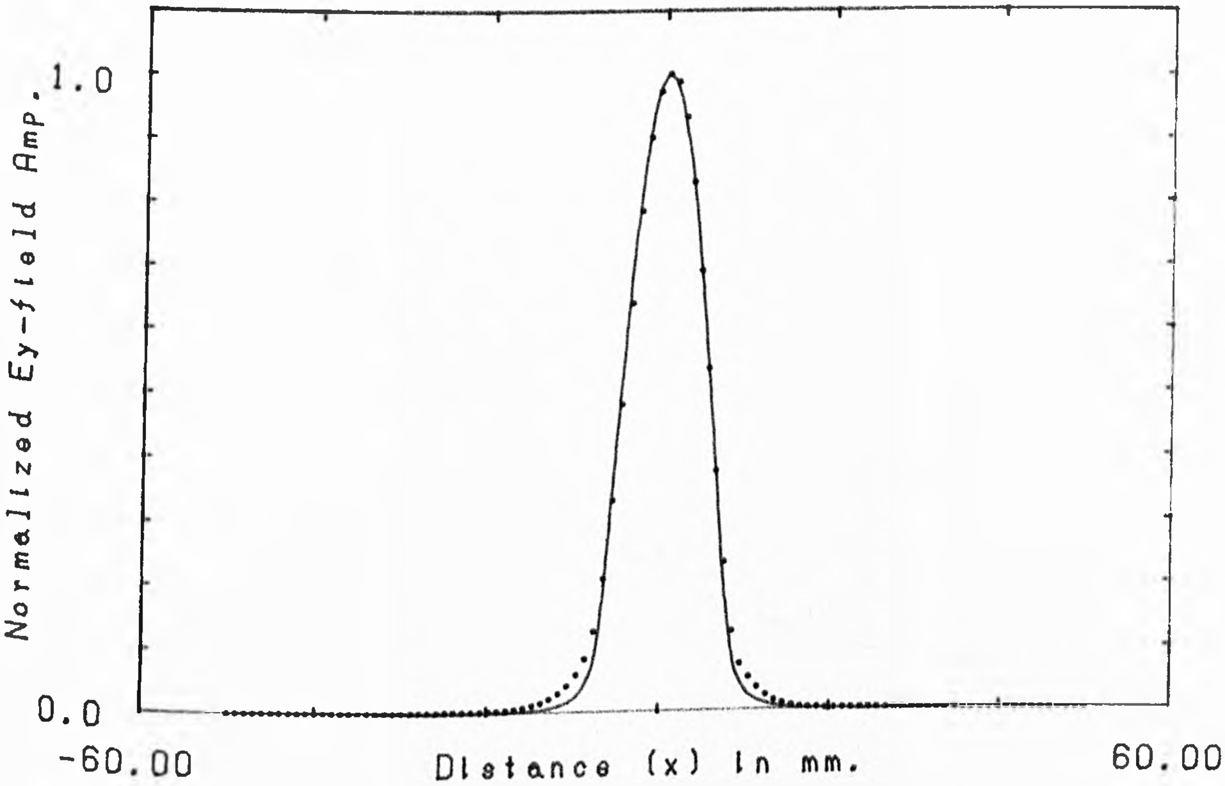

Fig.3.5c: Comparison of measured (.) with
simulated (-) X scan.
Water T=35°C. 4.6 GHz. Z=1mm.

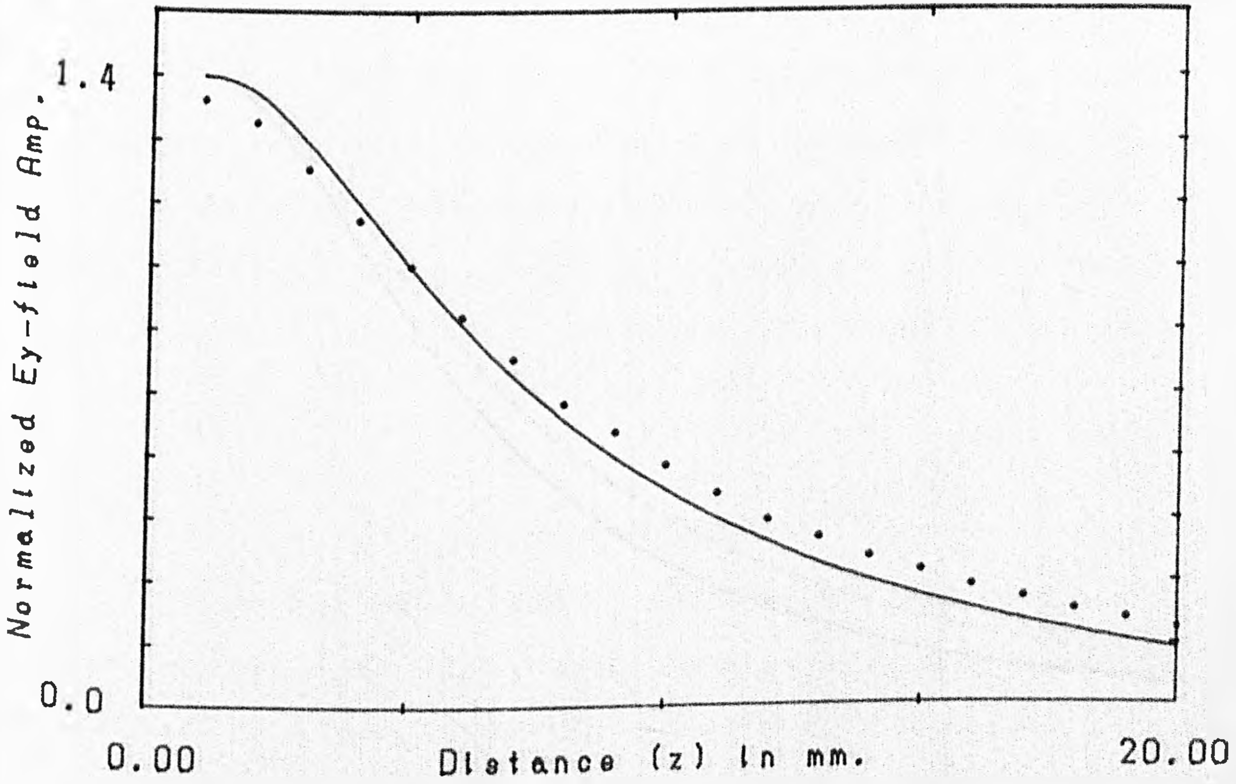

Fig.3.6b: Comparison of measured (.) with simulated (-) Z scan.
Water T=35 °C.

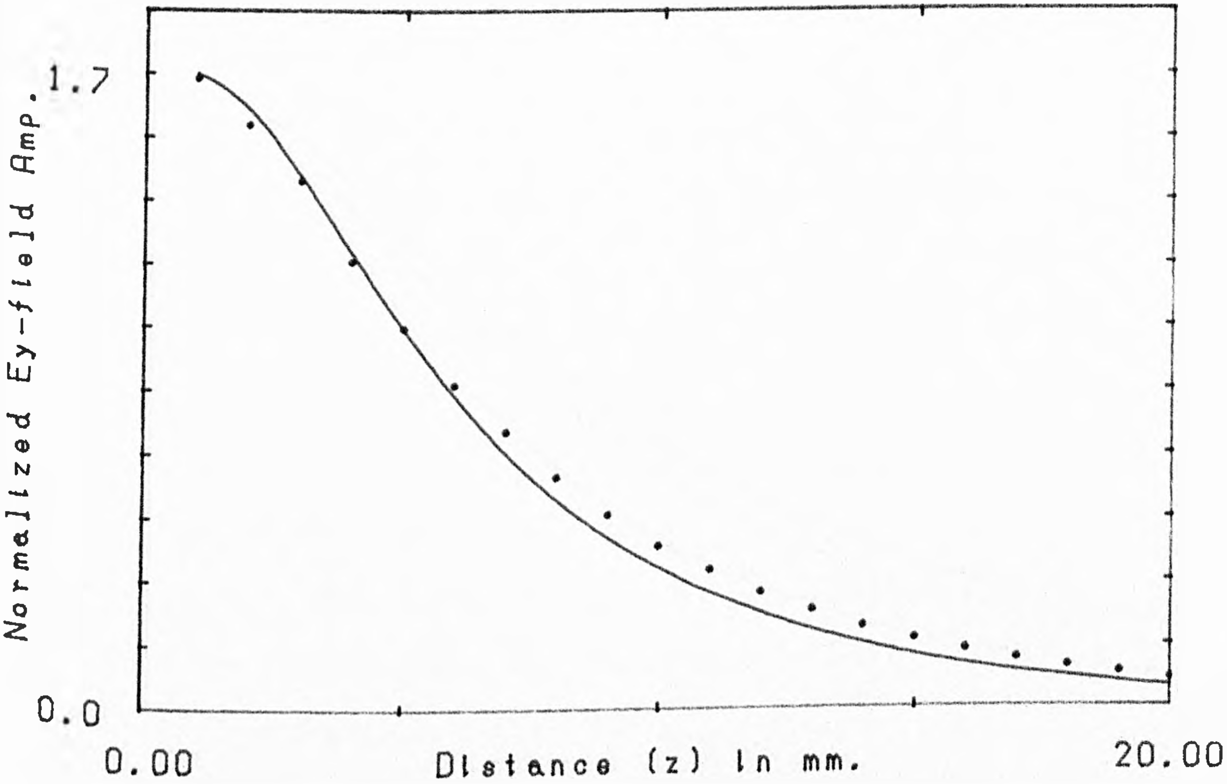

Fig.3.6a: Comparison of measured (.) with simulated (–) Z scan.
Water T=17°C.

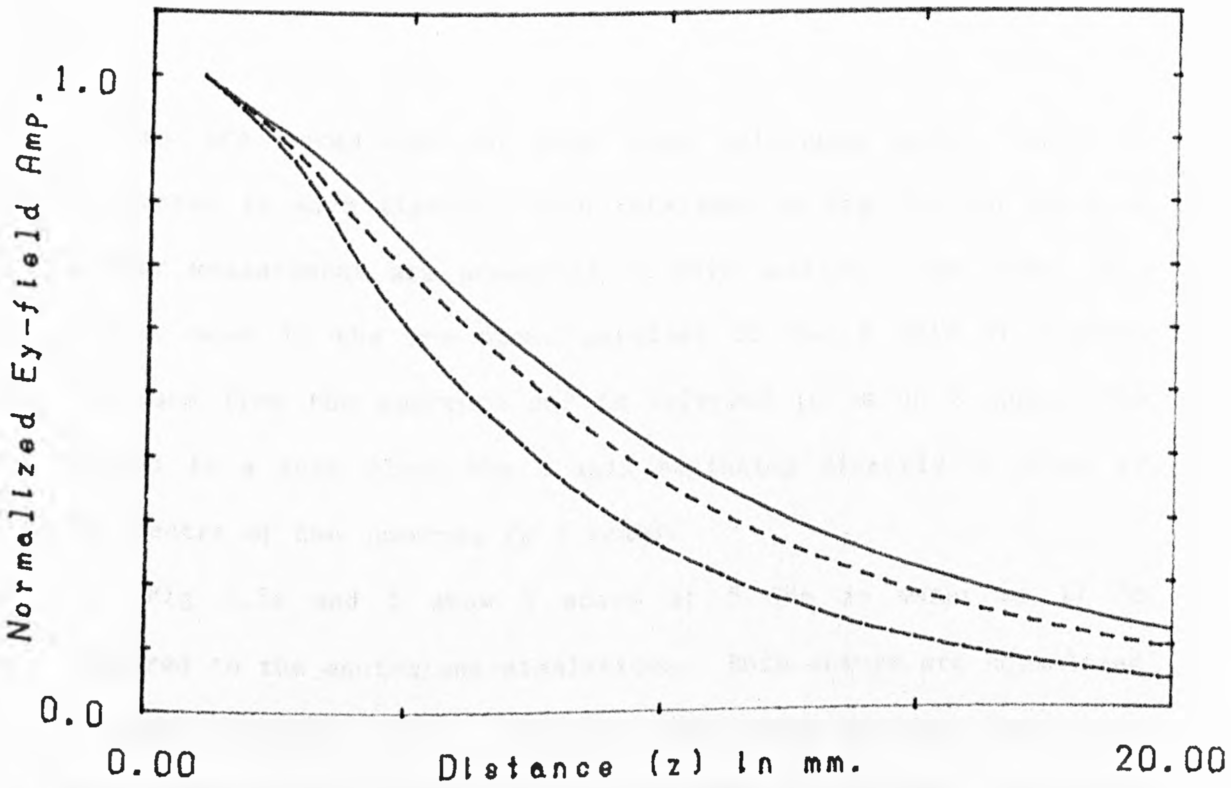

Fig.3.7a: Comparison of measured Z scans in water for three different water temperatures. (-) 37°C. (- -) 28°C. (--) 17°C.

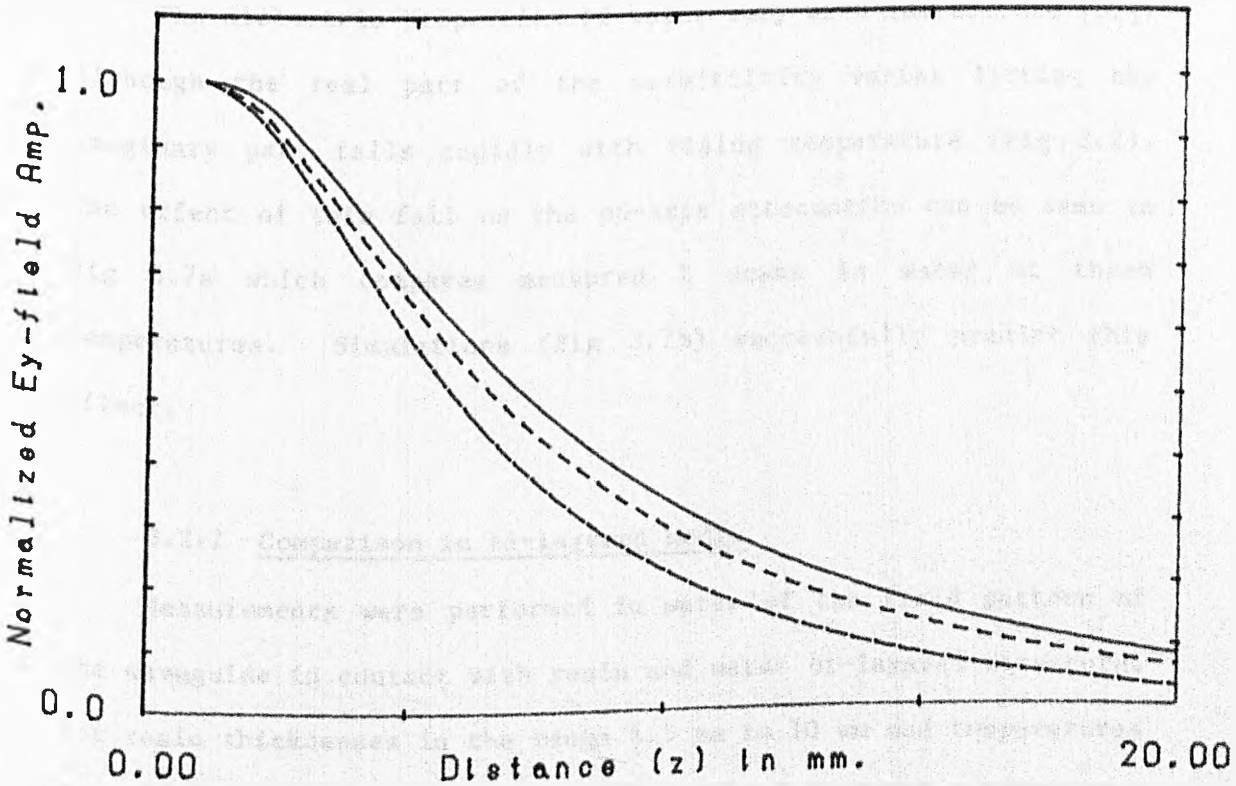

Fig.3.7b: Simulation equivalent to Fig.3.7a.

figure are normalized to this same reference point, which is indicated in each figure. With reference to Fig 3.4 two types of linear measurement are presented in this section. The first is a linear scan in the x-z plane parallel to the x axis at a given distance from the aperture and is referred to as an X scan. The second is a scan along the z axis beginning directly in front of the centre of the aperture (a Z scan).

Fig 3.5a and b show X scans at 5 GHz in water at 17 °C compared to the equivalent simulations. Both curves are normalized to their maximum values. Fig 3.5c and d show similar scans at a water temperature of 35 °C and a frequency of 4.6 GHz. Figs 3.6a and b show Z scan comparisons. Agreement between simulation and measurement is reasonable but not exact, the simulations slightly over-estimating the on-axis attenuation.

The dielectric properties of water vary with temperature [89]. Although the real part of the permittivity varies little, the imaginary part falls rapidly with rising temperature (Fig 3.2). The effect of this fall on the on-axis attenuation can be seen in Fig 3.7a which compares measured Z scans in water at three temperatures. Simulations (Fig 3.7b) successfully predict this effect.

3.2.2 Comparison in bi-layered media

Measurements were performed in water of the field pattern of the waveguide in contact with resin and water bi-layered structures for resin thicknesses in the range 4.5 mm to 10 mm and temperatures from 17 °C to 37 °C at 4.6 and 5 GHz. Fig 3.8a shows a comparison between simulated and measured field values for 3 X scans at different distances from the resin/water boundary for a 10 mm resin

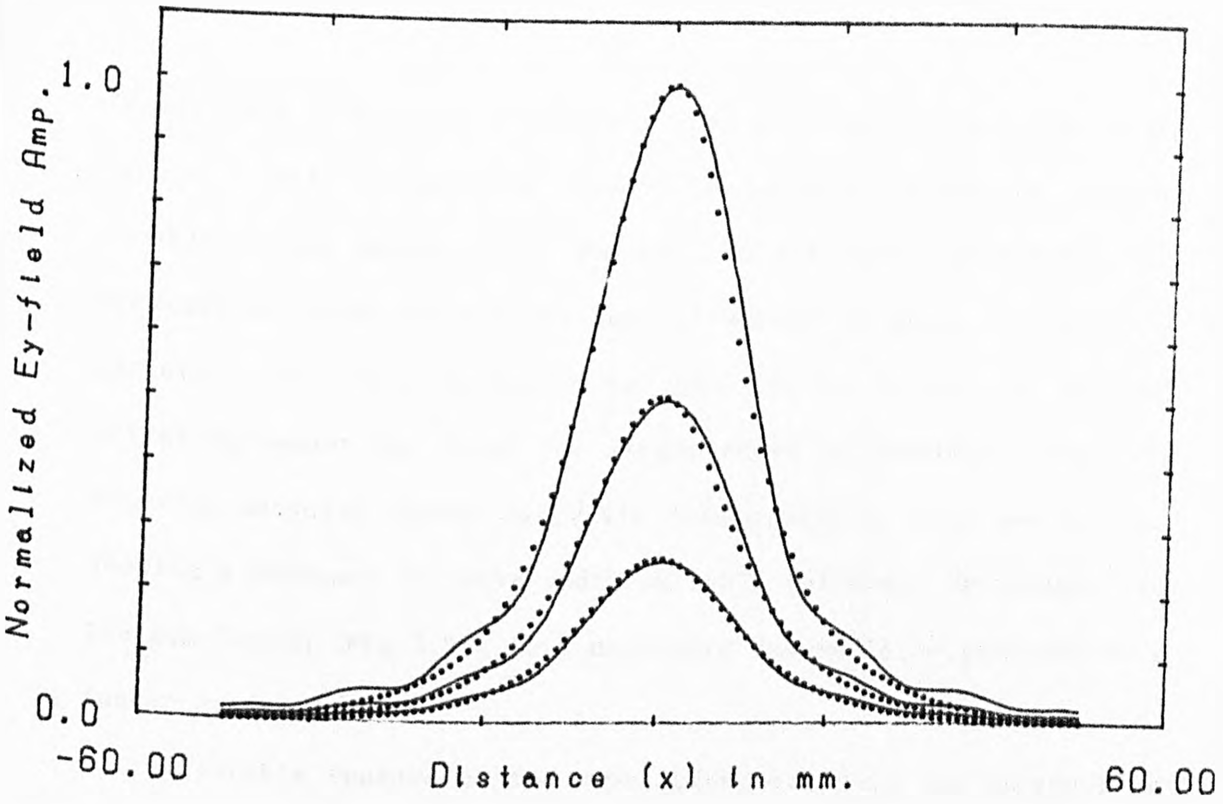

Fig.3.8a: Comparison of measured (.) with simulated (-) X scans. Z=11mm,16mm,21mm. 10mm resin + water T=28°C. 5.0 GHz.

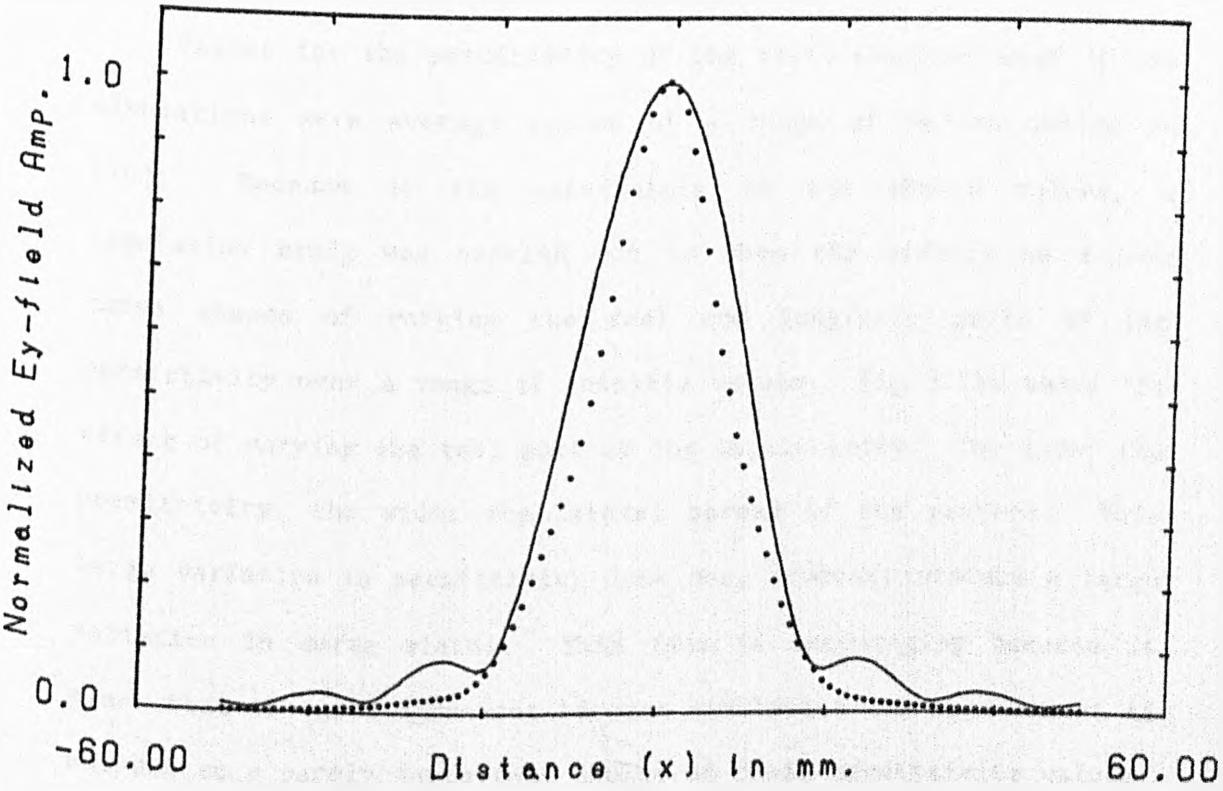

Fig.3.8b: Comparison of measured (.) with simulated (-) X scan. Z=5.5mm. 4.5mm resin + water T=28°C. 5.0 GHz.

layer. Fig 3.8b shows a single X scan at 1 mm from a 4.5 mm resin layer. All comparisons showed reasonable agreement between simulation and measurement; however, in all cases considered, the simulations overestimated the lateral spread or width of the field pattern. The best agreement is seen in Fig 3.8a. In general better agreement was found for larger resin thicknesses. Fig 3.9a compares measured curves for resin thicknesses of 9 mm and 4.5 mm, showing a decrease in curve width as resin thickness decreases. In the simulation (Fig 3.9b) this narrowing can again be seen but to a lesser extent.

A notable feature of the simulation curves is the presence of a low amplitude side lobe structure, which cannot be seen on the measured results. A logarithmic plot (Fig 3.10) of a measured curve (6 mm from a 5 mm resin layer) reveals that side lobes are indeed present but at a much lower amplitude.

Values for the permittivity of the resin material used in the simulations were average values of a range of values quoted in [70]. Because of the uncertainty in the chosen values, a simulation study was carried out to show the effects on X-scan curve shapes of varying the real and imaginary parts of the permittivity over a range of possible values. Fig 3.11a shows the effect of varying the real part of the permittivity. The lower the permittivity, the wider the lateral spread of the pattern. This large variation in permittivity does not, however, produce a large variation in curve widths. This fact is encouraging because it means that the good agreement between simulation and measurement is not due to a purely fortuitous choice of resin permittivity values. No effect on curve width can be observed by varying the imaginary part of the permittivity (Fig 3.11b). Increasing the loss term

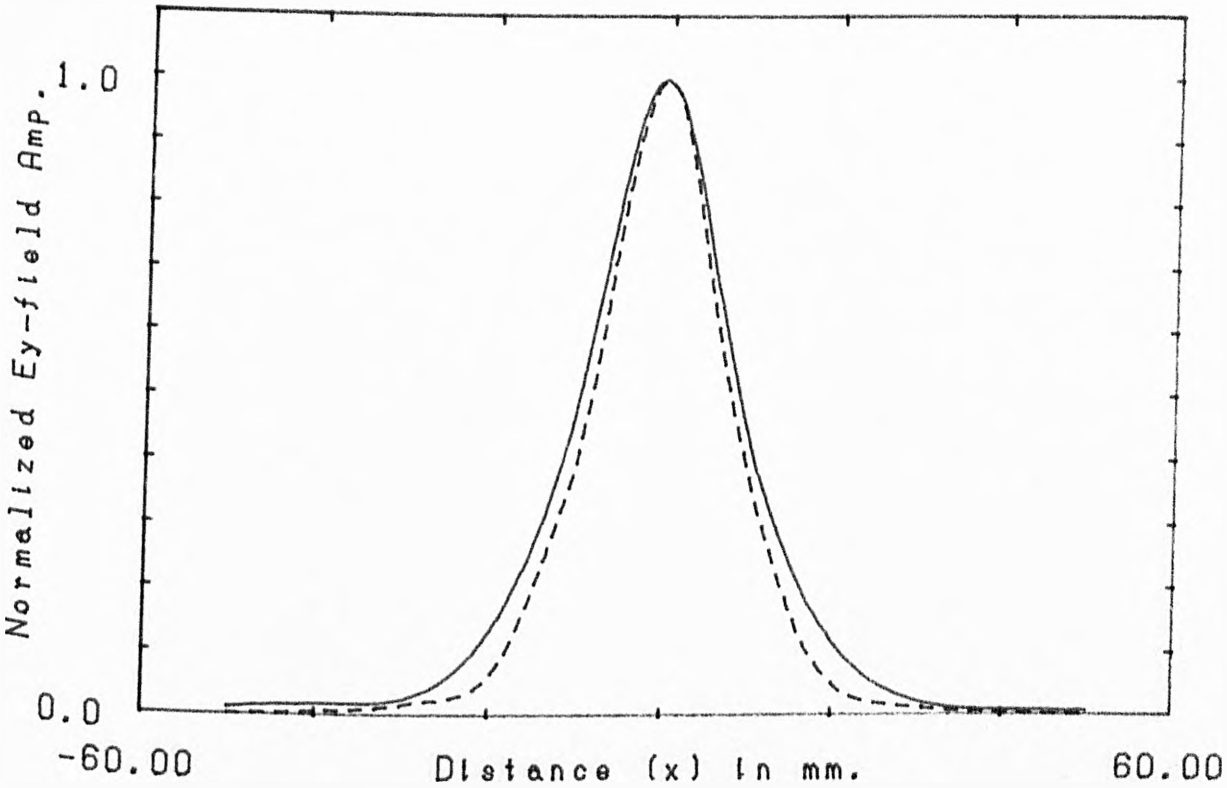

Fig.3.9a: Comparison of X scans measured 1mm from resin layers of two different thicknesses. (-) resin thickness=9mm. (- -) 4.5mm.

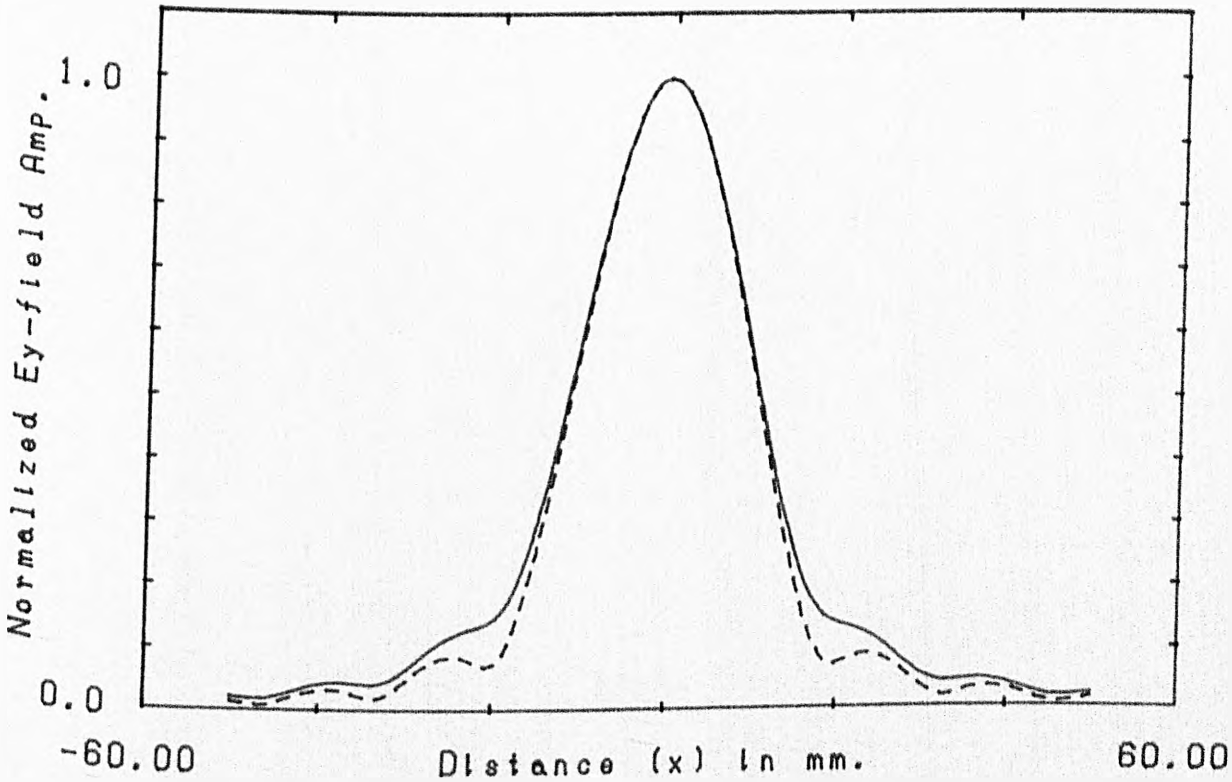

Fig.3.9b: Simulation equivalent to Fig.3.9a.

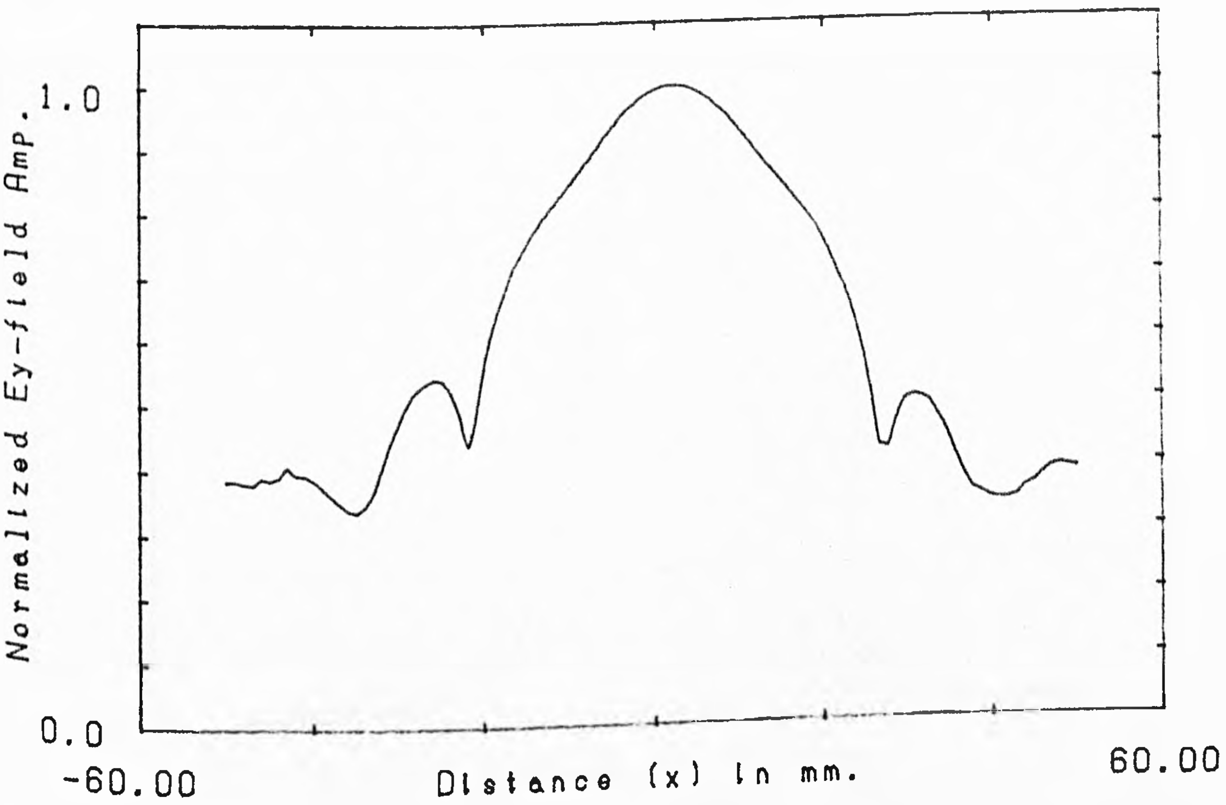

Fig.3.10: Logarithmic plot of measured X scan.
6mm from a 5mm thick resin layer.
T=37°C, 4.6 GHz.

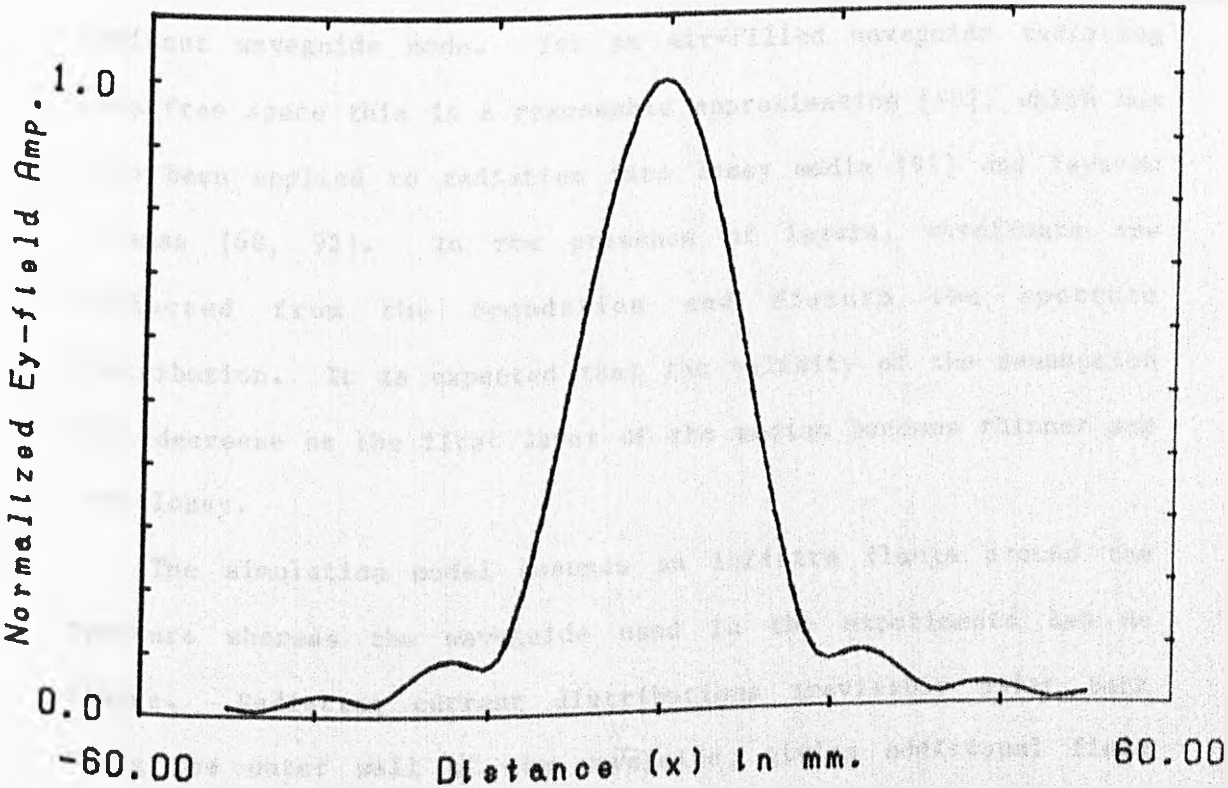

Fig.3.11b: Simulated X scans varying the imaginary part of permittivity of resin. 10mm resin + water. Z=11mm. (- -) $\varepsilon''=0.4$ (-) $\varepsilon''=0.8$ (--) $\varepsilon''=1.2$.

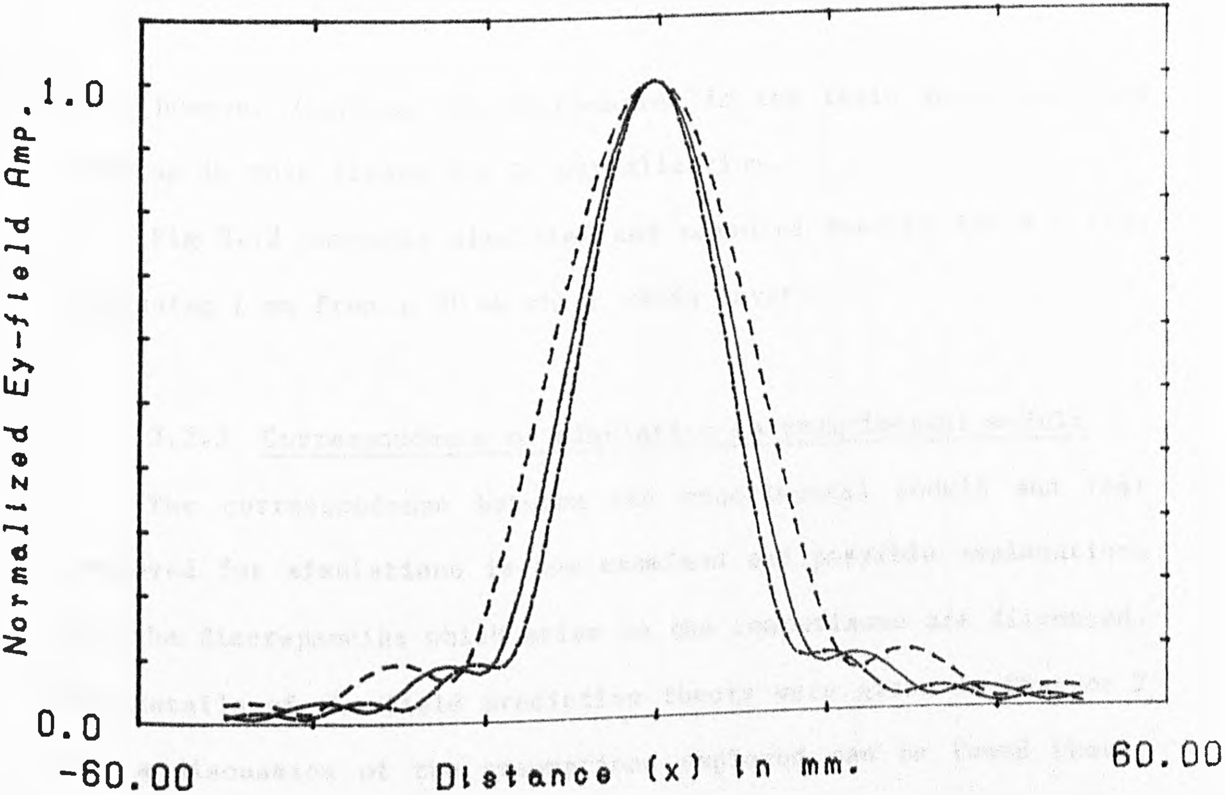

Fig.3.11a: Simulated X scans varying the real part of permittivity of resin. 10mm resin + water. Z=11mm. (- -) ε'=4 (-) ε'=6 (--) ε'=8.

does however increase the attenuation in the resin which does not show up in this figure due to normalization.

Fig 3.12 compares simulated and measured results for a Z scan beginning 1 mm from a 10 mm thick resin layer.

3.2.3 Correspondence of simulation to experimental models

The correspondence between the experimental models and that employed for simulations is now examined and possible explanations for the discrepancies which arise in the comparisons are discussed. The details of the field prediction theory were given in Chapter 2 and a discussion of the assumptions employed can be found there. This section concerns the application of the theory in modelling the experimental situation.

In the simulation model it is assumed that the distribution of field in the medium just in front of the aperture is that of the dominant waveguide mode. For an air-filled waveguide radiating into free space this is a reasonable approximation [90], which has also been applied to radiation into lossy media [91] and layered plasmas [68, 92]. In the presence of layers, wavefronts are reflected from the boundaries and disturb the aperture distribution. It is expected that the validity of the assumption will decrease as the first layer of the medium becomes thinner and less lossy.

The simulation model assumes an infinite flange around the aperture whereas the waveguide used in the experiments had no flange. Radiating current distributions inevitably exist back along the outer wall of the waveguide, giving additional field contributions in the very near field. The effects of flanges on waveguide radiation patterns have been examined in [93]. The good

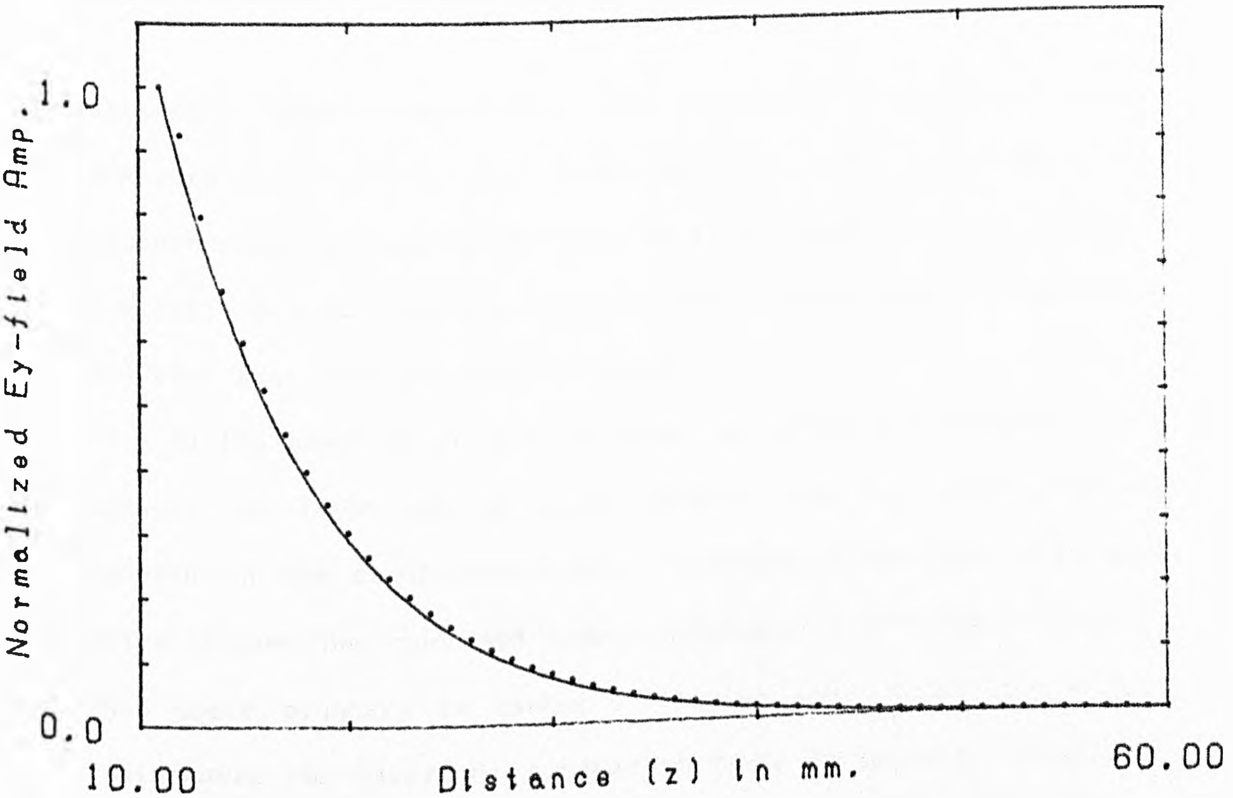

Fig.3.12: Comparison of measured (.) with simulated (-)
Z scan. X=0.
10mm resin + water T=28 °C. 5.0 GHz.

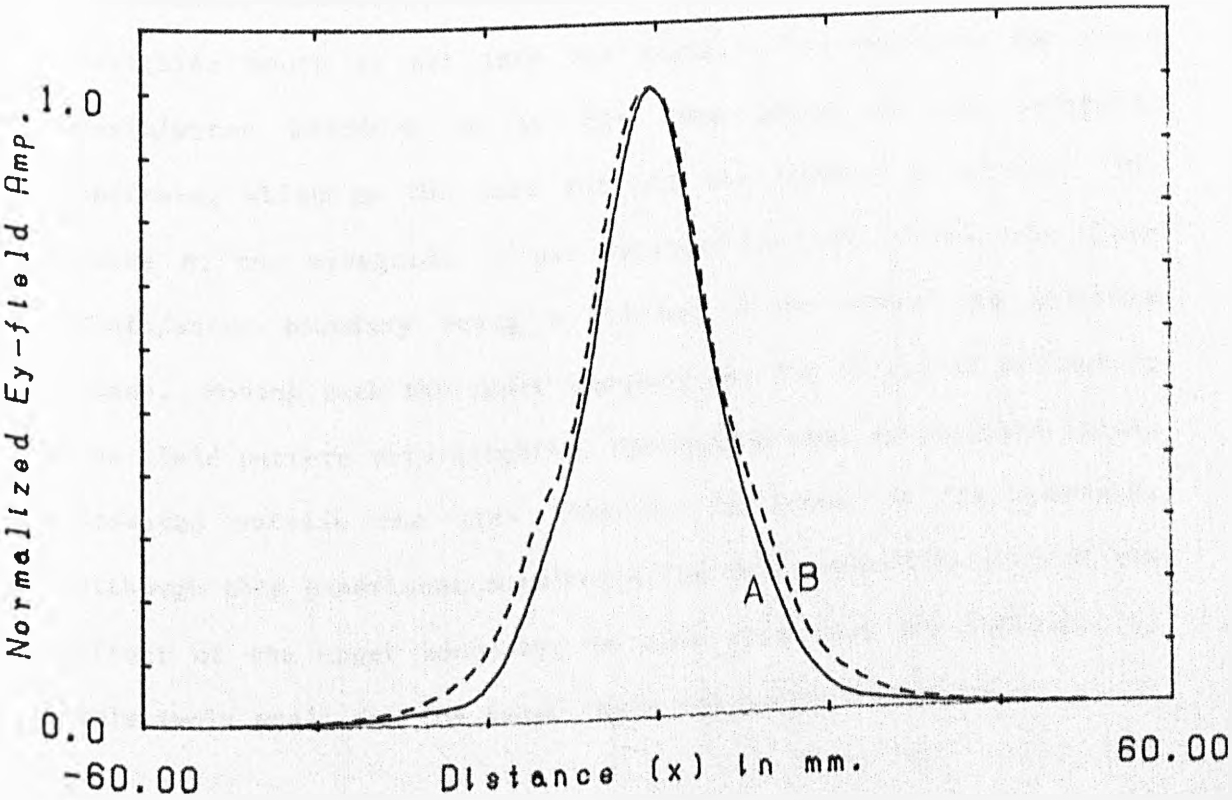

Fig.3.13: Comparison of measured X scans for different locations of upper resin/water boundary. Z=5.5mm
(- -) upper boundary at Z=-5mm. (-) Z=0mm.

agreement between simulation and experiment very close to the aperture ($z < \lambda/7$ in Fig 3.5a) suggests that these additional contributions are negligible at a small distance from the aperture. However, this discrepancy may have some effect when the waveguide radiates into less attenuative resin.

In the presence of a resin layer an additional problem occurs because the layer has an upper surface (see Fig 3.4b) which is ignored in the simulation model. Multiple reflections will take place between the upper and lower resin/water boundaries. In fact, this upper boundary is rather a complex one, consisting of the resin/waveguide interface surrounded by a resin/water interface. Experiments have been performed to assess the influence of this upper boundary on the field measurements. Fig 3.13 compares the results of two X-scans, both measured 1 mm from the lower resin/water boundary (5.5 mm from the aperture). In both cases the waveguide mouth is set into the resin. For curve A, the upper resin/water boundary is in the same plane as the waveguide aperture, which is the case for all the results of #3.2.2. For curve B, the waveguide is set further into the resin, the upper resin/water boundary being a further 5 mm behind the aperture plane. Moving back the upper boundary has the effect of broadening the field pattern very slightly, increasing most those field values measured outside the area directly in front of the aperture. Although this experiment does not allow exact quantification of the effect of the upper boundary, it does show that its influence is relatively small for the least resin thickness considered.

3.2.4 Discussion of results

The results show good agreement between simulation and measurement, although generally better at greater distances from the aperture, as can clearly be seen in the results for bi-layered structures. For small resin thicknesses, the simulations show a wider field pattern spread with a more pronounced side lobe structure when compared to measurement. The discrepancy may be accounted for by considering the limitations of the spectral propagation/cascade algorithm. With reference to # 2.2.3, the propagating spectrum is cut off for $(\lambda s_x)^2 + (\lambda s_y)^2 > 1$, when layers are present. Since the aperture represents a relatively wide bandwidth source when in contact with resin, this curtailment leads to the loss of some higher spectral components. Application of the inverse Fourier transform thus gives a broader distribution with a more pronounced sidelobe structure. The discrepancy is reduced at greater distances since propagation in a lossy medium acts as a low pass filter on the angular spectrum, heavily attenuating these higher spectral components.

Assumptions which were made in order to simplify the simulation model lead to many of the near field effects (eg fields due to currents on the waveguide) being neglected. This problem is not serious in water because its high permittivity and high loss confine these effects to an area very close to the aperture. The low loss of resin allows these effects to extend to greater distances. Additional discrepancies between simulation and experimental models arise with the presence of boundaries (# 3.2.3). As a result, the model for a homogeneous case is more accurate than that for the layered case.

The results illustrate the influence of a low permittivity overlying layer on the field pattern in water. The fat simulating resin leads to greater lateral spreading of the field pattern. This is due to the aperture being electrically smaller ($3\lambda_m/4 \times 3\lambda_m/8$) when in contact with resin rather than water ($2\lambda_m \times \lambda_m$). For bi-layered media it must be noted that comparison of field patterns was only carried out in the second medium because of the difficulty of measuring field in the solid resin material. Although good agreement in the second medium suggests that the simulations are correctly predicting field, it is not possible to say that the method has been completely validated. In the next section, this prediction method is used to reproduce some previously reported results, for extra validation, and in Chapter 6 field predictions are employed to simulate radiometric temperature data. Successful comparison of temperature predictions with experiment will provide additional evidence of the method's validity.

3.3 Simulated field patterns of rectangular apertures radiating into lossy media

Comparison of simulation with measured results has established that the computer algorithm can successfully predict field patterns in both homogeneous and bi-layered media. In this section, computer simulations are employed to model a number of situations which were not considered experimentally. Previously, only a single aperture size has been considered. In practice, any size of aperture and any aperture field distribution can be accommodated by the programme, giving the capability for modelling any type of contacting aperture antenna. In addition, the program is capable of modelling situations where any number of layers are present.

Figure 3.14 gives a two-dimensional plot of the field pattern for a 16 mm x 8 mm waveguide radiating into water at 28 °C. Fig 3.14a is a cut through the y = 0 or x-z plane (see Fig 3.4a) and 3.14b is a cut through the x = 0 or y-z plane. Fig 3.14c gives the half-amplitude width of the field in the x-z plane; in this figure each line of constant z (ie parallel to the x axis) is curtailed at the point where the field amplitude drops to half of the maximum value on that line (the maximum value in this case is always on the z axis). This representation allows the spreading of the emergent field to be seen. Fig 3.14d shows the half-amplitude width in the y-z plane. The field is quite directional in the x-z plane but spreads rapidly in the y-z plane, a consequence of the aperture being larger in the x dimension ($2.4\lambda_m$ in water) than in the y dimension ($1.2\lambda_m$). The smaller the aperture becomes, the field pattern tends towards that of a point source; a large aperture gives a field distribution which tends towards that of a plane wave. Further illustration of this fact is given in Figs 3.15 which show the half-amplitude widths in the x-z plane for a range of aperture sizes from 8 mm x 4 mm ($1.2\lambda_m$ x $0.6\lambda_m$) to 32 mm x 16 mm ($4.8\lambda_m$ x $2.4\lambda_m$). The increased directionality of the field pattern as the aperture size increases is evident. As well as influencing the spreading of the field pattern, the aperture size also affects the penetration depth. Figs 3.16 show field patterns for the same situation but in this case the field values are terminated at the point where they drop below 20 dB down in the maximum field value (just in front of the centre of the aperture). This decrease in attenuation as the aperture size increases has also been noted in

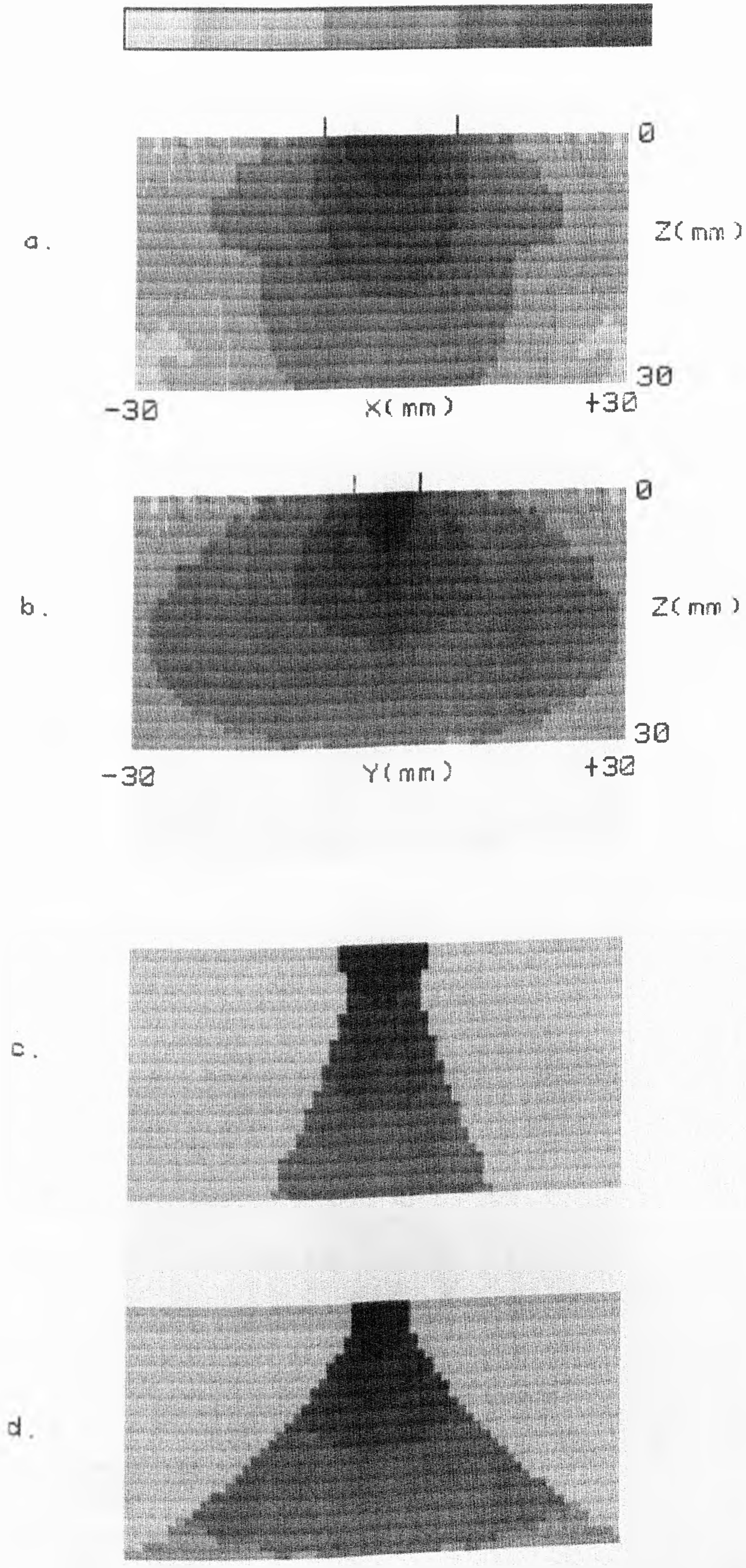

Fig 3.14 Field patterns of a waveguide radiating into water
Aperture = 16mm × 8mm (aperture marked on figures)

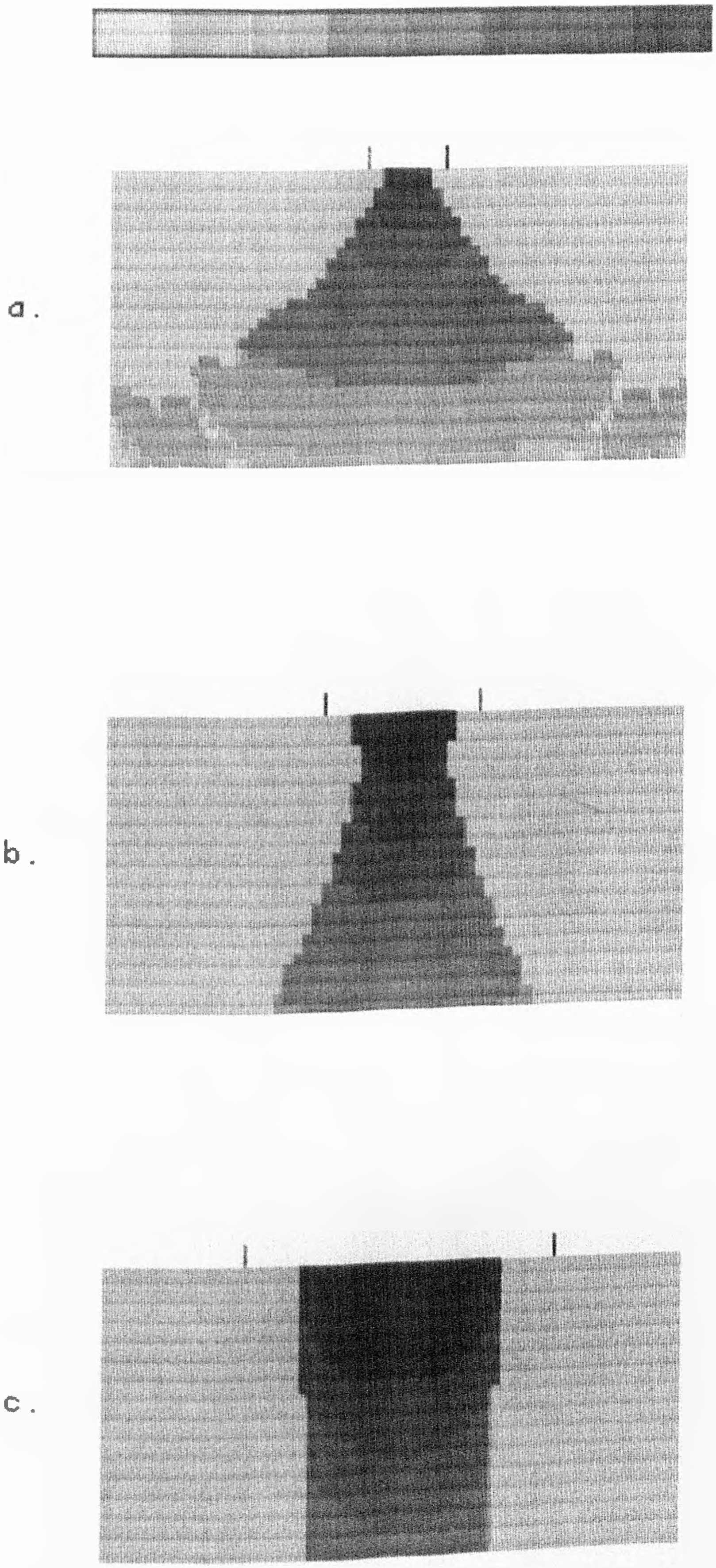

Fig.3.15 Half amplitude widths in the X-Z plane for three sizes of aperture radiating into water.

a. 8mm × 4mm
b. 16mm × 8mm
c. 32mm × 16mm

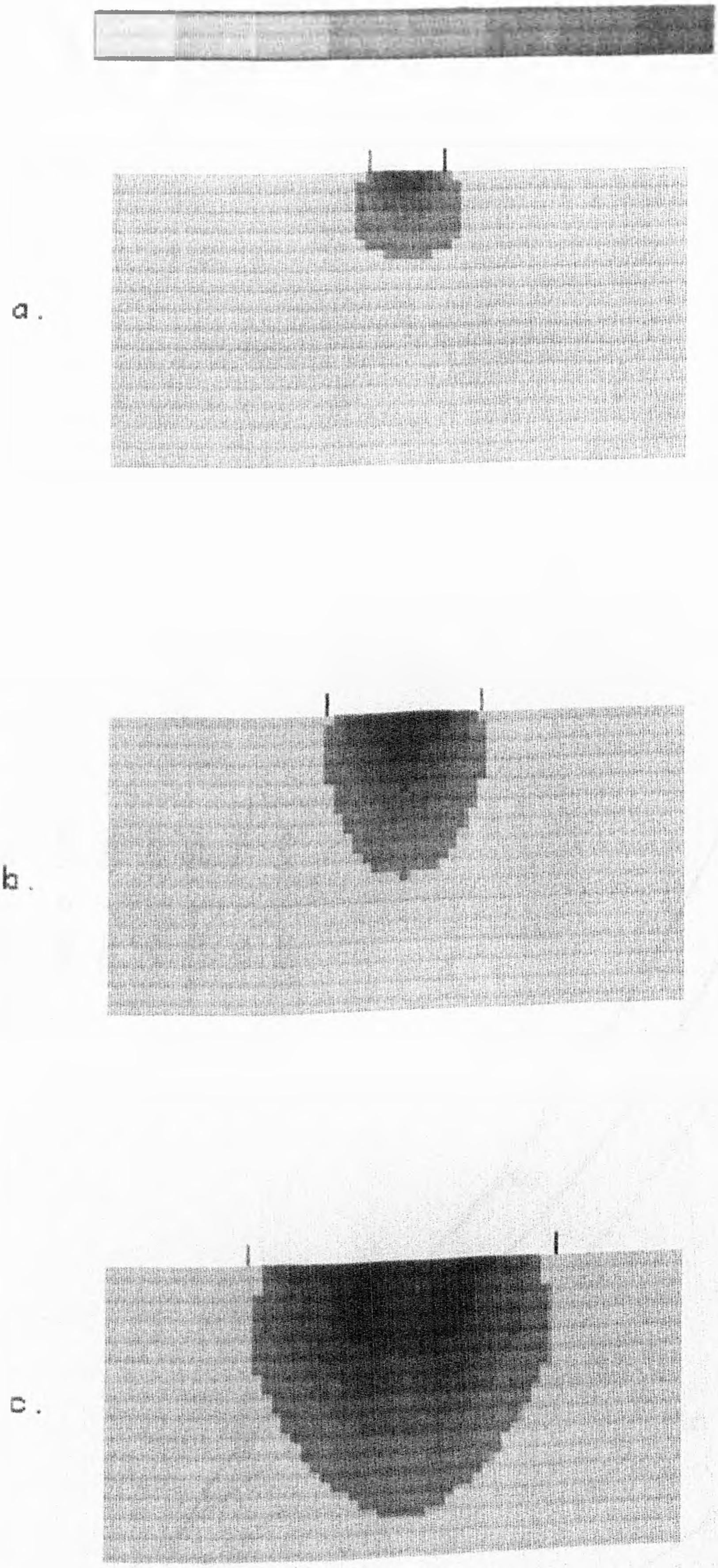

Fig.3.16 Field patterns in the X-Z plane cut off at -20 dB for three sizes of aperture radiating into water. 4 dB/level.

a. 8mm × 4mm
b. 16mm × 8mm
c. 32mm × 16mm

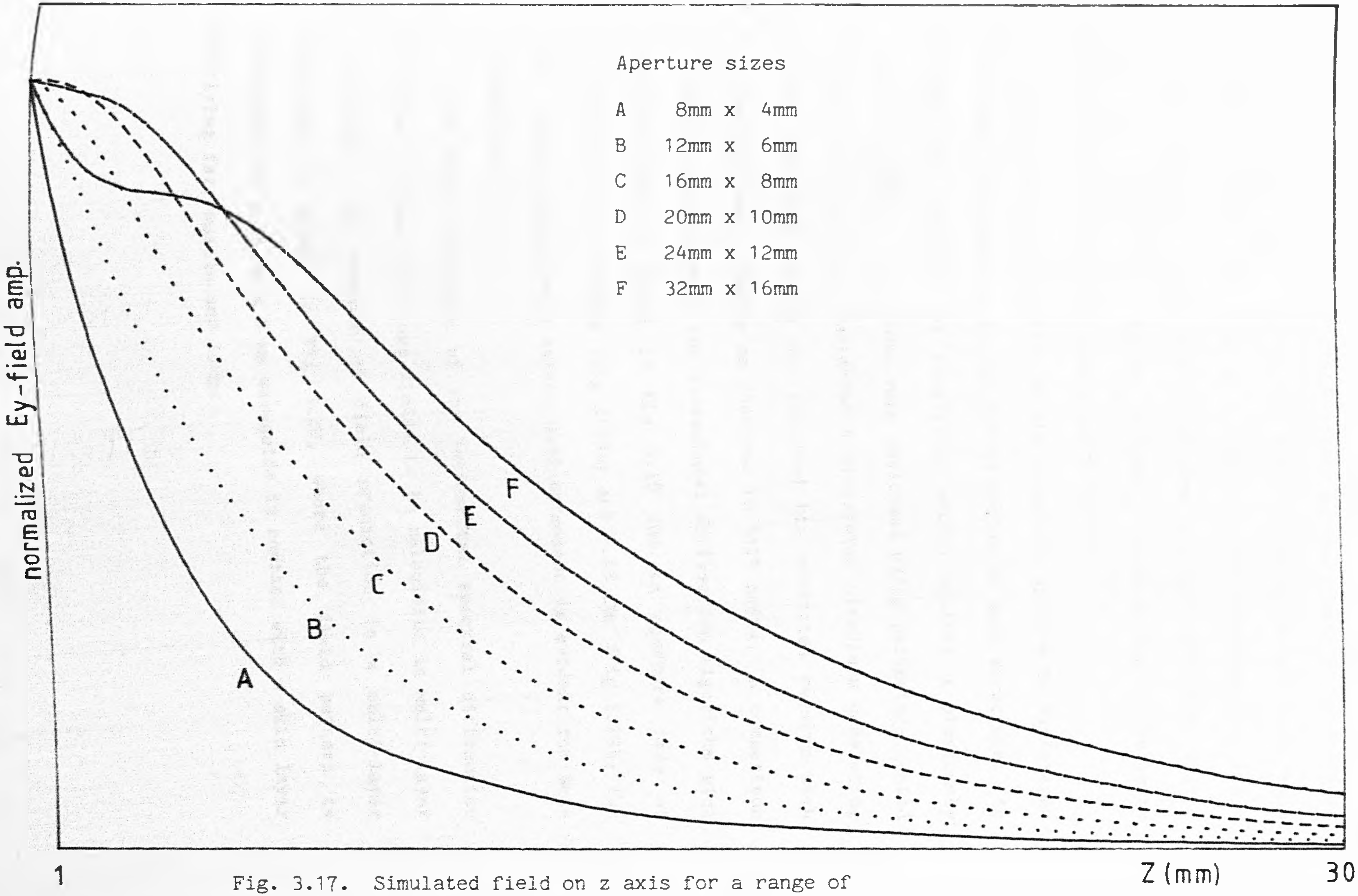

Fig. 3.17. Simulated field on z axis for a range of aperture sizes radiating into water.

[72] and [71]. Plots of field values on the z axis for a range of aperture sizes are shown in Fig 3.17. Figs 3.18a and 3.18b show the field patterns for a 16 mm x 8 mm aperture radiating into resin material and Figs 3.18c and 3.18d show the half-amplitude width. This size of aperture ($0.68\lambda_m$ x $0.34\lambda_m$) leads to rapid divergence of the field in this low permittivity medium.

Experimental validation of the algorithm applied to bi-layered media was only possible in the second medium of each structure. As a means of checking the prediction method against a previously reported method, simulations were performed using parameters quoted by Guy [67] who also considered a bi-layered structure consisting of fat overlying muscle and compared his predicted results with experimental measurements on phantoms in both media. A comparison of results predicted by the incremental diffraction algorithm with those of Guy is given in Fig 3.19 for an aperture size of 12 cm x 16 cm at 919 MHz (Fig 3.19a) and 2.45 GHz (Fig 3.19b) for field values along the z axis. Good agreement is evident for both frequencies.

The major advantage of the incremental spectral diffraction technique is that it allows fields to be calculated in multi-layer structures. An example of field prediction in a multi-layer structure is given in Fig 3.20, where the field pattern is predicted for a 16 mm x 8 mm waveguide in contact with a skin layer overlying fat, muscle and lung.

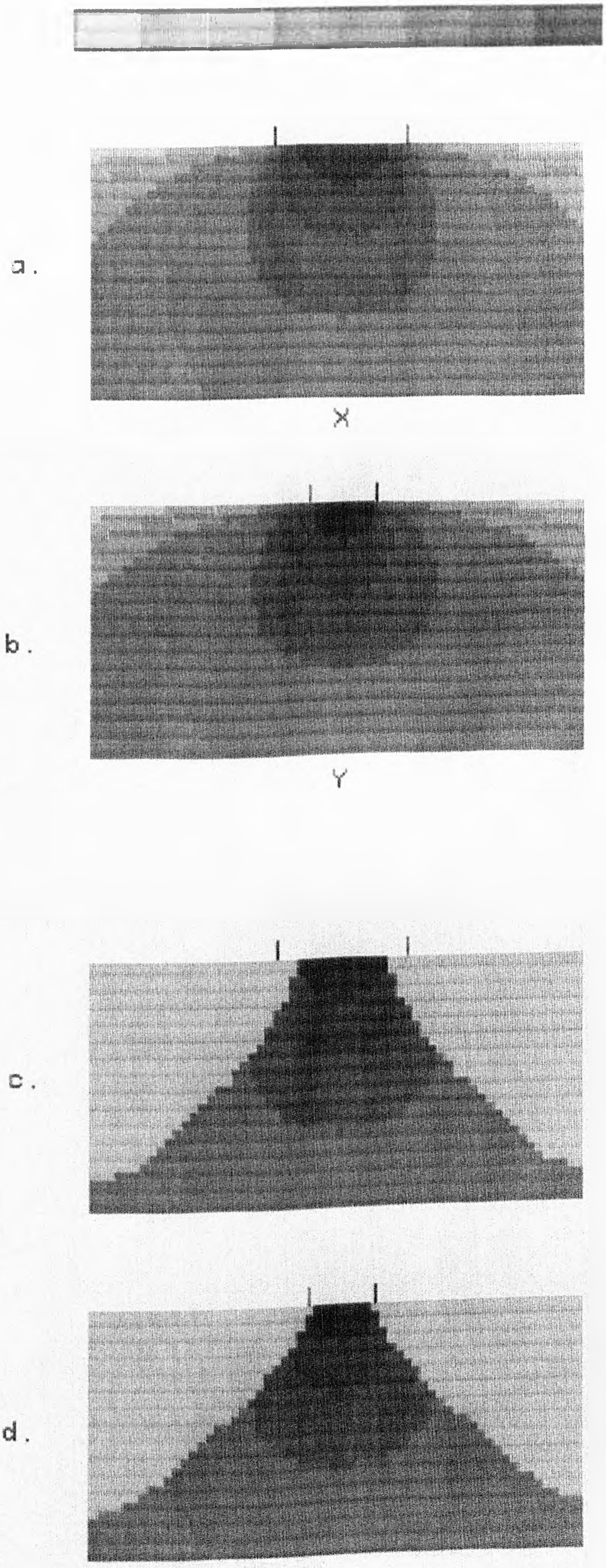

Fig.3.18 Field patterns in the X-Z (a. and c.) and Y-Z (b. and d.) planes of a waveguide radiating into resin. Aperture = 16mm × 8mm.

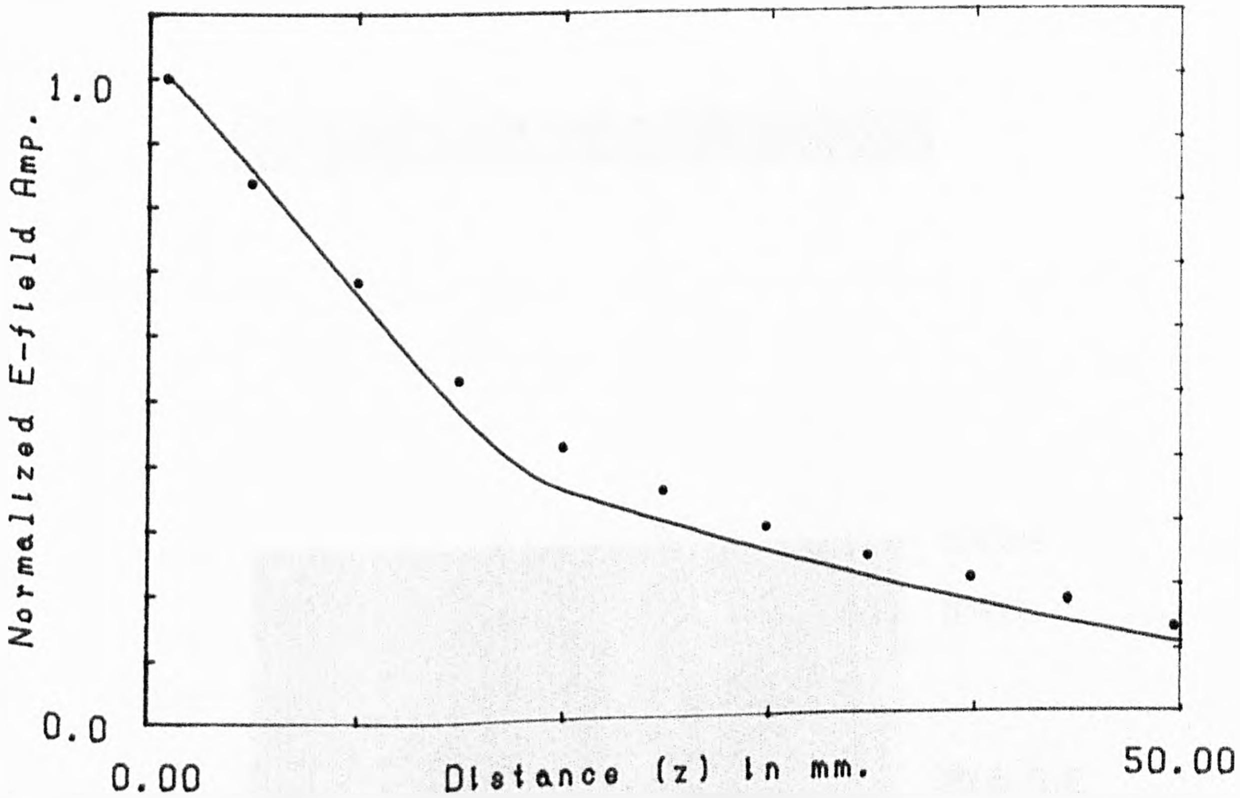

Fig.3.19a: Comparison of simulated results (Ey only) (-) with those of Guy (total E-field) (.). 919 MHz. 20mm fat + muscle. Aperture = 120mm x 160mm. X=0.

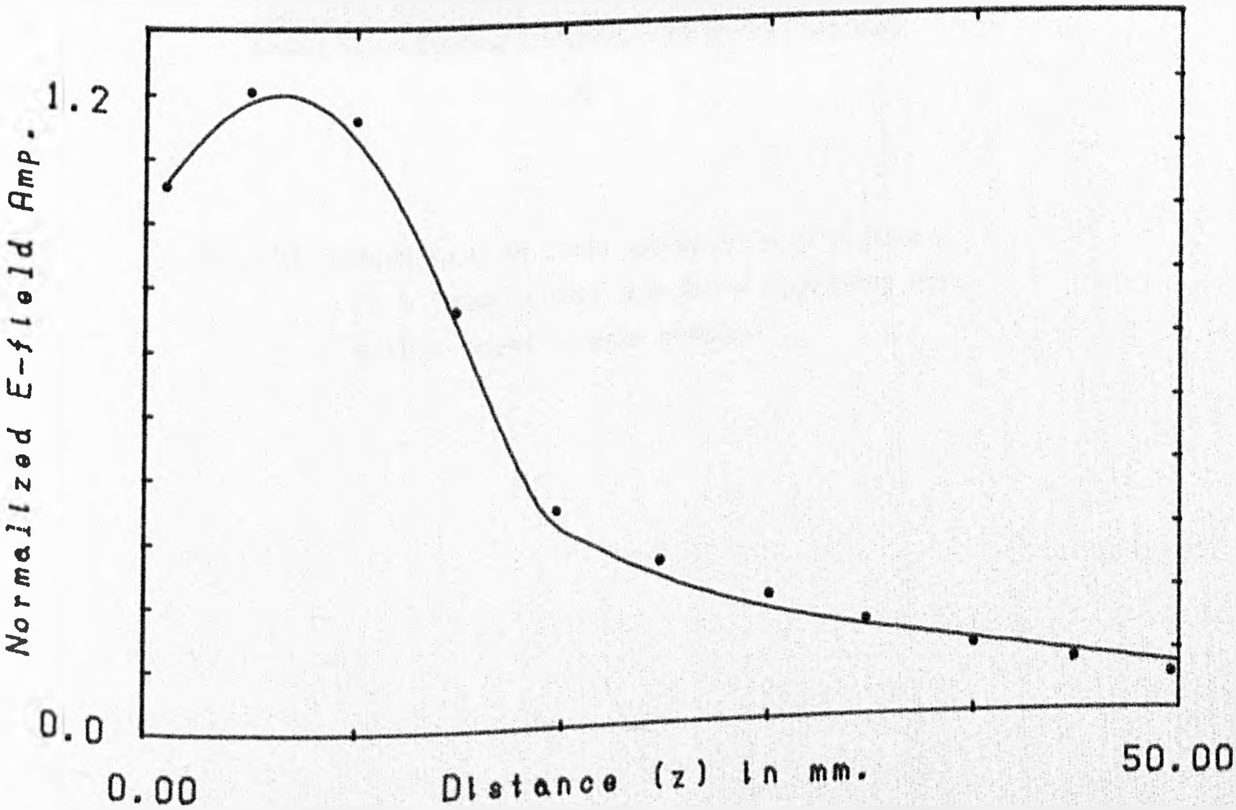

Fig.3.19b: Comparison of simulated results (Ey. only) (-) with those of Guy (total E-field) (.). 2450 MHz. 20mm fat + muscle. Aperture = 120mm x 160 mm. X=0.

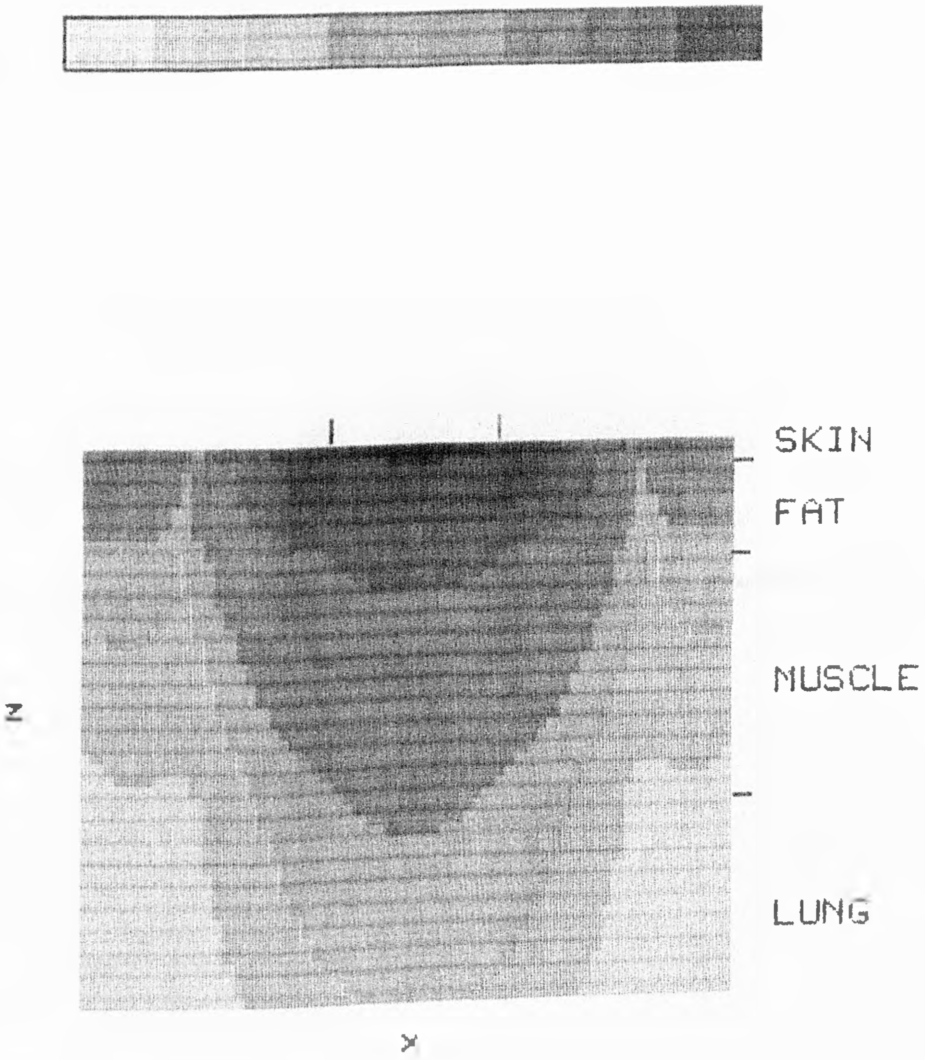

Fig.3.20 Simulation of field pattern in X-Z plane of a 16mm x 8mm aperture radiating into a four layer tissue medium

Chapter 4

Prediction of radiometer response to temperature distributions in layered tissue

4.1 Prediction of radiometric temperature by radiative transfer
    4.1.1 Incoherent Radiative Transfer theory
    4.1.2 Coherent Radiative Transfer theory

4.2 A method for predicting radiometric temperature

4.3 Practical implementation of the temperature prediction method

4.1 The prediction of radiometric temperature by radiative transfer

From knowledge of the dielectric structure of the medium, its temperature distribution and details of the radiometer probe, we wish to calculate the radiometric temperature, that is the temperature as measured by a radiometer. The radiometric temperature may be directly related to the power level received. In order to calculate the radiative power reaching the receiver, the emission, absorption and propagation of radiation in the lossy medium must be studied, together with the electromagnetic coupling of the medium to the receiving antenna or probe.

In this section, methods of solution to the above problem by radiative transfer theory are reviewed. Both incoherent and coherent radiative transfer solutions have been applied in the field of medical microwave radiometry, most notably in the prediction of multi-frequency data for use in the inverse process of reconstructing temperature depth profiles. A brief summary of the theory is given together with a review of its application by various authors.

4.1.1 Incoherent radiative transfer theory

The propagation of radiation in a medium is regarded as a purely incoherent process and is examined in terms of radiative power flow. Initially, the flow of radiative power through a small volume of the medium in a given direction is studied [94]. The interaction between radiation and matter is described by two processes; extinction and emission. Radiation is reduced in intensity by absorption in the medium and by scattering. In this analysis a non-scattering medium is assumed, so that the loss in intensity is controlled by the power absorption coefficient, α. The radiation intensity is augmented by emission, the emission coefficient is given by

$$\alpha\ F(T) \tag{4.1}$$

where F(T) is a linear function of temperature.

Examining the relative levels of extinction and emission, an equation of transfer can be written down for radiation travelling in a given direction. The solution of this equation for a scatter-free medium can be written in terms of the apparent brightness temperature, T_{AP}

$$T_{AP}(r) = T_{AP}(0)\ e^{-\tau(0,r)} + \int_0^r \alpha(r')\ T(r')\ e^{-\tau(r',r)}\ dr' \tag{4.2}$$

where $\tau(r',r) = \int_{r'}^{r} \alpha\ dr$ for radiation travelling in a direction $\underline{\hat{r}}$, where r' is the location of the small volume and r is the point of observation.

This solution has been applied by several workers to the field of microwave radiometry. Myers, Sadowsky and Barrett [35] assume a planar skin, fat tumour and muscle model and calculate the excess brightness temperature incident on the skin surface due to a hot tumour buried in the fat layer. An estimate of the effect on the calculated temperature of partial coherence of the emergent radiation, due to multiple reflections within the skin layer, is given and they conclude that incoherent raditive transfer theory is a reasonable approach. A one-dimensional solution only is applied to the equation of transfer (equation 4.2) giving the excess temperature at the surface but not allowing for the influence of the radiometer probe on the measured temperature.

Edenhofer [61] applied this theory to a three layer planar model consisting of skin, fat and muscle. The transport of energy at a given angle to the boundaries is described by a transmission line model using successive multiplication of transmission matrices. The model used for the simulation of radiometric data assumes that the temperature is a function of depth only (a feature which is common to most models) and is constant within each tissue layer. The receiving properties of the radiometric probe are included by considering the angular directivity of the antenna's radiation pattern, a technique which is employed in remote sensing of the earth by satellite [65]. In the case of an aperture antenna in contact with tissue, the probe is receiving from its near field and the concept of its radiation pattern being a function of angle only simplifies the real situation.

Schaller [58] has chosen a homogeneous tissue model having a temperature distribution which varies with depth only. A plane parallel solution is again employed to calculate the temperatures measured by idealised radiometers working within a range of frequencies.

Robillard [50, 95] also employs a homogeneous tissue model. However, the temperature distribution is allowed to vary laterally as well as with depth. The effect of the radiometer probe is also included by considering its radiation pattern and applying the principle of reciprocity of antennas. The results from this theoretical work have been validated experimentally.

4.1.2 Coherent radiative transfer theory

The emission of radiation from a lossy medium is essentially an incoherent process. However, because of the layered structure of biological tissue, multiple reflections between the layer boundaries can result in interference effects. This in turn can lead to partial coherence of the emergent radiation, significantly affecting the apparent brightness temperature of the medium [66].

A three layer model similar to that in [35] has been considered by Miyakawa [96]. He presents a plane parallel solution to the equation of radiative transfer, considering only radiation travelling perpendicular to the boundaries and a temperature distribution varying only with depth. The power transmission coefficients across the boundaries are calculated by solving Maxwell's equation in the medium with suitable boundary conditions. In this way, the multiple reflections between the layer boundaries are accounted for, leading to a more exact solution.

Bardatti and Solimini [63] have approached the problem of radiation from a biological medium by the coherent method described by Stogryn [97]. This model consists of defining the radiation source as the second order moment of a fluctuating current. According to the fluctuation-dissipation theorem [98] this second order moment is dependent on the local temperature, on the imaginary part of the dielectric constant of the medium and, in fact, corresponds to the emission coefficient defined for incoherent radiative transfer theory (Eqn 4.1). The electromagnetic field emerging from the medium is expressed as a function of the fluctuating current by a dyadic Green's function method of solution to Maxwell's equation with the appropriate boundary conditions.

A closed form solution to this problem is presented in [63] for a three layer biological medium with a temperature distribution varying with depth only. Results showing the variation of brightness temperature with frequency and with the angle of emergence of the radiation are presented. For the simulations of radiometric data a fixed direction of observation, perpendicular to the surface is assumed. The effect of the radiometer probe on the measurements is not considered.

In the next section, a method of solving the radiative transfer problem in a structure containing any number of layers is suggested. The method follows the approach described in [50] but applies the spectral diffraction/ cascade algorithm of Chapter 2 to solve the coherent propagation of radiation through a layered structure and to account for the effect of the radiometer probe on measured temperature.

4.2 A method for predicting radiometric temperature

Consider the case of a radiometer probe in contact with a semi-infinite isotropic lossy medium of uniform temperature T. The power received from the medium by the radiometer can be specified in two ways.

(i) If the antenna is perfectly matched to the medium, the medium can be replaced by a matched load of temperature T [5]. The power available at the receiver input is given by the expression for Johnson noise

$$P = kT\,\Delta f \qquad 4.3$$

This expression is equivalent to the definition for radiometric temperature for a given input power P; the radiometric temperature T_r is therefore equal to T.

(ii) The medium can be divided into an infinite number of elementary source volumes (ΔV_i), each making a contribution to the total power received by the radiometer. In order to calculate the contribution that each element makes to the total power received by the radiometer, consider a system in thermodynamic equilibrium where the radiometer probe is in contact with a uniform temperature (T) medium, with heterogeneous permittivity (Fig 4.1). For this discussion, the probe is considered to be an open-ended waveguide, but in practice this analysis is equally applicable to any type of probe. The waveguide and waveguide-to-coaxial line transition are considered lossless and a matched load terminates the coaxial line. The load is at the same temperature (T) as the medium. A constant interchange of radiative power takes place between the matched load and the lossy medium and, since the system is in thermodynamic equilibrium, the power transfer from the medium to the load is equal to the power flow from the load to the medium.

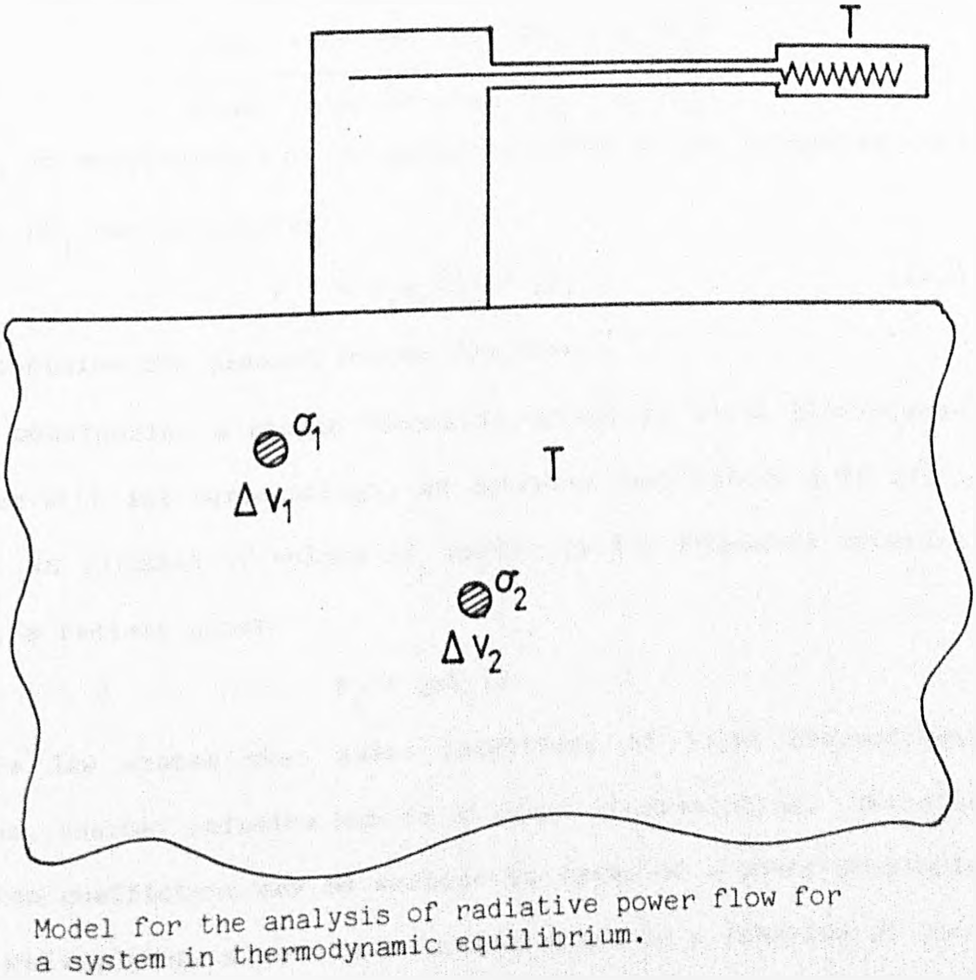

Fig. 4.1 Model for the analysis of radiative power flow for a system in thermodynamic equilibrium.

First, consider a single frequency emission from the matched load which travels down the waveguide and is absorbed by the medium. The distribution of absorbed power can be calculated by considering the load as a monochromatic coherent source and computing the radiation pattern of the waveguide into the medium. If the electric field created in volume ΔV_i is E_i, then the power absorbed in ΔV_i is $\sigma_i|E_i|^2\Delta V_i$ where σ_i is the conductivity of the elementary volume. The waveguide antenna is a reciprocal device and therefore exhibits the same radiation pattern for reception as for transmission [65]. This statement is also true for incoherent radiation. The flow of radiation between the matched load and any element of the medium is reciprocal [99]. Thus, for a constant temperature medium, the ratio of power received by the matched load from two elementary volumes in the medium is

$$\frac{\text{power received from } \Delta V_1}{\text{power received from } \Delta V_2} = \frac{\sigma_1|E_1|^2}{\sigma_2|E_2|^2}$$

Therefore, an expression for the power received by the waveguide due to an element ΔV_i can be written

$$P_{ir} = B_i\sigma_i|E_i|^2\ \Delta V_i \qquad (4.4)$$

where B_i contains the element source function.

Now, considering a single elemental volume in local thermodynamic equilibrium with its surroundings, an emission coefficient j is defined such that an element of volume ΔV_i emits, in the frequency interval f to f + Δf, a radiant power

$$P_i = j\Delta V_i\Delta f$$

Kirchhoff's law states that under conditions of local thermodynamic equilibrium, thermal emission has to be equal to absorption. Therefore the emission coefficient may be written in terms of a power absorption factor α_i multiplying a source function which is a function of local temperature

$$j = \alpha_i F(T)$$

where, assuming the Rayleigh-Jeans approximation to Planck's radiation law

$$F(T) = \frac{2k}{\lambda^2} \Delta f \ T$$

Taking Δf to be small, λ can be considered to be approximately constant. The power emitted by each elementary volume can thus be written

$$P_{ie} = Ck\alpha_i T \ \Delta V_i \Delta f \qquad (4.5)$$

where C is a constant.

Comparing equation 4.5 and equation 4.4, it can be seen that B_i in equation 4.4 must be linearly dependent upon the local temperature ($B_i = D_i T$) and that the absorption factor α_i can be directly related to the local conductivity σ_i. Combining the two equations, an expression can be written for the power received from a volume ΔV_i by the matched load.

$$P_i = A_i \ k\Delta fT \ \sigma_i |E_i|^2$$

where A_i depends upon the volume ΔV_i and incorporates D_i and C.

This analysis applies if the waveguide antenna, instead of being connected to a matching load, is connected to a radiometer. The contribution to the total signal measured by the radiometer from each elemental volume is proportional to its temperature, conductivity and to $|E_i|^2$, which can be regarded as a coupling parameter between the element and the radiometer.

The individual signals from the elements received by the radiometer can be assumed to be uncorrelated. Therefore, the signals can be summed to give the total power received:

$$P = \sum_i P_i = A \ k\Delta f \sum_i \sigma_i |E_i|^2 T \qquad (4.6)$$

$$= A \ k\Delta fT \sum_i \sigma_i |E_i|^2$$

where $A = \sum A_i$.

Two expressions for the power received by a radiometer from a constant temperature medium have now been formulated. Equating 4.6 and 4.3 gives an expression for the constant of proportionality A.

$$A = \frac{1}{\sum \sigma |E_i|^2}$$

A constant temperature medium has been assumed up to now in this discussion. However, this constraint is not generally necessary. Although Kirchhoff's law is defined for conditions of strict thermodynamic equilibrium, it has also been found to hold with good accuracy where the spatial temperature gradient of the temperature within the medium are small [65]. This practical limit on the theory corresponds to the conditions in which we are interested in the human body, where temperature gradients can never be large due to heat conduction and thermoregulation by blood flow.

For a medium with non-uniform temperature distribution, a local temperature T_i can be defined in each of the elemental volumes [94]. Equation 4.6 becomes

$$P = A\, k\Delta f \sum_i \sigma_i |E_i|^2\, T_i \tag{4.7}$$

Comparing 4.7 with 4.3, the radiometric temperature T_r must now be viewed as an average temperature weighted by the receiving pattern of the antenna and the emitting characteristics of the elements within the volume.

$$T_r = A \sum_i \sigma_i |E_i|^2\, T_i$$

Since, to the first order, the term A does not depend on temperature, a good approximation is to take A to be the same as for a constant temperature medium.

$$T_r = \frac{\sum_i \sigma_i |E_i|^2\, T_i}{\sum_i \sigma_i |E_i|^2} \tag{4.8}$$

4.3 Practical implementation of the temperature prediction method

The analysis of the previous section was formulated for the case of a radiometer connected to a waveguide in contact with a lossy medium. A method for predicting the field radiated into a lossy medium by a contacting waveguide antenna was given in Chapter 2. By combining equation 4.8 and the field prediction algorithm, the temperature measured by a radiometer can be calculated. The necessary parameters for this calculation are the temperature distribution, the dielectric structure of the medium, the type and size of probe and the operating frequency of radiometer.

An example serves to illustrate how this method can be implemented to model a practical situation. One procedure, which has been used in clinical diagnostics with microwave radiometry, is scanning the radiometer probe across the skin surface and mapping the measured temperature at each position to locate subcutaneous temperature abnormalities [68]. Consider a medium to be scanned, consisting of two dielectric layers, a fat layer (f) overlying muscle (m) with a raised temperature tumour (t) buried in the muscle (Fig 4.2). The waveguide is in contact with the fat layer. The first step is to calculate the field pattern of the probe (the field patterns for this situation was calculated in #3.2.2). The field prediction algorithm requires that only linear parallel boundaries are present. As a consequence, it is assumed that the field pattern remains constant as the probe is scanned along the surface. The temperature signal reaching the radiometer (T_r) can now be calculated for any relative position of the probe to the raised temperature tumour. For this example consider that the medium (fat and muscle) has a uniform temperature T and that the tumour is at a higher temperature T_t.

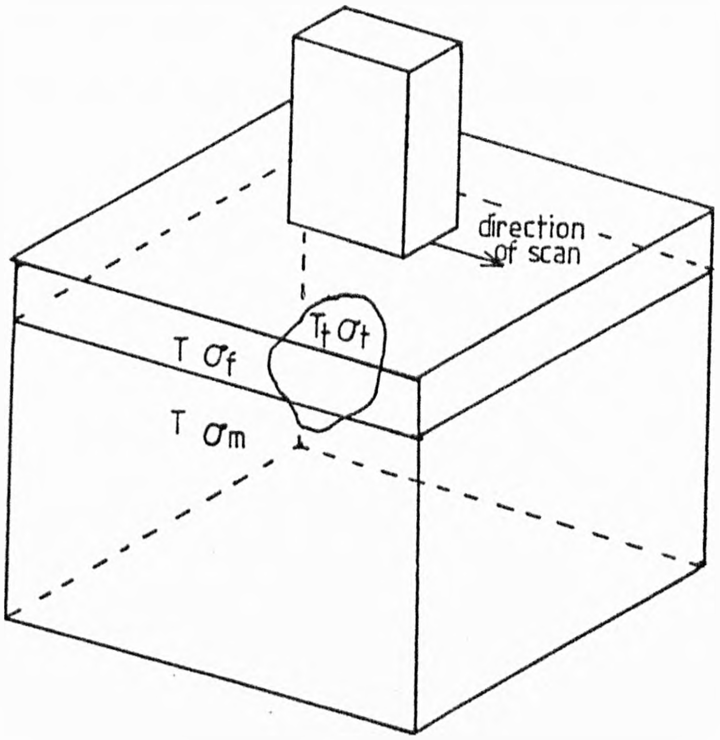

Fig. 4.2 Linear scanning over a bi-layered fat and muscle medium containing a raised temperature tumour using a contacting waveguide probe.

$$T_r = \frac{\sigma_t T_t \sum_{i_t} |E_{i_t}|^2 + \sigma_m T \sum_{i_m} |E_{i_m}|^2 + \sigma_f T \sum_{i_f} |E_{i_f}|^2}{\sigma_t \sum_{i_t} |E_{i_t}|^2 + \sigma_m \sum_{i_m} |E_{i_m}|^2 + \sigma_f \sum_{i_f} |E_{i_f}|^2}$$

The assumption that the field pattern remains constant as the probe is scanned does not correspond to the practical situation. In reality, the presence of the tumour modifies the field pattern. At present, the field prediction algorithm will not consider boundaries which are either non-linear or not parallel to the aperture plane. For the purposes of field prediction, the raised temperature region is assumed to have the same dielectric properties as that in which it is buried. This assumption may correspond to the physical situation, as many tumour types have shown similar dielctric properties to muscle tissue [100]. Inserting the actual conductivity of the tissue in the detection volume into the equation for measured temperature (Eqn 4.8) partially accounts for variations in dielectric properties.

Chapter 5

Design, construction and operation of a 4.6 GHz radiometer

5.1 Description of the radiometer

5.2 The design and construction of a contacting waveguide probe

- 5.2.1 Design considerations
- 5.2.2 Construction of the filled waveguide probe

5.3 Radiometer performance

- 5.3.1 Calibration of the radiometer
- 5.3.2 Temperature resolution and stability

5.4 The radiometer in a null-balancing mode

5.1 Description of the radiometer

A microwave radiometer collects and measures emitted microwave power. An antenna or probe couples microwave radiation from the body into the radiometer receiver. The function of the radiometer receiver is to detect and measure the power levels delivered to it. The radiometer was designed for use in phantom experiments and for clinical applications, although the latter has not yet been realised [101].

Radiometer receivers include active components (eg amplifiers) whose parameters may fluctuate. The effect of these variations was reduced by the use of a comparison type radiometer [5], where the input signal is compared with that from a matched load of known temperature at a switching frequency higher than the highest gain fluctuation frequency. Three configurations of the receiver following the switch were considered. A radio-frequency (RF) amplifier followed by RF detector [36] is the most costly configuration due to the high cost of RF amplifiers compared to intermediate frequency (IF) amplifiers, but gives the greatest temperature resolution. The single side-band (SSB) and double side-band (DSB) superhetrodyne systems [34] are least expensive. The preferred configuration for these studies was a superhetrodyne system with RF pre-amplification [45, 35], a compromise which gives good signal to noise characteristics at reasonable cost.

Figure 5.1 shows the comparison type double sideband superhetrodyne radiometer which was constructed. A list of components and their specifications is given in Table 1.

The contacting waveguide probe (#5.2) couples radiation via a low loss flexible cable into one side of a 3 pole solid state switch. The switch is modulated by a 220 Hz clock frequency and alternately switches between the input signal and the signal from a temperature controlled matched load. This allows comparison of the input signal

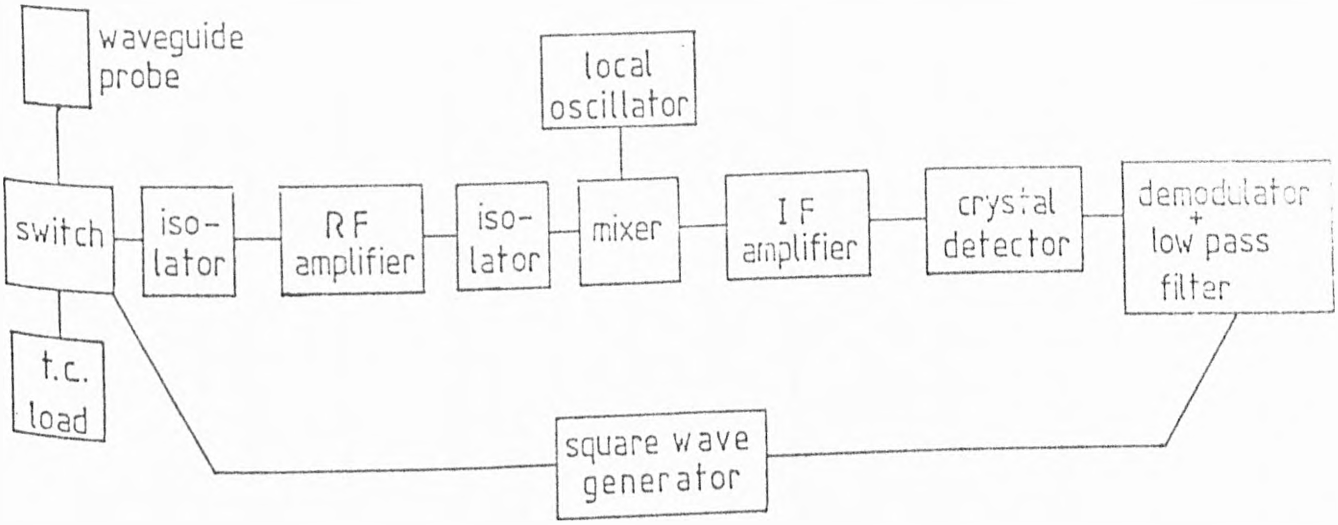

Fig. 5.1a Schematic diagram of the 4.6 GHz comparison radiometer.

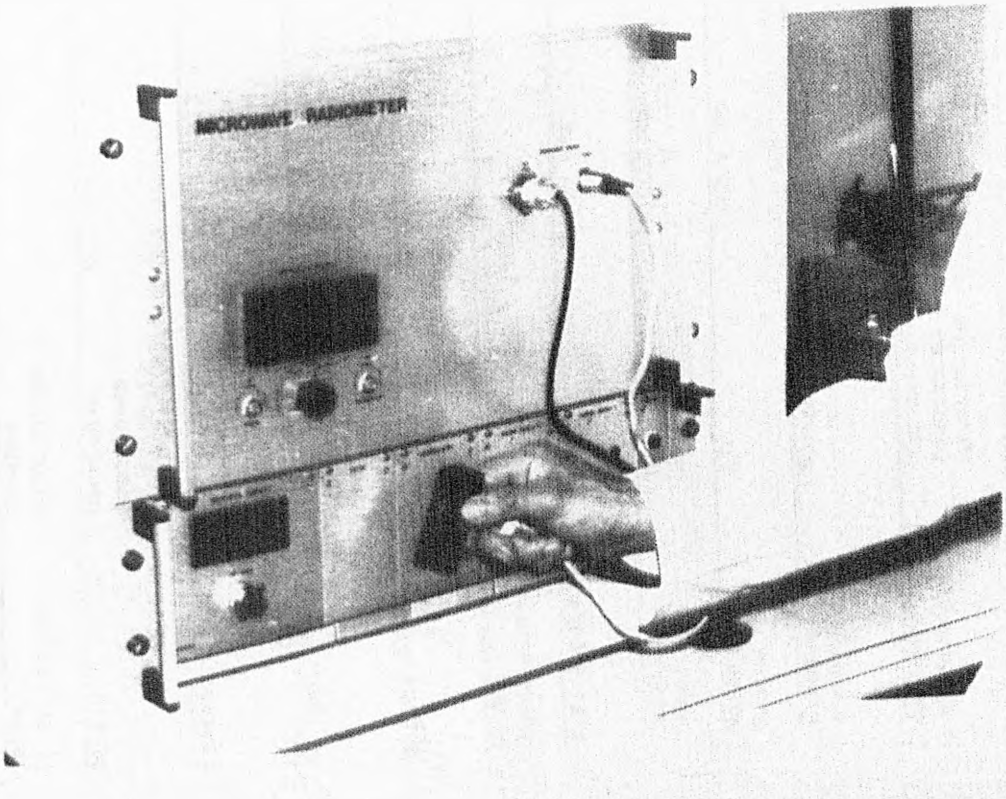

Fig. 5.1b 4.6 GHz radiometer.

Component	*Make & Model*	*Frequency Range*	*Insertion Loss (dB)*	*Isolation (dB)*	*Noise Figure (dB)*	*Gain (dB)*	*Comments*
Cable (5 ft length)	Goretex G3P01P01060.0		0.8	-	0.8	-	High quality, low loss cable. Long and flexible for patient scanning.
Switch	Microwave Associates ML 17430-12	4-8 GHz	<1.15	>53	1.15	-	Lower loss ferrite switches now available.
Isolators	Microwave Associates ML2G - 6100	4-8 GHz	0.4	20	0.4	-	
RF Amplifier	Amplica ACM 635301	4-8 GHz	-	-	3.0	45.6	A wide bandwidth amplifier for prototype radiometer. Lower noise figure amplifiers now available.
Mixer	ANZAC MDC-180	4-8 GHz	4.8	25	4.8	-	
Local Oscillator	Watkins - Johnson V402	4-6 GHz	-	-	-	-	
I.F. Amplifier	Amplica AVD 705301	5-250 MHz	-	-	1.5	51.5	
Crystal Detector	Texscan CD-50	1-1000 MHz	-	-	-	-	
Noise Source	AIL	1-12.4 GHz	-	-	15.5	-	
Fixed attenuators	Marconi	DC-12 GHz	20 + 6	-	-	-	
Switched attenuator	Microwave Associates MA-8437-354	4-8 GHz	2.4-45	-	-	-	Very high quality switched attenuator.
Circulator	Microwave Associates ML3G-6100	4-8 GHz	0.4	20	0.4	-	

Table 1 Component Specifications

with an accurately known signal level every 4 ms. The modulated output from the switch is amplified by the high gain RF amplifier. The components up to this point (known as the radiometer 'front-end'), including the RF amplifier operate in the RF frequency band 4-8 GHz. The mixer and local oscillator convert the signal to an intermediate frequency (IF), the mixer output then being amplified again by an IF amplifier. The bandwidth of the IF amplifier defines the total bandwidth of the system. As the RF bandwidth is large, the IF signal band contains signals from two RF bands centred at frequencies f_1 and f_2 where

$$f_1 = f_{LO} - f_{IF}$$

$$f_2 = f_{LO} + f_{IF}$$

where f_{LO} is the local oscillator frequency

and f_{IF} is the centre frequency of the IF amplifier.

Hence the system is a double sideband system with a bandwidth (B) twice that of the IF amplifier. This large ratio of RF bandwidth to IF bandwidth (8:1) together with a variable frequency local oscillator allows the centre frequency of the system to be set at any value between 4.4 GHz and 5.6 GHz. However, the radiometer measurements reported in following chapters were performed at a centre frequency of 4.6 GHz due to superior probe matching around this frequency (Figure 5.2b).

The signal from the output of the IF amplifier is converted to a voltage signal by a square law crystal diode detector, which gives a voltage out proportional to the power level input. The resulting square wave voltage is demodulated at the switching frequency and the output fed into a low pass filter. The integration time constant (τ) of this post detection low pass filter decides the system response time to input temperature changes and is one factor in the temperature resolution of the radiometer (# 5.3.2). The time constant can be set to any value in the range 0.2 to 10 seconds. The final output of the radiometer is a dc voltage proportional to the difference in temperature between the tissue under investigation and the temperature controlled (tc) load [102].

$$V_{dc} = G\, C_d\, G_p kB\, (T_s - T_c) \qquad (5.1)$$

T_c is the temperature of the tc load

B is the system bandwidth

k is Boltzmann's constant

G is the pre-detection gain

C_d is the detector constant (in volts per watt)

G_p is the post detection gain

and T_s, the measured temperature, is given by

$$T_s = \frac{T_r(1 - \rho)}{L} + (1 - \frac{1}{L})T \qquad (5.2)$$

where T is the physical temperature of the probe, cable and switch

ρ is the reflection coefficient of the probe/tissue interface

L is the loss factor of the probe and cable

T_r is the radiometric temperature (see Chapter 4).

The output from the radiometer is connected to the analogue input of the BBC microcomputer. The A to D converter is sampled by the computer every 20 ms and the voltage is displayed on the VDU. Statistical analysis of the output can be carried out by running the BASIC programme 'SAM'. This programme calculates the average, range and root standard deviation from the mean of the sampled voltages over a specified time interval. This information, in conjuction with the radiometer calibration curve can be used to calculate the temperature resolution and stability of the radiometer.

Figure 5.1b shows the radiometer. The pre-detection radiometer components are housed in the central rack together with the temperature control equipment. The lower rack contains the post-detection processing electronics.

5.2 The design and construction of a contacting waveguide probe

5.2.1 Design considerations

The probe performs the function of coupling the required microwave signal emitted by the body into the radiometer receiver. A successful design of probe is very important for optimization of the radiometer performance. In designing the probe, the following points were considered:

- The wave impedance of the tissues varies greatly over the body surface (50-150 ohms [103]). The probe should be matched to a mean impedance value to keep the reflection coefficient at the probe/tissue interface to a minimum. An additional requirement for these studies is that the probe be matched to water for use in the phantom experiments.
- The range of frequencies over which the probe is matched can be a limiting factor on the bandwidth of the radiometer, and so should be as broad as possible.
- In a clinical environment it is desirable to have a small and robust probe for portability and ease of operation.
- The receiving pattern of the probe is highly dependent upon its design.

A dielectric filled open-ended rectangular waveguide with waveguide to coaxial line transition was chosen as the probe. This design is one of the most widely used probe types for microwave thermography and can be matched to a given impedance over a bandwidth

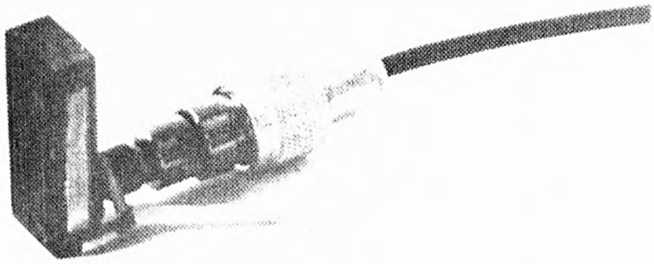

Fig. 5.2a Radiometer probe.

which is limited but sufficient for radiometer operation. By filling a waveguide with a dielectric of relative permittivity ε' its dimensions can be reduced by a factor of $\sqrt{\varepsilon'}$ resulting in a probe which is small, light and robust. Very low loss dielectrics can be obtained, keeping probe losses to a minimum.

5.2.2 Construction of the filled waveguide probe

The probe used in all the experimental work consisted of waveguide with cross-section 16 mm x 8 mm filled with Emerson and Cuming two part (powder and resin) low loss dielectric $\varepsilon' = 9$ to give a cut-off frequency of 3.5 GHz. A back plate was fitted to the waveguide and the waveguide to coaxial line transition was achieved by inserting the inner conductor of the coaxial line into the waveguide approximately $\lambda_g/4$ from the back plate where λ_g is the guide wavelength. Filling the waveguide with a solid material made it difficult to alter the geometry of the waveguide to coaxial line transition to give optimum matching. This problem was overcome by making a number of probes, each slightly different. The insertion distance of the coaxial inner conductor and its distance from the back plate and the total waveguide length were

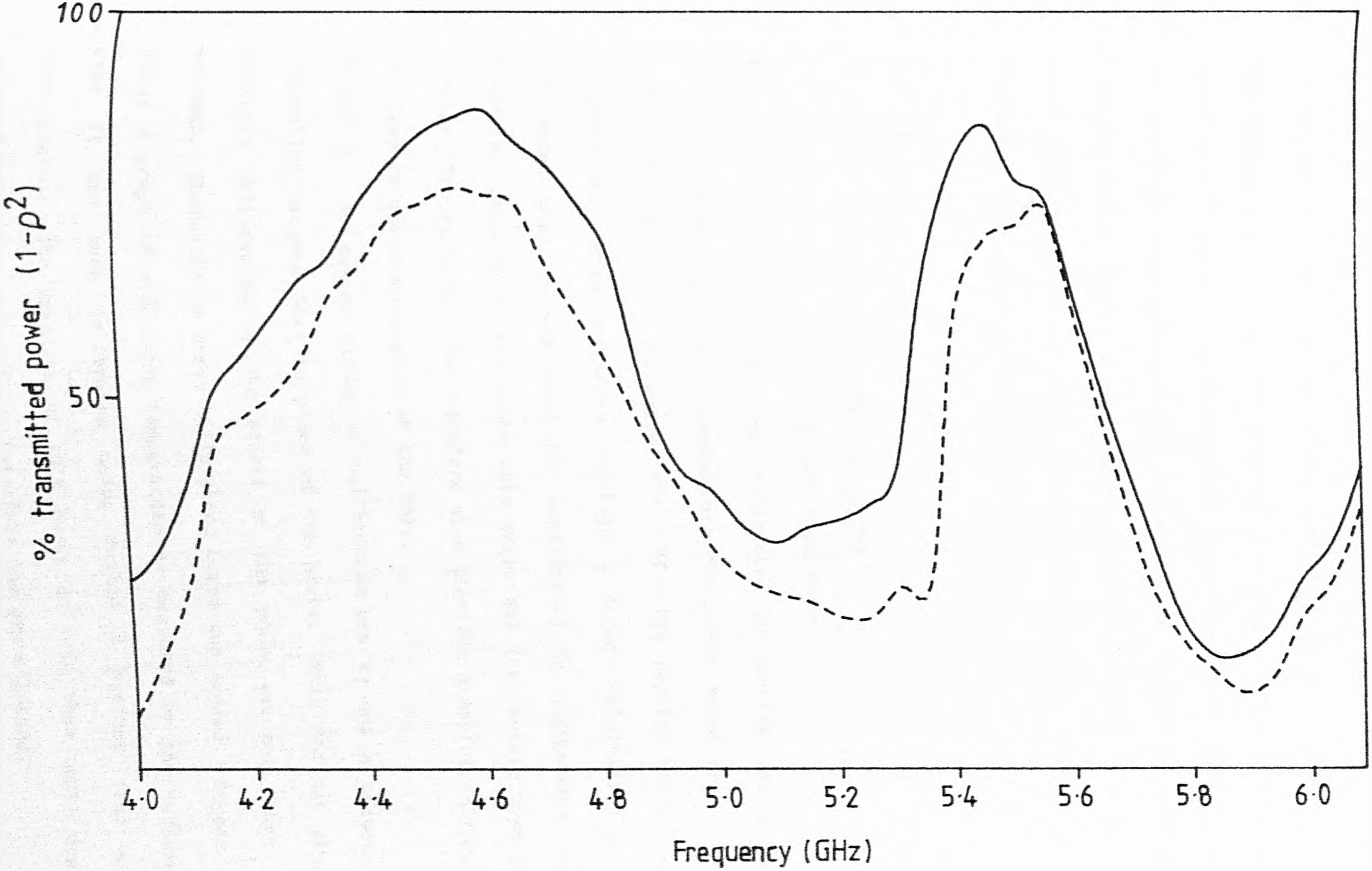

Fig. 5.2b Power transmitted for radiometer probe in contact with water (——) and a muscular area of the arm (---). Calculated from $1-\rho^2$ where ρ is the reflection coefficient.

varied. The voltage reflection coefficient (ρ) looking into the transition when the open end of the waveguide was in contact with water was measured with a network analyser for each probe over a frequency range 4 - 6 GHz and the transmitted power calculated from $(1 - \rho^2)$. The selected probe (Figure 5.2a) had the lowest reflection coefficient over the widest bandwidth when radiating into water (Figure 5.2b). The power transmitted by the probe when in contact with a muscular area on the arm is also shown in Figure 5.2b.

5.3 Radiometer performance

5.3.1 Calibration of the radiometer

Two methods of calibration were employed:-

Method 1: The radiometer was calibrated by placing the probe in contact with the water in a temperature controlled water bath. Figure 5.3a shows the output voltage of the radiometer plotted against water temperature. This procedure provided a direct calibration of the radiometer when it was used for experiments in homogeneous water. Since the matching of the probe into water and into muscle tissue are similar (Figure 5.2b), the procedure also provided a useful calibration for temperature measurements of the body.

Method 2: An easier method of calibration was to use a temperature controlled matched load in place of the probe. This did not give an absolute calibration as the effect of the probe was not taken into account. Therefore an extra calibration curve was needed. Figure 5.3b shows a graph of the water temperature as measured by the radiometer when it has been calibrated using method 2 against true water temperature. The gradient of this curve is less than unity due to reflections at the probe/tissue interface and probe losses.

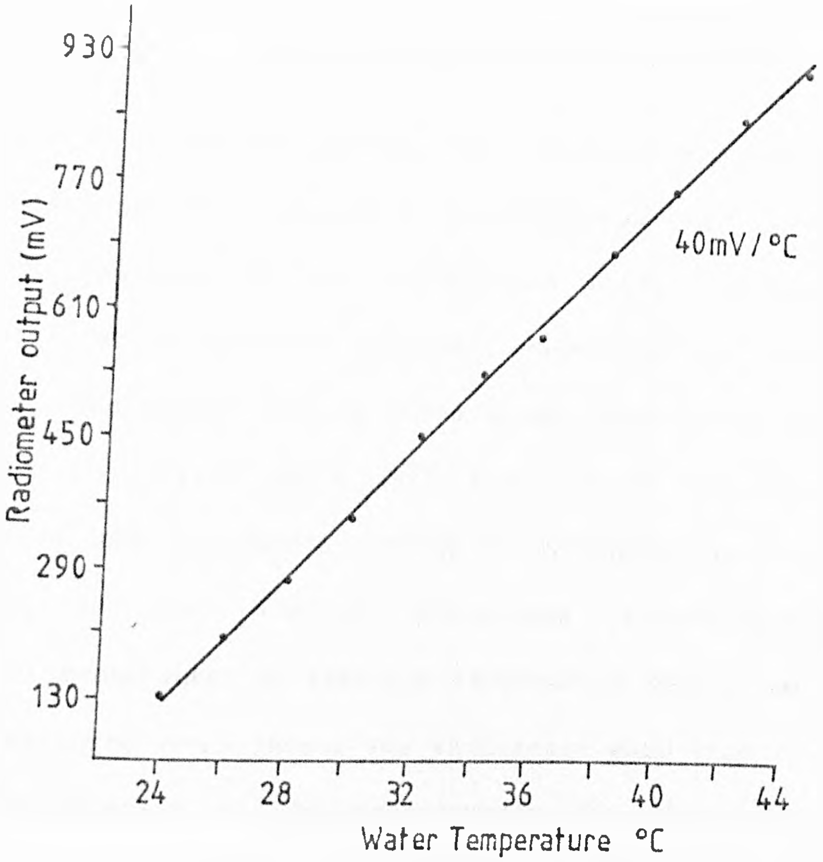

Fig. 5.3a Calibration curve for radiometer with the probe in contact with a heated water bath. (Method 1)

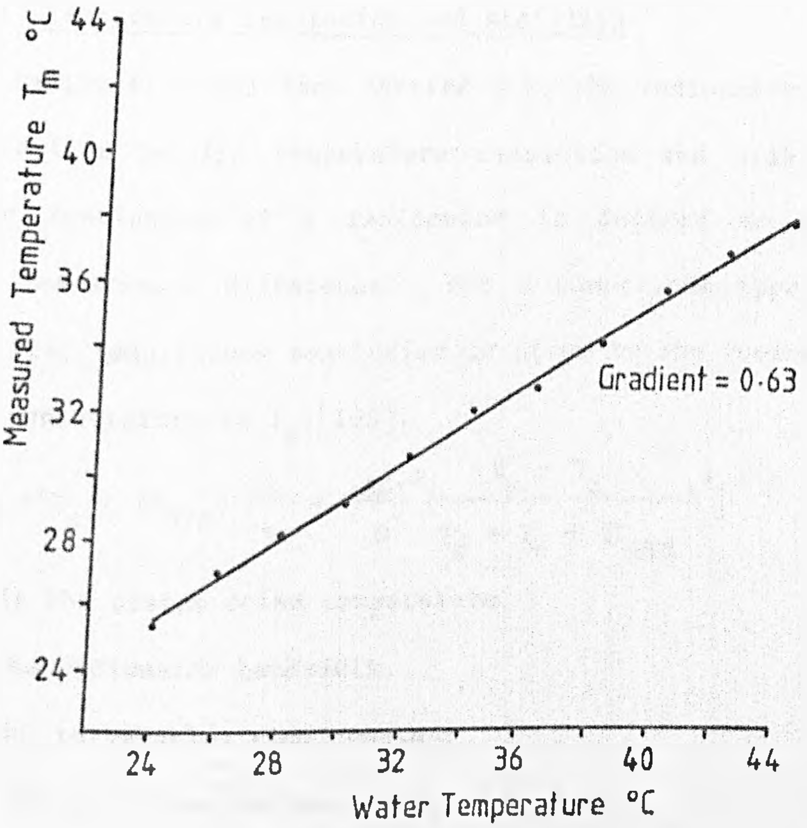

Fig. 5.3b Temperature as measured by the radiometer with the probe in contact with a heated water bath against true water temperature. Tm is read from the calibration curve with a heated load in place of the probe (Method 2).

Calibration was essential to ensure the accuracy and reproducibility of the radiometer measurements. It was found that although the gradient of the calibration curve was constant, the absolute calibration could be different each time the radiometer was switched on. The output voltage for a given input noise power depends on a number of factors which vary from day to day including the temperature of the components (which is dependent upon the ambient temperature), and the level of background radio-frequency noise. Therefore, if measurement of absolute temperature values was required, it was necessary to re-calibrate the radiometer each time it was used. However, the majority of the measurements for these studies only involved the measurement of temperature differences for which recalibration was not required.

5.3.2 Temperature resolution and stability

Once calibration has been carried out, the radiometer performance is characterized by its temperature resolution and stability. The temperature resolution of a radiometer is defined as the minimum detectable temperature difference. For a comparison type radiometer the theoretical temperature resolution is given by the root mean square measurement uncertainty in T_s [102].

$$\Delta T = (T_s + T_c + 2T_{SYS}) \left[\frac{1}{B\tau} + \left(\frac{\Delta G}{G}\right)^2 \left(\frac{T_s - T_c}{T_s + T_c + 2T_{SYS}}\right)^2\right]^{1/2} \qquad (5.3)$$

where T_{SYS} is the system noise temperature

B is the radiometer bandwidth

τ is the integration time constant

ΔG is the gain fluctuation.

The temperature resolution is governed by those noise factors which fluctuate with a period shorter than the integration time. The stability of the radiometer is defined by the stability of its output for a constant noise power input over periods longer than the integration time constant. A number of factors which influence the temperature resolution (equation 5.3) and also the stability are now examined.

(i) The system noise temperature

The system noise temperature is a measure of the degradation in signal to noise ratio between the system input and output. The components of the radiometer add noise due to their own physical temperature. The noise temperature of a component is given by

$$T_n = (F_n - 1)T$$

where F_n is the noise figure and T is the component temperature. The noise figure of an active component (eg an amplifier) is usually stated in the component specifications. The noise figure of a passive component (eg a cable) is equal to its loss factor L.

The system noise temperature may be found from the general definition of noise temperature of a cascade [65]

$$T_{SYS} = (L_{WG} - 1)T_{WG} + L_{WG}(L_C - 1)T_C + L_{WG}L_C(L_{SW} - 1)T_{SW}$$
$$+ L_{WG}L_C L_{SW}(L_{IS} - 1)T_{IS} + L_{WG}L_C L_{SW}L_{IS}(F_{RF} - 1)T_{RF}$$

where WG denotes waveguide, C denotes cable, SW denotes switch, IS denotes isolator and RF denotes RF amplifier. The series is terminated at the RF amplifier because its gain is so high as to render unimportant the contributions of any components which follow.

(ii) Radiometer bandwidth

Figure 5.4 shows the output of the radiometer measured as a function of frequency by inputting a coherent signal of constant

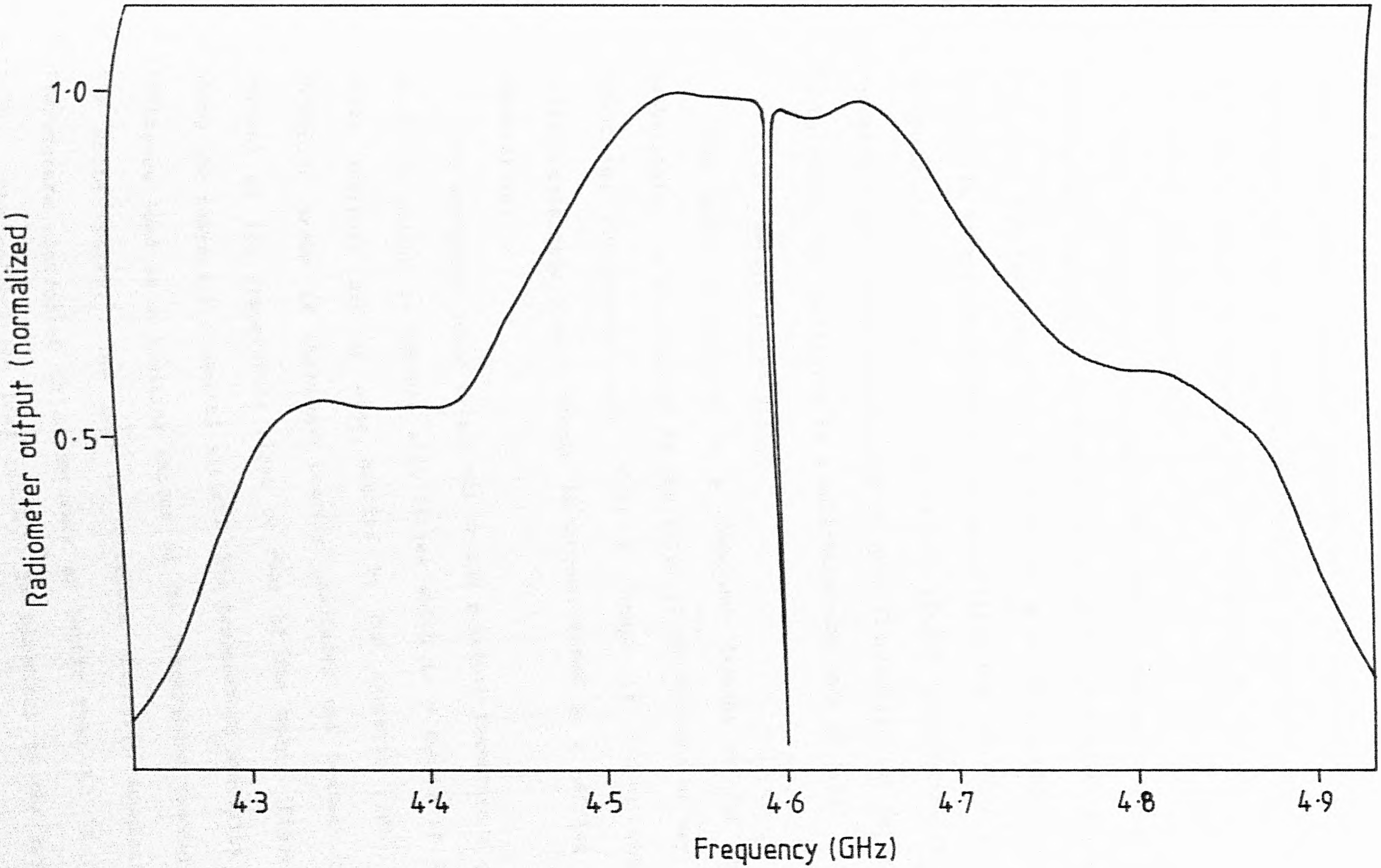

Fig. 5.4 Pass band of the radiometer for a centre frequency of 4.6 GHz.

amplitude from a Hewlett Packard synthesised signal source. The graph shows the double sideband nature of the system, the frequency characteristic being symmetrical about the local oscillator frequency (4.6 GHz). The 3 dB bandwidth (B) of the output is 550 MHz.

(iii) Gain fluctuations

Gain fluctuations are inevitable when a system contains active components. The higher the quality of an active component, the smaller the gain fluctuations. The effects of gain fluctuations and gain drifts can be kept to a minimum by controlling the reference load at a temperature (T_c) close to that of the signal temperature (T_s) (see equation 5.3). Total suppression of gain fluctuation can be achieved by operating the radiometer in a null-balancing mode (# 5.4).

(iv) Temperature stability

The noise temperature of a component depends on its physical temperature. A fluctuation in the physical temperature of any of the front-end components will cause a change in output which is indistinguishable from a change in output caused by a varying tissue temperature.

The waveguide probe is subject to the greatest temperature changes as it is placed in contact with tissue which is a number of degrees above ambient, and is also handled by the operator [104]. The waveguide probe is therefore heavily insulated and heated allowing control of its temperature close to that of the body. Figure 5.5a shows the temperature control system. The temperature stability of the reference load is a limiting factor on the temperature resolution of the whole system. The load is therefore thermally insulated and temperature controlled to an accuracy of better than 0.1 °C (Figure 5.5b). The calibration load (#5.3.1) is identical to the reference load. The temperature of all three components are controlled by means

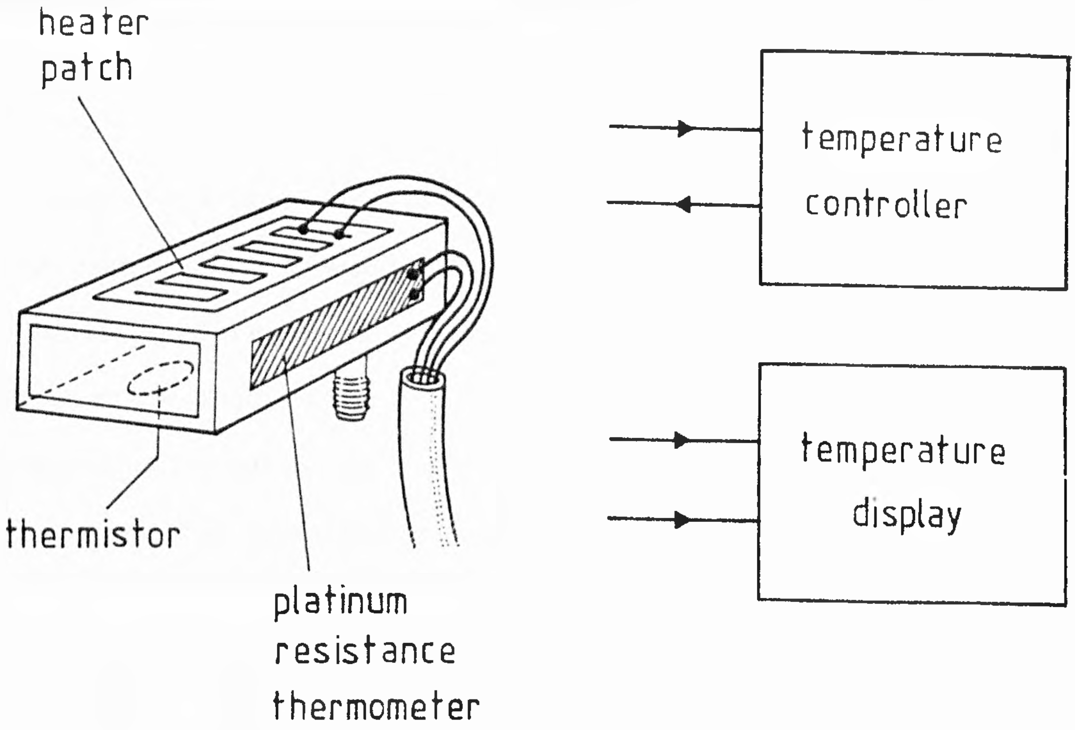

Fig. 5.5a Temperature control system for waveguide probe

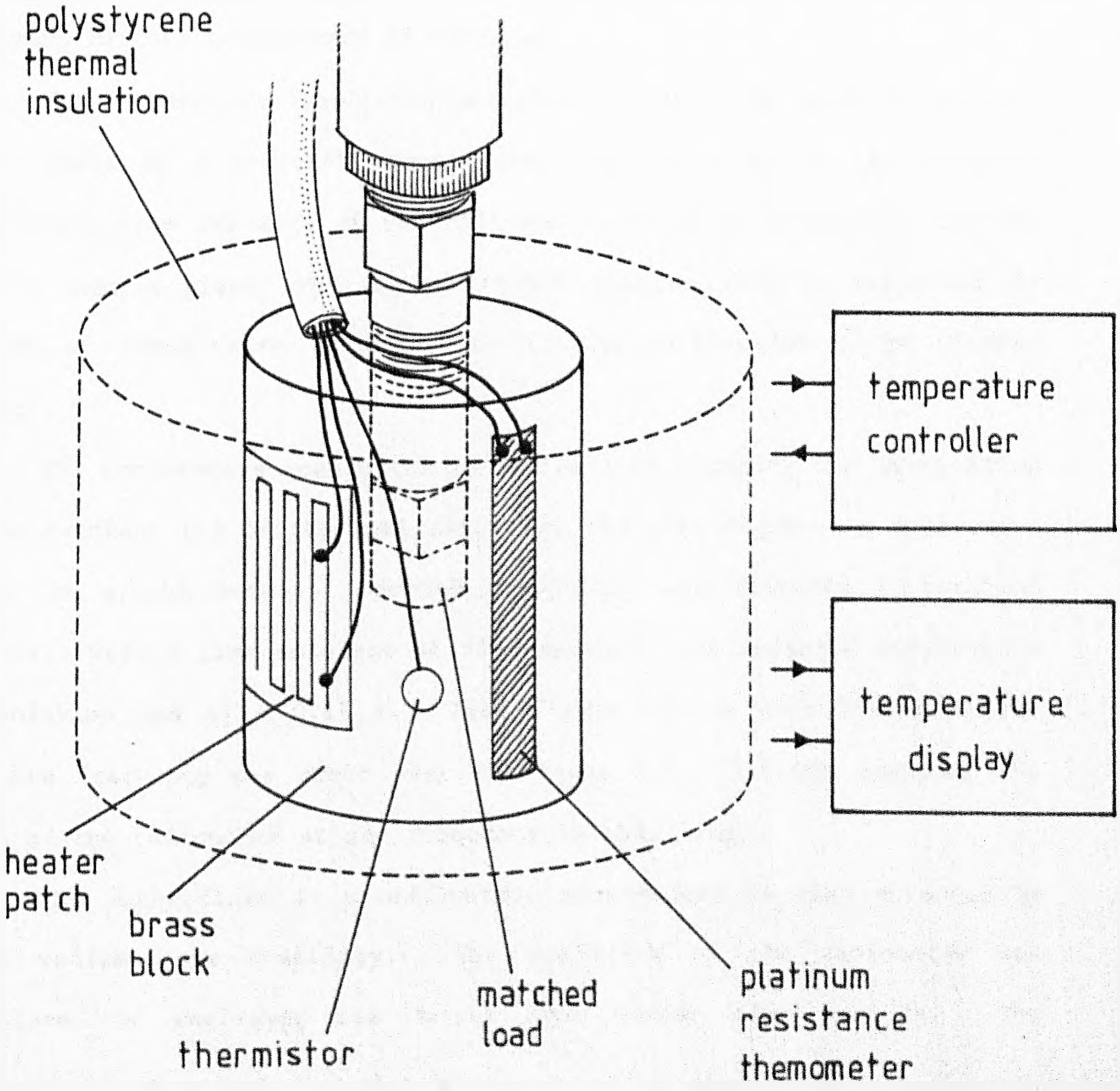

Fig. 5.5b Temperature control system for reference load and calibration load

of a small heater and thermistor affixed to their outer surfaces and connected to proportional temperature controllers within the receiver cabinet. The temperature can be varied over the range 25 °C to 45 °C, controlled to an accuracy of 0.05 °C (manufacturer's specification), and is independently measured by a platinum resistance thermometer connected to a digital thermometer. The LED display of the digital thermometer on the front of the radiometer housing can be switched to show the temperature of any of these components.

The receiver components are not temperature controlled; however, the radiometer must be switched on at least one hour before use to allow the active components to attain their operating temperature. These components are secured to a heat sinking aluminium plate to help prevent further temperature fluctuation.

The temperature resolution was measured with the probe in contact with water at a constant temperature, and was given by the standard deviation from the mean of the radiometer output as sampled by the BBC micro over a given time period (BASIC program "SAM"), expressed in terms of temperature by reference to the calibration curve (Figure 5.3a).

The temperature resolution is variable by altering the integration time constant (τ) of the post detection low pass filter. A compromise must be sought between improved resolution and extended integration times. With a time constant of five seconds, the measured temperature resolution was $\Delta T = 0.17$ K. This figure varied very little as the centre frequency was swept over the range 4.4 → 5.6 GHz enabling the use of the radiometer at any frequency in this range.

The uncertainty in a radiometric measurement is also affected by the radiometer's stability. The stability of the radiometer was measured by analysing its output over longer time periods. The standard deviation of the output voltage was 15% greater after 30 minutes (the period of a typical phantom experiment) than after 15 secs (the time for a single point measurement) indicating acceptable long term stability. The total radiometric measurement uncertainty is $\Delta T_u = \pm 0.2°C$.

5.4 The radiometer in a null-balancing mode

The signal measured by the radiometer depends not only upon the temperature of the tissue but also upon its emissivity and hence upon the power reflection coefficient at the probe-tissue interface (equation 5.2). In order to achieve true temperature measurements and to compensate for changes in tissue emissivity a null-balancing feedback circuit [105] has been incorporated.

Figure 5.6 shows the design for the null-balancing radiometer. The output voltage acts on a feedback circuit to control the level of noise injected into the front end via a circulator. A simple analysis of the various power levels involved shows how a balance may be achieved. In this analysis, all components are assumed to be lossless.

When the switch is connected to the probe, the noise temperature at the input to the RF amplifier is

$$T_r(1 - \rho) + \rho T_N \qquad (1)$$

where T_r is the radiometric temperature

T_N is the injected noise

ρ is the power reflection coefficient at the probe/medium interface.

When the switch is connected to the short circuit there is complete reflection, giving a temperature

$$T_N \qquad (2)$$

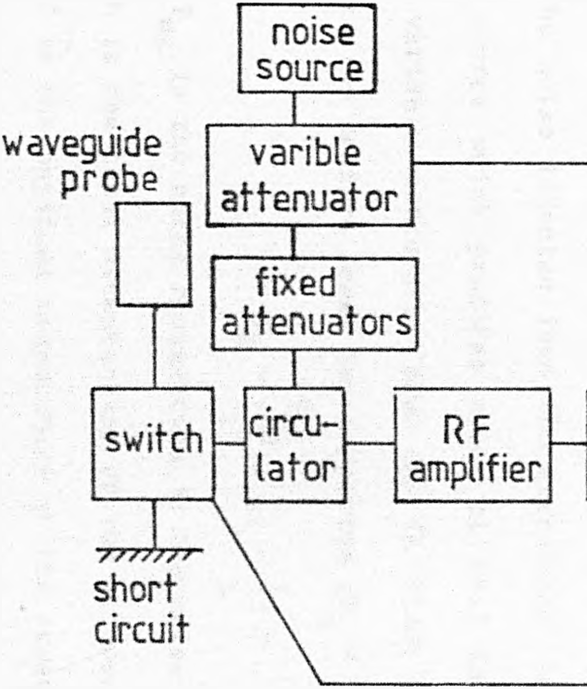

Fig. 5.6 Schematic diagram of the

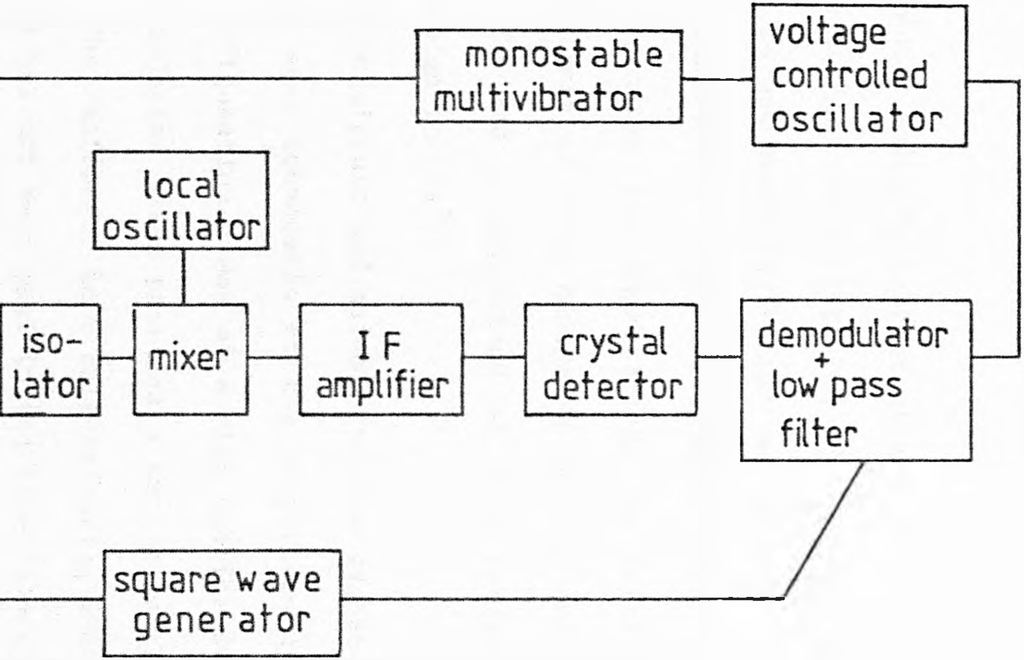

radiometer in a null-balancing mode.

The radiometer measures the difference between the two signals (1) - (2)

$$= T_r(1 - \rho) + \rho T_N - T_N$$
$$= (T_r - T_N)(1 - \rho)$$

if the injected noise T_N is controlled so that $T_N = T_r$ then the effect of the reflection coefficient on the signal is suppressed. This calculation is not exact as it does not take into account losses in the front end components, and consequently this system design cannot entirely compensate for fluctuations in reflected power. A more thorough analysis of this design of null-balancing radiometer can be found in [49] and a comparison of this design with another null-balancing design in [55].

A feedback circuit and noise injection system has been constructed which allows easy conversion of the comparison radiometer to a null-balancing configuration. Use of a high quality switched attenuator to control the injected noise provides a very accurate and stable balance condition. The radiometer in a null-balancing mode has yet to be fully evaluated and has not been used in the experimental measurements.

The noise injected into the circulator is provided by a constant noise source which produces noise at 15.5 dB above ambient. A PIN diode variable attenuator plus 26 dB fixed attenuation reduces the noise to the desired level for injection ($T_N = T_r$) which is given by

$$T_N = \frac{T_{NS}}{L} + \left(1 - \frac{1}{L}\right) T$$

where T_{NS} is the noise temperature of the noise source,

L is the total attentuation of the attenuators,

T is the physical temperature of the attenuators.

The PIN diode attenuator is most stable in its OFF and fully ON states. The desired attentuation is therefore achieved by switching the attenuator between the two states with a TTL pulse of fixed width τ_p, control of the attenuation being achieved by varying the repetition frequency, f_p. L is given by [102]:

$$L = \tau_p f_p L_{ON} + (1 - \tau_p f_p)L_{OFF} + L_{Fixed} \qquad (5.4)$$

where L_{OFF} is the insertion loss of the attenuator,

and L_{ON} is the maximum attenuation.

The integrator is followed by a voltage controlled oscillator (VCO) which produces a square wave whose frequency is proportional to the input voltage. This is followed by a monostable oscillator which produces a constant width ON pulse.

An example of the operation of the radiometer in its null-balancing mode illustrates the function of the feedback system. If the probe is moved to a position where the body temperature is higher, the input signal will increase and lead to a positive voltage at the integrator input, causing its output voltage to fall at a constant rate. This will cause the output frequency of the VCO to drop and so decrease the attenuation (equation 5.4). As a result, T_N will increase until $T_N = T_r$ once more. The condition necessary to compensate for the reflection coefficient is therefore maintained. The output signal of the radiometer is the voltage at the output of the integrator. If the probe is moved to a position where the temperature is the same but the reflection coefficient is different, the balance condition at the radiometer front end ensures that the output signal does not change.

Chapter 6

Radiometric measurement of raised temperature regions in homogeneous and bi-layered tissue-equivalent phantoms and comparison with simulations

6.1 Radiometric measurements in a homogeneous water phantom

    6.1.1 Radiometric linear scanning of a raised temperature region within a constant temperature water bath

    6.1.2 Sources of measurement uncertainty

    6.1.3 Comparison of simulated with measured results

6.2 The influence of tissue layers on radiometric measurements

    6.2.1 Comparison of radiometric scans in homogeneous and bi-layered structures

    6.2.2 Discussion

6.1 Radiometric measurements in a homogeneous water phantom

6.1.1 Radiometric linear scanning of a raised temperature region within a constant temperature water bath

The procedure for scanning of raised temperature regions in a lossy medium employed similar set-up to that used for the measurement of probe field patterns. The measurement media in these two cases were identical. The experiments were designed to allow temperature data to be collected immediately following field measurements, ensuring the same conditions for both sets of measurements. This was important as the field data could be used in the predictions of radiometer response (# 6.1.3). Much of the experimental equipment has been described previously. Details of the computer controlled scanning and data logging system were given in # 3.1.3 and of the tissue-simulating phantoms in # 3.1.2. Additional apparatus required for temperature measurement were: the microwave radiometer, a full description of which can be found in Chapter 5, and the temperature hot-spot. The single temperature hot-spot consisted of a 10 cm length of perspex tube (inside diameter 12.8 mm, and outside diameter 14 mm) through which water was pumped at a controlled temperature via a water circulator (Grant Instruments). The water temperature could be maintained at any level from fractionally above ambient with a stability of ± 0.1 °C up to 60 °C ± 0.5 °C. Twin hot-spots were also produced consisting two 12 cm polyethylene tubes, inside diameter 9 mm and outside diameter 9.6 mm, held parallel to each other at a given separation by perspex collars.

Figure 6.1 shows the experimental set-up. The waveguide probe was clamped to the side of the water tank, with the aperture facing outwards into the tank and the small aperture dimension vertical.

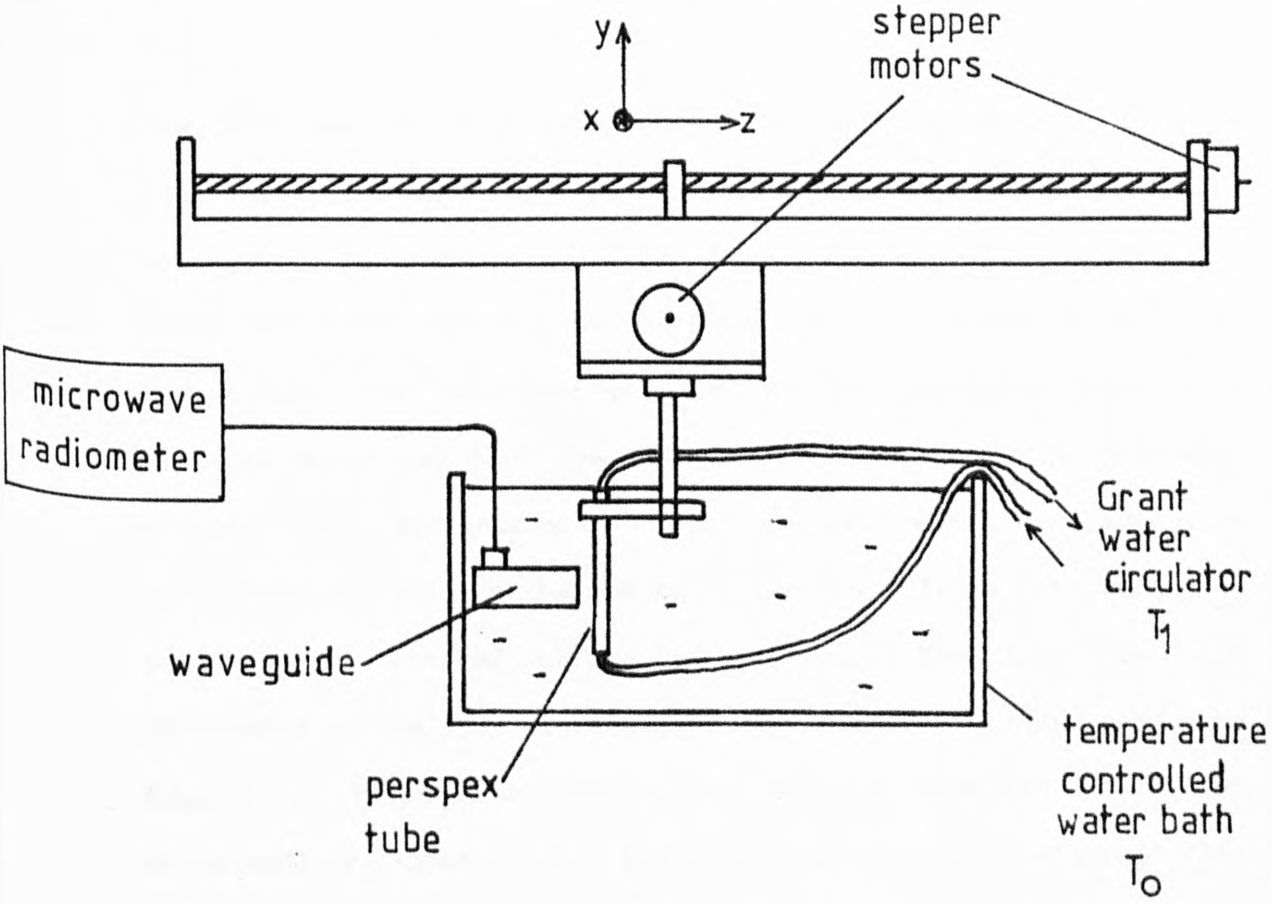

Fig. 6.1 Radiometric measurement system for linear scanning

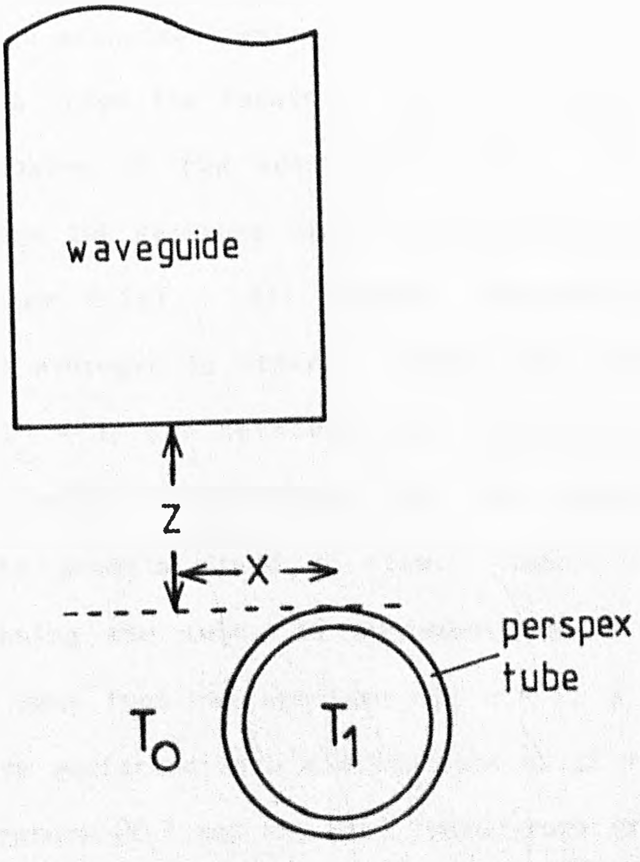

Fig. 6.2a Plan view of configuration of waveguide and hot-spot

The tube was attached with its axis vertical, to the moveable platform of the scanning frame by a perspex clamp, and was fed with water from the circulator via flexible rubber tubing. The scanning frame and probe clamping device could be individually adjusted to ensure that the tube was parallel to the waveguide face in a vertical plane and that the tube moved parallel to the face when scanned. All measurements of distance were taken relative to a tube position touching the centre of the probe face. The reference position was checked before each scan. The tube was then positioned at the scan start position. Automatic scanning and data logging was effected by running the program "SCANNER" on the BBC microcomputer (Appendix 2). For a radiometer time constant of five seconds, settling times were set to ten seconds and sampling times to five seconds. Water temperature stability was critical for accurate data measurement. The temperature controlled water bath and the tube's water circulator had to be left running for at least 24 hours before a scanning session.

Figure 6.2b shows the result of scanning the hot tube across the large dimension of the aperture (X scan) at a distance of $z = 8$ mm between the aperture plane and the nearest point of the tube (see Figure 6.2a). All results represent a number of identical scans averaged in order to reduce the noise level. The base level ($\Delta T_m = 0$) was obtained from a mean of the first three and last three points in the final data set, where the tube was remote from the probe's field of view. Figure 6.2c shows the result of scanning the tube, in increments of 1 mm, along the probe's z-axis away from the aperture (ie $x = 0$, $z = 1 \rightarrow 20$ mm). These scans were performed with a difference of $\Delta T = 10$ °C between the tube temperature (T_1) and the bath temperature (T_0).

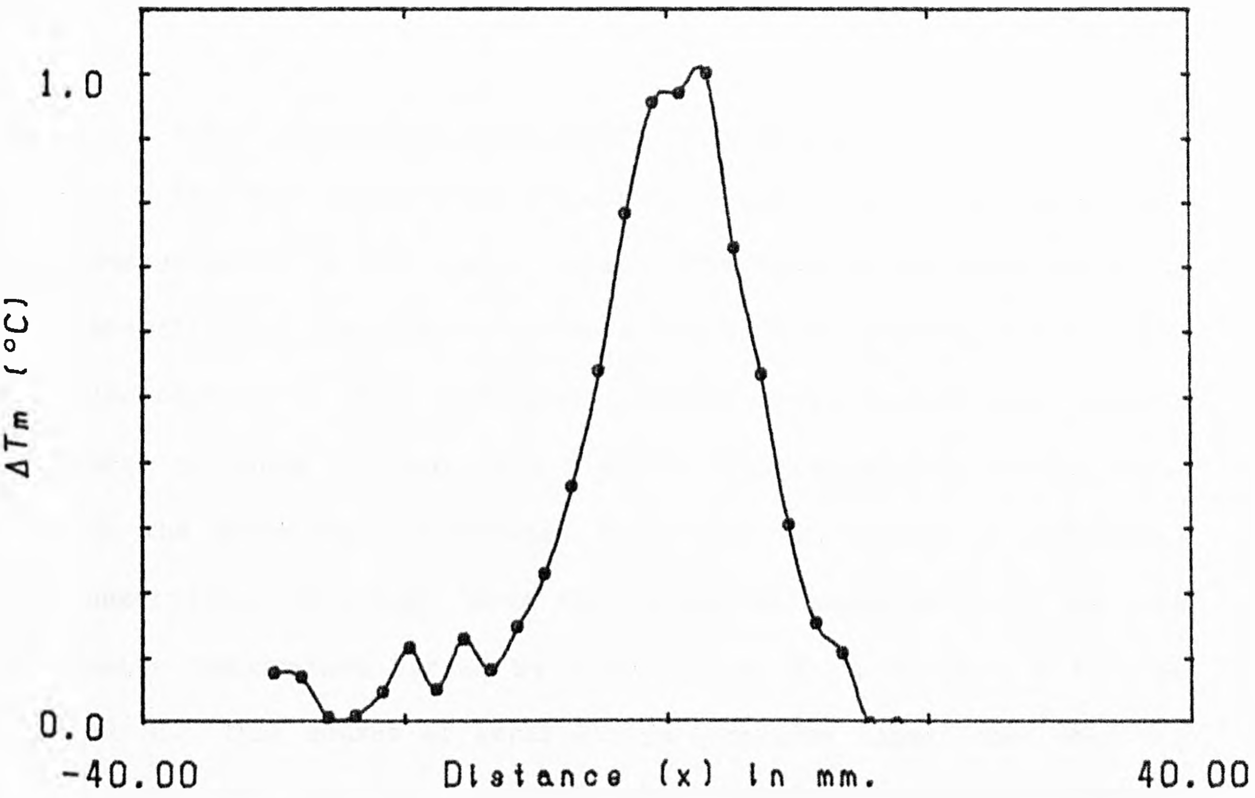

Fig.6.2b: Measured radiometric temperature difference X scan in water. Z=8mm. ΔT=10°C.

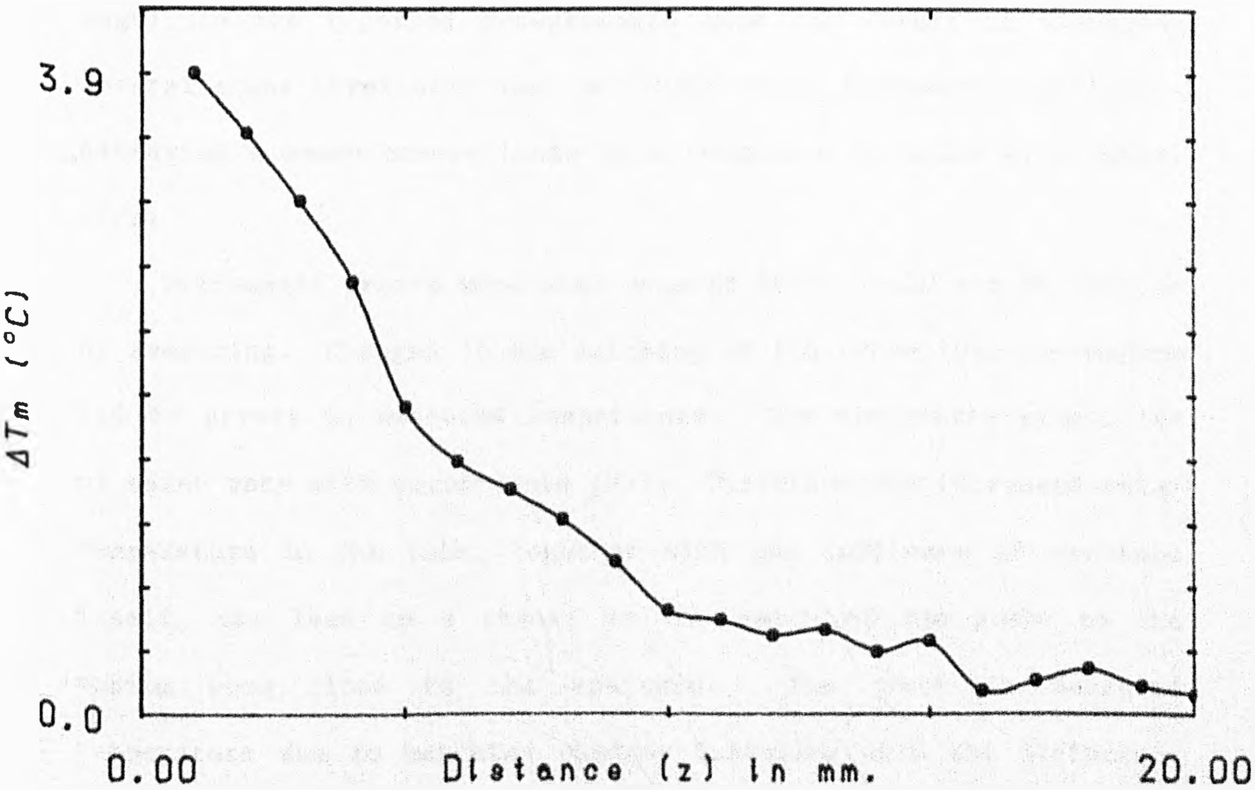

Fig.6.2c: Measured radiometric temperature difference. Z scan in water. X=0. ΔT=10°C.

6.1.2 Sources of measurement uncertainty

The most significant source of possible error in radiometric measurements is the system noise. The temperature resolution and stability of the radiometer were examined in section 5.3.2. The uncertainty in each radiometric measurement, taking into account both of these factors, is ± 0.2 °C. The temperature of the water in the water tank fluctuated by ± 0.05 °C, giving an additional uncertainty of ± 0.05 °C in the radiometer measurements. The tube water temperature varied by ± 0.1 °C at 20 °C up to ± 0.5 °C at 60 °C. This source of error was particularly significant when the signal from the tube gave maximum contribution to the measured temperature, causing errors ranging from 0.05 °C to 0.25 °C; however, typical error figures for those measurements reported here were 0.01 °C to 0.05 °C. All of these sources of error were randomly fluctuating or noise errors. In order to reduce their magnitude the reported measurements were the result of averaging several scans (typically six) performed under identical conditions. Averaging n measurements leads to a reduction in noise by a factor $1/\sqrt{n}$.

Systematic errors were also present which could not be reduced by averaging. Changes in the matching of the probe into the medium led to errors in measured temperature. The dielectric properties of water vary with temperature [89]. Therefore the increased water temperature in the tube, together with the influence of the tube itself, may lead to a change in the match of the probe to the medium when close to the aperture. The error in measured temperature due to matching changes increases with the difference between the water temperature and the radiometer's physical temperature. In the reported results the water temperature was set equal to the radiometer's physical temperature (= 28 °C). This temperature was measured by placing the radiometer probe in the constant temperature water bath and introducing a mismatching medium (at the same temperature as the water) in front of the probe. At 28 °C no change in radiometer output was noted when the mismatch was introduced, indicating a noise power balance condition at the probe/medium interface. Measurement error was thus proportional to the temperature change measured by the radiometer only. An estimate of the maximum error due to matching can be gained by examining the case where the tube is placed directly in front of the aperture. The matching change, averaged over the radiometer bandwidth, is + 0.03, leading to an increase in power transmission to the radiometer of 3%.

The accuracy in location of the tube relative to the aperture is dependent on the precision of setting the reference position. This error is estimated to be ± 0.25 mm, giving a possible error in all distance measurements of 0.5 mm. Examination of curve gradients in Figs 6.2b and 6.2c indicate a consequent maximum error in radiometric temperature of about 10%.

6.1.3 Comparison of simulated with measured results

Before comparing the results of the simulations and measurements, the correspondence between the simulation model and the experimental situation will be discussed. The simulations employ field predictions described in Chapters 2 and 3. Many of the discrepancies between model and experiment have already been studied in # 3.2 and need no elaboration. However, some further differences arise due to experimental techniques and simplifying assumptions for the model which must be examined.

In the experimental situation, the raised temperature region is enclosed within a perspex tube (see Fig 6.2a). Perspex has a permittivity of approximately 2 whereas water has a permittivity (at 28 °C) of 73. Therefore, the perspex forms a double dielectric boundary to the propagating microwaves emitted within the enclosed hot water. The transmission function across this double, curved boundary cannot be estimated but inevitably reflections at the interface will lower the effective emissivity of the raised temperature region and thus reduce the signal measured by the radiometer due to the hot-spot.

In employing field predictions for the radiometric model, an implicit assumption is made that the hot-spot has the same dielectric properties as the surrounding medium. Fig 3.2 shows that, although the real part of the permittivity of water changes little with temperature, the imaginary part falls considerably as temperature increases. The values for field predicted within the hot spot are therefore incorrect, although the error should be small. The effect of the different dielectric properties of the raised temperature water is partly taken into account in the model by including the lower conductivity in the emissivity calculation (see # 4.3). Extension of the field prediction algorithm in the future to include non-planar boundaries should account for these effects.

The analysis of Chapter 4 was based on Kirchhoff's Law. The conditions existing in the model break one of the assumptions upon which this law is based, namely that no high temperatue gradients exist within the medium. The failure to meet this condition and its effect on the simulations cannot be assessed within the scope of this thesis.

The simulation model is shown in Fig 6.3a. Simulations are calculated from three dimensional field pattern predictions, and assume a circularly cylindrical hot-spot which is infinitely long in the y direction. This assumption is appropriate for these comparisons as the hot-water tube used in the experiments was long compared to the y dimension of the aperture.

In Fig 6.3b, an X scan is simulated. The hot tube is scanned across the large dimension of the aperture in increments of 2 mm at a distance z = 8.3 mm from the aperture. This is compared with the measured scan which is reproduced from Fig 6.2b. The outer edge of the tube is z = 8 mm from the aperture but the finite perspex tube thickness places the hot water at z = 8.3 mm. This compensation for tube thickness is carried out in all of the other comparisons. The z distance quoted in the figures are from the aperture to the outer edge of the perspex tube. Fig 6.3c shows a comparison between simulation and measurement for a Z scan. The agreement is satisfactory at distances greater than 2 mm from the aperture. Closer to the aperture the prediction over-estimates radiometric temperature. A possible explanation for this lies in the discrepancies between simulation model and experimental situation. These are more important, in absolute terms, when the hot area makes a greater contribution to the measured temperature. Close to the aperture the dielectric structure of the tube may distort the field pattern greatly compared to the situation for a homogeneous medium.

These simulations were carried out using a three dimensional simulation routine and employing three dimensional field predictions. To illustrate the historical development of this work, some more results are included for comparison. Fig 6.4a and

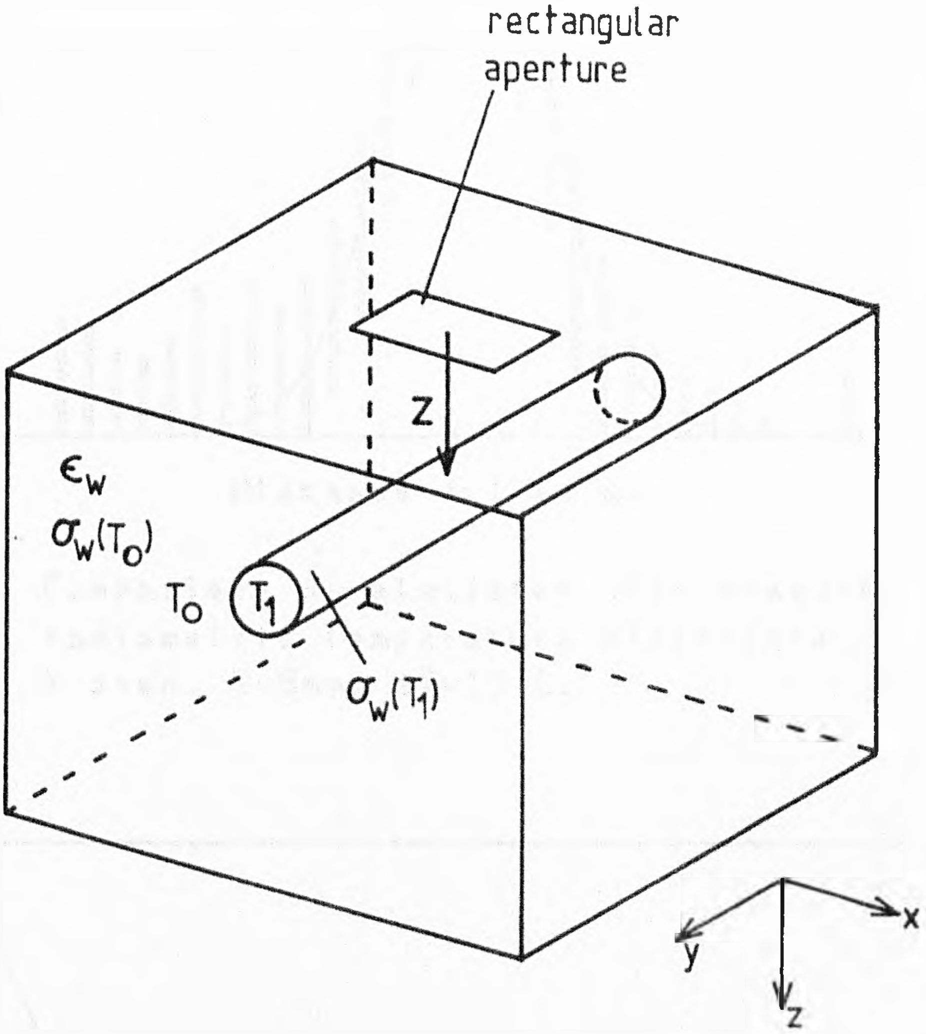

Fig. 6.3a Simulation model for linear scanning in a homogeneous water medium

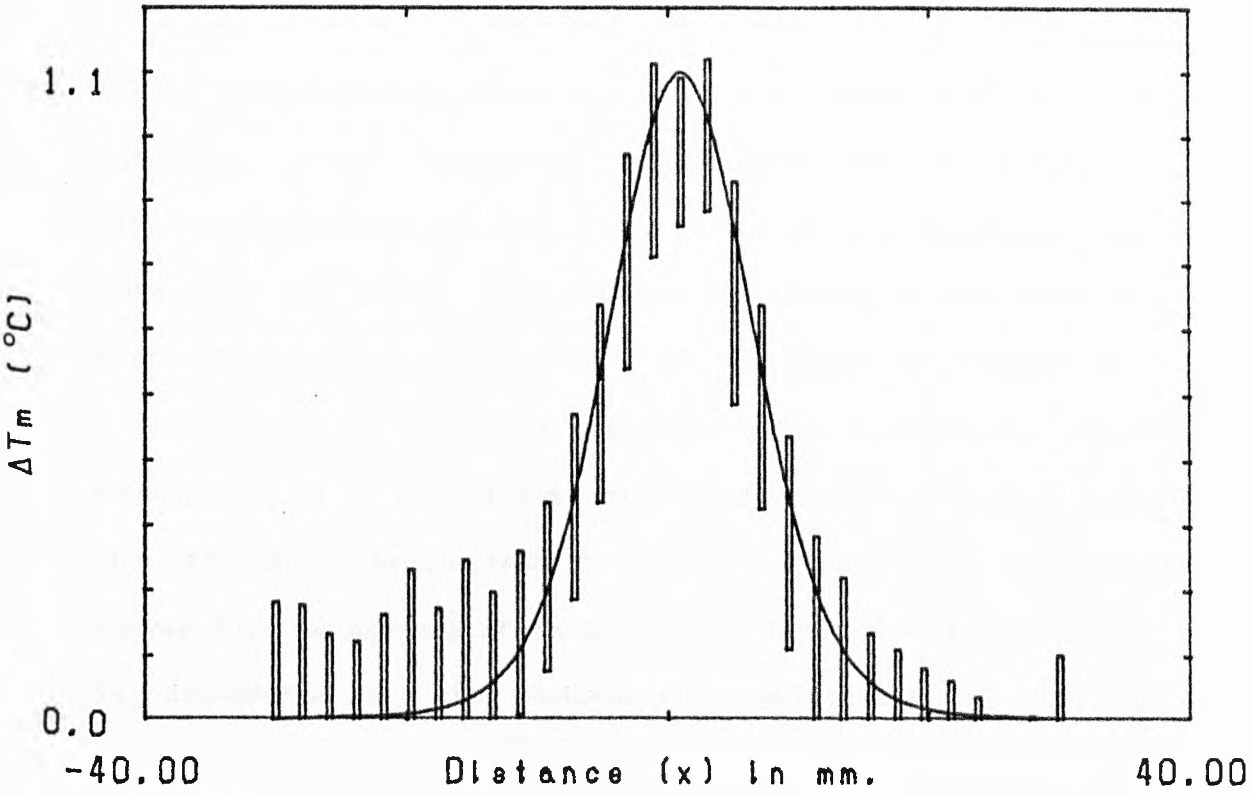

Fig.6.3b: Comparison of simulated with measured radiometric temperature difference. X scan. Z=8mm. ΔT=10 °C.

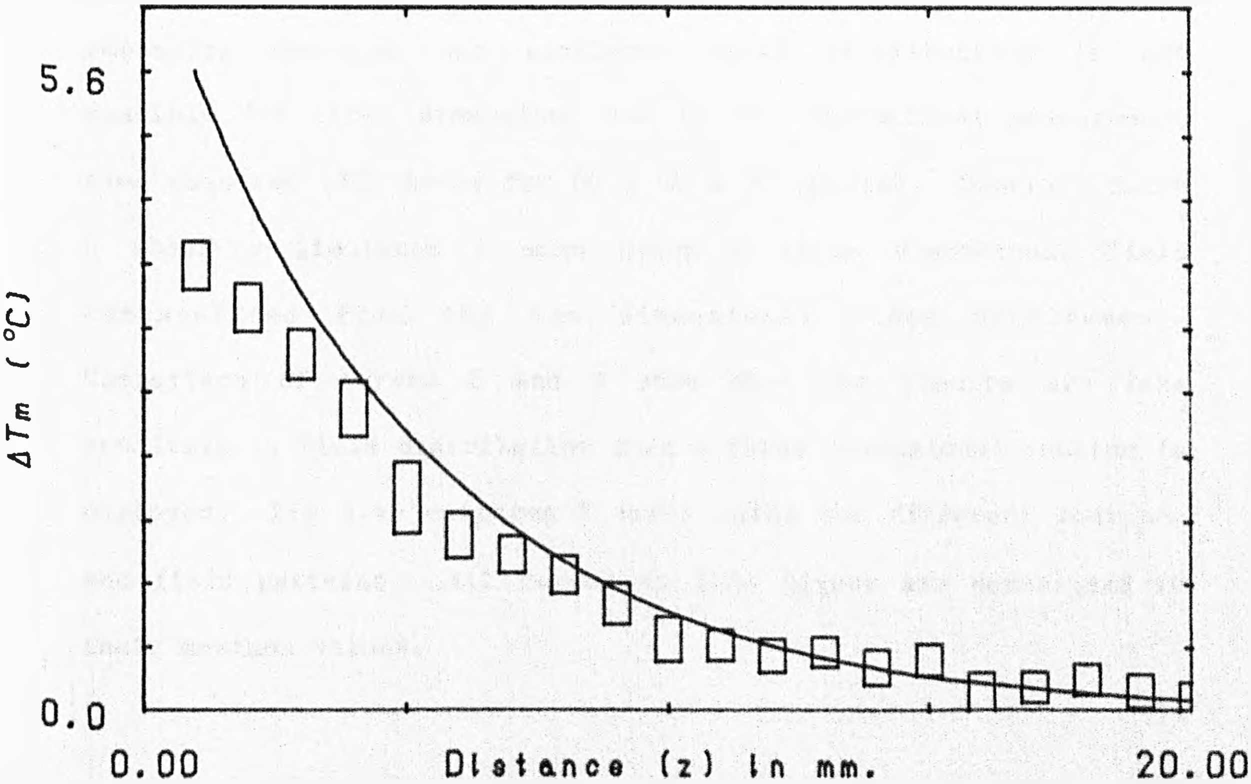

Fig.6.3c: Comparison of simulated with measured radiometric temperature difference. Z scan. X=0. ΔT=10°C.

b show predicted temperature scans for a number of different cases. Initially, a two dimensional model which did not inlcude the dimension parallel to the short side of the aperture (the y dimension) was used. Calculations were based on two dimensional field measurements, carried out as described in Chapter 3. A Z scan simulation with this method is given in Fig 6.4a, curve A. Development of a two dimensional field prediction method allowed the temperature predictions to be carried out solely by computer (curve B). Comparison of these curves illustrates the sensitivity in dependence of the radiometric temperature on the field distribution when a two-dimensional routine is employed. A small discrepancy between fields measured and predicted in Fig 3.6, result in a large difference in the predicted temperature depth curve. Extension of the field prediction method to three dimensions led to a three dimensional temperature simulation routine (curve C). An equivalent comparison between results employing measured and simulated field distributions is not possible for three dimensions due to the impractical measurement time required (300 hours for 60 x 60 x 30 points). However, curve D shows a simulated Z scan using a three dimensional field extrapolated from the two dimensional field measurement. Comparison of curves C and D show that the results are less sensitive to field distribution when a three dimensional routine is employed. Fig 6.4b compares X scans using the different routines and field patterns. All curves in this figure are normalized to their maximum values.

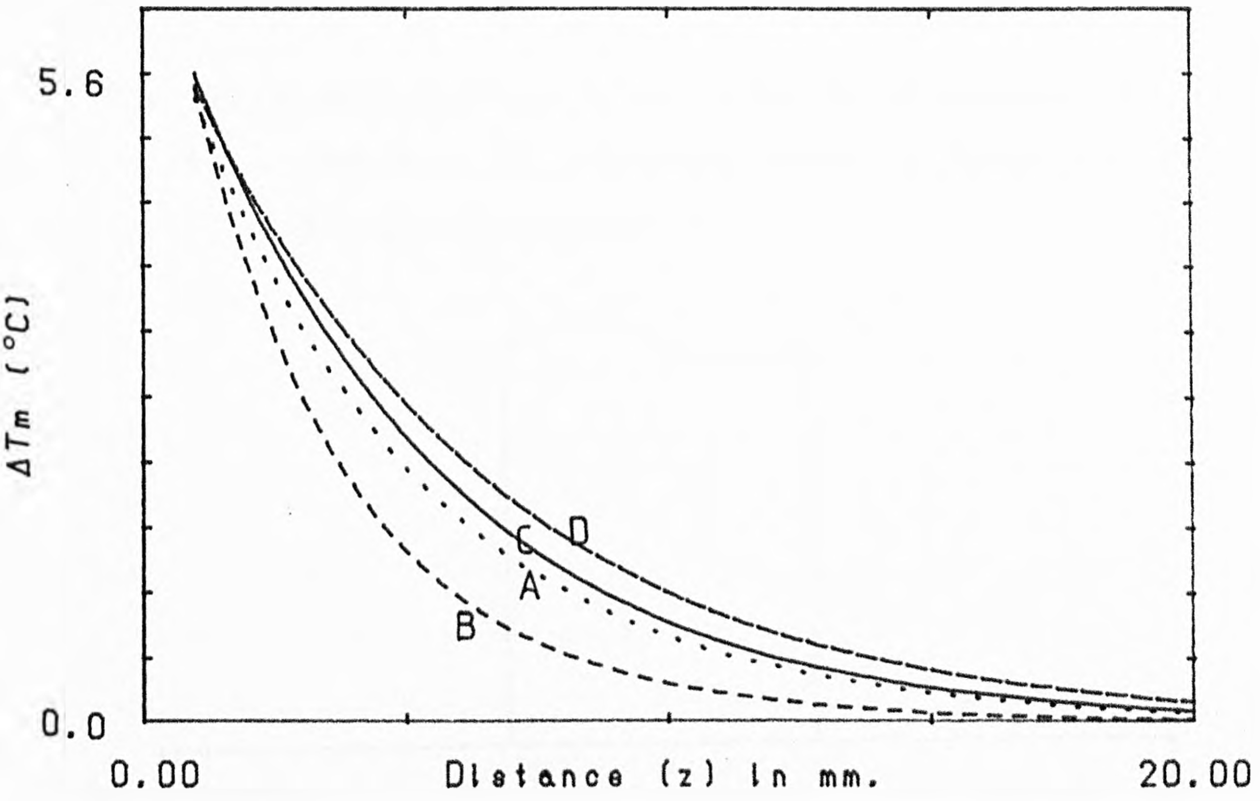

Fig.6.4a: Comparison of simulated Z scans using different simulation routines and field patterns. See text for details.

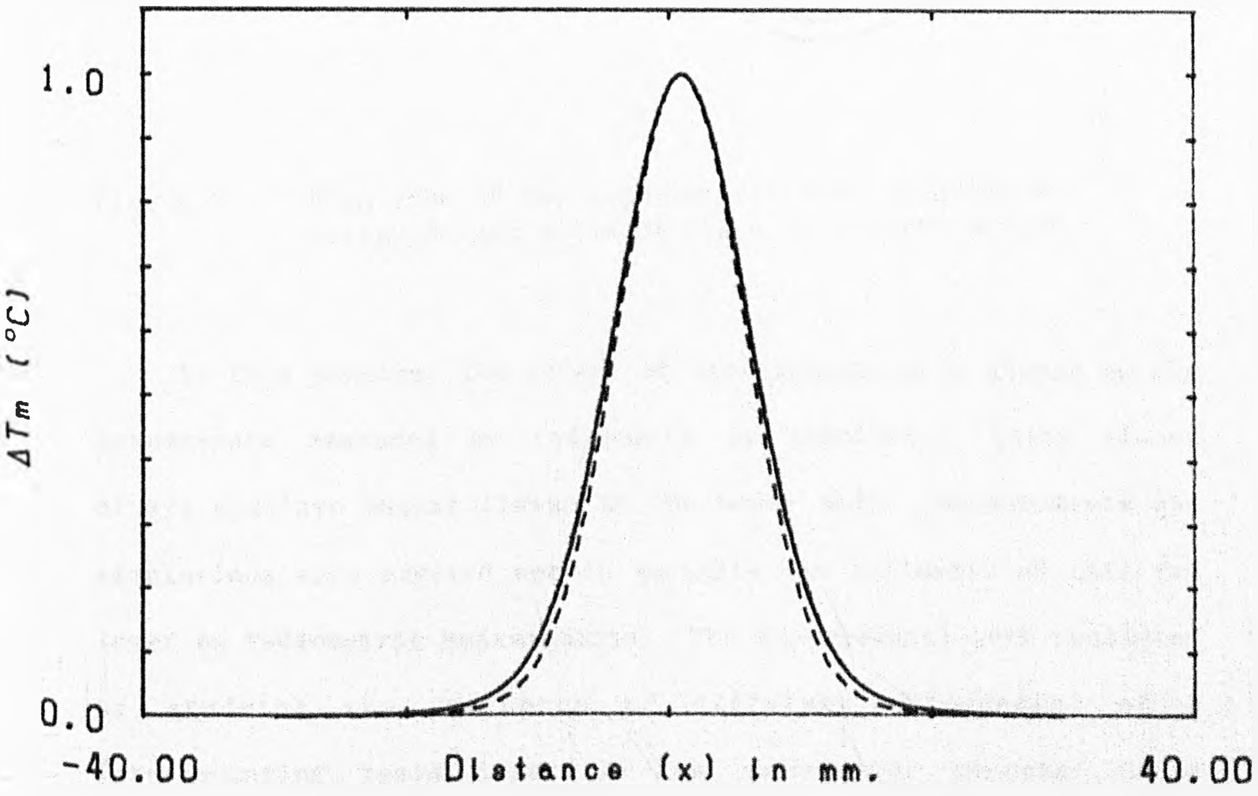

Fig.6.4b: Comparison of simulated X scans using different simulation routines and field patterns. See text for details.

6.2 The influence of tissue layers on radiometric measurements

6.2.1 Comparison of radiometric scans in homogeneous and bi-layered structures

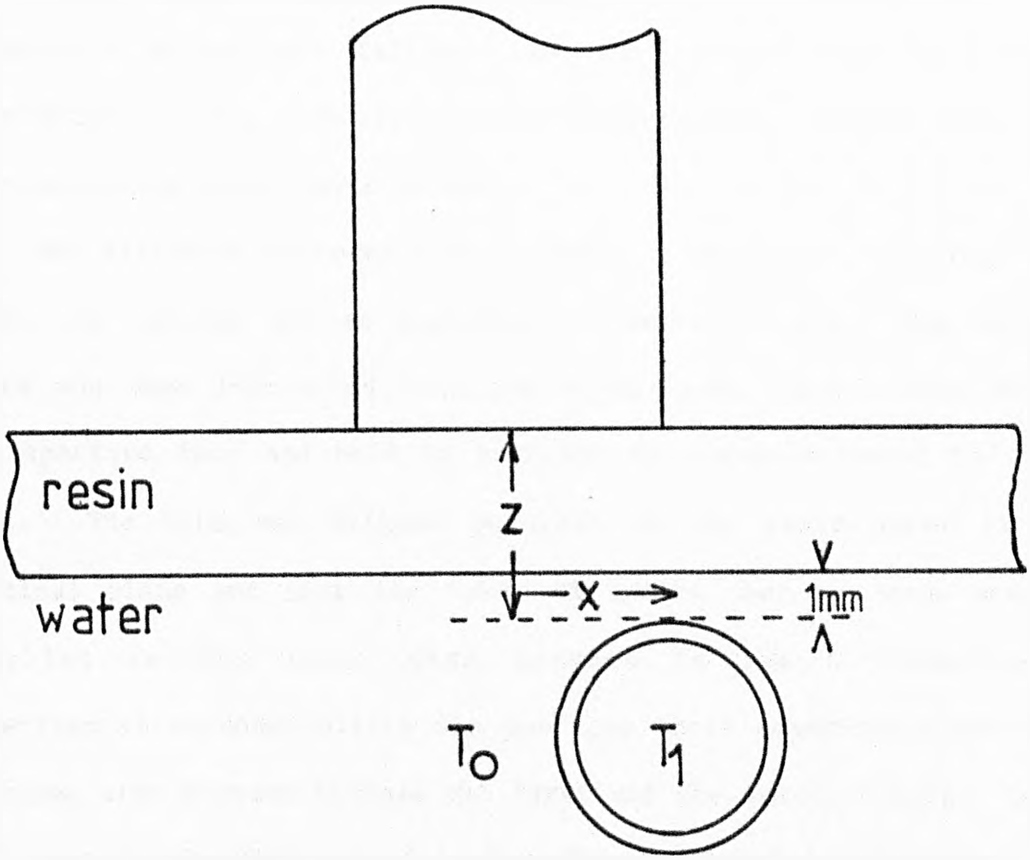

Fig. 6.5 Plan view of the experimental configuration of waveguide and hot-spot for a bi-layered medium

In this section, the effect of stratification of tissue on the temperature measured by radiometry is examined. Fatty tissue always overlays muscle tissue in the human body. Measurements and simulations were carried out to quantify the influence of this fat layer on radiometric measurements. The experimental work consisted of studying the influence of different thicknesses of a fat-simulating resin layer on the radiometric response to a temperature hot-spot buried in muscle-simulating water. This was achieved by comparing scans of a hot water tube in a water medium with scans when the resin layer was present between the water and the aperture. Both measurements were carried out with the same separation between hot-spot and aperture. By employing this comparison method the influence of the perspex tube wall was eliminated. Fig 6.5 shows the experimental set-up with a fat-simulating resin layer present.

Two different procedures were used. In the first, scanning in water was carried out as described in section 6.1.1. The resin layer was then introduced into the water tank, placed flush with the aperture face and held in position by clamps attached to the tank. The tube was aligned parallel to the resin layer in a vertical plane and care was taken to ensure that the tube moved parallel to the layer when scanned in the x dimension. Experimental reproducibility was poor for these experiments due to problems with contact between the layer and the aperture face. Low tolerance in the flatness of both surfaces allowed a thin layer of water of variable thickness to form. Contact conditions therefore changed between each experiment. This was highlighted by measuring the probe matching by a network analyser before each scan, which showed that the reflection coefficient looking into the coaxial connector of the probe could vary between 0.2 and 0.6 at 4.6 GHz.

A more reproducible configuration was achieved by setting the probe aperture into the resin layer. The aperture face of the waveguide was introduced into the resin in its liquid state which was then allowed to harden, giving perfect contact conditions. The probe and layer were positioned in the water tank with the edge of the hot water tube 1 mm from the face of the layer, this being measured relative to a reference point on the probe. A scan in the bi-layered structure was then performed. The layer could then be removed carefully from the probe which was replaced in the tank with the tube set up in the same relative position, and a scan in homogeneous water performed. A disadvantage of this technique was that damage could occur to the probe when removing the resin layer. Only a few results using this technique are therefore available. Additional sources of experimental error to those described in section 6.1.2 were present. Removal and replacement of the probe between measurements increased the inaccuracy in setting the reference position to the required ± 0.5 mm in both the x and z dimensions. Reproducibility of measurements was worse due to differences between the fabrication thickness of the resin layers; tolerance in measured thickness was estimated to be 0.4 mm. Also, errors arose because the fabrication method sometimes resulted in the layer face not being perfectly parallel to the aperture.

Network analyser measurements showed that probe reflection coefficient and thus radiometer calibration was a function of resin layer thickness. For each resin layer the radiometer was re-calibrated by placing the layer and the face of the waveguide in the calibration water bath (# 5.3.1) and measuring radiometer output as a function of water and resin temperature. The long time period necessary for the resin layer to attain the temperature of the bath also resulted in heating of the probe and cable. To allow direct comparison of scan results the calibration of the radiometer and probe without the resin layer was carried out over an equivalent time period. Since this does not give a true calibration of the radiometer in terms of temperature, all the following results are presented with a normalized ordinate.

Fig 6.6a shows a scan taken at a tube to aperture distance of z = 5.5 mm in water compared with an identical scan but with 4.5 mm resin and 1 mm water as the intervening medium. Fig 6.6b shows the same situation with the hot-spot at a higher temperature of 30 °C above the surrounding water temperature, this maximizes the data accuracy by increasing the signal to noise ratio. Since all the data is normalized, scans at different temperatures are equivalent and any discrepancy is due to noise. A simulation of these measurements is given in Fig 6.6c; the model for the bi-layered structure is shown in Fig 6.7. A similar situation is presented in Fig 6.8 for a tube depth of z = 4.5 mm and a resin thickness of 3.5 mm. Fig 6.9 shows a comparison of three scans at a distance of z = 10 mm with three differing intervening structures (9 mm resin and 1 mm water, 4.5 mm resin and 5.5 mm water, no resin and 10 mm water). These scans were carried out by first fabricating a 9 mm resin layer then machining this down to 4.5 mm thick and finally removing the layer completely.

The influence of the resin layer on the spatial resolution of the scanning procedure was studied by scanning two parallel hot water tubes fixed a small distance apart. Fig 6.10a shows an X scan of two 9 mm diameter tubes separated by 3 mm, in water. The tubes are easily resolved. When a layer of resin is present, the spatial resolution is reduced. Fig 6.11a indicates that the two tubes may be just resolvable, although the variation is well within the measurement noise level. The simulation (Fig 6.11b) suggests that the tubes cannot be resolved when the resin layer is present.

6.2.2 Discussion

These results indicate that an intervening fat-simulating resin layer has a two-fold effect. Firstly, the resin layer tends

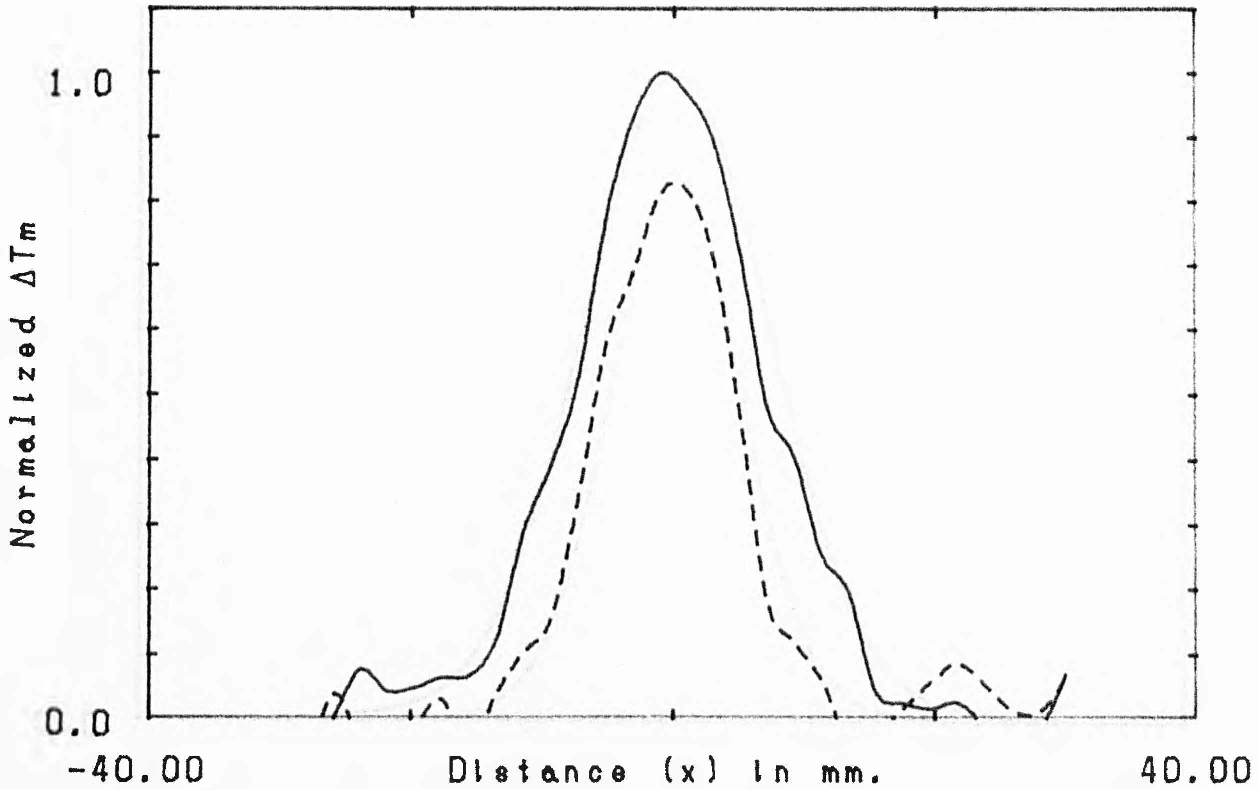

Fig.6.6a: Comparison of measured radiometric temperature differences for two X scans at Z=5.5mm. ΔT=10°C.
(- -) Homogeneous water. (-) 4.5mm resin + water.

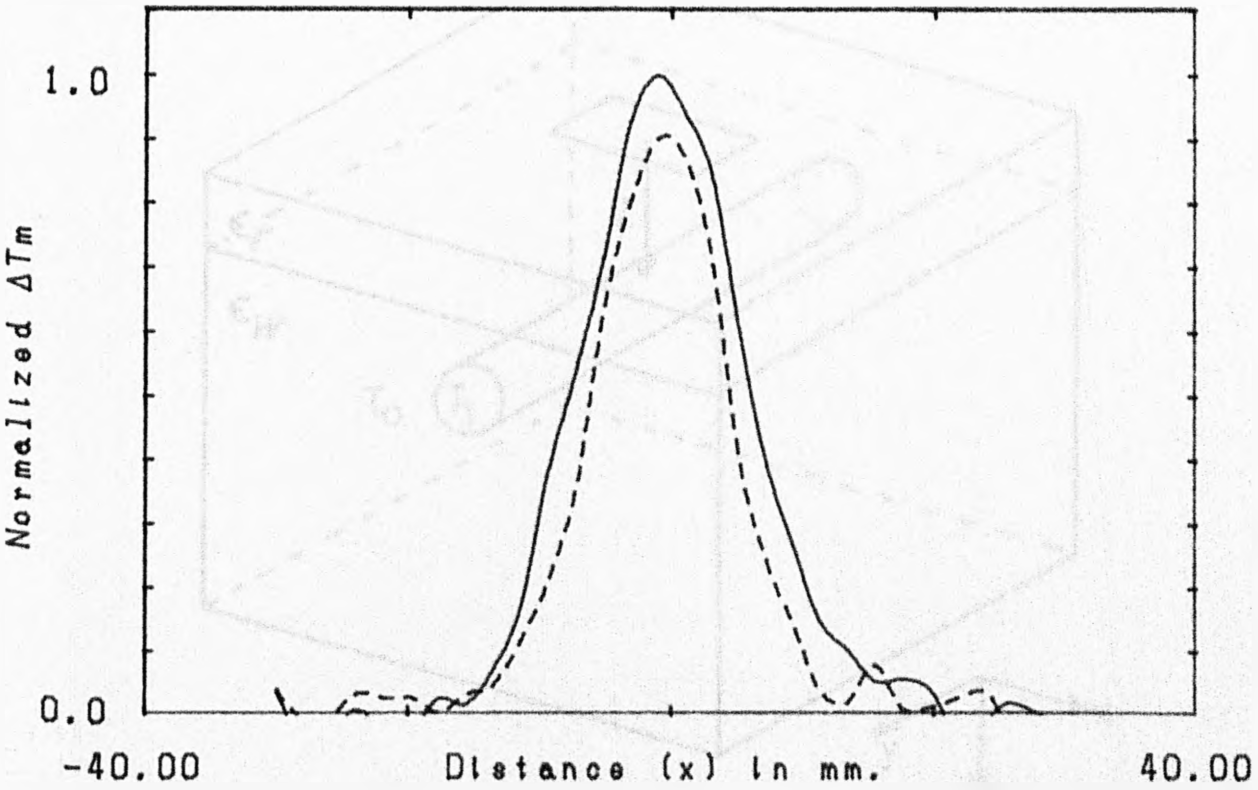

Fig.6.6b: Equivalent measurement to Fig.6.6a. ΔT=30°C.

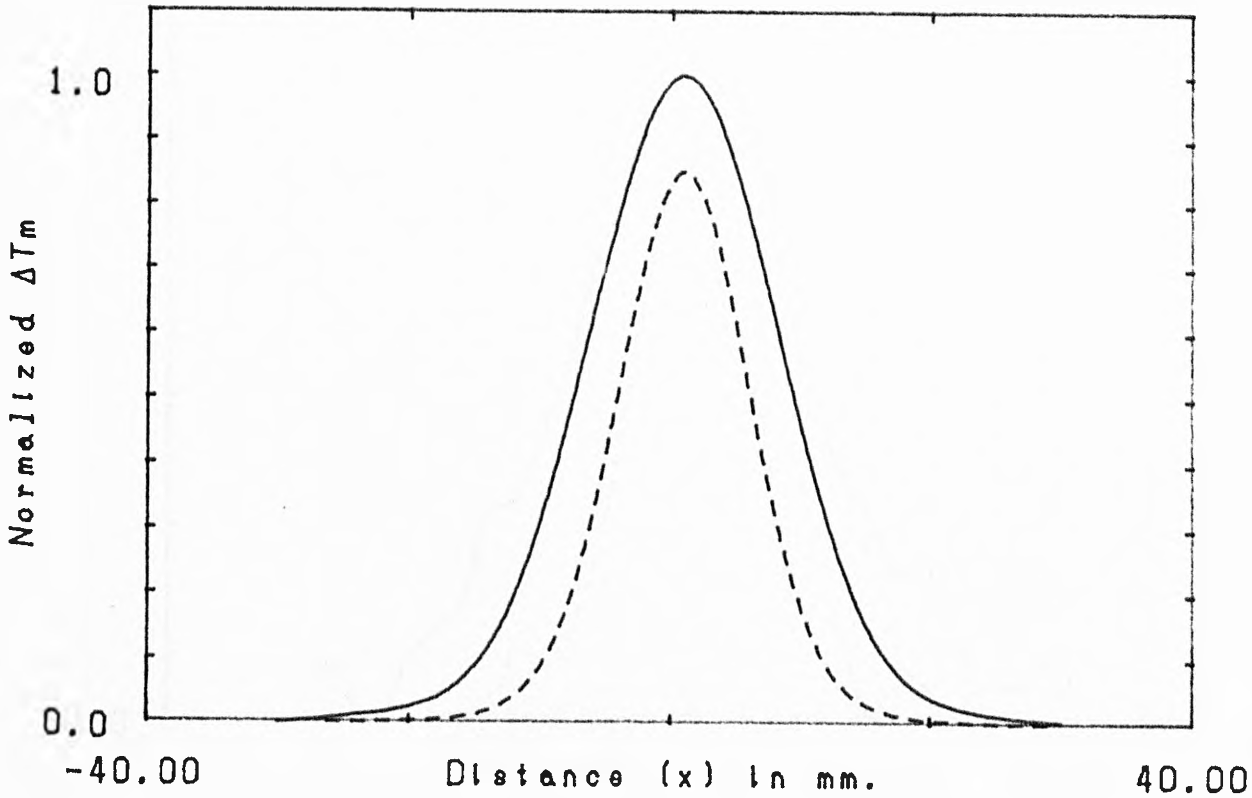

Fig.6.6c: Simulation of Figs.6.6a and 6.6b

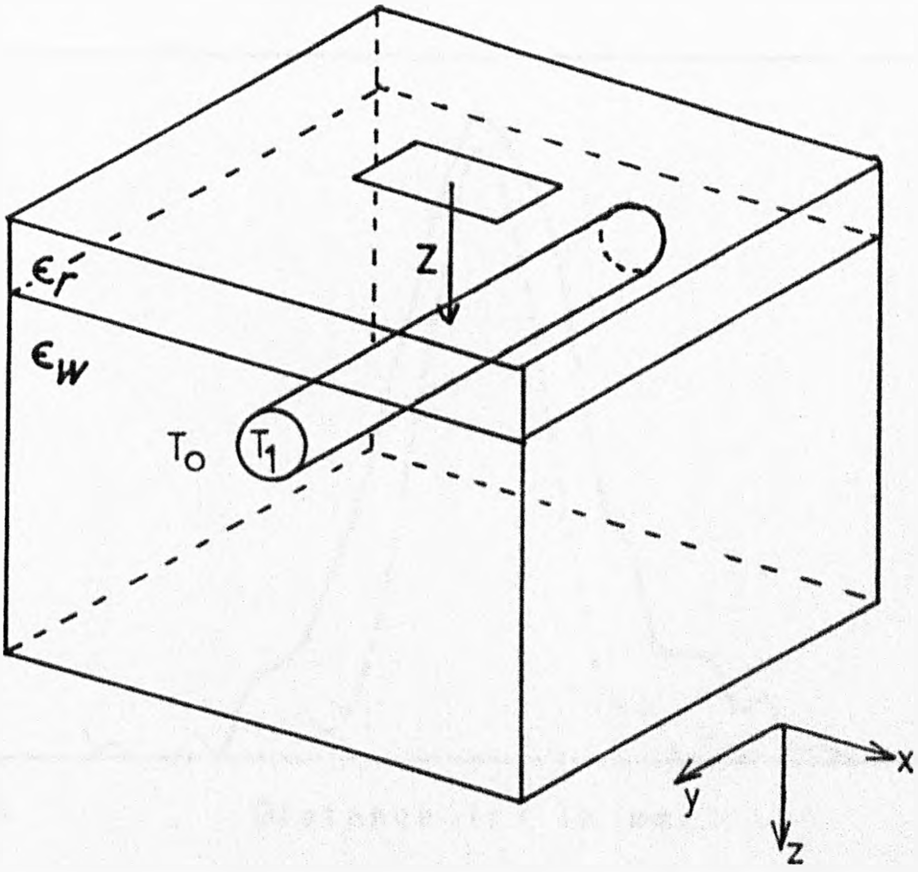

Fig. 6.7 Simulation model for linear scanning in a bi-layered resin and water medium

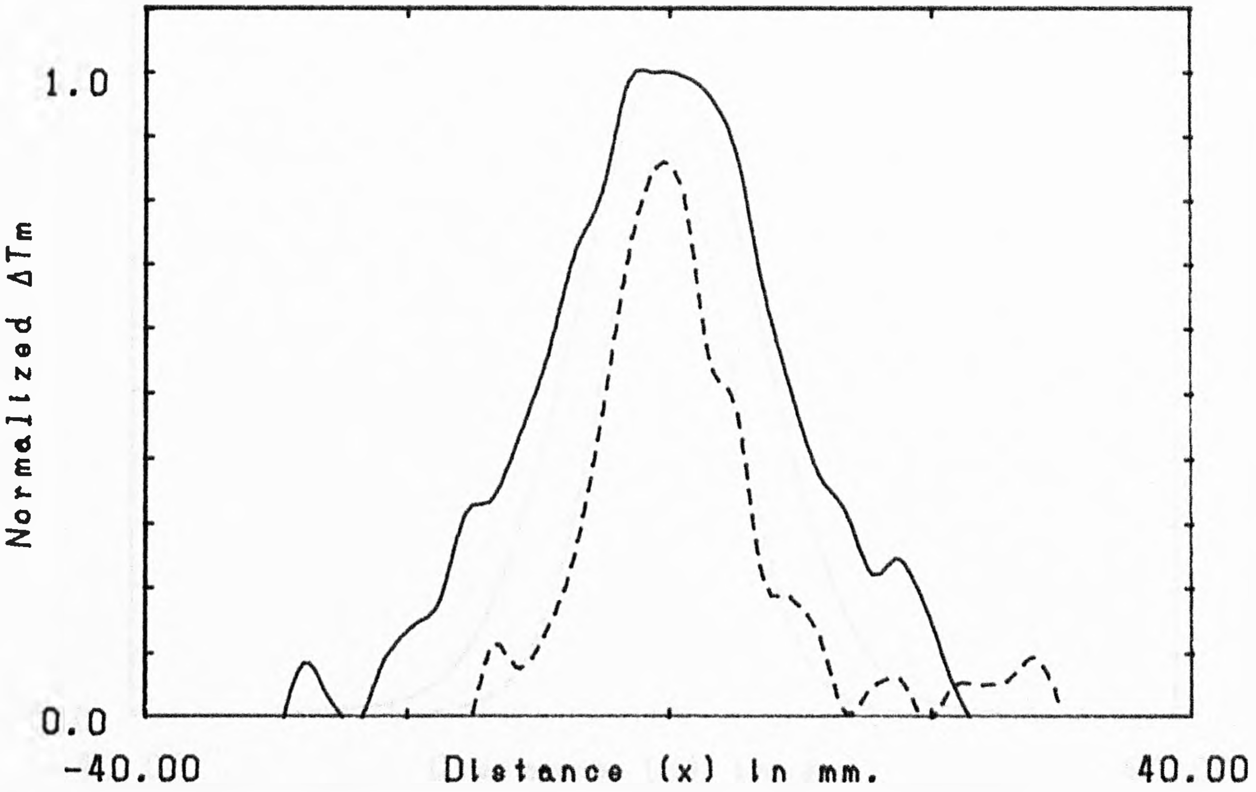

Fig.6.8a: Comparison of measured radiometric temperature difference for two X scans at Z=4.5mm. ΔT=10°C.
(- -) Homogeneous water. (-) 3.5mm resin + water.

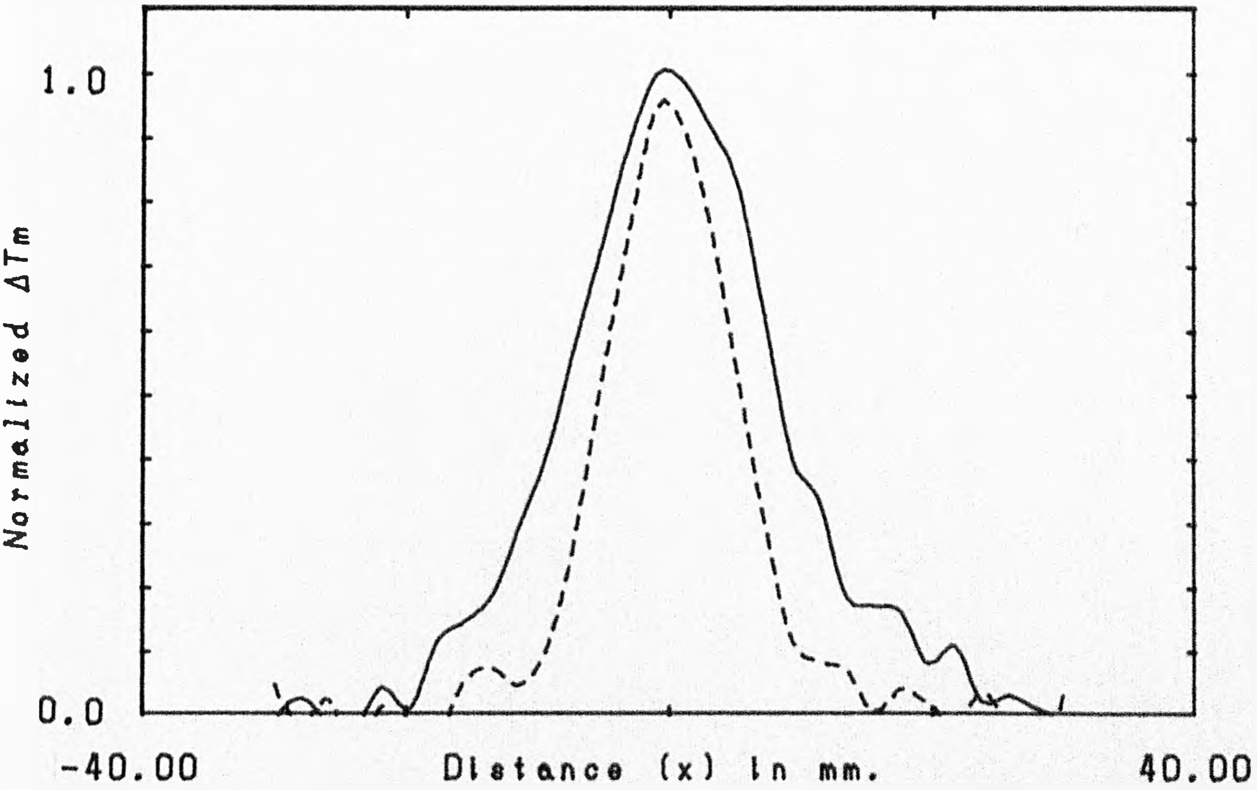

Fig.6.8b: Equivalent measurement to Fig.6.8a. ΔT=30°C.

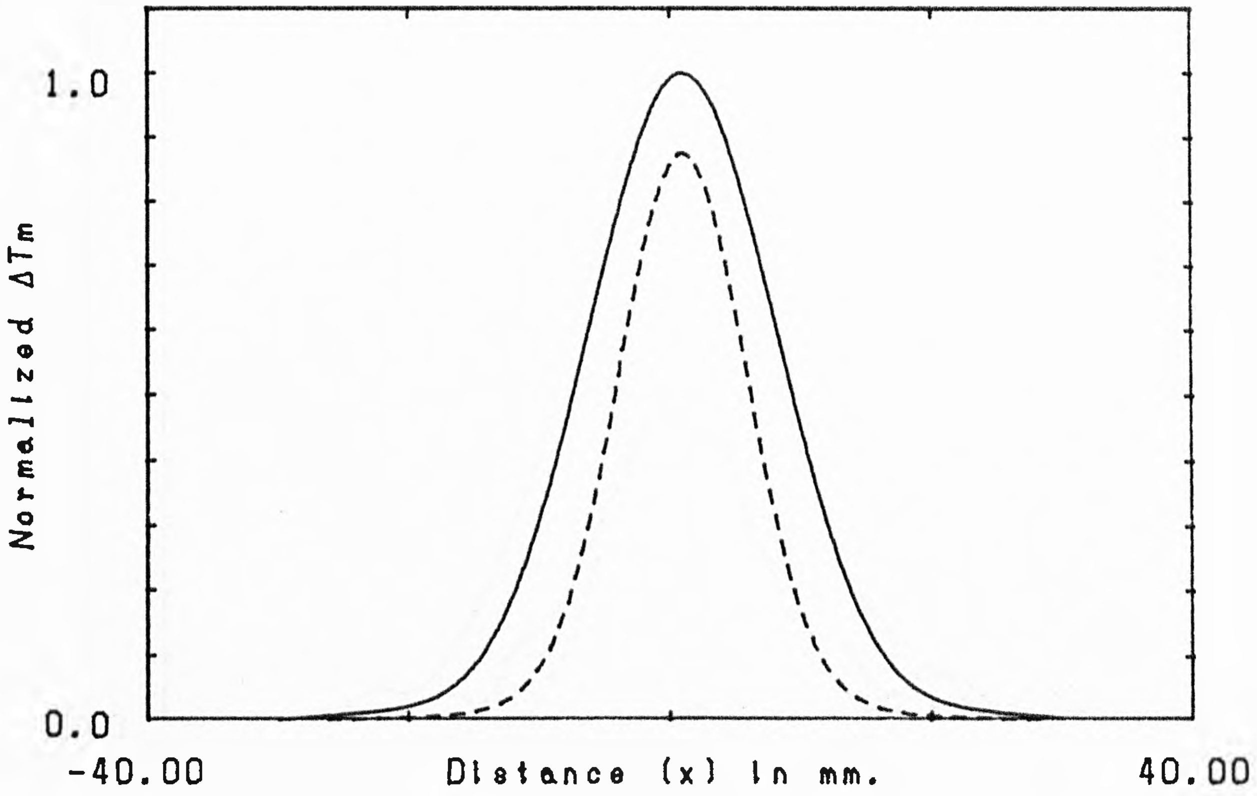

Fig.6.8c: Simulation of Figs.6.8a and 6.8b.

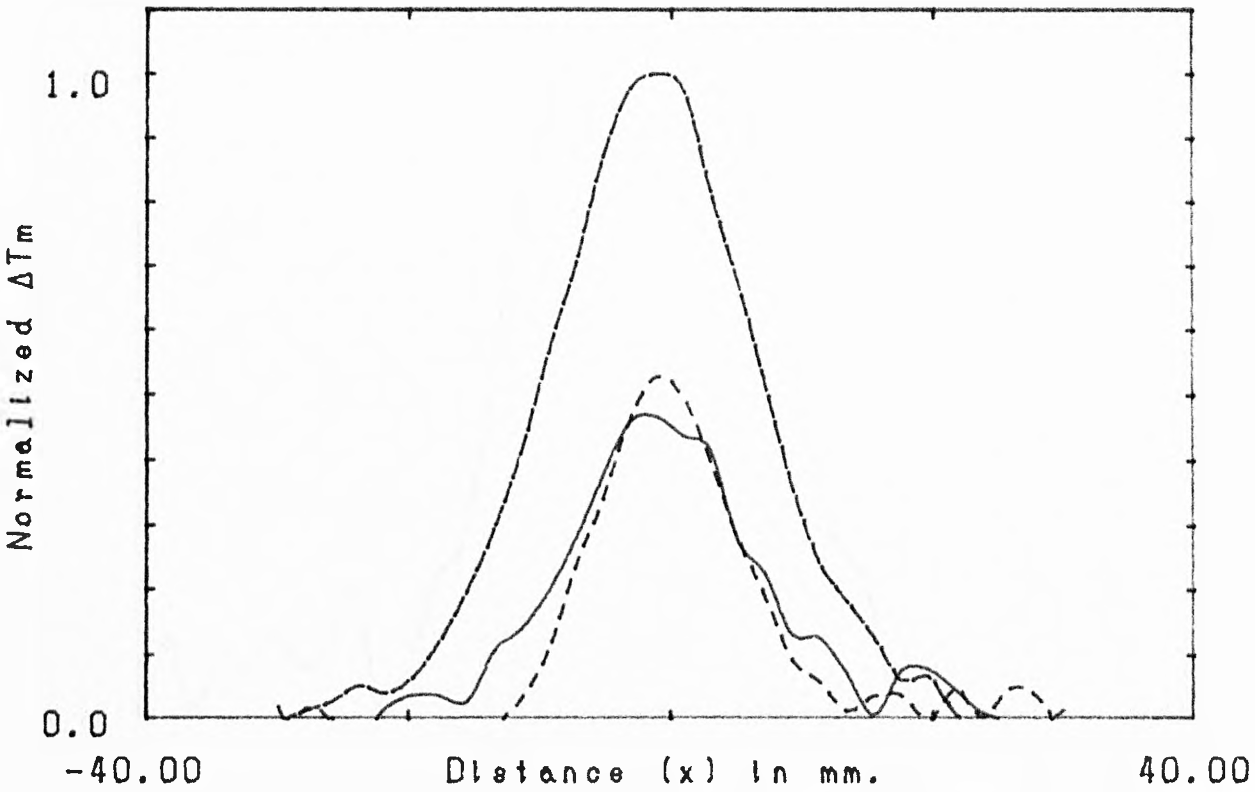

Fig.6.9a: Comparison of three measured X scans at Z=10mm.
ΔT=30 °C. (-) Homogeneous water.
(- -) 4.5m resin + water. (--) 9mm resin + water.

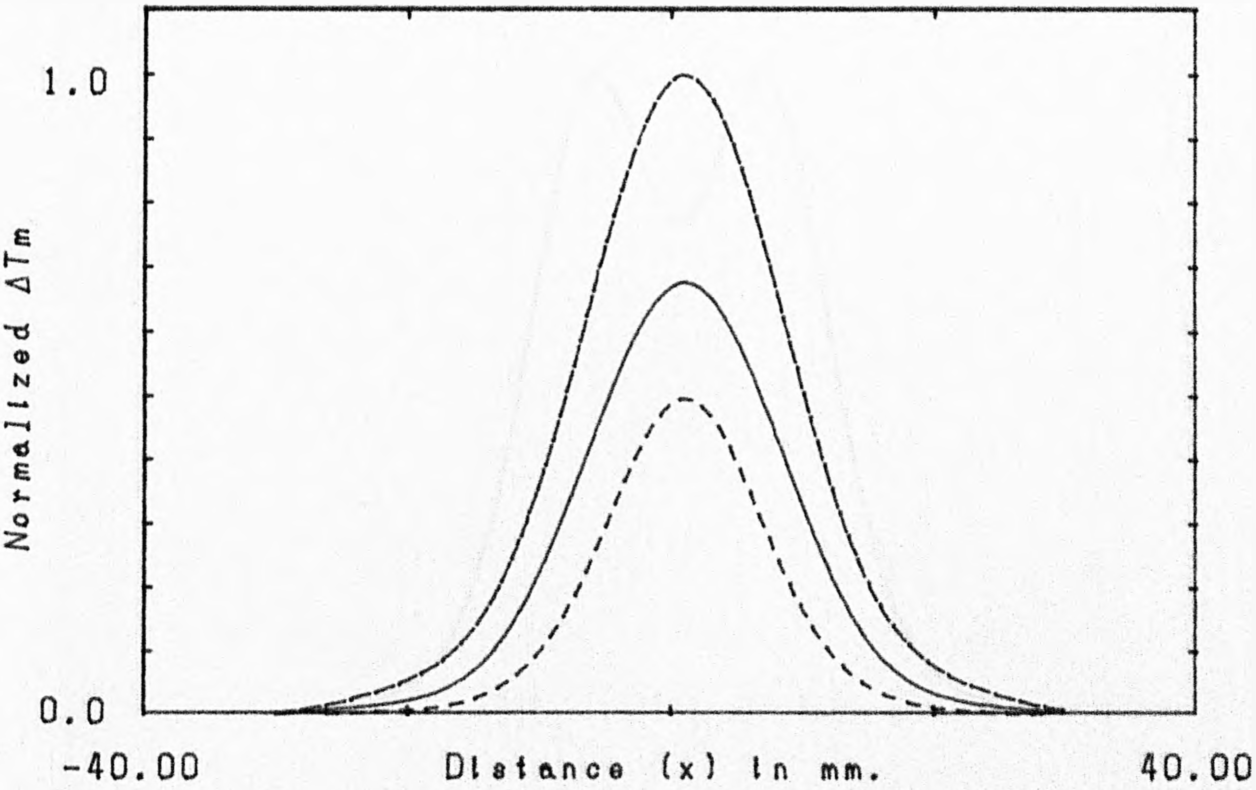

Fig.6.9b: Simulation of Fig.6.9a.

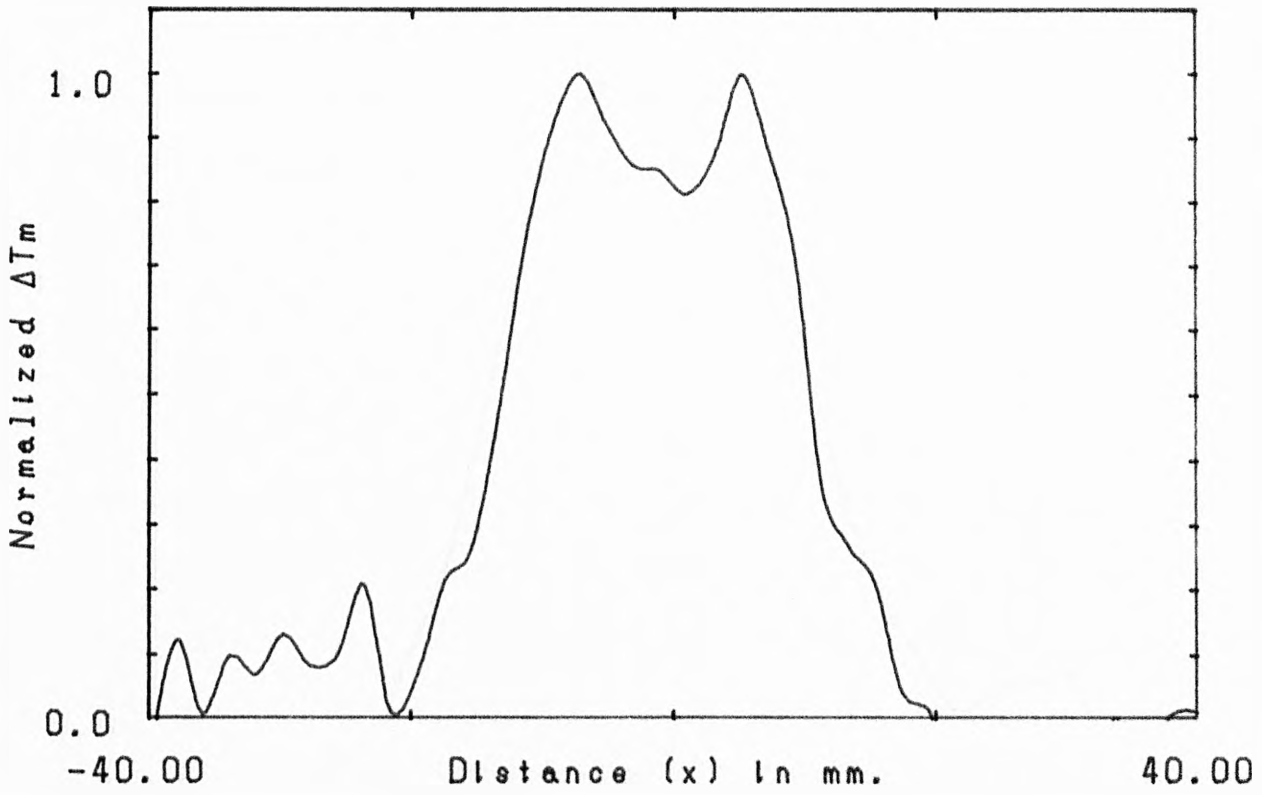

Fig.6.10a: Measured X scan in water.
Two tubes 9mm diameter seperated by 3mm
Z=10mm. ΔT=30 °C.

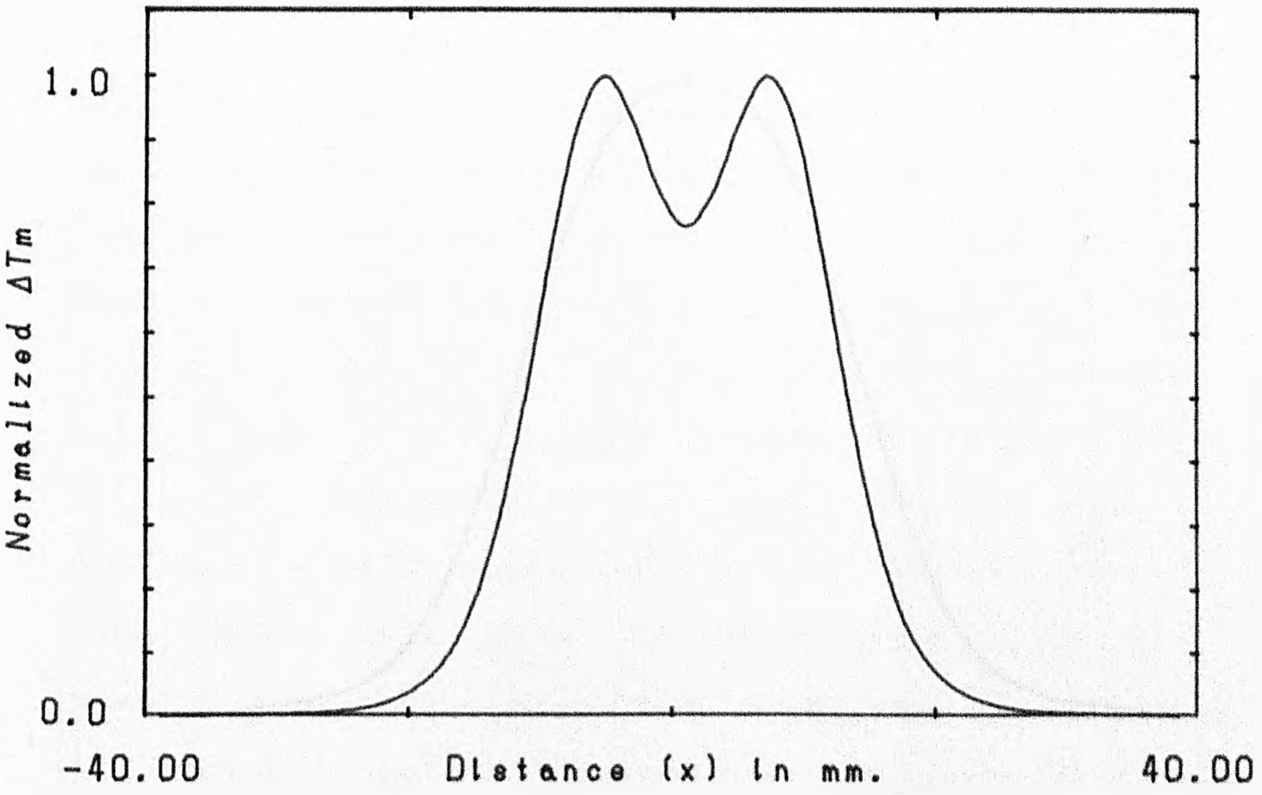

Fig.6.10b: Simulation equivalent to Fig.6.10a.

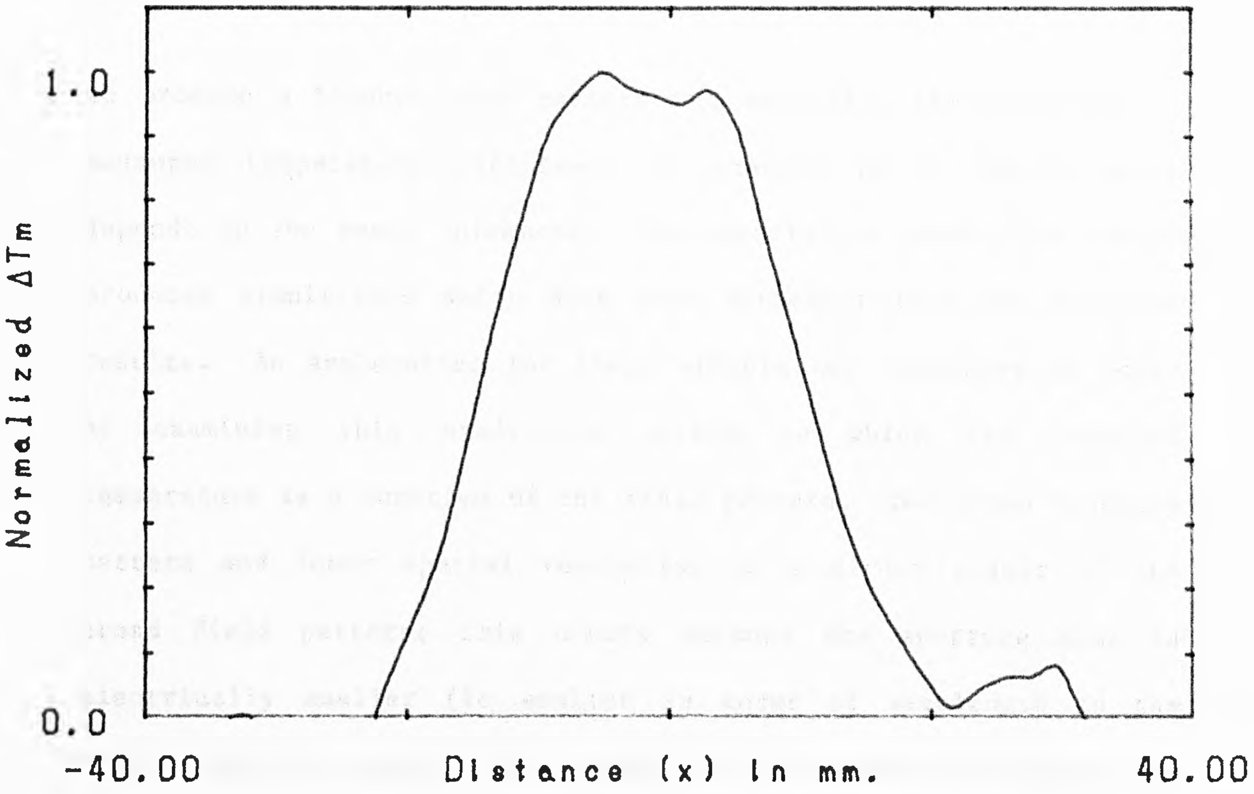

Fig.6.11a: Measured X scan in 9mm resin + water.
Two tubes 9mm diameter seperated by 3mm
Z=10mm. ΔT=30 °C.

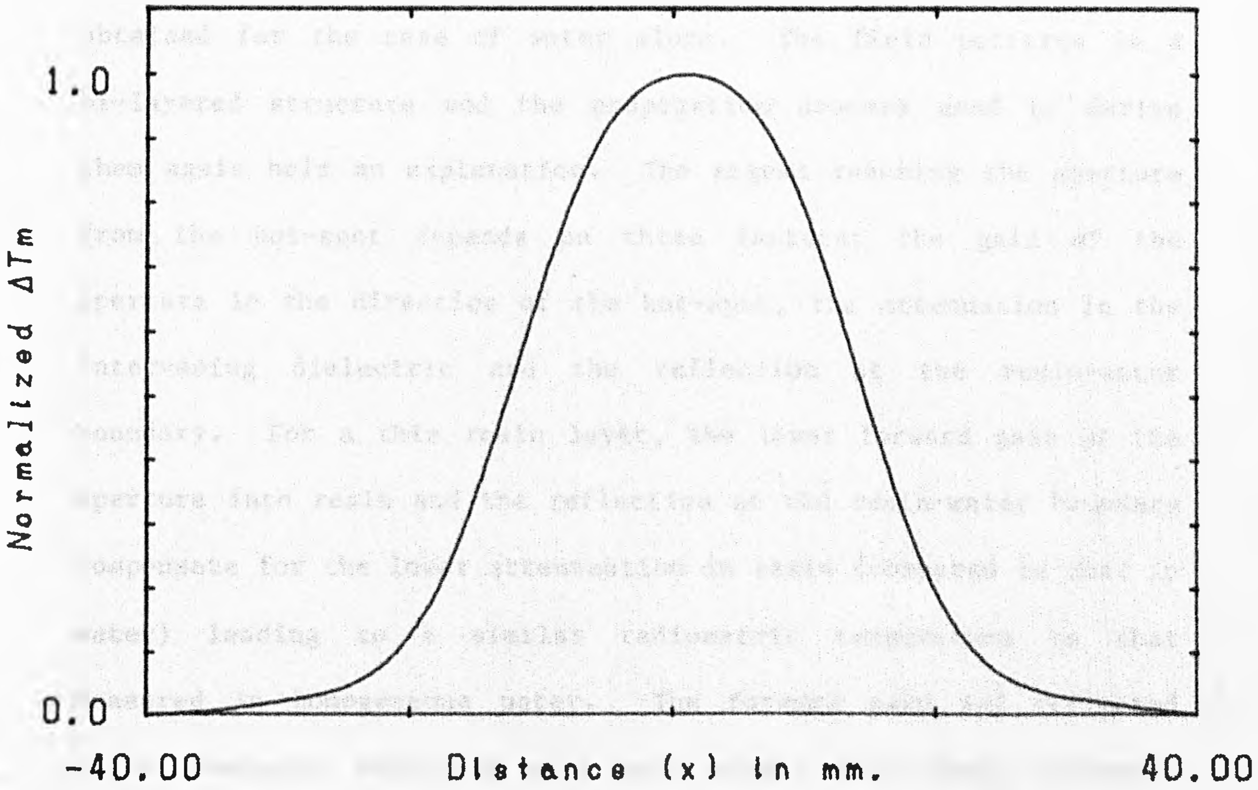

Fig.6.11b: Simulation equivalent to Fig.6.11a.

to produce a broader scan pattern and secondly, the amplitude of measured temperature difference is changed by an amount which depends on the resin thickness. The temperature prediction method produces simulations which show good agreement with the measured results. An explanation for these effects may therefore be found by examining this prediction method in which the received temperature is a function of the field pattern. The broad response pattern and lower spatial resolution is a direct result of the broad field pattern; this occurs because the aperture size is electrically smaller (ie smaller in terms of wavelength in the medium) when in contact with resin (fat) than when contacting the water (muscle). Figures 6.6, 6.8 and 6.9 demonstrate that resin layers of 3.5 mm and 4.5 mm thick have only a slight effect on absolute values of measured temperature. However, a thicker resin layer (Fig 6.9) leads to a measurement which is almost double that obtained for the case of water alone. The field patterns in a bi-layered structure and the propagation process used to derive them again hold an explanation. The signal reaching the aperture from the hot-spot depends on three factors; the gain of the aperture in the direction of the hot-spot, the attenuation in the intervening dielectric and the reflection at the resin-water boundary. For a thin resin layer, the lower forward gain of the aperture into resin and the reflection at the resin-water boundary compensate for the lower attentuation in resin (compared to that in water) leading to a similar radiometric temperature to that measured in homogeneous water. The forward gain and reflected field component amplitude vary more slowly with resin thickness compared to the decrease in forward attenuation for every millimetre of water replaced with resin. Consequently, for large resin thicknesses the lower attenuation leads to a higher radiometric temperature measurement compared to that found in homogeneous water.

The implications of these effects for clinical application of microwave radiometry are great. Simulation models for radiometric results have often, in the past, involved the assumption of homogeneous tissue. Results presented here show that such an assumption can lead to errors in measurement interpretation. An overlying layer of fat can lead to a hot volume below the fat appearing hotter and larger to the radiometer. The gain of the probe into the medium has also been shown to be important, influencing both the spatial resolution of the measurement procedure and the absolute value of temperature measured. Many temperature prediction models do not consider the effects of the measuring probe. In conclusion, the size, temperature and depth of a hot area cannot be estimated without knowledge of the intervening tissue structure and its electromagnetic interaction with the radiometric probe. Interpretation of radiometric results must take these factors into account.

Chapter 7

A feasibilty study of tomographic reconstruction of microwave radiometric data for thermal mapping during hyperthermia treatment

7.1 Proposal for a radiometric measurement system to monitor hyperthermia treatment

7.2 Back-projection algorithm for tomographic reconstruction of temperature difference data

- 7.2.1 Tomographic reconstruction by back-projection
- 7.2.2 An algorithm for reconstruction of radiometric data
- 7.2.3 Tomographic computer model

7.3 Measurement and reconstruction of experimental tomographic data

- 7.3.1 Measurement and reconstruction of elliptical scan data
- 7.3.2 Measurement and reconstruction of linear scan data

7.4 The feasibility of tomographic reconstruction of temperature distributions in the body

7.1 Proposal for a radiometric measurement system to monitor hyperthermia treatment

The safe and successful application of hyperthermia in the treatment of cancer relies on adequate monitoring of temperature throughout the heated volume. An ideal temperature monitoring system would combine non-invasive measurement with a tomographic thermal imaging capability. This chapter describes research into the feasibility of tomographic reconstruction of microwave radiometric data for thermal mapping during hyperthermia treatment [101] and also considers possible diagnostic applications.

The radiometric imaging system was proposed for use with a 2.45 GHz phased array deep hyperthermia system being developed at Sheffield University. Implementation of a tomographic monitoring system required consideration of certain aspects of the imaging method, and a number of initial system design features were established.

The imaging requirement was for only low spatial resolution; the purpose of the monitoring system was to confirm the correct location of the heated volume and check for unwanted hot-spots. Maximising the coupling of microwave power to the radiometer receiver required contacting probes. The number of probes which could be employed was therefore limited by their size. The sensitivity of radiometers to stray microwave radiation precludes simultaneous heating and radiometric measurement, as has been noted for other hyperthermia systems controlled by radiometry [24]. The applicator must therefore be switched off during the collection of temperature data. Consequently, minimising the duration of the measurement cycle was a requirement to maintain therapeutic temperatures within the treatment volume. High microwave component costs limited the number of radiometric receivers which could be employed. Switching between a number of probes connected to one receiver was considered. As a consequence the theoretical measurement time increased by a factor equal to the number of probes per receiver, plus an additional factor to compensate for the increase in system noise incurred by the inclusion of an extra lossy component (the multi-port switch) in the receiver front end.

These considerations led to a design for a system to monitor hyperthermia induced within the human lung, initially by a non-contacting phased array applicator. Fig 7.1a shows the system envisaged. The applicator consists of a remote array of dipole elements, each individually phase and amplitude controlled [15, 106]. To ensure minimum interaction between the applied microwave field and the radiometer probes, the latter were placed on the opposite side of the body from the applicator. The possible angular spread of radiometric data was thus restricted to less than 180°. The new version of the phased array system [107] employs contacting waveguide applicator elements. Placing of the radiometer probes was less restricted in this case due to reduced stray microwave fields. Fig 7.1b shows a possible arrangement for use with this contacting applicator system. The radiometer probes could be placed between the applicator elements, allowing data retrieval around the entire body section.

The monitoring process is intended to be carried out during pauses in the hyperthermia treatment, when the signal from each of the radiometer probes is sampled by switching to a radiometer receiver. The measured data is then computer processed using a tomographic algorithm to reconstruct a low resolution map of the temperature distribution within the image slice. The temperature

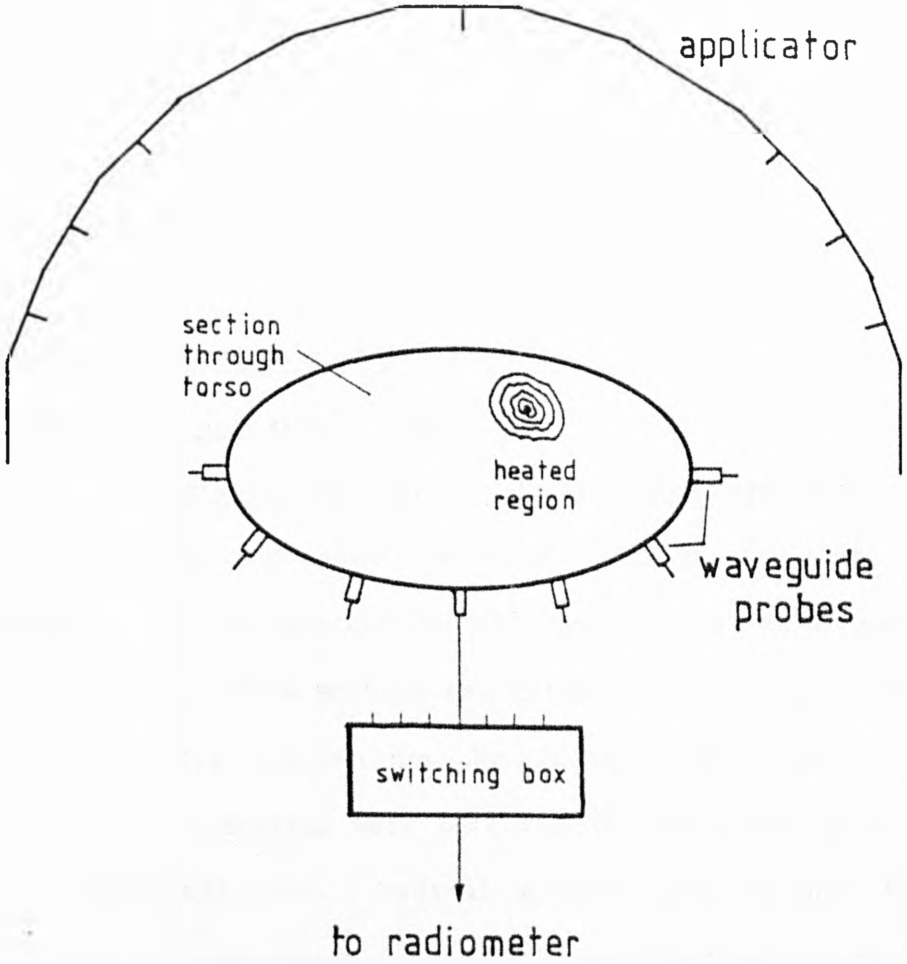

Fig. 7.1a Section through envisaged hyperthermia monitoring system showing configuration of radiometer probes and non-contacting applicator.

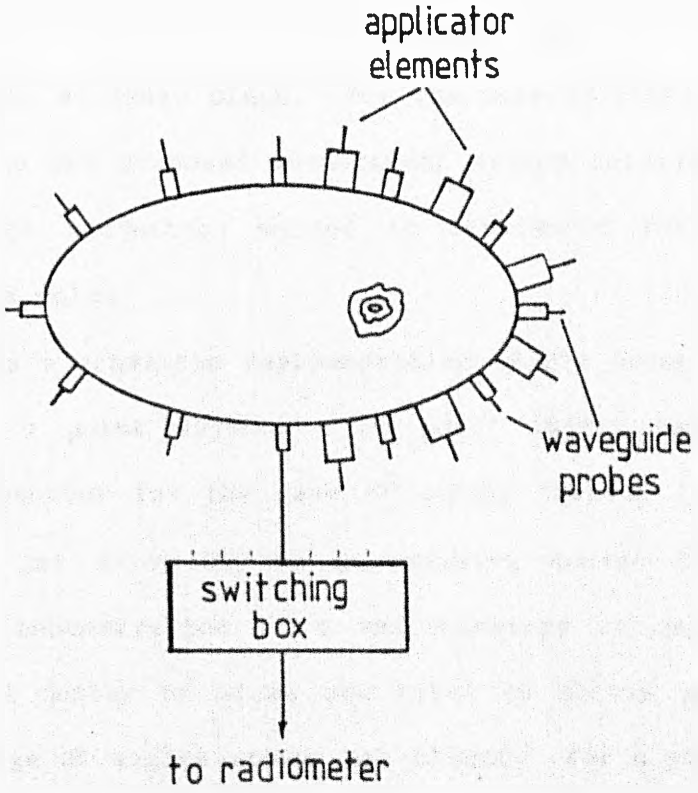

Fig. 7.1b Configuration for hyperthermia monitoring with contacting applicator elements.

map can then be used as feedback to correct the phase and amplitude settings of the applicator elements.

7.2 Back-projection algorithm for tomographic reconstruction of temperature difference data

7.2.1 Tomographic reconstruction by back-projection

The problem addressed in this section is that of the reconstruction of an internal distribution from a set of externally measured signals. This problem was first considered mathematically for straight line projections by Radon [108], and the first practical reconstructions were performed by Bracewell [109] in the field of radioastronomy. Medical applications include X-ray CT [110], Isotope γ-ray emissions [111], and NMR [112]. Tomographic techniques have also been applied to active microwave imaging using diffraction theory [113]. For these methods the problem is usually reduced to the two dimensional one whereby the reconstruction of a cross-section of an object is from straight line projections of this section onto an image plane. For the sake of simplicity, and to correspond to the proposed measurement system described in the # 7.1, the back projection method is considered for this two dimensional case only.

Fig 7.2a is a schematic representation of the process of data collection for a point object. The point object represents a scatterer or absorber for the case of active imaging (eg differential density for X-ray CT) or an emissive source for passive imaging (eg a concentration of a radio-isotope in gamma camera tomography). A number of views are taken to obtain projections from a full range of angles around the object. For a point object each projection consists of a delta function if infinitely narrow

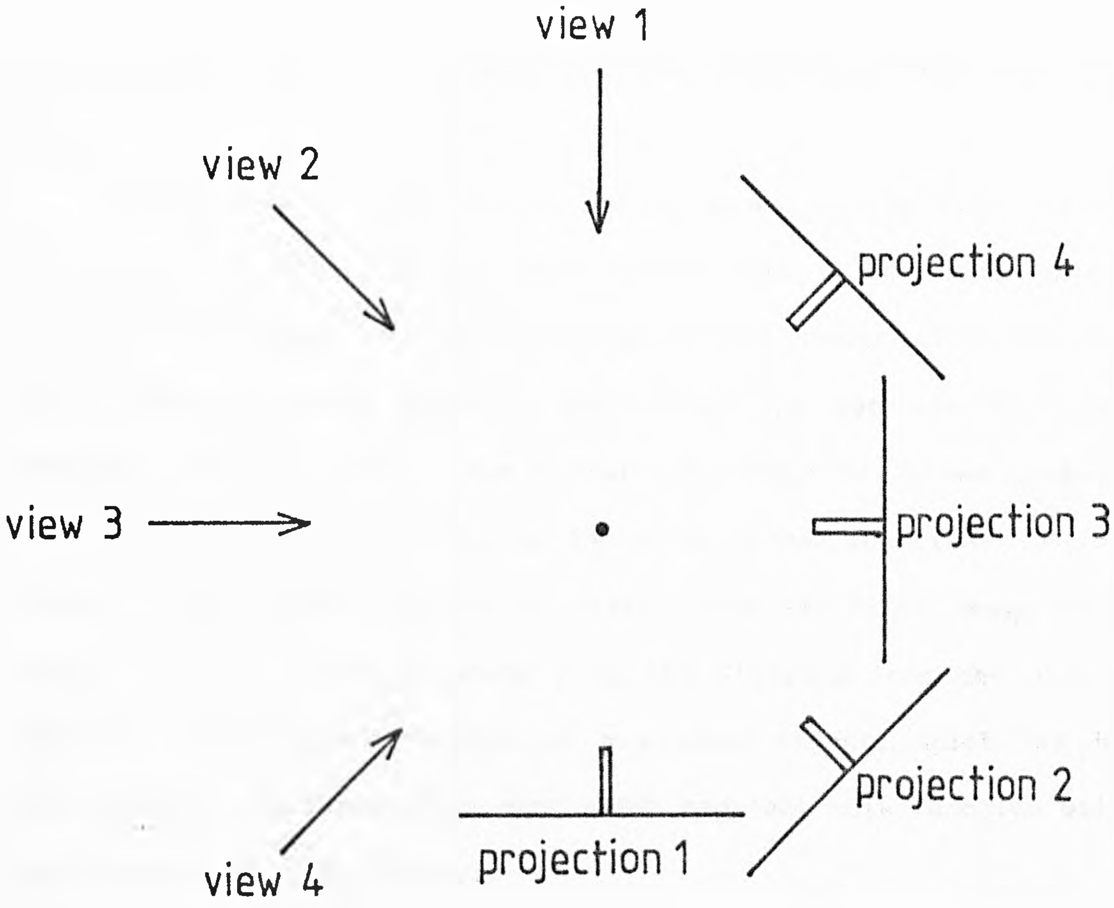

Fig. 7.2a Data collection process for four projections of a point object.

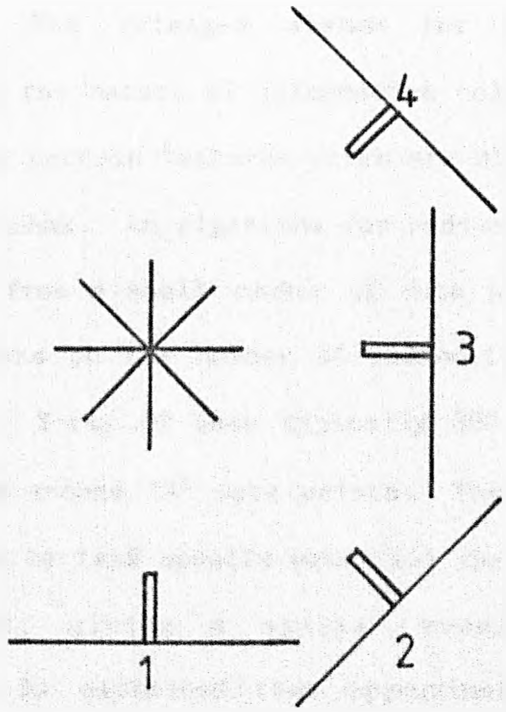

Fig. 7.2b Back projection of each view followed by summation to generate 'star-like' point spread function.

interrogating rays (active mode) and infinitely small detectors are assumed.

The process of back projection is shown in Fig 7.2b. Each projection is simply spread back across the object space in a direction orthogonal to the projections and summed with all the other back-projected views. The object is not reconstructed perfectly by this method, but a star-like image is formed centred on the object position, known as the point spread function. In the limit of an infinite number of views, this star-like image will tend to a 1/r function, where r is the distance from the object centre. In a reconstruction of a complex object, which can be considered to be formed from many point sources, this function will act to blur the final image.

7.2.2 An algorithm for reconstruction of radiometric data

The concept of tomographic reconstruction by back projection forms a starting point for the design of a reconstruction algorithm for radiometric data. The evisaged system for monitoring hyperthermia treatment and the nature of information collection by microwave radiometry impose certain features which are different to standard tomographic algorithms. An algorithm for radiometric data must allow reconstruction from a small number of data points, due to the physical restrictions on the number of radiometric probes discussed in section 7.1. X-ray CT uses typically 300 detectors and 300 views resulting in around 10^5 data points. The number of pixels displayed is limited by (and usually equal to) the number of independent measurements, giving a spatial resolution of approximately 2 mm. It is estimated that approximately sixty radiometric probes would fit around the human thorax and so a spatial resolution of no better than 5 cm can be expected.

Because of the requirement for contacting probes the scanning method of data collection cannot be employed. The data must be reconstructed from a number of individual point measurements sampled from locations on the outer contour of the slice to be imaged. This arrangement cannot be constrained to a circular geometry which is the usual practice for tomographic reconstruction, but must take on the geometry of the particular body shape under investigation. The algorithm must therefore be able to deal with random positioning and orientation of the detectors. In addition, the detection beam area (ie the area from which information is gathered) of the probes cannot be specified as precisely as for X-ray CT, so the algorithm must cope with a variety of beam shapes. Successful monitoring of hyperthermia treatment entails measurement of temperature change as the therapy progresses. The reconstruction algorithm must therefore have the ability to image the change in temperature between the present distribution and a previously measured distribution.

With reference to Fig 7.1, initially, each probe is sampled to give a data set for the natural temperature distribution of the body. A second data set for the new temperature distribution is taken after the application of hyperthermia treatment. Both sets of data are utilized by the computer algorithm, together with the positions, orientations and beam shapes of each probe. The measured data is processed by the method described below.

For each data point, the initial measured value is subtracted from the second measured value to give the radiometric temperature change as measured by each probe. This temperature difference is then back-projected into a beam shape which approximates the probe detection area. The reconstructed value at each pixel is given by the sum of the back projected difference data of all probes that are capable of 'seeing' that pixel. To reduce the point spread function, a secondary procedure is carried out. Each data point is checked for a 'no change' condition. This occurs if the probe has been unable to detect a temperature increase within its detection area, that is if the measured temperature difference is lower than the uncertainty in the radiometer measurement (# 5.3.2). If this 'no change' condition has occurred for a particular probe, each pixel within its back-projected beam area is reassigned a zero value. The blurring of the image due to the back projection process is reduced. In addition, making use of temperature difference data gives a reconstructed distribution which is a picture of temperature change.

7.2.3 Tomographic computer model

A computer simulation of the data collection and reconstruction procedures was carried out in order to test and refine the reconstruction algorithm. The programme initially requests the contour shape of a two-dimensional slice through the body, the number of probes to be considered, and the beam shape. All examples given here consider the body contour as an ellipse with dimensions 40 cm by 20 cm, which is an approximation to a transverse slice through the human torso. The position and orientation of each probe is then calculated. For the purpose of simplifying the model, a homogeneous tissue medium was assumed. Two different representations of beam shape were used. Firstly, the probe was assumed to have a fan beam detection area with a field of view limited by an angle θ, the probe only receiving from the area subtended by this angle (Fig 7.3). The second beam shape considered was a rectangular one (Fig 7.4).

The first phase of the programme simulates the data collection process. Matrix points within the body are assigned an initial temperature value T_{i1}. The temperature measured (T_j) at each radiometer probe j is then given by

$$T_{j1} = \frac{\sum_i (T_{i1} \exp(-\alpha Z_i) \cos^2\pi \cdot \frac{X_i}{w})}{\sum_i (\exp(-\alpha Z_i) \cos^2\pi \frac{X_i}{w})}$$

where the summation is performed for those matrix points within the beam.

X_i, Z_i and w are shown in Fig 7.3 and 7.4 and α is a power attenuation coefficient. This equation gives a good approximation to the radiometric temperature measured by a waveguide probe contacting a high loss homogeneous medium for an appropriate value of α, especially for a rectangular beam shape [50]. The matrix points are then assigned a new temperature distribution which includes a hot-spot and the process is repeated to calculate the data set T_{j2}.

The second phase of the programme is the reconstruction algorithm. The temperature change measured at each probe ($T_{j2} - T_{j1}$) is back projected into each probe's beam shaped and summed to give a reconstruction of the heated region. The value reconstructed at each pixel (R_i) is given by

$$R_i = \begin{cases} \sum_j (T_{j2} - T_{j1}) & \text{if } T_{j2} - T_{j1} > \Delta T_u \\ 0 & \text{if } T_{j2} - T_{j1} < \Delta T_u \text{ for any j} \end{cases}$$

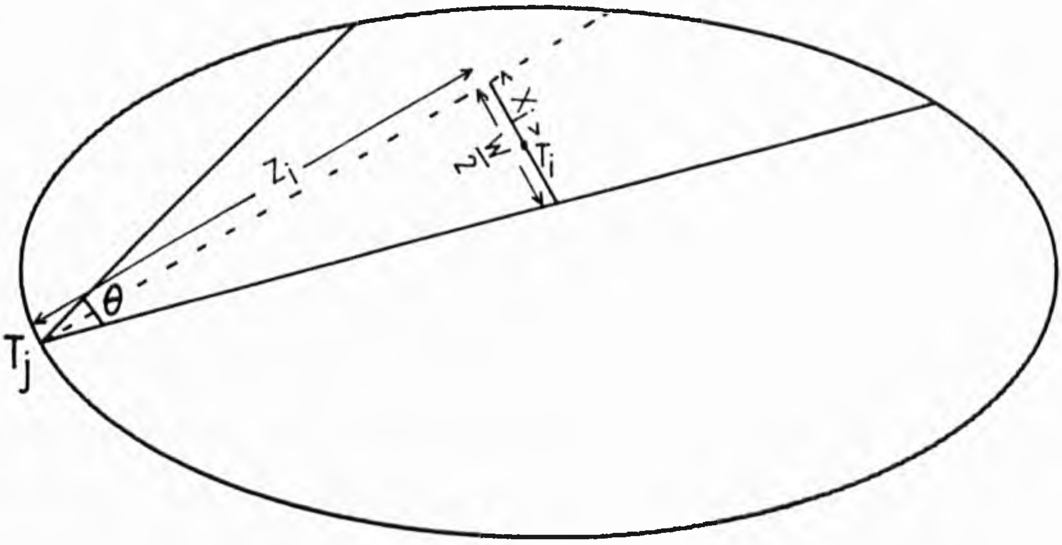

Fig. 7.3 Computer model geometry with fan beam detection area.

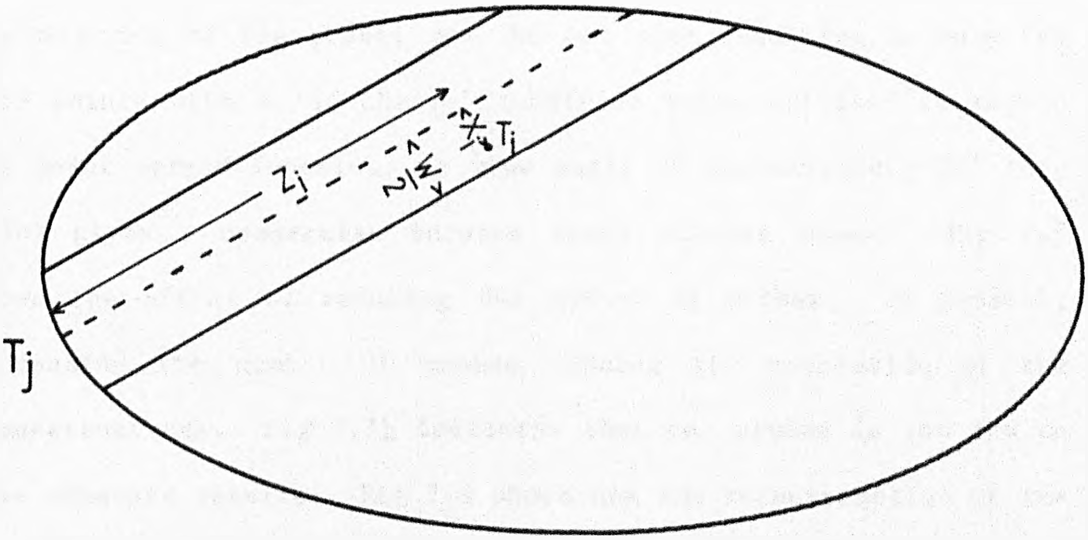

Fig. 7.4 Computer model geometry with rectangular detection area.

where the summation is carried out over those probes for which the pixel i is inside the beam and ΔT_u is the uncertainty in the measured radiometric temperature.

Reconstructions were performed, using a fan beam shape, for a number of different situations. In each of the following sets of reconstructions, Figs 7.5 to 7.9, the effect on the quality of reconstructed image for a single hot-spot, caused by varying a measurement parameter, is investigated. Fig 7.5a shows the input distribution and Fig 7.5b is an image produced using the default measurement parameters. Fig 7.6 shows the effect of varying the view angle. A small view angle ($\theta = 10°$) produces some noise outside the reconstruction area. This is because the probe views do not cover the full reconstruction area and so the secondary procedure designed to reduce the point spread function cannot operate efficiently. At the other extreme, with a probe view of 60°, the secondary procedure again cannot work efficiently because the majority of the probes see the hot spot resulting in only few data points with a 'no change' condition being utilized to reduce the point spread function. A view angle of approximately 20° (Fig 7.5b) gives a compromise between these extreme cases. Fig 7.7 shows the effect of reducing the number of probes. In general, decreasing the number of probes reduces the resolution of the reconstructions. Fig 7.7b indicates that ten probes is too few to give adequate results. Fig 7.8 shows how the reconstruction of the hot-spot deteriorates as the attenuation of the medium increases. The reason for this is that as the attenuation is increased, more of the measurement points fall within the 'no change' condition and the points within their beams are set to zero. In Fig 7.9, the attenuation remains constant and the theoretical temperature

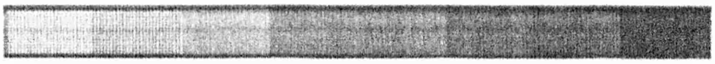

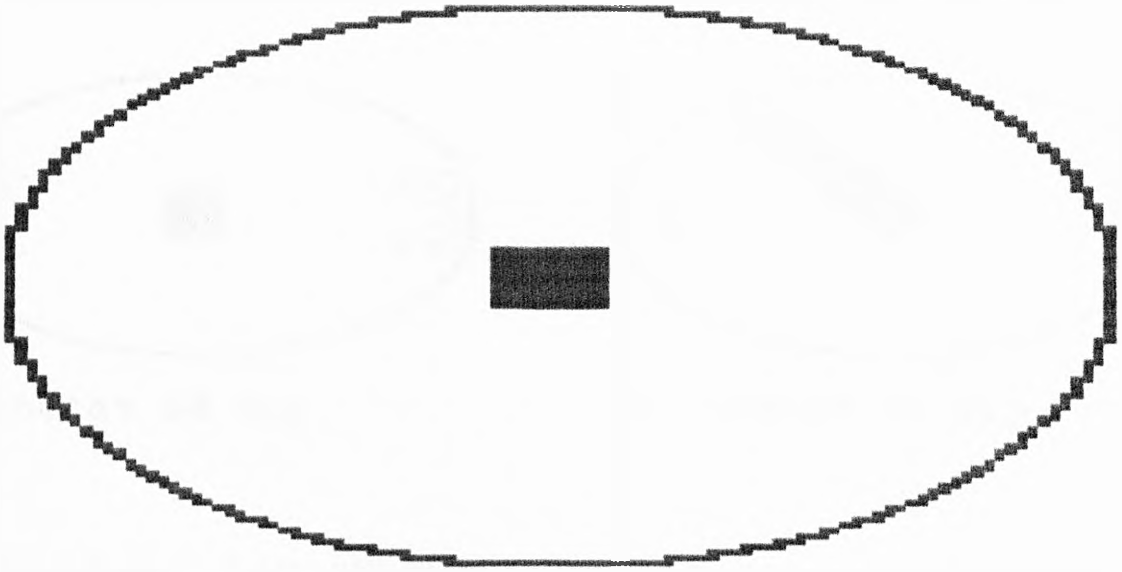

Fig 7.5a Input distribution for Figs 7.5b to 7.9

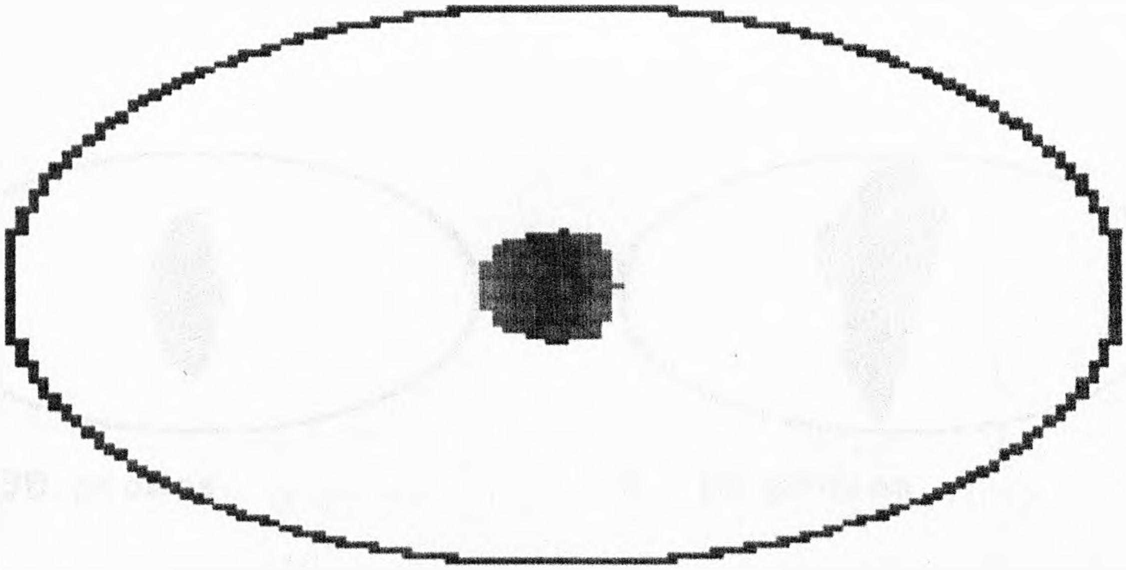

Fig 7.5b Reconstruction using the default parameters

The parameters for this figure and all other figures are, unless otherwise stated :-

View angle (theta) = 20 degrees

Number of probes = 60

Attenuation factor (alpha) = 12 Np/m = 110dB/m

Radiometer measurement uncertainty (delta Tu) = 0.001

Each grey level represents a drop of 10% from max. value

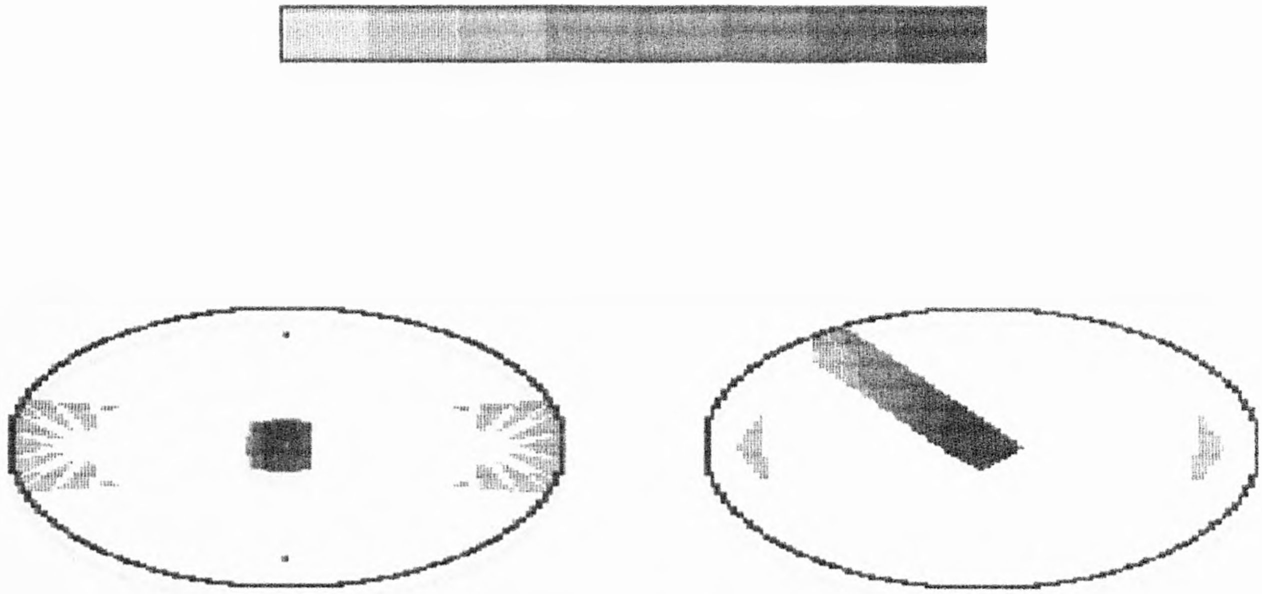

a. theta= 10 deg.

b. theta= 60 deg.

Fig 7.6 Influence of the view angle

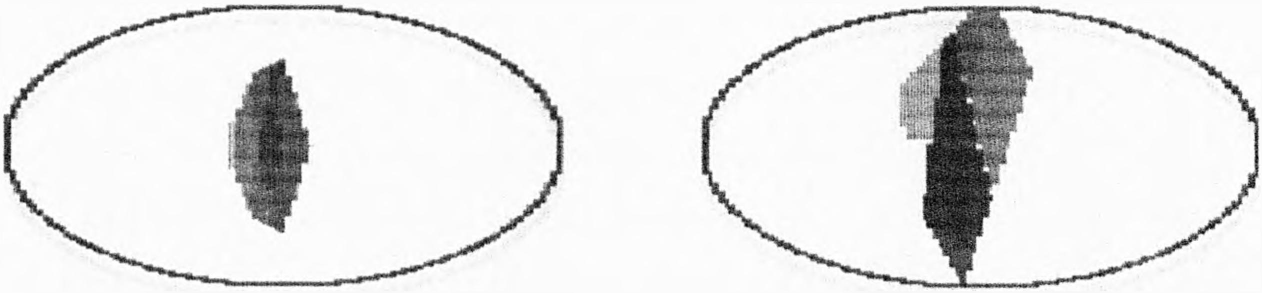

a. 30 probes

b. 10 probes

Fig 7.7 Influence of the number of radiometer probes

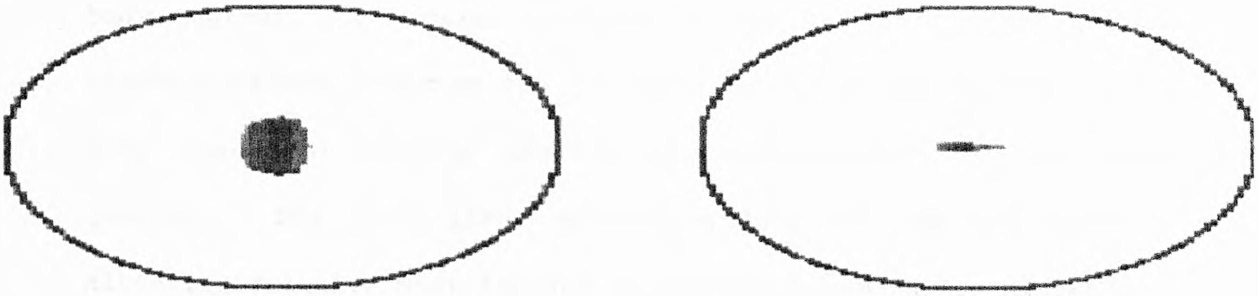

a. alpha= 36 Np/m b. alpha= 48 Np/m

Fig 7.8 Influence of attenuation of medium

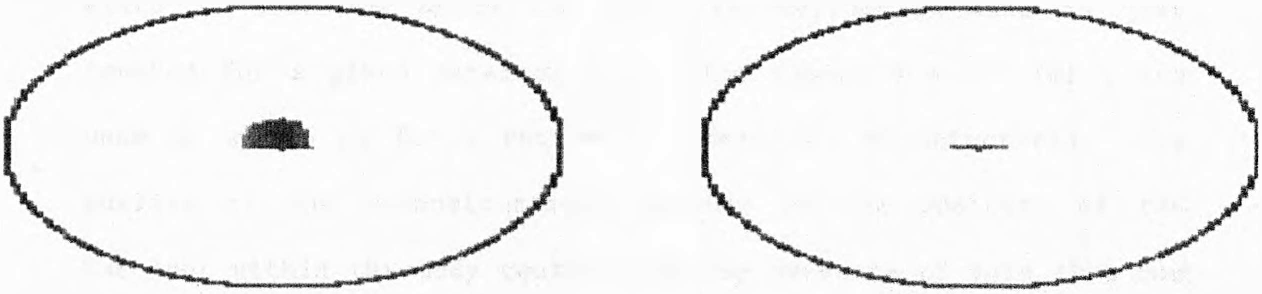

a. delta Tu = 0.05 C b. delta Tu = 0.1 C

Fig 7.9 Influence of the radiometer's measurement uncertainty, delta Tu resolution of the radiometer is reduced. The same deterioration of image can be seen. Fig 7.10 shows the sensitivity of the reconstruction algorithm to the position of the hot spot within the body contour. A central position within the body gives optimum reconstructions. Moving the hot-spot closer to the surface of the body leads to varying degrees of deterioration in the image quality. Fig 7.11 gives reconstructions of two hot-spots in differing relative position and at different separation distances.

Fig 7.12a is reconstructed from 30 data points confined to the underside of the body only. Fig 7.12b is reconstructed assuming a rectangular beam shape.

Some general observations may be deduced from these figures. Due to the small number of measurement points, the probe receiving pattern must not be too directive otherwise the whole reconstruction volume is not sampled. Too broad a receiving pattern leads to deterioration of image resolution. The ideal beam width is that for which the whole reconstruction area is just covered for a given detector separation (about $\theta = 20°$ for a fan beam or $w = 3$ cm for a rectangular beam for 60 detectors). The quality of the reconstructions depends on the position of the hot-spot within the body contour and the presence of more than one hot area leads to a deterioration of the imaging capability. The attenuation values considered give an estimated range of plane wave attenuation values for inflated lung. Even the lowest attenuation shows some breakdown of the image of a central hot-spot when a realistic value for radiometer temperature resolution is considered. From these results it was concluded that experimental verification of the imaging techniques for a realistic situation was necessary.

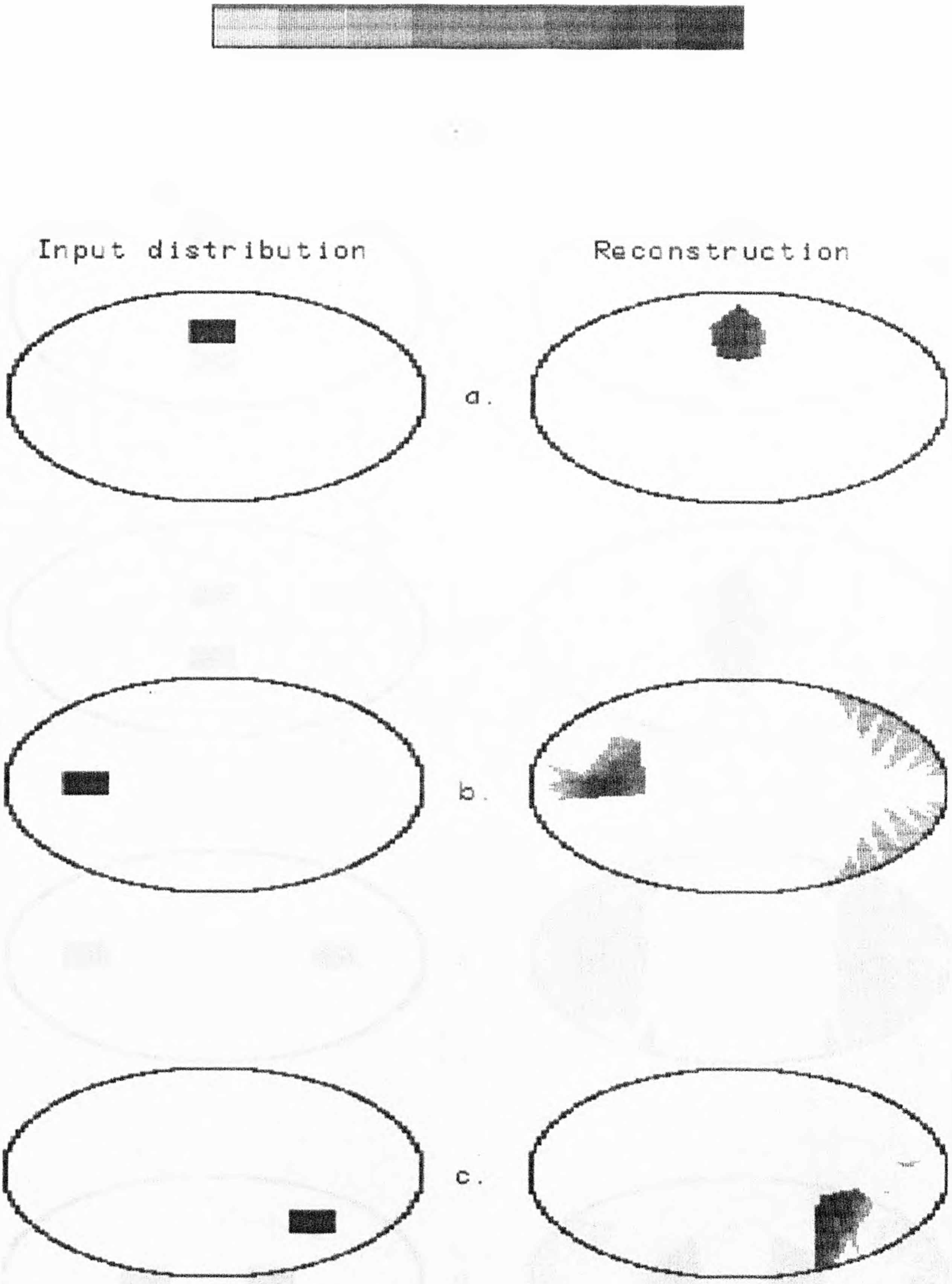

Fig 7.10 Reconstructions for different positions within body contour

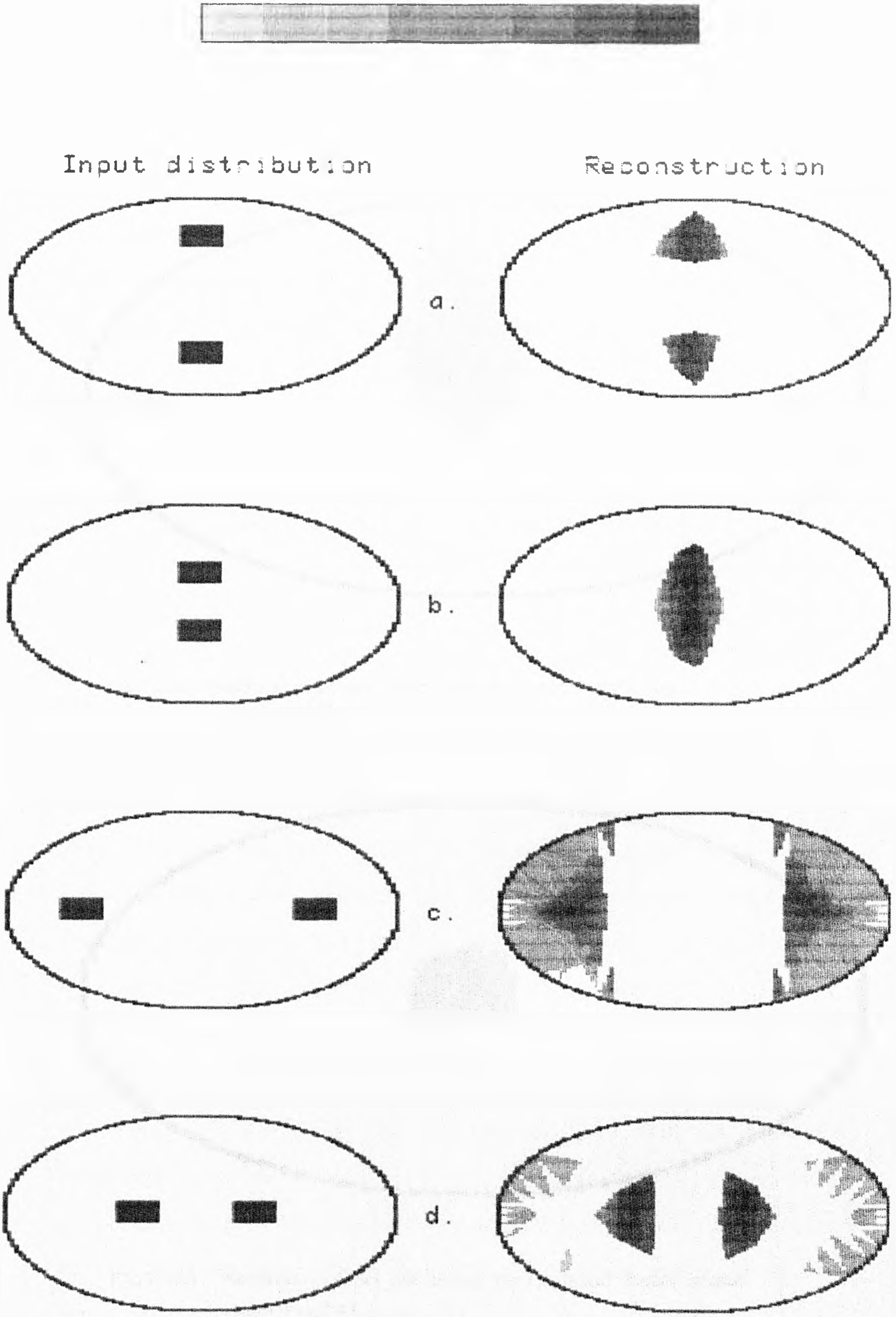

Fig 7.11 Reconstructions of two hot-spots

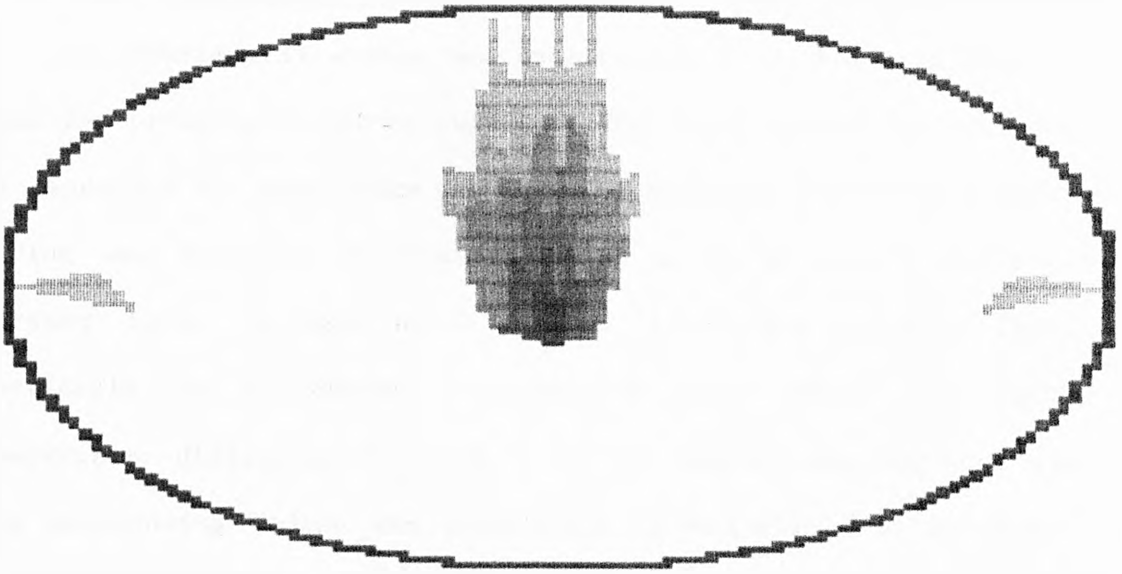

Fig.7.12a Reconstruction from semi-elliptical data set (see Fig.7.1a)

Fig.7.12b Reconstruction assuming rectangular beam shape (see Fig.7.4)

7.3 Measurement and reconstruction of experimental tomographic data

7.3.1 Measurement and reconstruction of elliptical scan data

An experimental system was constructed to collect radiometric data for tomographic reconstruction. The first system was designed to reproduce the simulation model. The hot area buried in a lossy medium was modelled experimentally by a 10 mm inside diameter perspex tube, through which heated water was pumped, fixed vertically in a constant temperature water bath. A large temperature difference ($T_1 - T_0 = 40$ °C) between the hot-spot and the surrounding medium was maintained to maximise data accuracy. The measurements were performed by moving a single radiometer probe within the water bath, around the circumference of an ellipse with the hot tube at its centre by means of a scanning frame. The probe was attached to the scanning frame by a rotatable arm designed to allow precise positioning and orientation of the probe aperture (Fig 7.13a). The movement of the scanning frame was effected by computer-controlled stepper motors; the programme used for tomographic scanning was the 'pre-set position' scanning routine (see Appendix 2). A set of coordinates for sixty locations around the circumference of an ellipse were entered into the BBC microcomputer. At each of these pre-set positions, the appropriate orientation of the probe was calculated, such that the aperture plane lay along the tangent to the circumference of the ellipse (see Fig 7.13b). The orientation angle was set manually, by means of the rotating arm. The radiometric temperature was measured and the probe was then moved to the next position. With this method it was possible to model experimentally the situation where a maximum of sixty probes were arranged around the outer contour of an

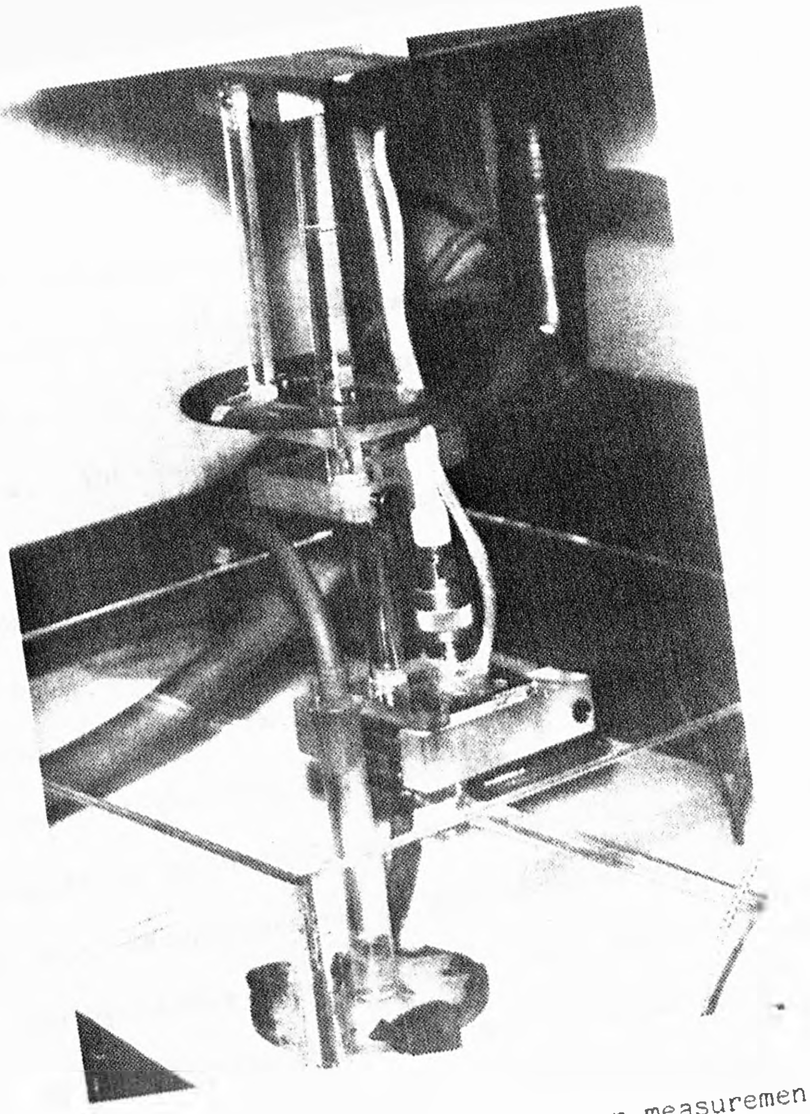

Fig. 7.13a Set-up for elliptical scan measurements.

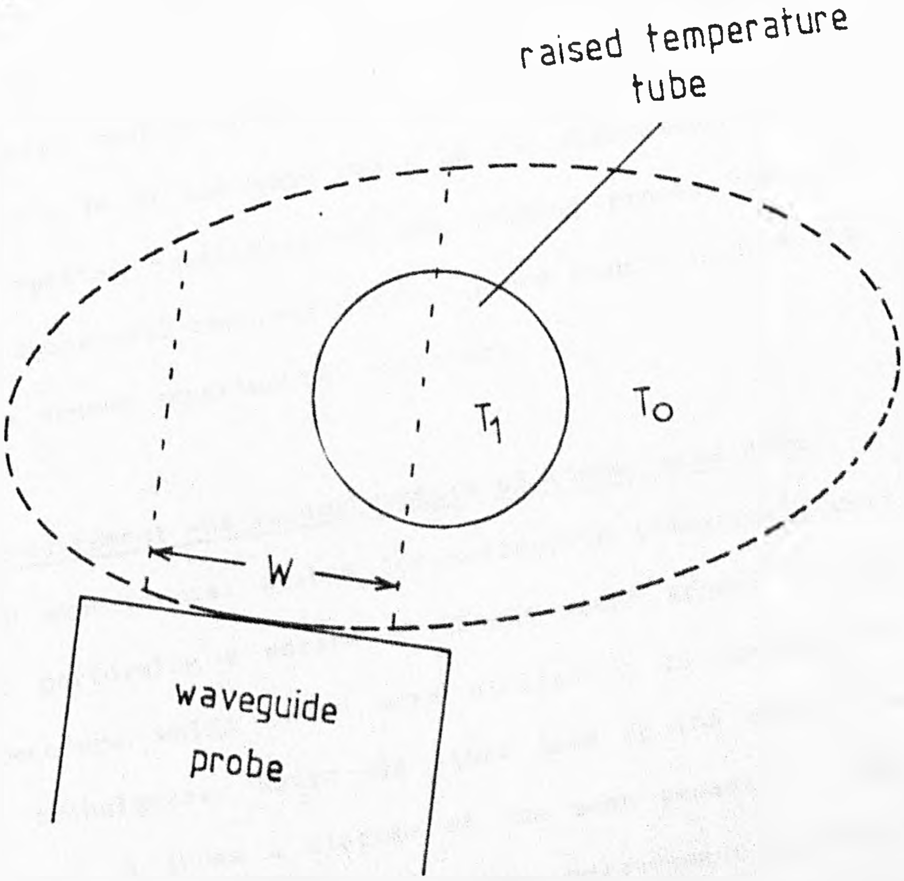

Fig. 7.13b Geometry of the elliptical scan experiment in water, also showing approximation for detection area.

elliptical body of homogeneous lossy tissue by scanning a single probe. Results from initial scans indicated the limitations, set by the high attenuation of microwave signals in water, on the maximum scan area. The largest size of ellipse considered had a semi-major axis of 2 cm.

Before reconstruction could be carried out, an estimate of the reconstruction beam shape was required. Linear scan measurements of the hot tube in water (a procedure which was described in Chapter 6) showed that the detection area (and thus the beam shape) could be approximated by a rectangular shape (Fig 7.13b) with a width w = 10 mm. Reconstruction of the measured data failed to retrieve a recognisable hot-spot for any size of ellipse considered. An explanation for this can be found by comparing Fig 7.13b with 7.4. The success of the simulated reconstructions relied on a narrow beam shape, compared to the dimensions of the reconstruction area. For the experimental case, the high attenuation of water restricts the size of the reconstruction area and the beam width is of the same order as the dimensions of the ellipse. The spatial resolution of the imaging process is not sufficient for successful reconstruction. These results led to the initiation of a second experimental procedure.

7.3.2 Measurement and reconstruction of linear scan data

A second experimental system for collecting tomographic data consisted of performing a series of linear scans around the hot tube, a procedure which bears more similarity to conventional tomographic techniques. Water was again used as the measurement medium. Fig 7.14 shows a diagram of the scan geometry. Eight linear scans were performed with fifteen measurement points per

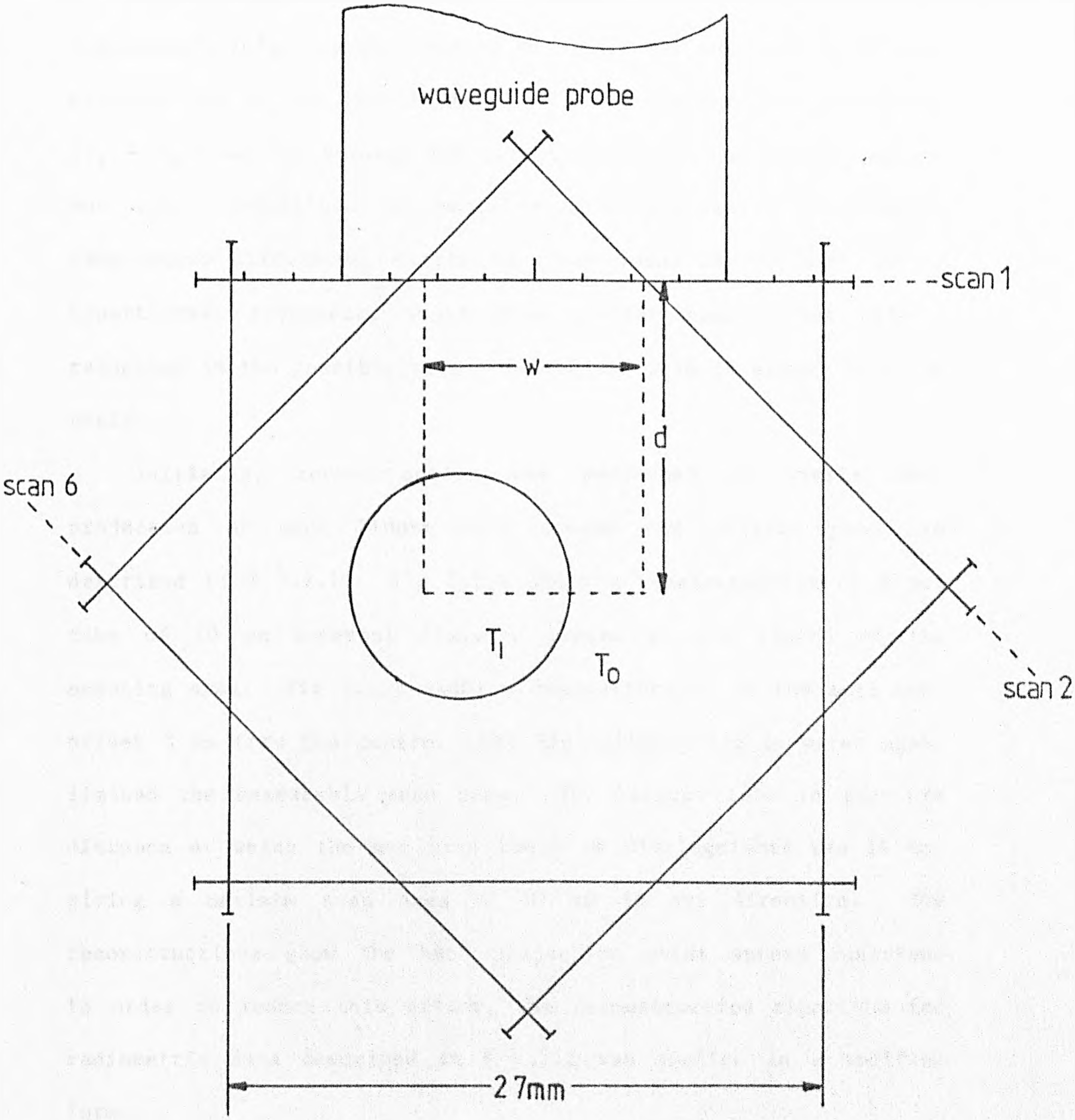

Fig. 7.14 Geometry of the tomographic linear scan experiment in water, also showing effective detection area of waveguide probe.

scan with a point separation of 2 mm. The measurements were taken in two stages. Firstly, the scans were performed with the hot-spot at the same temperature as the surrounding medium. The constant temperature reference scan served to check that no matching changes occurred due to the plastic tube. A large temperature difference ($T_1 - T_0$ = 40 °C) between the hot-spot and the surrounding medium was again maintained to maximise data accuracy. A smaller temperature difference, closer to those found in the body during hyperthermia treatment, would give similar results but with a reduction in the possible scan area and decrease in signal to noise ratio.

Initially, reconstruction was performed by simple back projection of each linear scan across the object space, as described in # 7.2.1. Fig 7.15a shows a reconstruction of a hot tube of 10 mm internal diameter placed at the centre of the scanning area. Fig 7.15b shows a reconstruction of the same tube offset 3 mm from the centre. The high attenuation in water again limited the measurable scan area. The largest tube to aperture distance at which the hot area could be distinguished was 14 mm, giving a maximum scan area of 27 mm in any direction. The reconstructions show the back projection point spread function. In order to reduce this effect, the reconstruction algorithm for radiometric data described in # 7.2.2 was applied in a modified form.

Two different beam shapes were defined, depending on whether the hot-spot was detectable at a given scan position. The basis of these beam shapes was the effective detection area, defined as the area in front of the probe within which a hot-spot would give a detectable response (ie a response greater than the measurement

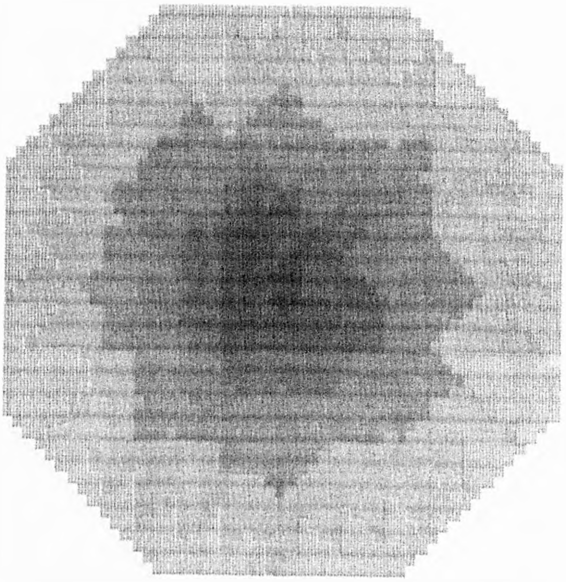

Fig.7.15a Reconstruction of tube at centre by simple back projection

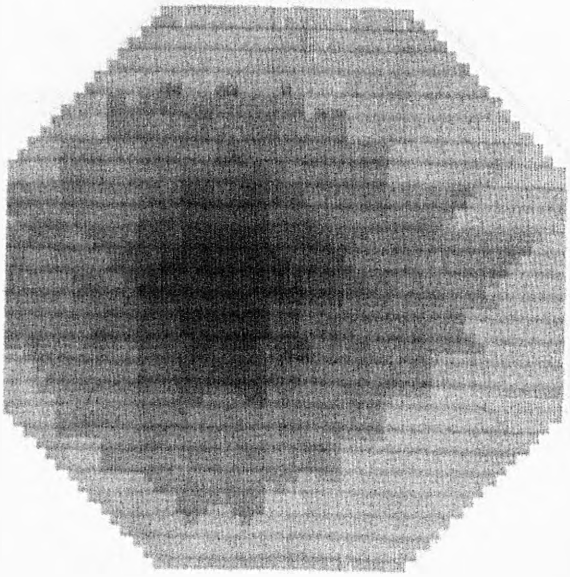

Fig.7.15b Reconstruction of tube offset to left by simple back projection

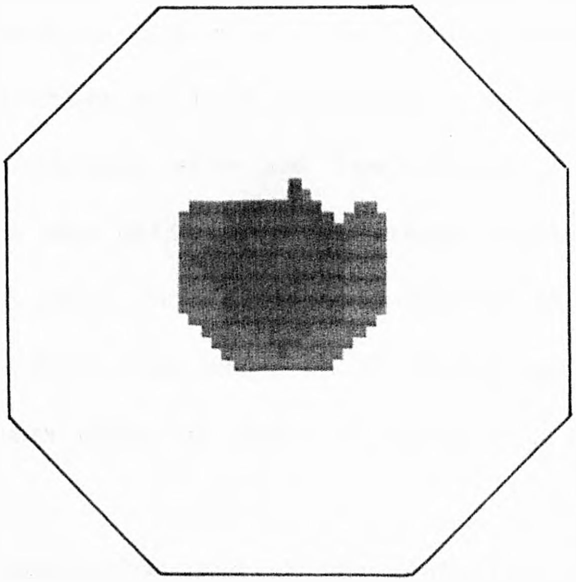

Fig.7.16a Reconstruction of tube at centre using modified algorithm

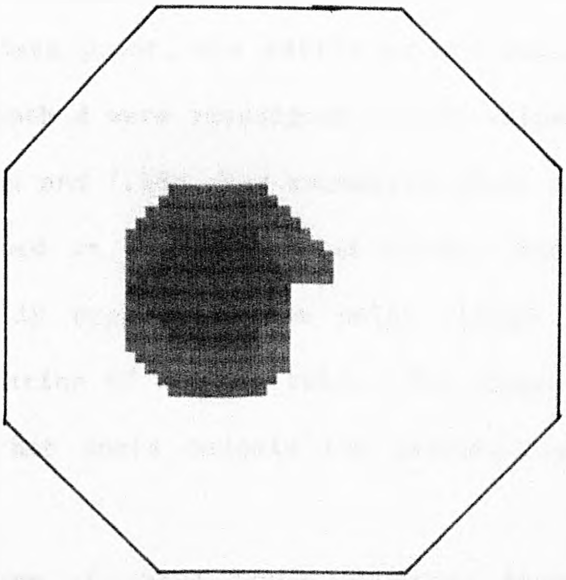

Fig.7.16b Reconstruction of tube offset to left using modified algorithm

uncertainty (see # 6.1.2)). The primary factors which determine the detection area are the permittivity of the measurement medium, the probe aperture dimensions and the frequency of operation. However, definition of this detection area assumes some a priori knowledge of hot-spot size and temperature. For this case, the detection area was estimated from linear radiometric scans of the hot tube which gave, for an aperture size of 16 mm x 8 mm in water, an effective detection area which could be approximated by a rectangular beam shape of width 10 mm (w = 10 mm) and depth 14 mm (d = 14 mm).

The reconstruction process was equivalent to that used in the computer simulations but employed two beam shapes. The measured temperature difference ($T_j - T_0$) at each data point was back-projected into a strip of width w which extended across the image plane (Fig 7.14). If the 'no change' condition ($T_j - T_0 < \Delta T_u$) existed at a data point, the matrix points inside the beam area of width w and depth d were reassigned a zero value.

Figs 7.16a and 7.16b show reconstructions of the same measured data as was used in Figs 7.15a and 7.15b. The modified algorithm has successfully suppressed the point spread function, giving a good representation of the hot tube. The assymetrical shape of the reconstructed hot spots reveals the sensitivity of this algorithm to noise.

The success of these reconstructions depends largely on the appropriate assignment of the parameters d and w. Altering these parameters would adversely affect the image, giving the correct position for the hot-spot but incorrectly estimating its size. Calculation of these parameters is possible by employing the temperature prediction method, applicable for homogeneous or layered media, although a priori knowledge of the hot-spot temperature and size is necessary. However, estimating these factors for a given situation should allow reasonable estimates of d and w to be obtained.

7.4 The feasibility of tomographic reconstruction of temperature distributions in the body

The ability to reconstruct both body contour geometry and linear scan data is predominantly influenced by the receiving pattern of the radiometric probe. Experimental measurements illustrate the importance associated with the depth of maximum sight ('view depth') of the probe in a lossy medium. In practice, tomographic data is available from small areas only; the view depth places an upper limit on the area which can be reconstructed.

Simulation of tomographic reconstruction for a body contour geometry have established that the computer algorithm is capable of providing a low resolution map of internal differential temperature from a relatively small number of external radiometric measurements. The relationship between detection area and image resolution is complex. Although image resolution improves with decreasing beam width, reduced area coverage can lead to higher background noise (Fig 7.6). Experimental elliptical scans have shown, however, that the beam width is of the same order as the maximum scan dimensions giving a spatial resolution which is too poor to allow successful reconstruction. Although a lower radiometric operating frequency or larger aperture size would allow data to be collected from greater depth, the spatial image resolution would also diminish, giving no advantage over the present case. In conclusion, due to the unsuitability of the detection area found for apertures contacting lossy media, reconstruction from body contour measurements does not appear to be feasible for temperature mapping in the human body.

Tomographic measurement by linear scanning allowed reconstruction of a hot tube for small scan areas. The number of measurements required, however, was twice the maximum considered for body contour measurements, leading to a data collection time with the present radiometer of at least fifteen minutes. These factors, together with the requirement for a complete circumferential data set, would seem to preclude use of this technique for hyperthermia monitoring.

An alternative application may be in diagnostic radiometry. Reconstruction of larger scan volumes is feasible by employing lower frequency measurements, although at the cost of poor spatial resolution. Additional problems are inevitable in a clinical situation. A matching medium would be required in which to move the probe, further attenuating the emitted signal. Linear scanning over a curved body surface would no longer allow the simplifying assumption of a homogeneous medium, or even parallel dielectric boundaries. Assignment of reconstruction beam shape to each scan point would be a formidable task. Simple back projection algorithms may be more appropriate. Despite these problems, linear radiometric scanning for tomographic imaging cannot be ruled out as a diagnostic technique. A possible clinical application, due to the small scan area involved, is the imaging of a limb submerged in a matching medium to locate, for example, the site of a thrombosis.

Chapter 8

Conclusions

Non-invasive temperature measurement, both absolute and differential is recognised as an important objective in medicine for diagnostic applications and for monitoring of hyperthermia treatment. This study has assessed the capability of microwave radiometry for imaging subcutaneous thermal structures and has provided a means for interpretation of radiometric data in terms of internal temperature distribution.

Interpretation of radiometric signals via the propagation of microwave radiation through lossy tissue has been achieved by developing a spectral diffraction algorithm employing the computationally efficient fast Fourier transform. Application of the spectral technique to layered media has been effected by applying the cascade transmission line analogue to the plane wave spectrum, allowing reflection and transmission at each boundary between different dielectric media, taking into account all subsequent boundaries, to be rapidly computed. A consequent requirement for TEM plane waves necessitated the formulation of an approximate form for the spectral filter. An incremental approach was employed to calculate the field at any plane in the medium by addition of the forward propagating wavefront to the backward propagating (reflected) wavefront. This technique was applied to predict the field radiated into lossy, layered dielectric media by contacting aperture antennas.

Measurement of the field pattern of a waveguide antenna contacting tissue-simulating phantoms was carried out, validating the field prediction method in both homogeneous water and bi-layered resin/water structures. Further validation was achieved by comparing results with those of previously reported simulation methods for bi-layered structures.

The field measurements also served to illuminate the effect of employing this approximate form of the spectral filter. Band-limiting the propagating spectrum when layers are present leads to inaccuracies when the aperture distribution represents a wide spectral bandwidth source. This effect is negligible in high permittivity media but may become significant for very low permittivity media and small aperture sources. The spectral diffraction/cascade algorithm has provided good agreement with measurements in the situations considered.

The field prediction method has enabled the development of a theoretical model for calculating the radiometric temperature of layered tissue structures having any given temperature distribution. The model was formulated by analysing coherent radiative transfer within a system consisting of a radiometer probe in contact with a dielectric half space. A microwave radiometer operating at a centre fequency of 4.6 GHz has been constructed and evaluated during this study and was used to collect radiometric data in tissue-equivalent phantoms. Good agreement was found between these measurements and simulations using the temperature prediction model, thus validating this model and providing further validation of the field prediction algorithm.

This research has shown the capability of microwave radiometry for sensing temperature at depth in tissue. A radiometer frequency of 4.6 GHz gave a compromise between radiation penetration depth and spatial resolution. It was found that the depth of view is the factor which predominantly restricts the usefulness of radiometry.

In a future system, a lower frequency of, perhaps, 2 GHz should be employed; even so, the depth of view of microwave radiometers is fundamentally restricted by low signal to noise and high microwave attenuation in tissue. The prediction methods described here could be used to deduce the optimum frequency for a particular application.

The primary criterion for a successful thermometry system, both for diagnostic applications and for monitoring hyperthermia treatment, is the ability to provide reconstruction of internal temperature distributions. A common simplification used in the past by many workers when interpreting results has been to assume homogeneous tissue. It has been shown here that tissue layers greatly influence both the absolute values of measured temperature and the spatial resolution of scanning techniques. Correct interpretation of radiometric data in terms of internal temperature distribution cannot be achieved without knowledge of the dielectric structure of the medium under investigation. The probe type and its dimensions also influence radiometric measurements. Employing these prediction methods would allow more accurate interpretation of radiometric data by allowing for the effects of tissue layers and probe type in thermal imaging and absolute temperature measurement. Reconstruction of temperature profiles from multi-frequency data [58, 61, 63] could also be improved by application of these techniques.

One of the aims of the project was to assess the feasibility of using tomographic reconstruction of radiometric data as a means of mapping the thermal distibution induced during deep hyperthermia. The computer model developed for this purpose indicated that tomographic reconstruction would give a low resolution map of differential temperature with relatively few measurements compared to the number available in X-ray tomography. This small number of data points, however, led to the reconstructions being dependent on the receiving area, positioning and the number of probes, and the position of the raised temperature region within the body contour.

Experimental verification of the computer results showed the assumed probe receiving patterns to be unrealistic for measurement in a very lossy medium. Elliptical scanning around a raised temperature region failed to produce an image. Performing linear scans around the same hot-spot produced a successful image; however, the small depth of view restricted the maximum dimension of the area which could be reconstructed. Because of this, and the relatively long measurement times needed, radiometric tomography was found not to be promising as a means of monitoring deep hyperthermia. Diagnostic applications, employing reconstruction of linear scan data may, however, be feasible but with low spatial resolution.

References

[1] BARRETT, A H, MYERS, P C
'Subcutaneous temperatures: a method of non-invasive sensing'
Science, 190 (4215), 1975, pp 669-671

[2] EDRICH, J, HARDEE, P C
'Thermography at millimetre wavelengths'
Proc IEEE, vol 62, no 10, 1974, p 1391

[3] LUDEKE, K-M, KOEHLER, J, KANZENABACH, J
'A radiation balance microwave thermograph for medical applications'
Acta Electronica, 22, 1, 1979, pp 65-69

[4] LAND, D V
'A 3 GHz clinical microwave thermography system'
IEE Colloquium Digest No 1984/36

[5] DICKE, R H
'The measurement of thermal radiation at microwave frequencies'
The Review of Scientific Instruments, Vo 17, No 7, 1946, pp 268-275

[6] MANNING, M R, CETAS, T C, MILLER, R C, OLESON, J R, CONNOR, W G, GERNER, E W
'Clinical hyperthermia: Results of a phase I trial employing hyperthermia alone or in combination with external beam or interstitial radiotherapy'
Cancer Vol 49, Jan 1982, pp 205-216

[7] LAUCHE, H M, JUNG, G M, KOTEWICZ, A, HOEN, J, GAUTHERIE, M
'Critical review of phase II therapeutic trials of radiofrequency hyperthermia (13 MHz) alone or combined with radiotherapy with special reference to head-and-neck tumours'
7th meeting of the European Society for Hyperthermic Oncology (ESHO), Paris, Sept, 1985

[8] LARKIN, J M
'A clinical investigation of total-body hyperthermia as cancer therapy'
Cancer Research, vol 39, June 1979, pp 2252-2254

[9] LAGENDIJK, J J W, HOFMAN, P, SCHIPPER, J
'A clinical computer controlled microwave hyperthermia system'
Clinical Hyperthermia: Physical and technical aspects
Univ Hospital Utrecht, The Netherlands

[10] HAND, J W, TER HAAR, G
'Heating techniques in hyperthermia'
British Journal of Radiology, vol 54, 1981, pp 443-466

[11] VAN DIJK, J D P, BLANK, L, GONZALEZ, D G
'Capacitance heating for the treatment of rectum tumours'
7th meeting of ESHO, Paris, 1985

[12] VAN RHOON, G C, VAN DER ZEE, J, BROEKMEIJER-REURNIK, M P, VISSER, P M, VAN DER BERY, P M, REINHOLD, H S
'27 MHz water-filled ridged waveguides: experimental and clinical studies'
7th meeting of ESHO, Paris, 1985

[13] SATHIASEELAN, V, ISKANDER, M F, HOWARD, G C W, CROCKER, S M, BLEEHEN, N M
'Theoretically predicted effect of phase and amplitude variations on the em power deposition patterns for the annular phased array hyperthermia system'
7th meeting of ESHO, Paris, 1985

[14] TURNER, P F
'Regional hyperthermia with an annular phased array'
IEEE Trans BME-31, No 1, 1984, pp 106-114

[15] CUDD, P, HAWLEY, M S, ANDERSON, A P, CONWAY, J
'Non-invasive phased array technique for achieving deep hyperthermia'
Proc 15th European Microwave Conference, Paris 1985
Microwave Exhibitions and Publishers Ltd, pp 661-666

[16] GABORIAUD, G
Round table discussion - Clinical thermometry; Reality
7th meeting of ESHO, Paris, 1985

[17] CETAS, T C
'Invasive thermometry'
Physical aspects of hyperthermia, Medical Physics Monograph No 8, American Institute of Physics, 1982, p231

[18] CONWAY, J, HAWLEY, M S, SEAGAR, A D, BROWN, B H, BARBER, D C
'Applied potential tomography (APT) for non-invasive thermal imaging during hyperthermia'
Electronics Letters, Vol 21, No 19, 1985, pp 836-838

[19] DICKINSON, R J, HALL, A S, HIND, A J, YOUNG, I R
'Non-invasive measurement performed in-vivo using spin-lattice relaxation time (T_1)'
7th meeting of ESHO, Paris, 1985

[20] BOLOMEY, J-Ch
'Active and passive microwave imaging: complementary approaches to remote thermal sensing in hyperthermia treatments'
IEE colloquium 'Industrial and medical applications of microwaves' Digest No 1986/73

[21] NGUYEN, D D, MAMOUNI, A, LEROY, Y, CONSTANT, E
'Simultaneous microwave local heating and microwave thermography; possible clinical applications'
Journal of Microwave Power, vol 14, No 2, 1979

[22] NGUYEN, D D, CHIVE, M, LEROY, Y, CONSTANT, E
'Combination of local heating and radiometry by microwaves'
IEEE Transactions, vol IM-29, No 2, 1980, pp 143-144

[23] STERZER, F, PAGLIONE, R, WOZNIAK, F
'A self-balancing microwave radiometer for non-invasively measuring the temperature of subcutaneous tissues during localized hyperthermia treatments of cancer'
IEEE MTT-S Digest, 1982, pp 438-440

[24] CHIVÉ, M
'Technical aspects of microwave hyperthermia controlled by microwave radiometry'
Bruker: Medical report 85/1, pp 30-34

[25] DE NEVE, W, VAN BELLE, S, LYBREERT, M, VAN LOON, R, SCHARKEN, B, DAS, F, STORME, G, BAREL, A
'Clinical use of a modified hylcar-I hyperthermia system: physical aspects and evaluation of first clinical results'
7th meeting of ESHO, Paris, 1985

[26] GAUTHERIE, M
'Temperature and blood flow patterns in breast cancer during natural evolution and following radiotherapy'
Biomedical Thermology, Alan R Liss, NY, 1982, pp 21-64

[27] POCHACZEVSKY, R, PILLARI, G, FELDMAN, F
'Liquid crystal contact thermography of deep venous thrombosis'
AJR: 138, April 1982, pp 717-723

[28] WEXLER, C E
'Diagnosing spinal problems with thermography'
Diagnostic Imaging, March 1981

[29] GAUTHERIE, M
'Improved system for the objective evaluation of breast thermograms'
11th Annual Meeting of the American Thermographic Society, Washington DC, May 1982, Biomedical Thermology, Alan R Liss, NY, 1982, pp 897-905

[30] AMALRIC, R, GIRAUD, D, ALTSCHULER, C, AMALRIC, F, SPITALIER, J M, BRANDONE, H, AYME, Y, ALVAREZ GARDIOL, A
'Does infra red thermography truly have a role in present day breast cancer management?'
Biomedical Thermology, Alan R Liss, NY, 1982, pp 269-278

[31] WATMOUGH, D J
'The role of thermographic imaging in breast screening'
Medical Images: Formation, perception and measurement, John Wiley and Sons, 1976, p142

[32] CARR, K L, EL-MAHDI, AM, SHAEFFER, J
'Dual mode microwave system to enhance early detection of cancer'
IEEE Microwave theory and techniques symposium, Washington DC, 1980

[33] BIGU-DEL-BLANCO, J
'Some special applications of microwave radiometry of biological systems'
Proc 2nd symposium on Electromagnetic Compatibility, Montreux, June 1977, pp 469-475

[34] CACAK, R K, WINANS, D E, EDRICH, J, HENDEE, W R
'Millimeter wavelength thermographic scanner'
Med Phys 8(4) 1981, pp 462-465

[35] MYERS, P C, SADOWSKY, N L, BARRETT, A H
'Microwave thermography: principles, methods and clinical applications'
Journal of Microwave Power 14 (2), 1979, pp 105-113

[36] CARR, K L, EL-MAHDI, A M, SHAEFFER, J
'Dual-mode microwave system to enhance early detection of cancer'
IEEE Transactions vol MTT-29 no 3, 1981

[37] SHAEFFER, J, CARR, K L
'Cancer detection studies using a 4.7 GHz radiometer'
Cancer Detection and Prevention, vol 4, 1981

[38] THOUVENOT, P, ROBERT, J, MAMOUNI, A, RENARD, C
'Microwave thermometry in intracranial pathology'
Biomedical Thermology, Alan R Liss, NY, 1982, pp 501-508

[39] MAMOUNI, A, NGUYEN, D D, ROBILLARD, M, CHIVÉ, M, LEROY, Y
'Thermographic microonde: nouvelles methodes diagnostiques fondées sur la mesure du bruit thermique émis par les tissus vivants'
L'Onde Electrique, 1980, vol 60, no 12, pp 30-36

[40] MAMOUNI, A, NGUYEN, D D, LEROY, Y, CONSTANT, E
'La thermographie microonde. Principe et applications biomedicales'
Journées d'études SEE, January 1979, Gif-sur-Yvette, RGE, vol 88, No 9, 1979, pp 697-702

[41] BARRETT, A H, MYERS, P C, SADOWSKY, N L
'Detection of breast cancer by microwave radiometry'
Radio Science 12 (Supplement) 1977 pp 167-171

[42] EDRICH, J, JOBE, W E
'Imaging microwave thermography'
Temperature (Am Inst Phys) 1982, p 1379-1380

[43] HAHN, G M
'Potential of hyperthermia equipment in the United States'
Invited lecture, 7th meeting of ESHO, Paris, September 1985

[44] HILL, J C, GOLDNER, R
'A stabilized broadband correlator for medical microwave thermography'
IEEE symposium on MTT, San Fransisco, CA, May 1984

[45] LAND, D V
'Radiometer receivers for microwave thermography'
Microwave Journal vol 26 No 5, 1983, pp 196-201

[46] LAND, D V
'Radiometer input circuit requirements for microwave thermography'
Electronics Letters, 19, 1983, pp 1040-1042

[47] HARDWICK, B A
'Microwave thermography and image processing'
PhD Thesis, University of Leeds, 1981

[48] PLANCOT, M, CHIVE, M, LEDER, R, GIAUX, G, PREVOST, B
'Interest of microwave radiometry at two frequencies for thermal dosimetry in microwave hyperthermia'
7th meeting of ESHO, Paris, September 1985

[49] NGUYEN, D D
'Thermographie et chauffage microonde. Contribution à la conception et à la realisation de systèmes destinés au genie biologique et medicale'
Thèse de 3e Cycle, Université de Lille, 1980

[50] ROBILLARD, M
'Contribution à l'étude des sondes et à la réconnaissance d'objet thermique par la thermographie microonde (TMO)'
Thèse de 3e Cycle, Université de Lille, 1981

[51] NGYUEN, D D, ROBILLARD, M, CHIVÉ, M, LEROY, Y, AUDET, J, PICHOT, Ch, BOLOMEY, J Ch
'Microwave thermography; the modelling of probes; an approach toward thermal pattern recognition'
Proc 10th European Microwave Conference, Warsaw, 1980, pp 232-236

[52] ENEL, L, LEROY, Y, VAN DE VELDE, J C, MAMOUNI, A
'Improved recognition of thermal structures by microwave radiometry'
Electronics Letters, vol 20, No 7, 1984, pp 293-294

[53] MAMOUNI, A, VAN DE VELDE, J C, LEROY, Y
'A new correlation radiometer for microwave thermography'
Electronics Letters, vol 17, no 16, 1981

[54] MAMOUNI, A, LEROY, Y, VAN DE VELDE, J C, BELLARBI, L
'Introduction to correlation microwave thermography'
Journal of Microwave Power, 18 (3), 1983, pp 285-293

[55] LUDEKE, K M, SCHIEK, B, KOHLER, J
'Radiation balance microwave thermograph for industrial and medical applications'
Electronics Letters vol 14, No 6, 1978, pp 194-196

[56] LUDEKE, K M, KOHLER, J
'Microwave radiometric system for biomedical "True Temperature" and emissivity measurements'
Journal of Microwave Power, 18 (3), 1983, pp 277-283

[57] OSTERRIEDER, V S, SCHALLER, G
'Ein Mikrowellen-Radiometer für medizinische anwedungen'
Frequenz, 37 (1), 1983, pp 7-12

[58] SCHALLER, G
'Inversion of radiometric data from biological tissue by an optimization method'
Electronics Letters, vol 20, no 9, 1984

[59] HASLAM, N C, GILLESPIE, A R, HASLAM, C G T
'Aperture synthesis thermography - a new approach to passive microwave temperature measurements in the body'
Proc IEEE, MTT, 1984

[60] GILLESPIE, A R, HASLAM, C G T, HASLAM, N C
'Aperture synthesis thermography'
Proc 14th European Microwave Conference, Microwave Exhibitions and Publishers Ltd

[61] EDENHOFER, P
'Electromagnetic remote sensing of the temperature profile in a stratified medium of biological tissues by stochastic inversion of radiometric data'
Radio Science, volume 16, No 6, 1981, pp 1065-1069

[62] EDENHOFER, P, GRUNER, K, STEINER, H, SUSS, H
'Near-field characteristics of antenna sensors for microwave diagnosis: preliminary results of multispectral radiometric experiments'
Biomedical thermology, Alan R Liss, NY, 1982, pp 523-537

[63] BARDATTI, F, SOLIMINI, D
'Radiometric sensing of biological layered media'
Radio Science, volume 18, No 6, pp 1393-1401, 1983

[64] BARDATTI, F
'Physical models and computational techniques in microwave hyperthermia and thermography'
Proc 15th European Microwave Conference, Paris, 1985, Microwave Exhibitions and Publishers Ltd, pp 67-76

[65] ULABY, F T, MOORE, R K, FUNG, A K
Microwave remote sensing - active and passive
Volume 1: Microwave remote sensing fundamentals and radiometry
Addison Wesley, 1981

[66] TSANG, L, KONG, J A, SHIN, R T
Theory of microwave remote sensing
John Wiley and Sons, 1985

[67] GUY, A W
'Electromagnetic fields and relative heating patterns due to a rectangular aperture in direct contact with bilayered biological tissue'
IEEE Transactions, vol MTT-19, No 2, 1971, pp 214-223

[68] VILLENEUVE, A T
'Admittance of waveguide radiating into a plasma environment'
IEEE Transactions, vol AP-13, 1965, pp 115-121

[69] HARRINGTON, R F
Time harmonic electromagnetic fields
McGraw-Hill, 1961

[70] GUY, A W
'Analyses of electromagnetic fields induced in biological tissues by thermographic studies on equivalent phantom models'
IEEE Transactions, vol MTT-19, No 2, 1971, pp 205-214

[71] TURNER, P F, KUMAR, L
'Computer solution for applicator heating patterns'
National Cancer Institute monograph no 61: Cancer therapy by hyperthermia, drugs and radiation, pp 521-523

[72] CHEUNG, A Y, GOLDING, W M, SAMARAS, G M
'Direct contact applicators for microwave hyperthermia'
Journal of Microwave Power 16(2), 1981, pp 151-159

[73] TEOODRIDIS, V, SPHICOPOULOS, T, GARDIOL, F R
'The reflection from an open-ended rectangular waveguide terminated by a layered dielectric medium'
IEEE Transactions vol MTT-33, No 5, 1985, pp 359-366

[74] GOODMAN, J W
Introduction to Fourier Optics
McGraw Hill Book Co, 1968

[75] SHEWELL, J R, WOLF, E
'Inverse diffraction and a new reciprocity theorem'
J Opt Soc of America 58 (12), 1968, pp 1596-1603

[76] CLEMMOW, P C
The plane wave spectrum representation of electromagnetic fields
International series of monographs in electromagnetic waves, volume 12, Pergamon Press, 1966

[77] BRACEWELL, R
The Fourier transform and its applications
McGraw-Hill, 1965

[78] HOLDEN, G J, ANDERSON, A P, CHAMBERS, B
'A diffraction technique for the prediction of effects of space frame radome structures on the performance of reflector antennas'
Proc International Conference on Antennas and Propagation (ICAP), 1985, p158-161

[79] ANDERSON, A P, COOK, G G
'Incremental propagation procedure for calculating scattered fields from arbitrary conductors'
Proc 15th European Microwave Conference, Paris, 1985, Microwave Exhibitions and Publishers Ltd, pp 213-218

[80] CHEN, H C
Theory of electromagnetic waves: a coordinate-free approach
McGraw-Hill, 1983

[81] GUY, A W, LEHMANN, J F
'On the determination of an optimum microwave diathermy frequency for a direct contact applicator'
IEEE Transactions, vol ME-13, 1966, pp 76-87

[82] GAJDA, G, STUCHLY, M A, STUCHLY, S S
'Mapping of the near-field pattern in simulated biological tissues'
Electronics Letters, vol 15, No 4, Feb 1979, pp 120-121

[83] STUCHLY, M A, STUCHLY, S S
'Dielectric properties of biological substances - tabulated'
Journal of Microwave Power 15(1), 1980, pp 19-26

[84] HAND, J W
'Microwave Heating Patterns in simple tissue models'
Phys Med Biol, vol 22, No 5, 1977, pp 981-987

[85] SCHEPPS, J L, FOSTER, K R
'The UHF and microwave dielectric properties of normal and tumour tissues: variation in dielectric properties with tissue water content'
Phys Med Biol, 1980 Vol 25, No 6, pp 1149-1159

[86] PEDERSEN, P C, JOHNSON, C C, DURNEY, C H, BRAGG, D G
'Microwave reflection and transmission measurements for pulmonary diagnosis and monitoring'
IEEE Trans Vol BME-25, no 1, Jan 1978

[87] HAND, J W, ROBINSON, J E, SZWARNOWSKI, S, SHEPPARD, R, GRANT, E H
'A physiologically compatible tissue equivalent liquid bolus for microwave heating of tissues'
Phys Med Biol, 1979, vol 24, No 2, pp 426-431

[88] LAGENDIJK, J J W, NILSSON, P
"Hyperthermia dough: a fat and bone equivalent phantom to test microwave/radiofrequency hyperthermia heating system'
Phys Med Biol, vol 30 No 7, 1985, pp 709-712

[89] BERTAUD, A-J, HOFFMAN, F, MAYAULT, J-F
'Complex frequency perturbation of a microwave cavity containing lossy liquid'
Journal of Microwave Power, 10(3), 1975

[90] LEWIN, L
Advanced theory of waveguides
Published for "Wireless Engineer" by Iliffe and Sons Ltd, 1951

[91] COMPTON, R T
'The admittance of aperture antennas radiating into lossy media'
Rep 1691-5, Ohio State Univ, Antenna Lab Research Foundation, 1964

[92] GALEJS, J
Antennas in inhomogeneous media
International series of monographs in electromagnetic waves, volume 15, Pergamon Press, 1969

[93] REICH, H J, ORDUNG, P F, KRAUSS, H L, SKALNIK, J G
Microwave theory and techniques
D Van Nostrand and Co Inc, Princeton, NJ

[94] CHANDRASEKHAR, S
Radiative transfer
Dover Publications Inc, N York, 1960

[95] ROBILLARD, M, CHIVÉ, M, AUDET, J, PICHOT, Ch, BOLOMEY, J Ch
'Microwave thermography - characteristics of waveguide applicators and signatures of thermal structures'
Journal of Microwave Power, 17(2), 1982, pp 97-105

[96] MIYAKAWA, M
'Study on microwave thermography - application to the estimation of subcutaneous temperature profiles'
The transactions of the IECE of Japan vol E64, no 12, 1981, pp 786-792

[97] STOGRYN, A
'The Brightness temperature of a vertically structured medium'
Radio Science, vol 5, no 12, 1970, pp 1397-1406

[98] LANDAU, L D, LIFSHITZ, E M
Electrodynamics of continuous media
Pergamon Press, 1960

[99] HOTTEL, H C, SAROFIM, A F
Radiative transfer
McGraw Hill Book Company, 1967

[100] BURDETTE, E C
'Electromagnetic and Acoustic properties of tissues'
Physical Aspects of Hyperthermia, AAPM, 1982

[101] CONWAY, J, HAWLEY, M, ANDERSON, A P
'A feasibility study of microwave thermographic mapping for use during hyperthermia treatment'
Clin Phys Physiol Meas, 1984, Vol 5, No 4, pp 285-294

[102] Manual of Remote Sensing vol 1, Eds, SIMONETT, D S, ULABY, F T, American Society of Photogrammetry, 1983, pp 475-515

[103] SCHWAN, H P, FOSTER, K R
'Microwave dielectric properties of tissue'
Biophysics J, 1977, 17, p193-197

[104] SHAEFFER, J, EL-MAHDI, A M, BIELAWA, R J, REGAN, J F, CARR, K L
'Thermal drift in microwave thermography'
IEEE MTT-S digest, 1982, p441

[105] MAMOUNI, A
Thèse de 3e cycle, Université de Lille, 1978

[106] MELEK, M, ANDERSON, A P, CONWAY, J, BROWN, B H
'Measurements substantiating localised microwave hyperthermia within a thorax phantom'
Electronics Letters, 18, 1982, pp 437-8

[107] CUDD, P A, ANDERSON, A P, HAWLEY, M S, CONWAY, J
'Phased array design considerations for deep hyperthermia through layered tissue'
IEEE Transactions vol MTT-34, no 5, 1986, pp 526-631

[108] RADON, J
'On the determination of functions from their integrals along certain manifolds'
Ber Saechs Akad Wiss Leipzig, Math Physics Kl, vol 69, 1917, pp 262-277

[109] BRACEWELL, R N
'Strip integration in radioastronomy'
Aust J Phys, vol 9, 1956, pp 198-217

[110] SCUDDER, H J
'Introduction to computer aided tomography'
Proc IEEE vol 66, no 6, June 1978, pp 628-637

[111] BUDINGER, T F, GULLBERG, G T, HUESMAN, R H
"Emission computed tomography'
CT image reconstruction from projections, Ed HERMAN, G, vol 32, Topics in applied physics, Springer-Verlag, 1970, pp 147-245

[112] YOUNG, S W
Nuclear magnetic resonance imaging - basic principles, Raven Press, 1984

[113] ANDERSON, A P, ADAMS, M F
'Holographic and tomographic imaging with microwaves and ultrasound'
Inverse methods in electromagnetic imaging, NATO ASI Series, D Reidel, Holland, 1985, pp 1077-1105

[114] COLLIN, R E
Field theory of guided waves
McGraw-Hill, 1960

APPENDIX 1

The Cascade Technique

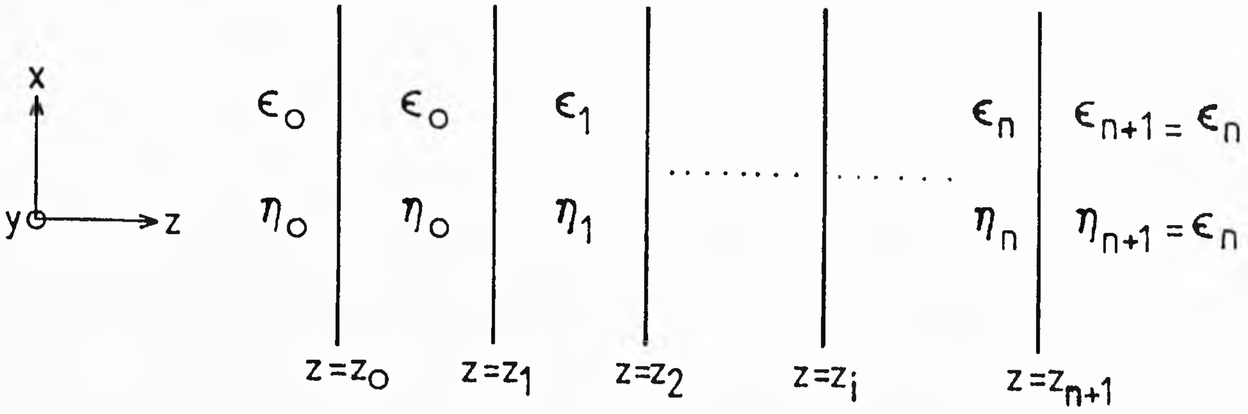

Fig. A1.1 Model for plane wave propagation in layered media
ε_i is the complex permittivity ($\varepsilon_i' + j\varepsilon_i''$) of each medium
η_i is the intrinsic wave impedence of each material

Consider Figure A1.1, where n parallel boundaries between different media are shown. Homogeneous plane waves have electric and magnetic field vectors which are transverse to the direction of propagation and therefore have similarities to the classical TEM waves that propagate on transmission lines. Indeed the propagation is similar. Consider forward and backward propagating waves exist throughout the structure shown in Figure A1.1, and that the complex wave amplitudes are represented by f(z) and b(z) respectively. Two important points should be noted; firstly the x,y,z field components of the plane waves propagating in the media are always determinable if the complex wave amplitude is known. Secondly, that to satisfy boundary conditions (and obtain a solution) all that is necessary is that the tangential field components across the boundary are continuous across it [114].

If $\varepsilon_i = \varepsilon_0$ for all i then $f(z_0)$, $b(z_0)$ are related to $f(z_1)$ and $b(z_1)$ as follows:

$$\begin{bmatrix} f(z_0) \\ b(z_0) \end{bmatrix} = \begin{bmatrix} e^{j\theta_0} & 0 \\ 0 & e^{-j\theta_0} \end{bmatrix} \begin{bmatrix} f(z_1) \\ b(z_1) \end{bmatrix}$$

where $\theta_0 = k(z_1 - z_0)/\cos \nu_0$ (electrical length),

k_0 is the propagation constant,

ν_0 is the angle of incidence (angle between direction of propagation of waves and $\hat{\underline{z}}$)

This can be equated to the transmission line case shown in figure A1.2, for this equivalent system it can be imagined that the

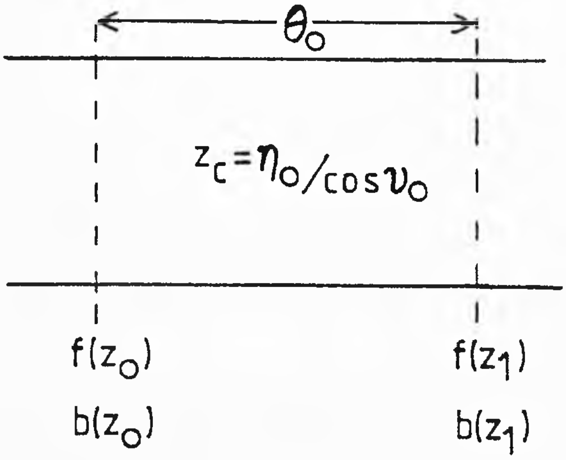

Fig. A1.2 Transmission line equivalent
Z_c is the characteristic wave impedence of the transmission line

y and x components of the incident wave fields are being propagated. This choice of Z_c is only appropriate for TEM plane waves, consequently in general is not applicable for inhomogeneous plane waves. Z_c could be chosen in figure A1.2 to be η_0, in which case the transverse field components of the incident wave would be propagating on the transmission line; this choice of Z_c however, would not work for propagation from one medium to another of different dielectric properties.

The analogy can be extended to model propagation through layered media; as a first step consider $\varepsilon_0 \neq \varepsilon_1$, $\varepsilon_i = \varepsilon_1$ for all

$i > 1$. Let $f(z_i-)$ and $b(z_i-)$ represent the complex wave amplitudes at z_i but still in medium $i-1$. In general, any wave incident on the boundary $z = z_1$ will create a reflected and transmitted wave; the proportion of the incident wave given to each is governed by the reflection and transmission associated with that boundary and the angle of incidence ν_0. If the waves $f(z)$ and $b(z)$ are propagating at an angle ν_0 at $z = z_1-$ then by Snell's law at $z = z_2-$ they will be propagating at an angle ν_1 given by

$$\sqrt{\varepsilon_0} \sin \nu_0 = \sqrt{\varepsilon_1} \sin \nu_1$$

where $N_0 = \sqrt{\mu_0 \varepsilon_0}$, $\mu_0 = 1$

$N_1 = \sqrt{\mu_1 \varepsilon_1}$, $\mu_1 = 1$

N_i = refractive index.

The reflection and transmission coefficients for the forward propagating case are well known and are given by the following expressions:

$$R_1 = \frac{\eta_1 \cos\nu_0 - \eta_0 \cos\nu_1}{\eta_1 \cos\nu_0 + \eta_0 \cos\nu_2}$$

$$T_1 = \frac{2\eta_1 \cos\nu_0}{\eta_1 \cos\nu_0 + \eta_0 \cos\nu_2}$$

Note that conservation of energy is maintained, ie $1 + R = T$ and that the backward propagating wave has $R_b = -R_1$ and $T_b = 1 - R_1$. The above expressions for R_1 and T_1 are determined from the boundary conditions. For the transmission line analogue choice of value for the characteristic impedances is now important, the equivalent is shown in figure A1.3.

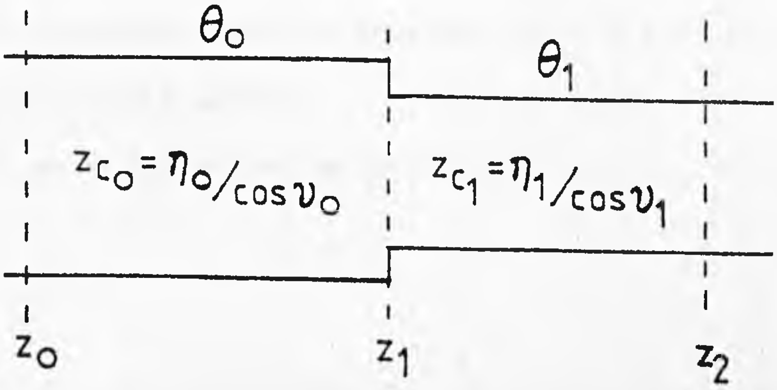

Fig. A1.3 Two media equivalent transmission line where $R_1 = \dfrac{Z_{c_1} - Z_{c_0}}{Z_{c_1} + Z_{c_0}}$ and $T_1 = \dfrac{2Z_{c_1}}{Z_{c_1} + Z_{c_0}}$.

The relationship between $f(z_1-)$, $b(z_1-)$ and $f(z_2-)$, $b(z_2-)$ is given by the following compression:

$$\begin{bmatrix} f(z_1-) \\ b(z_1-) \end{bmatrix} = \frac{1}{T_1} \begin{bmatrix} 1 & R_1 \\ R_1 & 1 \end{bmatrix} \begin{bmatrix} e^{j\theta_1} & 0 \\ 0 & e^{-j\theta_1} \end{bmatrix} \begin{bmatrix} f(z_2-) \\ b(z_2-) \end{bmatrix}$$

where $\theta_1 = k_1(z_2 - z_1)/\cos \nu_1$,

k_1 is the propagation constant for media 1 (line 1),

ν_1 is the angle of propagation (with respect to $\hat{\underline{z}}$).

If $\varepsilon_i \neq \varepsilon_{i+1}$ for all i and R_i, T_i denote the reflection and transmission coefficients appropriate to the ith boundary (when considered in the simple situation of two media as above) then

$$\begin{bmatrix} f(z_1-) \\ b(z_1-) \end{bmatrix} = \prod_{i=1}^{n} \frac{1}{T_i} \begin{bmatrix} e^{j\theta_i} & R_i e^{-j\theta_i} \\ R_i e^{j\theta_i} & e^{-j\theta_i} \end{bmatrix} \begin{bmatrix} f(z_{n+1}-) \\ b(z_{n+1}-) \end{bmatrix}$$

To apply the cascade technique to plane wave propagation through layered media and to determine the field values throughout the layers it is necessary to find the steady state reflection (Γ_i) and transmission (Π_i) coefficients for each boundary, ie $i = 1$ to n. The expressions for Γ_K and Π_K are as follows:

$$\Gamma_K = \frac{b(z_K-)}{f(z_K-)}$$

$$\Pi_K = \frac{f(z_K+)}{f(z_K-)}$$

where $b(z)$, $f(z)$ functions have been described from the previous expression. K indicates the Kth boundary and K = 1 to n. z_K^+ is 'just past' z_K in the Kth medium.

Γ_K and Π_K can be determined by evaluating

$$\begin{bmatrix} f(z_K-) \\ b(z_K-) \end{bmatrix} = \prod_{i=K}^{n} \frac{1}{T_i} \begin{bmatrix} e^{j\theta_i} & R_i e^{-j\theta_i} \\ R_i e^{j\theta_i} & e^{-j\theta_i} \end{bmatrix} \begin{bmatrix} f(z_{n+1}-) \\ b(z_{n+1}-) \end{bmatrix}$$

$$= \begin{bmatrix} A_{11}(K) & A_{12}(K) \\ A_{21}(K) & A_{22}(K) \end{bmatrix} \begin{bmatrix} f(z_{n+1}-) \\ b(z_{n+1}-) \end{bmatrix}$$

Since the nth and n+1th media are the same, $b(z_{n+1}-) = 0$.

Hence $f(z_K-) = A_{11}(K)\ f(z_n-)$

$b(z_K-) = A_{21}(K)\ f(z_n-)$

and $\Gamma_K = \dfrac{A_{21}(K)}{A_{11}(K)}$

$$\Pi_K = \frac{(\Gamma_K - R_K)e^{j2\theta_K}}{\Gamma_{K+1}(1 - R_K)}.$$

APPENDIX 2

The software for computer control of the scanning frame and automatic data logging is divided into two programs.

1) Scanning frame control and data logging: Program "SCANNER"

This program is divided into subroutines which can be called automatically by the function keys on the BBC.

(i) General scanner movement: allows movement of the object by a specified distance in a specified direction.

Inputs: distance required (in mm), direction (x or y, left or right).

(ii) Raster scan: this programme is used in measurement of field distributions and in linear scanning of temperature anomalies.

Inputs: Number of points, point separation
Number of lines, line separation
Settling time, sampling time.

The program performs a raster scan of a specified number of points in the x direction by a specified number of points in the y direction, each of a given separation. At a sample point, the system is allowed to settle and then the A to D input is sampled for a given time to collect the data. For use in field measurement, the settling and sampling time are set to a minimum (0.1 second); however, for use in radiometric scanning, the long time constant associated with the radiometer necessitates a settling time of ten seconds and a sampling time of five seconds. The data from the scan is then dumped to disk.

(iii) Pre-set position scan: for use in radiometric tomographic scanning (see Chapter 7).

Inputs: number of sample points
coordinates and angular setting of each sample point
sampling time

This program moves the scanning frame to a given number of positions whose coordinates have been input previously. The system will wait at a sample point until the required angular setting has been set manually and then sample its A to D for a given time, before moving to the next sample point. At the end of the scan the data, positional information and angular settings are dumped to disk. This data can then be processed using the VAX computer. In its present form the program will move the frame in a 60 point ellipse of any specified size.

2) Data processing and graphical output: Program "GRAPH"

This program is used with data collected in the Raster scan routine. The "GRAPH" program displays the input data to the raster program (number of points etc) and gives a choice of grey scale or line graph display on the VDU. A screen dump facility allows hard copies of these displays at the attached printer.

Additional processing and display facilities are available on the VAX 11/730 computer. The data from disk can be dumped to the VAX and displayed in grey-scale or colour two-dimensional pictorial form, or as line graphs.

Some of the results obtained in this work have also been presented in the following:

Conway, J, Hawley, M and Anderson, A P
A feasibility study of microwave thermographic mapping for use during hyperthermia treatment
Clin Phys Physiol Meas, vol 5, No 4, 1984, pp 285-294

Hawley, M, Conway, J, Anderson, A P and Melek, M
A microwave radiometer for non-invasive temperature measurement during hyperthermia treatment
Hospital Physicists Association 40th Anniversary Conference, Newcastle-upon-Tyne, September 1983
Med Phys Biol, vol 29, No 2, 1984, p 167 (Abstract)

Hawley, M, Anderson, A P, Conway, J and Melek, M
Microwave thermographic imaging for use during hyperthermia treatment of malignant disease
IEE Symposium on Medical Imaging, November 1983, Conf dig no 1983/89, pp 6/1-6/4

Conway, J, Hawley, M, Anderson, A P and Melek, M
A microwave radiometer for non-invasive temperature measurement during hyperthermia treatment
Anglo-Dutch Thermographic Society Meeting, December 1983
J Photographic Sci, vol 32, 1984, p 152 (Abstract)

Cudd, P A, Hawley, M S, Conway, J and Anderson, A P
Non-invasive phased array technique for achieving deep hyperthermia
15th Eutropean Microwave Conference, Paris, September, 1985
Microwave Exhibitions and Publishers Ltd, pp 661-666

Hawley, M S, Cudd, P, Conway, J and Anderson, A P
Microwave field predictions in layered tissue: effect on radiometer measurements
7th Meeting of the European Society for Hyperthermic Oncology, Paris, September, 1985
Strahlentherapie, vol 161, No 9, 1985, p 535 (Abstract)

Cudd, P A, Anderson, A P, Hawley, M S and Conway, J
Phased-array design considerations for deep hyperthermia through layered tissue
IEEE Transactions on Microwave Theory and Techniques, vol MTT-34, No 5, 1986, pp 526-531. Special issue on phased arrays for hyperthermia treatment of cancer.